



MONASH University

**Behaviour of Clayey Soils during Desiccation:
Experimental and Micromechanical Modelling**

By

Minh Khoa Tran

BEng (Hons), MEng.

A thesis submitted for the degree of Doctor of Philosophy at

Monash University in 2019

Department of Civil Engineering

This page intentionally left blank

Copyright Notice

© The author (2019).

I certify that I have made all reasonable efforts to secure copyright permissions for third-party content included in this thesis and have not knowingly added copyright content to my work without the owner's permission.

Abstract

Desiccation-induced soil curling and soil cracking are common phenomena in nature due to rearrangement of soil particles caused by moisture loss. The occurrence of soil curling and cracks in soils significantly reduces their load-bearing capacity and thus is the main cause of damage to many civil and geotechnical engineering earth structures. Therefore, understanding the mechanism of soil desiccation is vital to deal with these issues from both theoretical and practical standpoints.

The aims of this research are to establish a comprehensive understanding of soil curling and soil desiccation cracking as well as to develop numerical tools capable of accurately capturing the formation and development of soil curling and cracking. To achieve these aims, experimental tests were carried out on different types of soils and under different environmental conditions. It was found that clays with higher portions of Smectite underwent concave-up curling first and then convex-up curling, while Kaolin clay underwent only concave-up curling. Concave-up curling initiated when samples were close to saturation, while convex-up curling started when water content was close to the plastic limit. Factors including clay type, drying temperature, initial water content and sand content had a profound effect on moisture evaporation and therefore the water content of the sample when soil curling initiates and its lift-off height. A conceptual model based on the development of the capillary force was then proposed to explain the soil curling mechanism and the effect of different factors on soil curling. Further experiments on soil cracking revealed that cracks initiated and propagated in zones of high tensile strain concentration and undergoing a combined shear-tensile load. Wind velocity was also found to have a profound effect on soil desiccation cracking. Under high wind speeds, cracks initiated sooner at higher water contents to form a complex crack pattern with a higher number of cracks and the crack density factor was larger. However, when samples were almost completely dried, the crack density factors of all samples were similar regardless of the magnitude of wind velocity.

Based on the understanding of clayey soils obtained from the experimental tests and from experimental studies reported in the literature, DEM-based numerical frameworks were developed to predict soil curling and soil desiccation cracking. In the first DEM framework, interactions between soil-soil and soil-water at the micro-level were considered to predict behaviour of clayey samples at the lab-scale. Clayey samples were created by a mixture of two groups of DEM particles representing clay and water, and a liquid bridge force model was extended to simulate the soil-soil and soil-water interactions. This approach allowed a more accurate description of slurry soils mimicking actual experimental conditions, enabling simulations of soil particles suspended in water including their

transformation to the semi-solid state as water evaporates during drying, and thereby facilitating the comprehensive understanding of soil curling process. To enable the modelling of soil cracking process at a large scale, the second DEM framework capable of capturing hydro-mechanical behaviour of clayey soil was developed. In this approach, unsaturated flow was assumed to be governed by Darcy's law and to occur through the contact points between two DEM particles, directing from the centre of the particle with a higher water content to the centre of the particle with lower water content. The effect of volumetric deformation of the soil on its hydraulic behaviour was also taken into consideration in the proposed framework. Furthermore, to capture the mechanical behaviour of clayey soil, clayey soil was represented by a set of DEM particles, each represented a clay aggregate and the particles were linked by bonds. A cohesive model that considered a combination of tensile and shear failure modes was adopted to regulate development of cracks. A numerical algorithm was proposed to couple these two behaviours. All frameworks developed in this research were then validated against the experimental data and results obtained using the Finite Different Method. Good agreement was obtained, demonstrating that the proposed frameworks are able to capture the hydro-mechanical behaviour of clayey soil, the occurrence of soil curling and soil cracking during desiccation, as well as unsaturated flow through deformed and undeformed soil media.

This research has provided a comprehensive understanding of the macro-behaviour of clayey soils during desiccation. It has also proposed new numerical frameworks capable of providing insights into transition behaviour of clayey soils from slurry to semi-solid states involving saturated and unsaturated soil conditions, soil curling and soil cracking. The knowledge and numerical frameworks can be applied for analysis and design of civil and geotechnical engineering applications involving desiccation or unsaturated flow.

Declaration

This thesis contains no material which has been accepted for the award of any other degree or diploma at any university or equivalent institution and that, to the best of my knowledge and belief, this thesis contains no material previously published or written by another person, except where due reference is made in the text of the thesis.

Signature: Signed

Print Name: Minh Khoa Tran

Date: 26 August 2019

List of Publications

1. **Khoa M. Tran**, Ha H. Bui, Jayantha Kodikara, and Marcelo Sánchez (2019). Soil curling process and its influencing factors. *Canadian Geotechnical Journal* doi: 10.1139/cgj-2018-0489.
2. **Khoa M. Tran**, Ha H. Bui, Jayantha Kodikara, and Marcelo Sánchez (2019). A water particle approach in DEM for studying desiccation-induced curling in slurry clayey soils. *Computer and Geotechnics* (*Under review*).
3. **Khoa M. Tran**, Ha H. Bui, and Giang D. Nguyen (2019). An approach to model unsaturated flows through discrete pore-networks. *International Journal of Engineering Science* (*Under review*).
4. **Khoa M. Tran**, Ha H. Bui, et al. (2019). Soil desiccation cracking and effect of wind velocity. (*In preparation*).
5. **Khoa M. Tran**, Ha H. Bui, et al. (2019). Modelling of mixed-mode behaviour of soil cracking using a coupled hydro-mechanical DEM-based framework. (*In preparation*).
6. **Khoa M. Tran**, Ha H. Bui, Jayantha Kodikara, and Marcelo Sánchez (2018). Numerical simulation of soil curling during desiccation process. *Unsat2018 conference*, Hong Kong.

Thesis Including Published Works Declaration

I hereby declare that this thesis contains no material which has been accepted for the award of any other degree or diploma at any university or equivalent institution and that, to the best of my knowledge and belief, this thesis contains no material previously published or written by another person, except where due reference is made in the text of the thesis.

This thesis includes one paper published in peer reviewed journals. The core theme of the thesis is to establish a comprehensive understanding of soil curling and soil desiccation cracking as well as to develop numerical tools capable of accurately capturing the formation and development of these phenomena. The ideas, development and writing up of all the papers in the thesis were the principal responsibility of myself, the student, working within the Department of Civil Engineering under the supervision of Dr. Ha Hong Bui. The inclusion of co-authors reflects the fact that the work came from active collaboration between researchers and acknowledges input into team-based research.

In the case of Chapter 3 my contribution to the work involved the following:

Thesis Chapter	Publication Title	Status	Nature and % of student contribution	Co-author name(s) Nature and % of Co-author's contribution*	Co-author(s), Monash student Y/N*
Chapter 3	<i>Soil curling process and its influencing factors</i>	<i>Accepted</i>	<i>70%. Idea, doing experiments, analysis, interpretation and writing up</i>	<ol style="list-style-type: none"> 1. <i>Ha H. Bui, technical review, interpretation and input into manuscript 20%</i> 2. <i>Jayantha Kodikara, Data analysis, input into manuscript 5%</i> 3. <i>Marcelo Sanchez, input into manuscript 5%</i> 	<i>No</i>

I have renumbered sections of published papers in order to generate a consistent presentation within the thesis.

Student signature: Signed

Date: 26 August 2019

The undersigned hereby certify that the above declaration correctly reflects the nature and extent of the student's and co-authors' contributions to this work. In instances where I am not the responsible author I have consulted with the responsible author to agree on the respective contributions of the authors.

Main Supervisor signature: Signed

Date: 26 August 2019

Acknowledgements

First of all, I would like to thank my primary supervisor Dr. Ha Hong Bui for his support, encouragement and guidance throughout my PhD journey. Thanks for giving me insightful lessons that have made my academic and personal life brighter.

I would also like to thank my associate supervisor Professor Jayantha Kodikara for his support, advice and valuable comments on my research. I would also like to express my sincere gratitude to Professor Marcelo Sanchez (Texas A&M University) and Associate Professor Giang D. Nguyen (the University of Adelaide) for reviewing and giving invaluable comments on some parts of my research.

I am grateful to Jane Moodie for helping me to improve the writing in my research papers and my thesis. Thanks to Joan Rosenthal for proofreading my thesis.

I acknowledge Monash University and Australian Research Council for providing financial support. Without this support, my PhD dream would not be fulfilled.

Thanks to my friends and colleagues at Monash, particularly Hieu Tran, for helping me to have a joyful and unforgettable time in Melbourne.

I would like to express my heartfelt gratitude to my parents, brothers and sisters for their endless love, encouragement and belief in me. Finally, my special thanks go to my wife Gam Cao and my daughter Nari Tran for their endless love, patience and sacrifice. Thank you for always making me happy and giving me strength to successfully complete my research.

Khoa Tran

August 2019

Table of Contents

Copyright Notice	i
Abstract	ii
Declaration	iv
List of Publications	v
Thesis Including Published Works Declaration	vi
Acknowledgements	viii
Table of Contents	ix
List of Figures	xiii
List of Tables	xxii
Chapter 1. Introduction	1
1.1. Introduction.....	1
1.2. Research Aims	4
1.3. Thesis Structure	4
Chapter 2. Literature Review	7
2.1. Introduction.....	7
2.2. Studies of Soil Curling	7
2.2.1. General observations.....	7
2.2.2. Soil curling mechanism	9
2.2.3. Factors influencing soil curling.....	11
2.3. Studies of Desiccation Cracking in Soils	13
2.3.1. General observations.....	13
2.3.2. Soil cracking mechanism	15
2.3.3. Factors influencing soil cracking	18
2.4. Numerical Methods for Modelling Soil Curling and Soil Cracking.....	26
2.4.1. Numerical methods for modelling soil curling.....	26
2.4.2. Numerical methods for modelling soil cracking	27
2.5. Conclusions.....	37
Chapter 3. Experimental Investigation of Soil Curling	40

3.1.	Introduction.....	40
3.2.	Materials and Methods	41
3.2.1.	Materials.....	41
3.2.2.	Methods	43
3.3.	Curling Process of Werrabee, Altona North and Kaolin NY Clays	45
3.3.1.	Water evaporation.....	45
3.3.2.	Curling process	46
3.3.3.	Curling water content	50
3.4.	Curling Mechanism	53
3.5.	Factors Influencing Soil Curling	55
3.5.1.	Effect of clay types	55
3.5.2.	Effect of initial water content	57
3.5.3.	Effect of drying temperature	59
3.5.4.	Effect of sand content	62
3.6.	Conclusions	65
Chapter 4.	Experimental Investigation of Soil Cracking	67
4.1.	Introduction.....	67
4.2.	Material and Methods	68
4.2.1.	Material and sample preparations	68
4.2.2.	Wind tunnel design.....	69
4.2.3.	Test procedures	71
4.2.4.	Digital image correlation technique	73
4.3.	Desiccation Cracking and Development of Strain Fields	74
4.3.1.	Rectangular sample	74
4.3.2.	Circular sample	81
4.4.	Effect of Wind on Desiccation Cracking.....	87
4.4.1.	Drying conditions and changes of water content.....	87
4.4.2.	General observations of crack networks	89
4.4.3.	Crack density factor and number of cracks	91
4.4.4.	Cracking water content	93

4.5. Conclusions.....	94
Chapter 5. A Micromechanics Approach to Model Curling of Slurry Soils	96
5.1. Introduction.....	96
5.2. Proposed Numerical Approach.....	98
5.2.1. DEM overview.....	98
5.2.2. A water particle approach	99
5.3. Validation of the Proposed Water Particle Approach.....	103
5.3.1. Sample preparation and input parameters.....	103
5.3.2. Water evaporation process	104
5.3.3. Calibration of water content shifting function for DEM simulations.....	105
5.3.4. Simulations of the desiccation process	107
5.4. Applications	111
5.4.1. Effect of soil layer thickness.....	111
5.4.2. Effect of water evaporation rate	114
5.5. Conclusions.....	115
Chapter 6. Modelling Unsaturated Flow through Discrete Pore-networks.....	117
6.1. Introduction.....	117
6.2. The Proposed Approach.....	119
6.2.1. General assumptions	119
6.2.2. Governing equation.....	120
6.2.3. The inter-particle diffusivity	123
6.2.4. Numerical time-step	125
6.2.5. Boundary conditions	126
6.2.6. Hydraulic properties	126
6.3. Numerical Validation.....	127
6.3.1. Infiltration tests.....	127
6.3.2. Evaporation test.....	136
6.4. Modelling Aspects of the Proposed Approach.....	140
6.4.1. The inter-particle diffusivity calculation approach.....	140
6.4.2. Effect of the number of updating cycles	141

6.4.3. Effect of the particle size	142
6.5. Conclusions	143
Chapter 7. Micromechanics Modelling of Coupled Hydro-Mechanical Behaviour of Soil during Desiccation	144
7.1. Introduction	144
7.2. The Hydro-Mechanical Framework.....	146
7.2.1. General assumptions	147
7.2.2. Governing Equations.....	148
7.2.3. Constitutive relations	153
7.2.4. Numerical Solutions	156
7.3. Numerical Validation.....	159
7.3.1. Model descriptions	159
7.3.2. Model parameters	160
7.3.3. Numerical prediction of experimental results.....	167
7.4. Conclusions	178
Chapter 8. Conclusions and Recommendations	179
8.1. Conclusions	179
8.1.1. Soil curling.....	179
8.1.2. Soil desiccation cracking	180
8.1.3. Development of numerical tools.....	180
8.2. Recommendations for Future Work	182
References	184

List of Figures

Figure 2.1. Shape of soil media when soil curling occurs: (a) concave-up curling; (b) convex-up curling.8

Figure 2.2. Evolution of a cross-section of a soil sample during drying (Zielinski et al. 2014).8

Figure 2.3. Profiles of the shrinkage strain increment and shrinkage stress increment: (a) concave-up curling; (b) convex-up curling (Kodikara et al. 2004).9

Figure 2.4. Conceptual model to explain concave-up curling (Zielinski et al. 2014). 10

Figure 2.5. Final stage of the desiccation tests: (a) pure kaolin; (b) mixture of kaolin and sand (Zielinski et al. 2014). 11

Figure 2.6. Mud curls occurred in a depression (Longwell 1928). 12

Figure 2.7. Evolution of a crack pattern of a specimen during desiccation (Tang et al. 2011c). 13

Figure 2.8. Non-orthogonal patterns: (a) mud cracks on a playa surface (Longwell 1928); (b) cracks in a slurry soil sample 3.4mm thick (Corte and Higashi 1960). 13

Figure 2.9. (a) layer thickness and surface crack ratio R_{sc} ; (b) void ratio and degree of saturation (Tang et al. 2011c). 14

Figure 2.10. Interfacial fracture markings in a sample 24mm thick (Corte and Higashi 1960). 14

Figure 2.11. Surface depression on the crack tip (Tollenaar 2017). 15

Figure 2.12. The development of tensile stresses and cracks during desiccation (Vo et al. 2018). 16

Figure 2.13. Strain field in a portion of a kaolin soil sample: (a) strain in x direction; (b) principal strain in zone II (Wei et al. 2016). 17

Figure 2.14. The mechanism of desiccation cracking in the micro-view (Shin and Santamarina 2011). 17

Figure 2.15. Changes of crack surface ratio during drying (Tang et al. 2010). 19

Figure 2.16. Cracking patterns of samples under different drying temperature (Uday and Singh 2013). 19

Figure 2.17. Crack patterns of bentonite samples dried under different relative humidity and a temperature of 50°C (Uday and Singh 2013).20

Figure 2.18. Crack patterns of a sample under different wetting-drying cycles (Tang et al. 2011a).....	21
Figure 2.19. Effect of thickness of soil layer: (a) effect on thickness on cracking water content (Corte and Higashi 1960); (b) effect of thickness on crack patterns (Lakshmikantha et al. 2012).....	21
Figure 2.20. Effect of sample size on characteristics of crack patterns (Lakshmikantha et al. 2012).....	22
Figure 2.21. Effect of bottom contact surface: (a) characteristics of crack patterns; (b) changes of adhesion (Corte and Higashi 1960); (c) crack patterns of ground coffee in moulds with different coating surface (Groisman and Kaplan 1994).	22
Figure 2.22. Cracks pattern: (a) Merri Creek clay sample; (b) potato starch sample (Costa et al. 2013).	24
Figure 2.23. Fabric parking in water with salt concentrations: (a) in fresh water, (b) in sea water; (c) in water with high salt concentration (Zhang et al. 2017).	24
Figure 2.24. Crack patterns in samples with different salt concentration (Zhang et al. 2017).....	24
Figure 2.25. Crack patterns of soils with different fibre contents (Tang et al. 2012).	25
Figure 2.26. Estimated suction curves for top and bottom halves of a specimen (Kodikara et al. 2004).....	26
Figure 2.27. Numerical results of soil curling (Kodikara et al. 2004).	27
Figure 2.28. Modified Mohr-Coulomb criterion (Trabelsi et al. 2012).	28
Figure 2.29. Typical crack patterns (Trabelsi et al. 2012).	28
Figure 2.30. Minor principal stress developed in a numerical sample: (a) stress field in half of the sample; (b) stress profile along the sample surface (Peron et al. 2013)	28
Figure 2.31. Crack patterns in soil samples with different thickness: (a-c) experimental results; (d-f) top views of the numerical samples; (g-i) distribution of the minimum principal stress on numerical samples (Sánchez et al. 2014).	29
Figure 2.32. Cracks in thick layer: (a) field observation; (b) numerical result (Sánchez et al. 2014).....	29
Figure 2.33. Numerical results with the coupled hydro-mechanical frameworks by FEM: (a) crack patterns in samples with different thickness (Hirobe and Oguni 2016); (b) development of cracks (Vo et al. 2017).....	30
Figure 2.34. Numerical results with the coupled hydro-mechanical frameworks by FEM: (a) evolution of moisture during drying (Levatti et al. 2019); (b) evolution of degree of saturation during drying (Vo et al. 2017).....	30

Figure 2.35. Numerical results of soil cracking with FDM: (a) crack patterns in experimental and numerical samples; (b) effect of hydraulic conductivity on soil cracking (Stirling et al. 2017).	31
Figure 2.36. Development of cracks in experimental and numerical samples (Tran 2019).	32
Figure 2.37 Evolution of water content in experimental and numerical samples (Tran 2019).	32
Figure 2.38. Initiation and development of cracks by using DEM (Peron et al. 2009a): (a) initiation of crack; (b) after a crack developed in the simulation with homogeneous shrinkage; (c) initiation of crack; (d) after a crack developed in the simulation with non-homogeneous shrinkage.	33
Figure 2.39. Development of crack patterns in experimental and numerical samples (Sima et al. 2014).....	34
Figure 2.40. Development of the crack patterns in both experimental and numerical samples (Guo et al. 2017).	34
Figure 2.41. Effects of parameters for the soil-soil interaction on numerical results (Sima et al. 2014).....	35
Figure 2.42. Discretisation of the numerical domain (Amarasiri et al. 2011b).....	35
Figure 2.43. Development of cracks in experimental and numerical tests (Amarasiri et al. 2011b).....	35
Figure 2.44. The development of cracks in a numerical soil domain (Gui et al. 2016)...	36
Figure 2.45. The development of cracks with different random ratios of properties: (a) random ratio = 5%, (b) random ratio =10%, (c) random ratio =30%, (d) random ratio =50%; (e) random ratio =0% (Gui and Zhao 2015).....	37
Figure 3.1. (a) SWRCs of Werribee, Kaolin NY and Altona North clay (the volumetric water content is roughly converted to the gravimetric water content in the case of Altona North clay); (b) particle size distribution (Nahlawi 2004; Shannon 2013).	42
Figure 3.2. Experimental set-up (side view).....	44
Figure 3.3. (a) typical drying conditions; (b) water content and water evaporation rate of Werribee clay; (c) water content and water evaporation rate of Altona North clay; (d) water content and water evaporation rate of Kaolin NY clay.	46
Figure 3.4. Time-lapse of shrinkage process of Werribee clay sample – test CL1_2. ...	47
Figure 3.5. Shrinkage process of Werribee clay sample (test CL1_2).....	48
Figure 3.6. Shrinkage process of Altona North clay sample (test CL2_1).	48
Figure 3.7. Shrinkage process of Kaolin NY clay sample (test CL3_1).	48

Figure 3.8. Soil curling mechanism: (a) soils start settling down; (b) soils detach from the mould; (c) concave-up curling starts; (d) concave-up curling reaches maximum elevations; (e) curved edges retreat; (f) convex-up curling begins and develops.	54
Figure 3.9. Effect of initial water content on water evaporation: (a) changes of water content during drying; (b) changes of drying rate during drying.	57
Figure 3.10. Effect of initial water content on soil curling: (a) water contents at particular stages; (b) the maximum lift-off height.	58
Figure 3.11. Effect of drying temperature on water evaporation: (a) changes of water content during drying; (b) changes of drying rate during drying.	59
Figure 3.12. Top and bottom strains of samples dried at different temperatures: (a) strains of samples dried at different temperatures; (b) strains of sample dried at 24.5°C (T1_1); (c) strains of sample dried at 27.8°C (T2_2); (d) strains of sample dried at 39.0°C (T3_2).	61
Figure 3.13. Transition period from concave-up curling to convex-up curling in sample dried at 39.0°C (T3_2): (a) concave-up with highest edges positions, w=57.45%; (b) convex-up curling started but edges still curled up, w=46.69%; (c) convex-up developed but edges still curled up, w=43.28%; (d) only convex-up curling, w=36.59%.	61
Figure 3.14. Effect of drying temperature on soil curling: (a) water contents at particular stages; (b) maximum lift-off height.	62
Figure 3.15. Effect of sand on water evaporation: (a) changes of water content during drying; (b) changes of drying rate during drying.	63
Figure 3.16. Soil curling of samples with different sand/clay fractions at the end of their drying processes: (a) sand/clay fraction of 0%; (b) sand/clay fraction of 10%; (c) sand/clay fraction of 20%; (d) sand/clay fraction of 30%.	64
Figure 3.17. Effect of sand on soil curling: (a) water contents at particular stages; (b) maximum lift-off height.	64
Figure 4.1. Design drawing of the miniature wind tunnel used in this study.	69
Figure 4.2. Wind tunnel body after fabricated.	70
Figure 4.3. Performance curve of fans (Fantech 2008).	70
Figure 4.4. Experimental setup for exploring the soil cracking process and strain development on the sample surfaces.	71
Figure 4.5. Typical sample surface for DIC analysis.	72
Figure 4.6. Experimental set-up for exploring the effect of wind velocity on soil cracking.	72

Figure 4.7. Main steps in image comparing work: (a) defining a square-grid system and subsets in the reference image; (b) finding locations of subsets in the deformed image; (c) obtaining displacement after matching deformed image with reference image; (d) calculating the strain field.	74
Figure 4.8. Evolution of water content in the rectangular samples during drying.	75
Figure 4.9. Development of the crack network on sample SR1.	76
Figure 4.10. ϵ_1 developed on the surface of sample SR1.	77
Figure 4.11. ϵ_2 developed on the surface of sample SR1.	78
Figure 4.12. ϵ_{12} developed on the surface of sample SR1.	79
Figure 4.13. Locations for strain measurements.	80
Figure 4.14. Development of axial strains of the selected locations.	81
Figure 4.15. Changes in water content of circular samples.	81
Figure 4.16. Development of the crack network on sample SC1.	82
Figure 4.17. ϵ_1 developed on the surface of sample SC1.	84
Figure 4.18. ϵ_2 developed on the surface of sample SC1.	85
Figure 4.19. ϵ_{12} developed on the surface of sample SC1.	86
Figure 4.20. ϵ_1 at the zone near cracks 1 and 2 when water content was 118.9%.	87
Figure 4.21. Drying conditions: (a) drying temperature and relative humidity; (b) wind velocity.	88
Figure 4.22. Effect of wind on water evaporation: (a) changes in water content; (b) relationship between initial drying rate and wind velocity.	88
Figure 4.23. Development of the crack network on the specimen dried under wind velocity of 0 m/s (Wind 1 -S1).	89
Figure 4.24. Development of the crack network on the specimen dried under wind velocity of 0.89 m/s (Wind 2 -S1).	90
Figure 4.25. Development of the crack network on the specimen dried under wind velocity of 1.89 m/s (Wind 3 -S1).	91
Figure 4.26. Image processing technique to calculate the area of cracks: (a) initial image of the sample surface; (b) binary image; (c) image after identifying soil cells.	92
Figure 4.27. (a) evolution of the CDF; (b) evolution of number of cracks.	93
Figure 4.28. Water content when the first crack initiated.	94
Figure 5.1. Basic contact model in DEM.	99

Figure 5.2. Water particle concept in DEM: (a) slurry clayey soils; (b) DEM model of slurry clayey soils; (c) liquid bridge model.	100
Figure 5.3. Numerical results of the RVE without hindered rotation (HR=0%) before benchmarking with experimental results: (a) changes in water content; (b) soil water retention curve (SWRC).....	106
Figure 5.4. (a) suction ratio between the experiment and simulation with $f(w) = 1.0$ and HR=0%; (b) SWRC after using the water content shifting function $f(w)$	107
Figure 5.5. Water content of the sample in the simulation without hindered rotation (HR=0%).....	108
Figure 5.6. Shrinkage deformation and curling development of the Kaolin NY clay....	109
Figure 5.7. Shrinkage deformation of the sample in the simulation without hindered rotation (HR=0%).....	110
Figure 5.8. Lift-off height in the experimental and numerical tests.....	111
Figure 5.9. Variation of water content during drying (HR=50%).....	112
Figure 5.10. Numerical samples with different thickness at three drying stages (HR=50%): (a) sample with 12.4 mm thick; (b) sample with 10 mm thick; (c) sample with 8 mm thick.	112
Figure 5.11. Effect of thickness of soil layer on lift-off height (HR=50%, left edge).....	113
Figure 5.12. Effect of evaporation rate: (a) evolution of water content, (b) evolution of lift-off height (HR=50%, left edge).....	114
Figure 6.1. Concepts of the proposed approach: (a) porous medium and boundary conditions; (b) idealised system in DEM model; (c) water flow directions between some particles.	120
Figure 6.2. Inflows and outflows through particle i (or through an imaginary equivalent V_i continuum volume occupied by particle i).	122
Figure 6.3. Hydraulic properties of an unsaturated porous medium: (a) soil water retention curve; (b) hydraulic conductivity curve.....	127
Figure 6.4. Boundary conditions of infiltration tests: (a) constant water content boundary; (b) constant flux boundary.	128
Figure 6.5. DEM model discretisation with cubic packing: (a) 2D model; (b) 3D model.	128
Figure 6.6. DEM model discretisation with random packing: (a) particle size distribution; (b) 2D and 3D models with the particle size distribution 1; (c) 2D and 3D models with the particle size distribution 2.....	129

Figure 6.7. Numerical results obtained from the FDM simulation and DEM simulations with cubic packing for the test with the constant water content boundary: (a) water content profile of the soil column; (b) relative error.....	131
Figure 6.8. Water distribution in the soil column after 15s due to infiltration with the constant water content boundary: (a) 2D DEM simulation with cubic packing; (b) 3D DEM simulation with cubic packing; (c) FDM simulation.	131
Figure 6.9. Water content profiles of the soil column due to infiltration with the constant water content boundary: (a) 2D DEM simulation with particle distribution 1, (b) 2D DEM simulation with particle distribution 2, (c) 3D DEM simulation with particle distribution 1, (d) 3D DEM simulation with particle distribution 2.	132
Figure 6.10. Water distribution in the soil column during infiltration with the constant water content boundary: (a) 2D simulation with particle distribution 1; (b) 3D DEM simulations with particle distribution 1; (c) 2D simulation with particle distribution 2; (d) 3D DEM simulations with particle distribution 2.	133
Figure 6.11. Numerical results obtained from the FDM simulation and DEM simulations with cubic packing for the infiltration test with the constant flux boundary: (a) water content at different depths; (b) relative error.	135
Figure 6.12. Water content profiles of the soil column due to infiltration with the constant flux boundary: (a) 2D DEM simulation with particle distribution 1, (b) 2D DEM simulation with particle distribution 2, (c) 3D DEM simulation with particle distribution 1, (d) 3D DEM simulation with particle distribution 2.	135
Figure 6.13. Water distribution in the soil column after 15s due to infiltration with the constant flux boundary: (a) 2D and 3D DEM simulations with cubic packing; (b) 2D and 3D DEM simulations with particle distribution 1; (c) 2D and 3D DEM simulations with particle distribution 2.....	136
Figure 6.14. Numerical results of the evaporation test obtained from the FDM simulation and DEM simulations with cubic packing: (a) water content profile; (b) relative error..	137
Figure 6.15. Water content profiles of the soil column due to water evaporation: (a) 2D DEM simulation with particle distribution 1; (b) 2D DEM simulation with particle distribution 2; (c) 3D DEM simulation with particle distribution 1; (d) 3D DEM simulation with particle distribution 2.	137
Figure 6.16. Water distribution in the soil column during water evaporation: (a) 3D DEM simulations with particle distribution 1; (b) 3D DEM simulations with particle distribution 2.	139
Figure 6.17. DEM simulation results with different inter-particle diffusivity calculation methods: (a) water content profile, (b) maximum relative error.	141

Figure 6.18. DEM simulation results with different numbers of updating cycles: (a) water content profile; (b) maximum relative error.	141
Figure 6.19. DEM simulation results with different particle size: (a) water content profile; (b) maximum relative error.	142
Figure 7.1. Concepts of the hydro-mechanical model: (a) clayey aggregates and boundary conditions; (b) idealised system in DEM model; (c) water flow directions between some particles.	148
Figure 7.2. (a) forces and moments acting on a particle; (b) forces at a contact.	152
Figure 7.3. Hydraulic constitutive relation: (a) soil water retention curve; (b) hydraulic conductivity curve.	154
Figure 7.4. Stress-displacement behaviour: (a) tensile stress; (b) shear stress.	156
Figure 7.5. Inflows and outflows through particle i (or through an imaginary equivalent V_i continuum volume occupied by particle i)	158
Figure 7.6. Numerical samples: (a) rectangular sample; (b) circular sample.	160
Figure 7.7. Numerical set-up of the three-point bending test.	161
Figure 7.8. Load-displacement curves of three-point bending tests.	161
Figure 7.9. Mechanical constitutive parameters for DEM modelling.	162
Figure 7.10. The shape of the sample during the free shrinkage test.	163
Figure 7.11. Results of the free shrinkage test: (a) changes in water content; (b) changes in volumetric strain.	164
Figure 7.12. Soil water retention curve of Werribee clay.	165
Figure 7.13. Water evaporation rates for the experimental data: (a) rectangular samples; (b) circular samples.	166
Figure 7.14. Evolution of water content during the simulation of the rectangular sample.	168
Figure 7.15. Development of cracks in rectangular samples: (a) experimental sample SR1; (b) numerical sample.	169
Figure 7.16. Cracks in two experimental samples: (a) sample SR1; (b) sample SR2.	170
Figure 7.17. Development of micro-cracks in the rectangular sample: (a) all micro-cracks; (b) soil-soil micro-cracks.	171
Figure 7.18. Evolution in the number of micro-cracks during the simulation of the rectangular sample: (a) the number of micro-cracks against drying time; (b) the number of micro-cracks against gravimetric water content.	172

Figure 7.19. Distribution of gravimetric water content in the numerical sample with rectangular shape at an average water content of 96.5%: (a) top view; (b) side view. 172

Figure 7.20. Evolution of water content during the simulation of the circular sample. .173

Figure 7.21. Development of cracks in the numerical sample and experimental sample (SC1). 175

Figure 7.22. Development of micro-cracks in the circular sample: (a) all micro-cracks; (b) soil-soil micro-cracks. 176

Figure 7.23. Evolution in the number of micro-cracks during the simulation of the circular sample: (a) the number of micro-cracks against drying time; (b) the number of micro-cracks against gravimetric water content..... 177

Figure 7.24. Distribution of gravimetric water content in the numerical sample with circular shape at an average water content of 71.6%: (a) top view; (b) side view. 177

Figure 7.25. SC1 sample after drying. 177

List of Tables

Table 3.1. Typical soil properties (Nahlawi 2004; Shannon 2013).	42
Table 3.2. Experimental program and conditions.....	44
Table 3.3. Summary of drying tests.	52
Table 4.1. Experimental program and conditions.....	73
Table 5.1. Parameters for the function $f(w)$	107

Chapter 1. Introduction

1.1. Introduction

Clayey soils are abundant throughout the world. Because of the molecular structures of their clay minerals and the arrangement of the mineral crystal sheets, such soils adsorb and retain a high volume of water. When these soils undergo desiccation, they shrink significantly, causing the development of curling and cracking in the soil media. Development of soil curling magnifies the formation of horizontal cracks (Berney et al. 2008; Style et al. 2011) and generates new vertical cracks, while development of desiccation cracking causes detrimental changes in physical properties of the soils. For example, cracks reduce soil strength, and increase soil compressibility and hydraulic conductivity (Morris et al. 1992; Yesiller et al. 2000). Consequently, soil curling and desiccation cracking are the root causes of many problems in engineering. For example, in geotechnical engineering, soil curling and the occurrence of cracks cause failure of slopes, embankments, dams, foundations (Foster et al. 2000; Morris et al. 1992; Take 2003; Teodosio et al. 2019) and nearby road pavements (Lytton et al. 1976). In addition, cracks create flow pathways for water, causing significant reduction in the performance of structures made of clayey soils such as dams, levees and clay liners (Albrecht and Benson 2001). In mining engineering, very deep or wide cracks often occur in mine tailings and degrade their stability. Therefore, understanding the mechanisms underlying the desiccation process in clayey soils is vital as it can be used to protect infrastructure or applications of clayey soils from the problems.

Many studies have investigated soil curling and reported that when clayey soils lose their moisture due to desiccation, they shrink significantly, causing the formation of vertical cracks. As the desiccation process continues, soil curling may occur in concern with the formation of horizontal cracks to form concave-up curling (\cup) or convex-up curling (\cap) or to form concave-up curling (\cup) first that then changes to convex-up curling (\cap). These studies have also identified influencing factors of the development of soil curling, such as the non-homogenous distribution of soil particles, clay minerals and boundary conditions (Allen 1986; Bradley 1933; Kindle 1917, 1923; Kodikara et al. 2004; Longwell 1928; Minter 1970; Style et al. 2011; Ward 1923). The occurrence of soil curling has been explained based on differential shrinkage strain (Allen 1986; Bradley 1933; Kindle 1917, 1923; Kodikara et al. 2004), or non-uniform distribution of the vertical component of surface tension and gravity force at the soil surface (Zielinski et al. 2014). However, existing studies describe the soil curling process of soil layers within the context of soil desiccation cracking and ignore the movement of the bottom face of the soil layers. In addition, these studies often use the final stage of the desiccation process to infer the soil

curling behaviour, and thus resulting in misinterpretation of the curling process. Although a recent study utilised time-varying observations of soil curling to study its mechanism, only curling of the top-soil surface was captured (Zielinski et al. 2014). In addition, no attempt has been made to quantify the effect of these factors on soil curling as well as to comprehensively discuss how these factors and the state of soil media influence the soil curling process. Therefore, further studies are required to establish a comprehensive understanding of soil curling and the influencing of factors on this phenomenon.

Many studies have investigated the formation and development of desiccation cracks and reported that soil desiccation cracking occurs when soils are fully saturated. The process of desiccation cracking occurs in the following sequence. First, cracks initiate from points inside or the boundaries of soil media and propagate towards the centre until they intersect or reach the sample boundaries again. With further drying, additional cracks initiate from existing cracks and propagate towards other existing cracks. After sufficient drying, no new cracks occur and crack patterns are formed, but existing cracks continue to widen (Corte and Higashi 1960; Costa et al. 2013; Tang et al. 2011c). This process and characteristics of crack patterns is governed by numerous factors, such as mineral composition, drying temperature, relative humidity, wetting-drying cycles, thickness and size of soil layers (Corte and Higashi 1960; Costa et al. 2013; Lakshmikantha et al. 2012; Rodríguez et al. 2007; Tang et al. 2008). However, the effect of wind velocity on desiccation cracking has not been studied, though wind velocity is one of the main factors accelerating the water evaporation process of soils (Hillel 2003).

The occurrence of desiccation cracks has been explained based on experimental observations as well as numerical results. It has been postulated that the development of tensile stress inside soil media during the desiccation process leads to desiccation cracking. When soil media undergo desiccation, tensile stresses develop due to the restrained shrinkage and cracks occur when the tensile stress reaches the tensile strength of the soil media (Corte and Higashi 1960; Konrad and Ayad 1997; Morris et al. 1992; Peron et al. 2009b). Shin and Santamarina (2011) and Tang et al. (2011c) postulated that, as water evaporates, capillary forces are generated that move soil particles away from each other, causing the formation and development of cracks. However, further studies with support of the latest techniques should be conducted to provide further understanding of the cracking mechanisms.

Numerical methods can assist in providing further understanding of soil curling and desiccation cracking. However, up to now, there has been only one attempt to investigate soil curling by using the Finite Different Method (FDM). Soil curling of slurry soils was simulated with assumptions that the soils behaved elastically and were saturated during the desiccation process. Experimental tests for soil curling were also conducted to obtain suction profiles along the height of soil samples during drying. These suction profiles were

then used as input for the model to generate the drying process of the numerical sample (Kodikara et al. 2004). Results of this study show that this approach could describe the overall response of the soil curling occurred in the experimental sample. However, since FDM is a continuum-based numerical method, this method does not reasonably reflect the behaviour of slurry soils during drying. Therefore, a new numerical approach, which can bridge the micro- to macro-behaviour, is required to reasonably capture the physical behaviour of slurry soils when they move from a slurry state to a semi-solid state during drying, and thus to achieve a better understanding of soil curling process.

In terms of soil cracking, various continuum-based and discontinuum-based numerical methods have been utilised in many studies to investigate both the soil cracking mechanism and its influencing factors. These numerical studies have shown that tensile stresses develop inside soil media undergoing drying, especially at the centre of a soil sample, Therefore, desiccation cracks normally initiate at this location. While these numerical methods have been shown to be capable of capturing the development of crack patterns and the effect of various factors on desiccation cracking (Amarasiri and Kodikara 2013; Amarasiri et al. 2011b; Asahina et al. 2014; Bui et al. 2015; Gui et al. 2016; Guo et al. 2017; Hirobe and Oguni 2016; Levatti et al. 2019; Manzoli et al. 2018; Peron et al. 2009a; Sánchez et al. 2014; Sima et al. 2014; Stirling et al. 2017; Trabelsi et al. 2012; Tran 2019; Vo et al. 2017), these methods still have some limitations. For example, to obtain crack patterns by using continuum-based methods such as the Finite Element Method (FEM) or FDM, interface elements or weak elements need to be pre-set, and thus the numerical results obtained from these methods strongly depend on the location and the number of these elements (Asahina et al. 2014; Hirobe and Oguni 2016; Levatti et al. 2019; Manzoli et al. 2018; Stirling et al. 2017; Vo et al. 2017). Although other continuum methods such as Smoothed Particle Hydrodynamics (SPH) has been shown to be a promising technique to overcome this problem, further developments are still required (Bui et al. 2015; Tran 2019). For discontinuum-based methods, in particular the Discrete Element Method (DEM), these limitations in naturally capturing the occurrence of cracks and micro-behaviour do not apply. However, existing DEM models are not capable of modelling unsaturated flow through soil media and thus failing to describe the coupled hydro-mechanical behaviour that occurs during desiccation cracking (Amarasiri and Kodikara 2013; Amarasiri et al. 2011b; Gui et al. 2016; Guo et al. 2017; Peron et al. 2009a; Sima et al. 2014). Therefore, an advanced computational framework capable of describing hydro-mechanical effects as well as micro- and macro-behaviour of the desiccation cracking process in clayey soils should be developed.

1.2. Research Aims

This study aims to understand the micro/macro mechanisms underlying the soil curling and desiccation cracking processes in clayey soils, and to develop numerical tools to predict these phenomena. The specific aims are as follows:

- To establish a comprehensive understanding of the soil curling mechanism and its influencing factors (i.e. clay type, temperature of drying, initial water content and sand content);
- To provide further understanding of the mechanism underlying the desiccation cracking process as well as the effect of wind velocity;
- To develop a DEM-based computational framework capable of describing the hydro-mechanical coupled effect to simulate soil curling and soil cracking.

1.3. Thesis Structure

This thesis reports the research undertaken to achieve the research aims. It consists of eight chapters. In each chapter, a brief introduction of the topic is first presented, followed by the explanations of material and methods used, the findings and conclusions drawn. Each chapter is outlined here:

Chapter 1 - Introduction

This chapter presents an introduction to the research problem, the research aims and the thesis structure.

Chapter 2 - Literature Review

This chapter comprehensively presents the current understanding of soil curling and desiccation cracking. Observations of soil curling and soil desiccation cracking obtained from both experimental and numerical studies are first presented. Studies that focused on the mechanisms underlying the soil curling and desiccation cracking processes are then reviewed. In addition, studies of the effect of various factors on soil curling and soil desiccation cracking is examined. Finally, numerical methods for modelling these phenomena are also examined and evaluated.

Chapter 3 - Experimental Investigation of Soil Curling

In this chapter, the detailed experimental program including material properties, experimental set-up, experimental procedure and test conditions, used to investigate soil curling as well as its influencing factors, is first presented. The experimental observations are then analysed to establish the soil curling process and soil curling mechanism. The

state of soils when soil curling initiates is established in detail. Finally, the effect of different factors (clay type, temperature of drying, initial water content and sand content) on soil curling are investigated and discussed.

Chapter 4 - Experimental Investigation Soil Cracking

This chapter reports a study of the measurement of strains that develops on the surface of soil samples during desiccation as well as the effect of wind velocity on the initiation and development of cracks. A detailed experimental program and the technique used to analyse the experimental results are first presented. These results are then presented and analysed to explain the initiation and development of these cracks. Furthermore, the effect of wind velocity on soil desiccation cracking is discussed with emphasis on the crack patterns and cracking water content.

Chapter 5 - A Micromechanics Approach to Model Curling of Slurry Soils

In this chapter, a DEM-based numerical approach is developed to study soil curling. This approach is capable of describing slurry soils mimicking actual experiment conditions as well as capturing the transformation of the soils from slurry to semi-solid state during desiccation. An overview of DEM is first given to provide background for the approach. The principles and the mathematical framework of the approach are then presented. The approach is then validated by modelling a desiccation experiment and comparing numerical and experimental results. Finally, the approach is employed to study the effect of the soil layer thickness and water evaporation rate on soil curling.

Chapter 6 - Modelling Unsaturated Flow through Discrete Pore-networks

This chapter presents the development of a numerical approach to model unsaturated flows through discrete porous media. The approach explicitly exploits the discrete contact network of solid particles in order to model unsaturated flow and the flow through this contact network is governed by Darcy's law. In this chapter, the assumptions of the approach are first presented. The mathematical framework is then derived. The proposed approach is then validated by using it to simulate water infiltration into an unsaturated soil column and water evaporation of an unsaturated soil column, and comparing the results against those obtained by using FDM. The effects of numerical aspects on the predicted results are also investigated.

Chapter 7 - Micromechanics Modelling of Coupled Hydro-Mechanical Behaviour of Soil During Desiccation

This chapter presents the development of a discrete-based computational framework capable of capturing the hydro-mechanical behaviour of clayey soils during desiccation to study soil cracking. In this chapter, the previous discrete-based approach proposed to

model unsaturated flows is first extended to simulate flows when soil media deform. A constitutive model capable of capturing the mixed-mode failure is then presented. Numerical techniques used to link hydro-behaviour and mechanical behaviour of soils are then introduced. The framework is then validated by simulating desiccation cracking on rectangular and circular samples and comparing the simulated results with the experimental results. The results are then analysed to provide further understanding of soil desiccation cracking.

Chapter 8 - Conclusions and Recommendations

This chapter summarises the main findings of the research and makes suggestions for future work on this topic.

Chapter 2. Literature Review

2.1. Introduction

Desiccation-induced soil curling and soil cracking are complex phenomena that occur due to moisture loss caused by changes in atmospheric conditions such as temperature, wind velocity or relative humidity. These phenomena can be encountered everywhere, especially in regions that consist mostly of reactive soils (Bell 2006; Shin and Santamarina 2011). For example, soil curling and desiccation cracking can occur in clay liners, embankments, slopes, dams and agricultural lands. The occurrence of these phenomena is the main reason behind damage to many civil engineering structures, and thus the formation and development of these phenomena as well as their influencing factors (e.g. temperature, relative humidity and soil properties) have been investigated extensively through both experimental and numerical studies.

Early experimental studies in soil curling and soil cracking focused on reporting observations and qualitative behaviour of soils, while more recent experimental studies have tried to quantify the behaviour of soils. In some of these studies, the mechanisms underpinning these phenomena were established based on experimental observations. Numerical studies have focused on the development of frameworks to predict the behaviour of soils undergoing soil curling and soil cracking, as well as to provide further confirmation of the understanding of soil curling and soil cracking mechanisms. In this chapter, both experimental and numerical studies are reviewed to highlight the behaviour of soils during soil curling and soil cracking, the mechanisms of these phenomena as well as numerical techniques used for predicting the occurrence of these phenomena in soils.

2.2. Studies of Soil Curling

2.2.1. General observations

When soil layers are subjected to desiccation, soil particles are rearranged, causing the soil layers to curve. This phenomenon is defined as soil curling. Generally, soil curling may occur in two ways, concave-up curling and convex-up curling. Concave-up curling is when the edges of the soil media lift up (Figure 2.1 (a)), while convex-up curling is when the middle of the soil media lifts up (Figure 2.1(b)).

In early studies, observations were made either in the field or by conducting drying tests on samples of mud. Researchers reported that during desiccation of clayey soil, water evaporates, vertical cracks appear and divide the soil into many polygons. With further evaporation of water, the edges of these polygons may curl upwards to form concave-up

curling or curl downwards to form convex-up curling (Allen 1986; Bradley 1933; Kindle 1917, 1923; Longwell 1928; Minter 1970; Ward 1923). However, these studies used observations only when the curling process was finalised to interpret the entire curling process, and thus the reported process may not fully cover the behaviour of the soil media from the beginning to the end of soil curling.

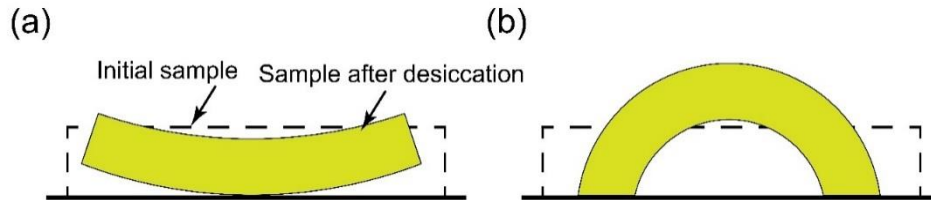


Figure 2.1. Shape of soil media when soil curling occurs: (a) concave-up curling; (b) convex-up curling.

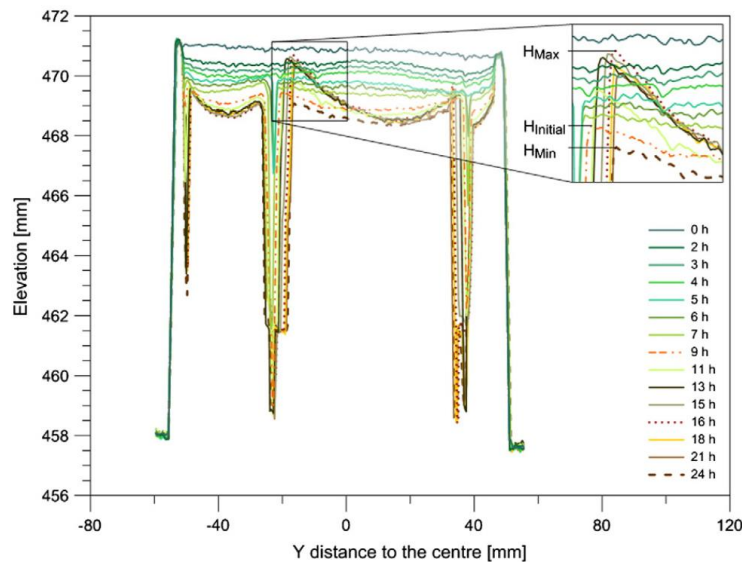


Figure 2.2. Evolution of a cross-section of a soil sample during drying (Zielinski et al. 2014).

Recently, several attempts have been made to capture the entire soil curling process. Kodikara et al. (2004) conducted shrinkage tests for samples prepared by both slurry and compacted clays. The samples were observed several times during the tests. This study showed that soil curling occurred in both slurry and compacted clays. In addition, both concave-up curling and convex-up curling occurred in one sample. Another recent study on soil curling was reported by Zielinski et al. (2014). In this study, the surface of a soil sample was tracked during drying. Figure 2.2 shows changes in the cross-section of a soil sample during drying. When the drying process started, the soil sample shrank, causing downward movement of the soil surface. With further drying, cracks appeared and after 9 hours, the edges of the cracks moved upwards to form concave-up curling on the soil surface. These edges reached a maximum elevation and then retreated downwards (Zielinski et al. 2014). Although the curling process of the soil surface was

recorded over time, the study did not provide a complete view on how soil curling occurs because no observations being of the movement of the bottom face of the soil sample.

2.2.2. Soil curling mechanism

Several theoretical explanations for the formation and development of soil curling have been proposed. In early studies, this phenomenon was explained based on the differential shrinkage along the height of soil layers. This differential shrinkage arises due to the differential water loss and non-homogeneous distribution of soil particles along the height of the soil layers. Consequently, the contracting surface pulls the edges of the soil layer up to form curling (Bradley 1933; Ward 1923). This explanation was used for both concave-up curling and convex-up curling. For example, Bradley (1933) reported the occurrence of convex-up curling in a soil layer prepared by distributing sand on the top bentonitic clay layer and explained this phenomenon based on the shrinkage of the top and bottom surfaces of the soil layer. Minter (1970) presumed that the presence of convex-up curling in a thin layer of mud deposited on a rocky shelf on the bank of a stream was due to the bottom surface drying faster than the top surface. However, the explanation based on the differential shrinkage cannot apply to the case where convex-up curling occurs when clays are dried from the top surface as the top surface always shrinks faster.

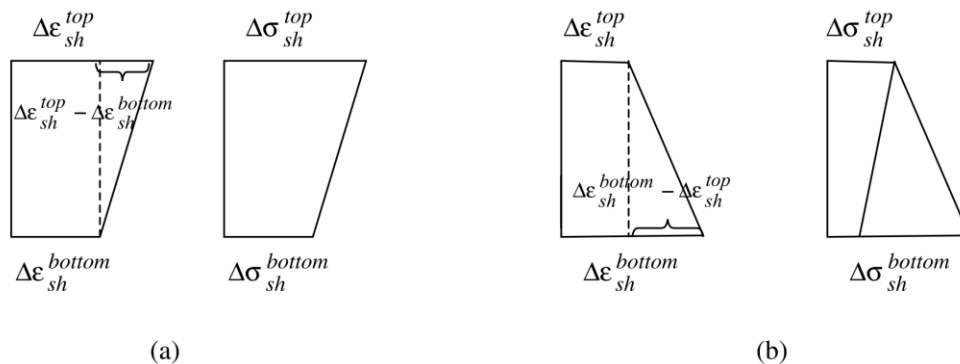


Figure 2.3. Profiles of the shrinkage strain increment and shrinkage stress increment: (a) concave-up curling; (b) convex-up curling (Kodikara et al. 2004).

In a recent study, another explanation was made based on profiles of the shrinkage strain increment and shrinkage stress increment. This explanation was used to explain the occurrence of both concave-up curling and convex-up curling in a sample of Werribee clay (Kodikara et al. 2004). Figure 2.3 shows the theoretical profiles of the shrinkage strain increment and shrinkage stress increment when a clay sample is dried from the surface. Initially, the soil surface dries faster, resulting in profiles of the shrinkage strain increment and shrinkage stress increment with a larger value on the top and a smaller value at the bottom. As explained by Kodikara et al. (2004), this non-uniform shrinkage stress increment creates a bending moment, lifting up the edges of the sample to form

concave-up curling. As drying continues, more water evaporates from the top surface as well as the bottom surface. The drying rate on the bottom surface becomes higher, and therefore the shrinkage strain increment and shrinkage stress increment on this surface also become higher. These profiles and the bending moment are now reversed, and thus convex-up curling initiates. However, the explanation for the formation of convex-up curling does not seem reasonable as the stress in soil layer is always larger on the top and smaller at the bottom, resulting in an upward moment, and therefore allowing only concave-up curling to occur (Style et al. 2011).

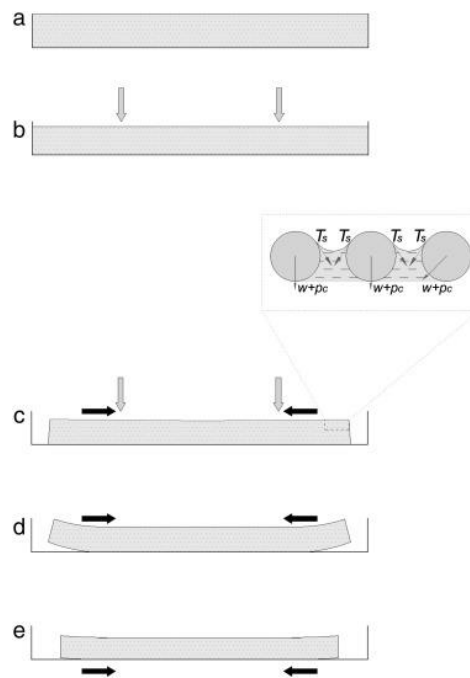


Figure 2.4. Conceptual model to explain concave-up curling (Zielinski et al. 2014).

A third explanation for the occurrence of concave-up curling was proposed based on the development of surface tension force at the surface of the soil layer. This explanation is summarised in Figure 2.4. At the beginning of the drying process, water evaporates from the surface of the soil sample, resulting in formation of menisci between soil particles that are located on, or near, the surface. The menisci induce surface tension forces that move the soil particles downward. Owing to the smaller force acting on particles which are located close to sides of the mould (i.e. lacking neighbouring particles on one side), these particles move downwards at a slower rate and concave-up curling is initiated at the surface. With further drying, the sample shrinks more and disconnects from the sides of mould. The water starts evaporating from the sides of the sample, strengthening this mechanism, and thus further soil curling occurs. As the drying process continues, water starts to evaporate from the bottom of the sample, leading to an increase in the surface tension force at the bottom of the sample. As a result, the soil sample may move downwards and the effect of soil curling is reduced (Zielinski et al. 2014). However, this explanation is limited as it cannot explain how the soil sample lifts off.

2.2.3. Factors influencing soil curling

Previous studies have reported that soil curling is governed by a number of factors including the drying temperature, non-homogenous distribution of soil particles, materials, thickness of soil layer, boundary conditions, and the existence of salt and its distribution in a soil mass (Bradley 1933; Kindle 1917, 1923; Minter 1970; Ward 1923; Zielinski et al. 2014). However, the effect of most of these factors on soil curling has been studied mainly in the field and only qualitative observations have been made with no attempt to quantify this effect. For example, while Longwell (1928) reported that curling occurred noticeably in fields during summer, Bradley (1933) also reported that an increase in drying temperature caused an increase in the curvature of soil curling.

In an early study, Bradley (1933) postulated that the occurrence of concave-up curling or convex-up curling depends on the non-homogenous distribution of soil particles. For example, concave-up curling occurs in soil layers with soil particles distributed from fine particles at the top to coarse particles at the bottom, while convex-up curling takes place when the particle distribution is reversed. This phenomenon was explained based on the shrinkage potential of the top surface and bottom surface of these soil layers. As the soil surface with finest grains tends to shrink more, the contracting surface may pull the edges of these soil layers towards the surface where fine grains are dominant. In this early study, Bradley (1933) reported the occurrence of convex-up curling when a soil layer of bentonitic clay with sand on its top surface was dried. In a recent study, Zielinski et al. (2014) conducted desiccation tests of slurries prepared by pure kaolin or mixtures of kaolin and sand at a very high water content, and reported that soil curling was more dominant in soil samples prepared by mixtures of kaolin and sand (as shown in Figure 2.5).



Figure 2.5. Final stage of the desiccation tests: (a) pure kaolin; (b) mixture of kaolin and sand (Zielinski et al. 2014).

In an early study of the effect of materials on soil curling, Longwell (1928) reported that a particular clay from the Muddy Valley may curl into rolls when it is dried. Silt found on floodplains and playas also curled but the curvature was not significant. However, in fine sand with some clay or silt, no curling was observed. In addition, the thickness of soil layers significantly influences curvature of soil curling where thinner soil samples were observed to possess greater curvatures. The similar effect of thickness on soil curling was also reported in the study of Minter (1970). As shown in Figure 2.6, thin layers near the edge of the depression can even curl into rolls.

Boundary conditions also influence soil curling. Ward (1923) made field observations along the Missouri River flood plain and found that both concave-up curling and convex-up curling occurred near each other because of a difference in the surfaces beneath soil layers. Beneath the soil layers with convex-up curling, the surface was rippled, while this rippled surface was not observed beneath the soil layers with concave-up curling.

In addition, the presence of salt in soil layers also changes the soil curling behaviour. Kindle (1917) conducted desiccation tests for mixtures prepared by mixing blue clay with fresh water or saline water and reported that significant concave-up curling occurred in the non-saline mixture, while no curling or convex-up curling was recorded for the saline mixture. This observation was confirmed by studies of Kindle (1923) and Bradley (1933) when field observations and desiccation tests of mixtures prepared by mud and fresh water or saline water were conducted. Bradley (1933) explained that when a soil layer prepared by mixing mud and saline water was dried, salt crystals grew in locations near the surface and thus the surface of the soil layer deformed less than the bottom of the soil layer, causing the development of convex-up curling.



Figure 2.6. Mud curls occurred in a depression (Longwell 1928).

The review in this section highlights that soil curling may occur in soil media during desiccation due to the differential shrinkage along the height of soil layers or the capillary force on the surface of the soil media. In addition, there are many factors that govern soil curling. However, existing studies described the soil curling process within the context of desiccation cracking and often use the final stage of the desiccation process to infer the soil curling behaviour. Consequently, the underlying soil curling mechanism is not fully understood. In addition, all studies only report the general effect of these factors, while no attempt has been made to quantify the effect and comprehensively discuss how these factors and the state of soil media influence the soil curling process.

2.3. Studies of Desiccation Cracking in Soils

2.3.1. General observations

Desiccation of soil media causes soil particles to rearrange, leading to shrinkage of the soil media. Consequently, some first cracks develop and divide the soil media into fragments. These cracks terminate after intersecting with each other or reaching boundaries. More cracks may appear and sub-divide these fragments into smaller fragments. This process continues until a stable pattern is achieved (as shown in Figure 2.7). All cracks may continue widening until the soil media reach their residual water content (Corte and Higashi 1960; Costa et al. 2013; Morris et al. 1992; Nahlawi and Kodikara 2006; Tang et al. 2011c).

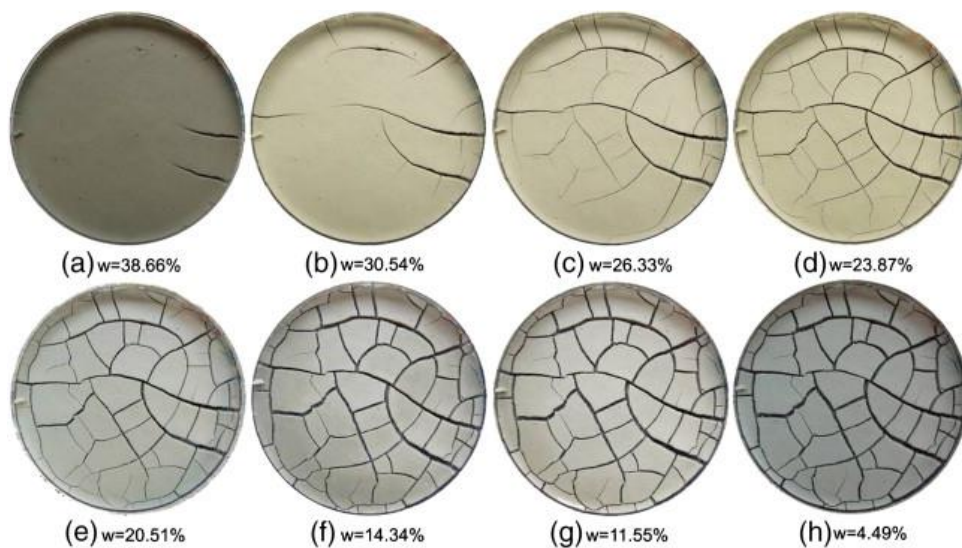


Figure 2.7. Evolution of a crack pattern of a specimen during desiccation (Tang et al. 2011c).

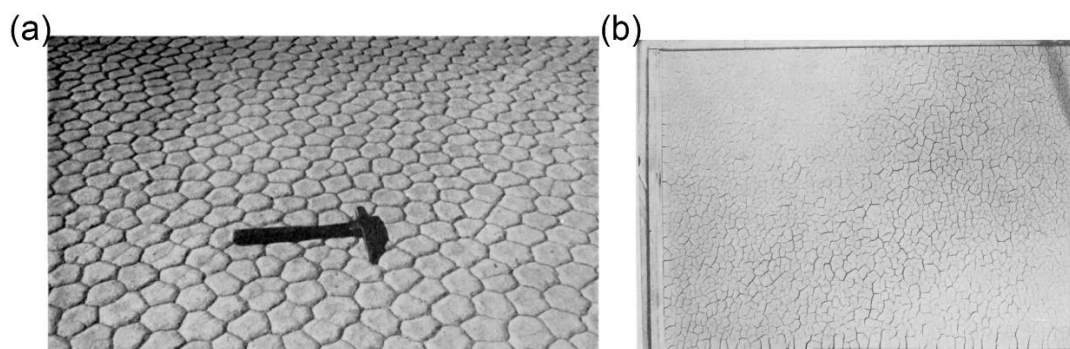


Figure 2.8. Non-orthogonal patterns: (a) mud cracks on a playa surface (Longwell 1928); (b) cracks in a slurry soil sample 3.4mm thick (Corte and Higashi 1960).

Crack patterns occurring in soils during desiccation can be classified into two main categories, orthogonal patterns and non-orthogonal patterns. In the orthogonal patterns, cracks occur sequentially and tend to meet each other orthogonally, while in the non-

orthogonal patterns, cracks meet obliquely (e.g. hexagonal pattern with cracks meet at angles of 120°) (Corte and Higashi 1960). In addition, the non-orthogonal patterns occur when soil layers are very thin, the drying rate is high and soils are homogeneous (Corte and Higashi 1960; Longwell 1928). Figure 2.7 shows an orthogonal crack pattern. In this figure, most of intersections of cracks were at 90° . Figure 2.8 shows non-orthogonal patterns.

Experimental results have also demonstrated that for slurry specimens, approximately 90% of cracks occur while the soil samples are still fully saturated (Peron et al. 2009b; Rodríguez et al. 2007; Shin and Santamarina 2011; Tang et al. 2011c). As shown in Figure 2.9, cracks started when water content of a specimen was about 42% and the degree of saturation was 100%. When the specimen became unsaturated, the surface crack ratio was around 12.5%, this ratio then reached around 14% when the specimen was almost dried.

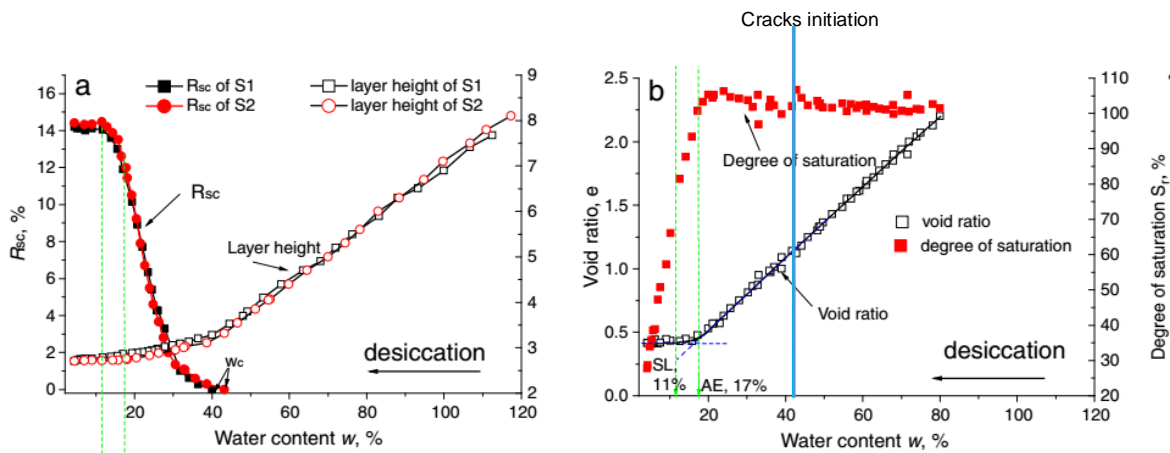


Figure 2.9. (a) layer thickness and surface crack ratio R_{sc} ; (b) void ratio and degree of saturation (Tang et al. 2011c).

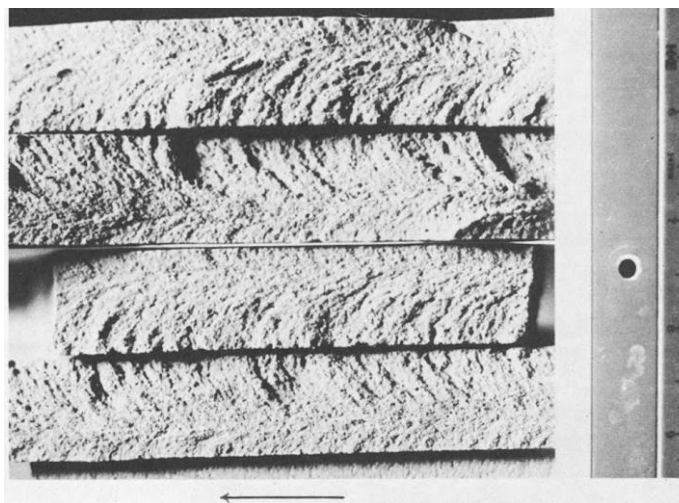


Figure 2.10. Interfacial fracture markings in a sample 24mm thick (Corte and Higashi 1960).



Figure 2.11. Surface depression on the crack tip (Tollenaar 2017).

Furthermore, most studies have reported that cracks start from the surface, then propagating to deeper layers (Costa et al. 2013; Peron et al. 2009b; Rodríguez et al. 2007; Shin and Santamarina 2011; Tang et al. 2011c). By looking at the interfacial fracture markings (as shown in Figure 2.10), Corte and Higashi (1960) hypothesised that cracks could initiate at some point below the soil surface and then propagate towards the top face, the bottom face or both. Recently, Tollenaar (2017) confirmed this finding by observing the surface depression on crack (as shown in Figure 2.11).

2.3.2. Soil cracking mechanism

Soil cracking has been discussed in the literature from a macro-view, in which development of tensile stresses in soils is analysed based on continuum mechanics. As desiccation starts, water evaporates and soil sample starts shrinking. However, movement of soil particles and the entire the samples are restricted due to the friction and adhesion occurring between soils and external boundaries or lower soil layers, and soil structure (i.e. soil fabric moisture gradient). Consequently, tensile stresses develop, and thus cracks occur when tensile stresses reach the tensile strength of the soil (Corte and Higashi 1960; Kodikara and Costa 2013; Morris et al. 1992).

This mechanism was illustrated by looking at the sequence of cracks occurring when long samples underwent desiccation. Nahlawi and Kodikara (2006) and Peron et al. (2009b) reported that during desiccation of a long sample, a crack first appeared at the centre of the sample, dividing the samples into two fragments. More cracks then appeared at the centre of these fragments. Vo et al. (2018) confirmed this mechanism by modelling the soil desiccation cracking process and analysing the tensile stress development in a soil sample. As shown in Figure 2.12, in a homogeneous sample, tensile stress developed at the middle of the sample during desiccation. When the suction was more than 0.024 MPa, the first crack occurred at the middle of the sample. The tensile stresses then developed in these fragments and always reached maximum at the middle.

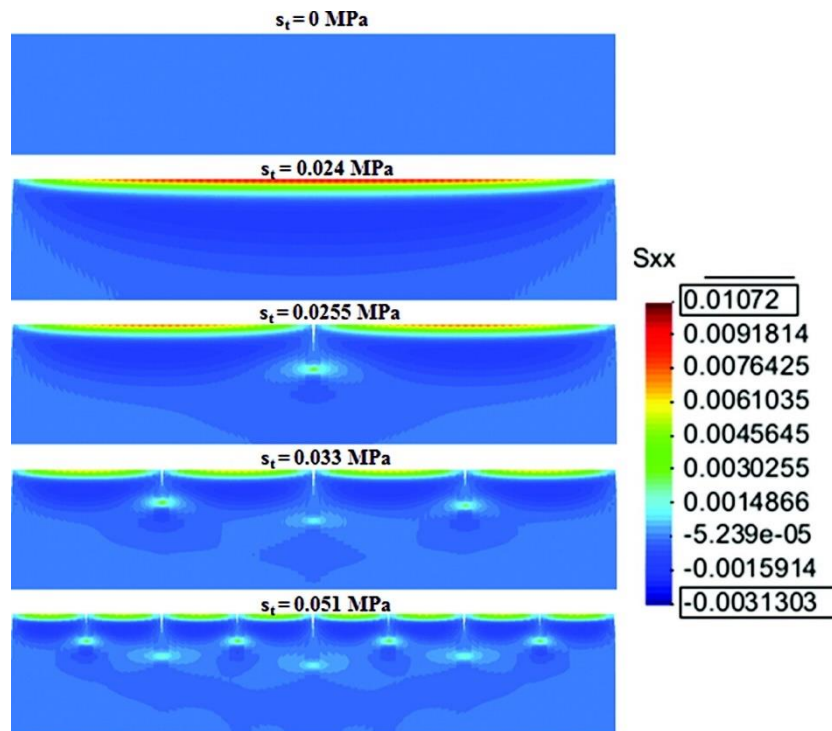


Figure 2.12. The development of tensile stresses and cracks during desiccation (Vo et al. 2018).

The mechanism based on the development of the tensile stresses in soils was then used to explain the direction of new cracks when they approach pre-existing cracks. Morris et al. (1992) and Tang et al. (2011c) conducted experiments and reported that angles forming between cracks were 90° . These researchers explained that as cracks occur due to the maximum tensile stress developing in soil media is larger than the tensile strength of soils, the direction of cracks is perpendicular to the direction of local maximum tensile stress. When cracks occur, the local maximum tensile stress is released, and thus the direction of maximum tensile stress in zones around these cracks is parallel to these cracks. Consequently, new cracks occur and may propagate toward the existing cracks. These new cracks meet the existing cracks at 90° .

However, Wei et al. (2016) argued that desiccation cracks can occur due to tensile failure and combination of tensile and shear failure. It was reported that as strain xx vectors on both sides of the crack were not perpendicular or parallel to the crack, the strain vectors can be decomposed into two components, one component was perpendicular to the crack and another was parallel to the crack (as shown in Figure 2.13). In addition, the directions of strain xx vectors on both sides of the crack were different, and thus they concluded that this crack occurred due to both tensile and shear failures. However, the author believes that the magnitude of principal strains, as well as the strain field before the formation of this crack should be provided to support this conclusion.

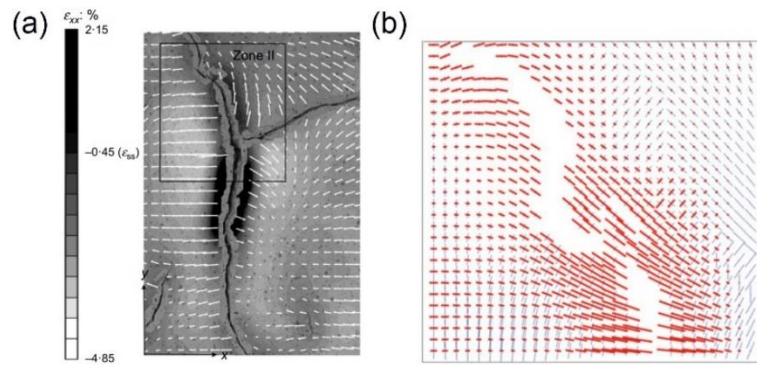


Figure 2.13. Strain field in a portion of a kaolin soil sample: (a) strain in x direction; (b) principal strain in zone II (Wei et al. 2016).

Stages	(a)	(b)	(c)	(d)	(e)
Global view					
Particle scale view					
Comments	Evaporation of supernatant water No suction No strain in the soil skeleton	Air-water interface membrane reaches the soil surface	Membrane forms around soil particles Suction increases Consolidation of soil skeleton and increase in stiffness	Air invades the largest pores The air-water interface membrane pushes particles away from the invaded pore Pore size increase at the tip and crack grows	Crack propagation and formation of polygons Vertical deformation ceases Eventually, the soil mass becomes unsaturated

Figure 2.14. The mechanism of desiccation cracking in the micro-view (Shin and Santamarina 2011).

The mechanism of desiccation cracking in soils can be also explained from the micro-view illustrated in Figure 2.14. This concept was drawn from experimental observation of desiccation cracking by Shin and Santamarina (2011) and Tang et al. (2011c). As the desiccation process of a soil sample begins, water evaporates and capillary suction develops, causing an increase in effective stress. Thus, soil particles start to settle down.

As water continues evaporating, capillary suction continues to increase, causing the initiation of air intrusion. The air intrusion pushes soil particles away from each other and cracks start forming. The pore size at crack tips increases and this process repeats, and thus cracks continue to propagate in the soil media. Shin and Santamarina (2011) then used this hypothesis to explain observations recorded during desiccation cracking, including the significant development of cracks in samples prepared by mixing clays with salty water, and the reduction in propagation speed of cracks when they approach existing cracks. Shin and Santamarina (2011) postulated that samples prepared using clays and salty water had larger pore diameters in comparison with samples prepared using mixtures of clays and fresh water, and thus air readily invaded into the samples with a higher salt concentration causing more cracks. Regarding the reduction in the propagation speed of cracks, Shin and Santamarina (2011) explained that there was a restriction in the increase in void ratio at the crack tips when cracks approached existing cracks, causing a reduction in the speed of air invasion, and thus the propagation speed of cracks reduced.

2.3.3. Factors influencing soil cracking

Many studies have been conducted to investigate the effect of various factors on desiccation cracking in soils. These factors can be classified into three groups: (1) drying conditions such as drying temperature, relative humidity, wetting-drying cycles and soil surface cover; (2) boundary conditions, such as thickness of the sample, sample size and bottom contact surface; and (3) materials including soil type, salt concentration, fibre and cement-like additives. In this section, studies of the effect of these factors on soil cracking are reviewed.

2.3.3.1. Drying conditions

As already discussed, cracks occur in soil media during desiccation due to tensile stresses reach the soil strength. These stresses develop because water evaporates and the shrinkage of the soil media is constrained (Corte and Higashi 1960). Consequently, drying conditions, particularly drying temperature, relative humidity, wetting-drying cycles and soil surface cover may significantly affect soil cracking.

Previous studies have reported that initiation and development of cracks are temperature-dependent (Tang et al. 2010; Tang et al. 2008). As drying temperature increases, cracks initiate earlier and water content when cracks appear is higher. In addition, in soil layers that have undergone a higher drying temperature, wider and longer crack segments appear. The surface crack ratio (R_{sc}) (i.e. the total surface area of cracks/the total surface area of specimen) is larger at any water content (as shown in Figure 2.15). However, the number of crack segments and the final value of crack intensity factor decrease (Tang et al. 2008). For thin soil layers, the effect of temperature on desiccation crack is negligible

(Costa et al. 2013). Tang et al. (2010) postulated that soil strength decreased with an increase in drying temperature, while the rate of suction developing in soils increased, and thus drying temperature significantly influenced soil cracking. However, Uday and Singh (2013) reported that for samples of slurry bentonite, the number of crack segments that appeared increased with an increase in temperature, while the width of cracks decreased (as shown in Figure 2.16). The contradictory findings of these studies may be attributed to the different materials used. Uday and Singh (2013) used artificial clay with very high liquid limit, plastic limit and plastic index, while Tang et al. (2008), Tang et al. (2010) and Costa et al. (2013) used natural clays that had lower liquid limit, plastic limit and plastic index.

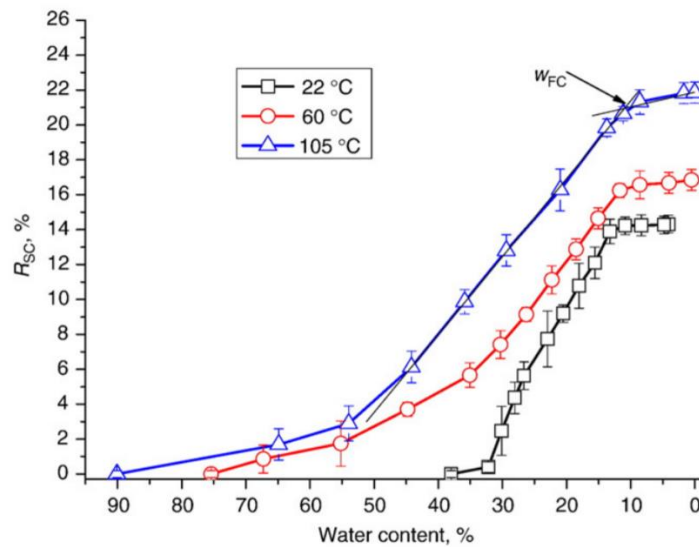


Figure 2.15. Changes of crack surface ratio during drying (Tang et al. 2010).

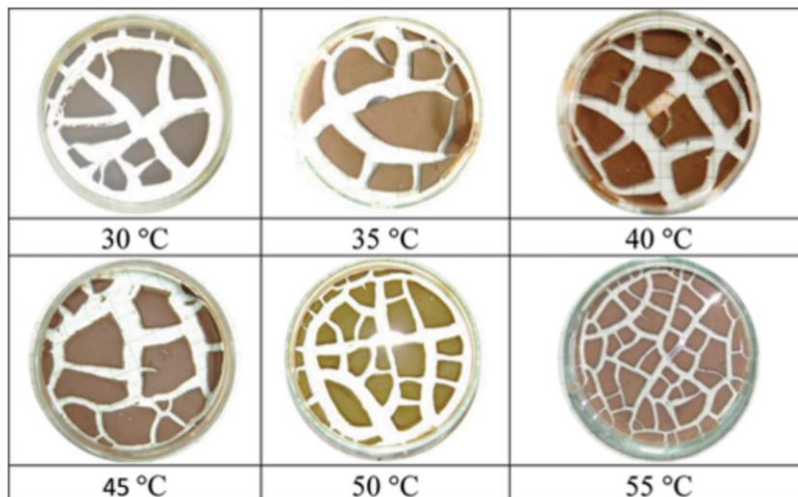


Figure 2.16. Cracking patterns of samples under different drying temperature (Uday and Singh 2013).

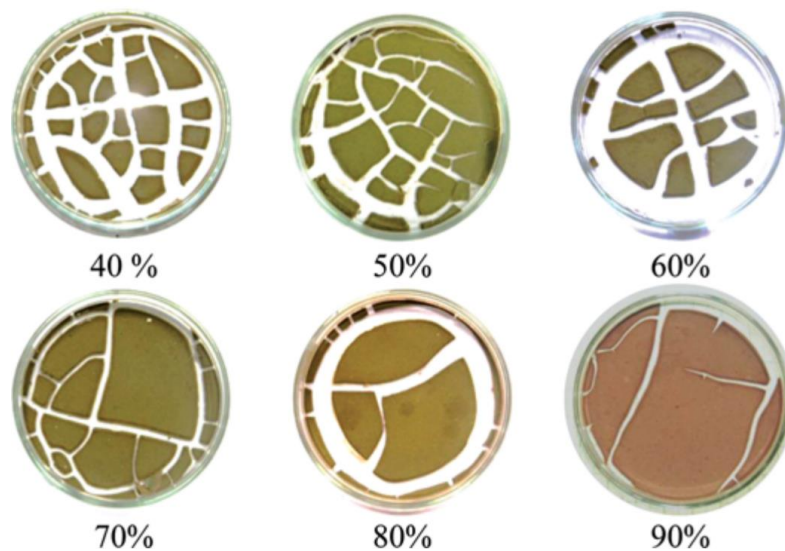


Figure 2.17. Crack patterns of bentonite samples dried under different relative humidity and a temperature of 50°C (Uday and Singh 2013).

The relative humidity also significantly influences soil cracking. Uday and Singh (2013) dried slurry bentonite samples under different humidity conditions and a constant temperature. They reported that, as the relative humidity increased, the number of cracks and crack intensity decreased. However, there was no clear trend for changes in crack width (Figure 2.17). Similarly, Safari et al. (2014) reported that crack segments with greater width and length occurred in samples without a geotextile cover. In addition, the crack intensity factor of samples without a geotextile cover was around twice that of samples with a geotextile cover. These results were attributed to a faster drying rate of samples without a geotextile cover.

Regarding the effect of wetting-drying cycles on soil cracking, previous studies have highlighted that, as the number of wetting-drying cycles increased, cracks occurred more easily, even at a very high water content. In addition, crack patterns became irregular, with thinner and shorter cracks (as shown in Figure 2.18). After the second wetting-drying cycle, main cracks appeared at the same locations as cracks that appeared after the first wetting-drying cycle. The significant effect of wetting-drying cycles on soil cracking was explained by reduction of soil strength. This reduction is caused by heterogeneity of the soil fabric and the increased number of weak zones formed during the wetting-drying cycle (Tang et al. 2011a; Tang et al. 2008). Although more cracks appeared, the crack intensity factor decreased with an increase in the number of wetting-drying cycles (Tang et al. 2011a; Tang et al. 2008). However, Yesiller et al. (2000) reported that crack intensity factor increased with an increase in the number of wetting-drying cycles. These contradictory findings could be attributed to the difference in compaction of samples used in these studies. Yesiller et al. (2000) conducted tests on compacted samples, while Tang et al. (2008) and Tang et al. (2011a) conducted tests on slurry samples.

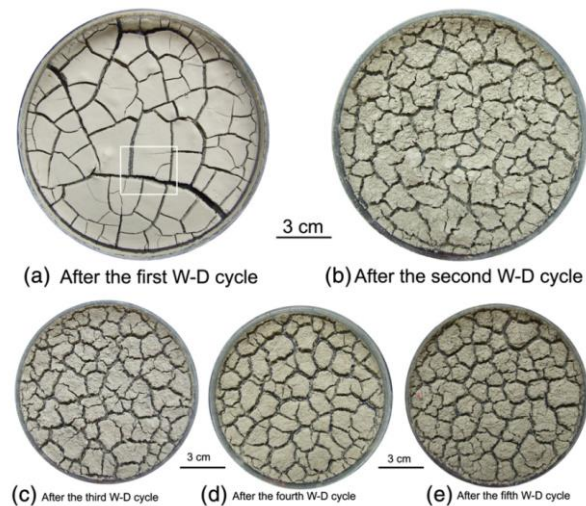


Figure 2.18. Crack patterns of a sample under different wetting-drying cycles (Tang et al. 2011a).

2.3.3.2. Boundary conditions

The first factor in the boundary conditions group is thickness of soil layers. Previous studies have reported that with an increase in the thickness of soil layers, the cracking water content increased (Corte and Higashi 1960; Nahlawi and Kodikara 2006). This tendency was consistent regardless of different materials used for moulds (as shown in Figure 2.19(a)). In addition, as thickness of soil layers increased, the number of cracks decreased, while crack length, width and intensity factor increased. These behaviours were explained to be due to significant development of differential shrinkage in thicker layers, which in turn influenced stress development inside the soil layers (Corte and Higashi 1960; Lakshmikantha et al. 2012; Nahlawi and Kodikara 2006; Rodríguez et al. 2007; Tang et al. 2008).

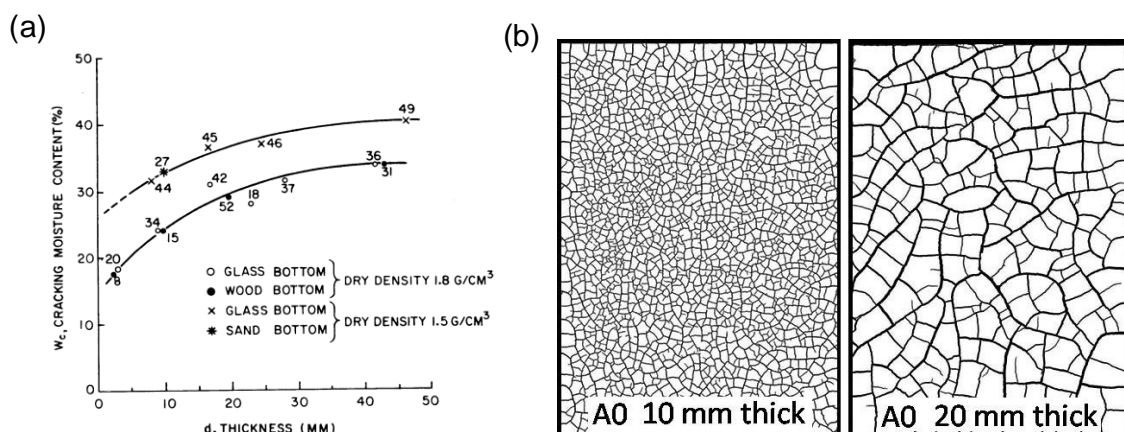


Figure 2.19. Effect of thickness of soil layer: (a) effect on thickness on cracking water content (Corte and Higashi 1960); (b) effect of thickness on crack patterns (Lakshmikantha et al. 2012).

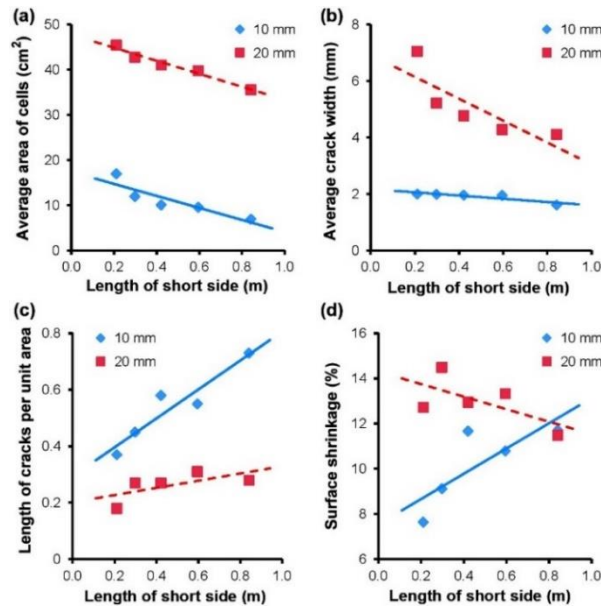


Figure 2.20. Effect of sample size on characteristics of crack patterns (Lakshmikantha et al. 2012).

Similarly, sample size also strongly affects soil cracking. Figure 2.20 shows that with an increase in sample size, average area of crack cells and average crack width decreased, while length of cracks per unit area increased (Lakshmikantha et al. 2012). In addition, more cracks occurred in larger samples (Tollenaar 2017). These behaviours can be explained based on the development of stresses inside soil samples. Larger samples built up stresses faster due to the larger constraint that comes from the larger contact surface between soils and the base of moulds (Tollenaar 2017), while strength of the larger samples decreased (Shogaki 2007), and thus cracks occurred more easily.

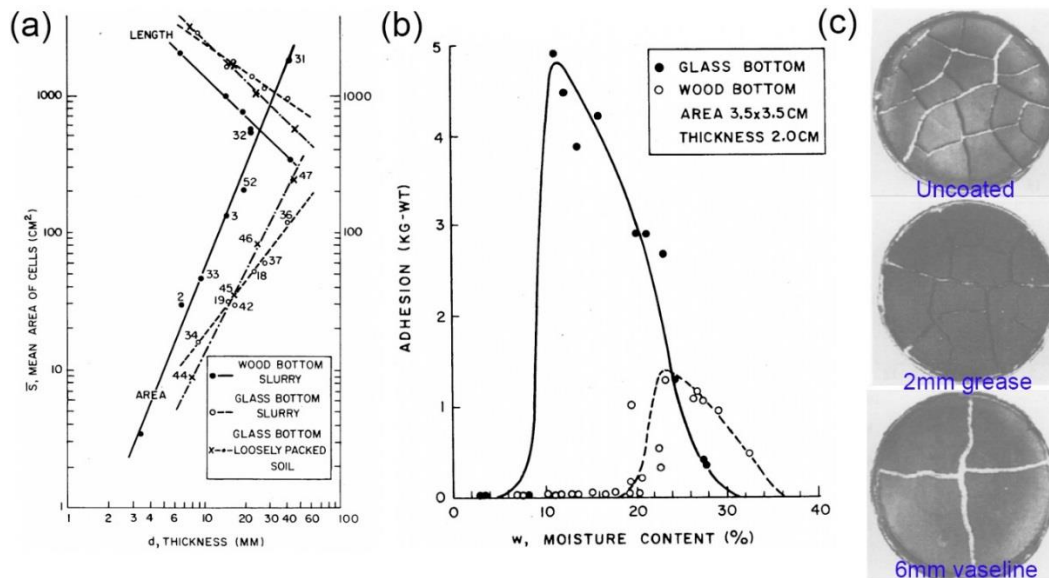


Figure 2.21. Effect of bottom contact surface: (a) characteristics of crack patterns; (b) changes of adhesion (Corte and Higashi 1960); (c) crack patterns of ground coffee in moulds with different coating surface (Groisman and Kaplan 1994).

Many studies have reported that the bottom contact surface also governs the initiation and development of desiccation cracks as it controls the development of shrinkage stresses (Corte and Higashi 1960; Kodikara and Costa 2013). Corte and Higashi (1960) conducted desiccation tests on wood and glass moulds, and reported that fragments (cells) separated by cracks in wood moulds were bigger than that in glass moulds, while the total length of cracks in wood moulds was shorter (as shown in Figure 2.21(a)). Corte and Higashi (1960) also conducted tests to determine the adhesion between soils and glass or wood. The results of these tests showed that the adhesion between soils and glass was much bigger than that between soils and wood (Figure 2.21(b)). Consequently, this study concluded that the difference in characteristics of crack patterns (i.e. fragments area, total length of cracks and number of cracks) recorded for different types of bottom contact surfaces could be attributed to the difference in adhesion. When the adhesion between soil and the bottom contact surface was large, desiccation stresses developed faster and thus more cracks could develop, dividing soils into many cells, and thus the average area of cells was smaller and crack length was longer. Groisman and Kaplan (1994) and Tollenaar (2017) reported similar observations in desiccation tests of clays and ground coffee in moulds with different bottom contact surfaces (as shown in Figure 2.21(c)).

2.3.3.3. Materials

Materials are one of the main factors governing soil cracking as materials control the fabric and strength of soil, and the development of shrinkage stresses. Costa et al. (2013) conducted desiccation tests for samples prepared from Merri Creek clay, potato starch and fine sand with particle size range 63-75 μ m. They reported that no visible cracks were observed in sand samples. The crack patterns in the potato starch samples were oblique with cracks fully penetrating the entire height of the sample, even in thick samples (i.e. 20mm and 30mm depth), while crack patterns in the clay samples were orthogonal. In thick samples (i.e. 20mm depth), horizontal cracks occurred (Figure 2.22). Tang et al. (2008) reported that crack patterns of samples of different clayey soils differed significantly and depended on the fines content or plastic index. Samples with higher fines content and plastic index had a higher crack intensity factor and average width of cracks. The researchers reported that soils with higher fines content shrank more, and thus cracks would occur more easily. However, clay minerals also control soil cracking. Gui (2014) reported that cracks occurred more in samples prepared with bentonite in comparison with samples prepared with kaolin.

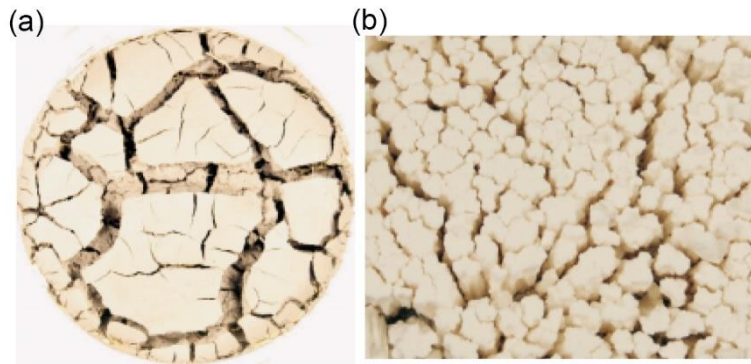


Figure 2.22. Cracks pattern: (a) Merri Creek clay sample; (b) potato starch sample (Costa et al. 2013).

Another factor that also governs the fabric and strength of soil media is the soil concentration in mixtures of clays. Zhang et al. (2017) highlighted that in fresh water, clay particles are grouped with edge-edge pattern, while in salty water, they are grouped with face-face pattern, and thus the fabric of the mixtures is significantly influenced. Zhang et al. (2017) also reported that the crack patterns of bentonite were also strongly affected by different salt concentrations. As the salt concentration increased, cracks occurred more, but their width was thinner. In addition, the crack density factor decreased. This behaviour was attributed to a slower evaporation process of the sample caused by an increase in the salt concentration (Zhang et al. 2017). However, it is possible that soil strength may decrease with an increase in salt concentration and therefore cracks would appear more easily.

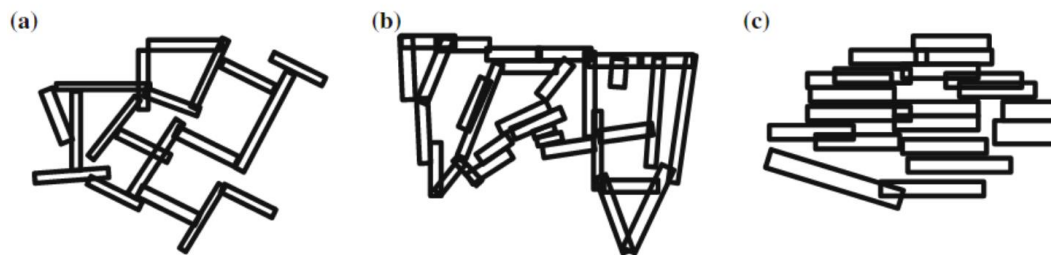


Figure 2.23. Fabric parking in water with salt concentrations: (a) in fresh water, (b) in sea water; (c) in water with high salt concentration (Zhang et al. 2017).

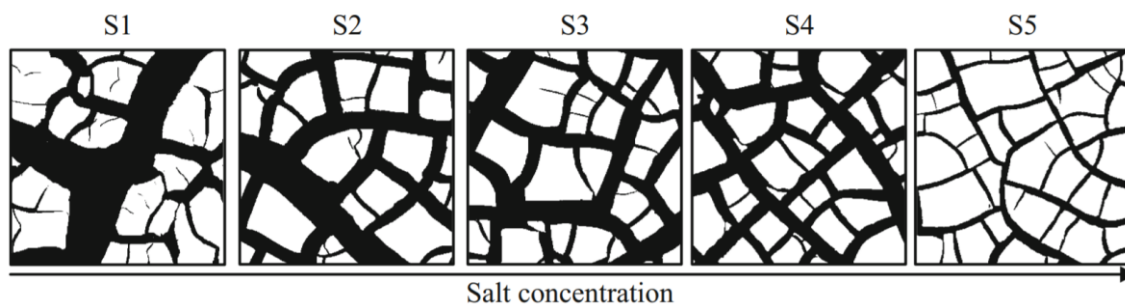


Figure 2.24. Crack patterns in samples with different salt concentration (Zhang et al. 2017).

In addition, existence of fibre and cement-like additives also improve strength of soils, especially the tensile strength. Tang et al. (2016) reported that tensile strength increased significantly when adding fibre to soils. For example, with a fibre content of 0.2% of dry soil weight, tensile strength of soils in Nanjing area increased more than 50%. In addition, soils with added fibre were more ductile. Similarly, Nahlawi et al. (2004) reported that with an addition of 3% general blended cement in Werribee clay, the tensile strength increased by more than 5 times. Therefore, it is believed that fibre and other cement-like additives may reduce the development of desiccation cracks. Tang et al. (2012) reported that as the content of fibre in soils increased, crack characteristics (i.e. surface crack ratio, number of cells, and average length and width of cracks) significantly reduced. Additionally, crack lines became more jagged and tortuous, and the number of dead-ends and single cracks increased (Figure 2.25). Similarly, cement-like additives such as silica fume also effectively reduce the number of cracks, crack width and crack length (Kalkan 2009).

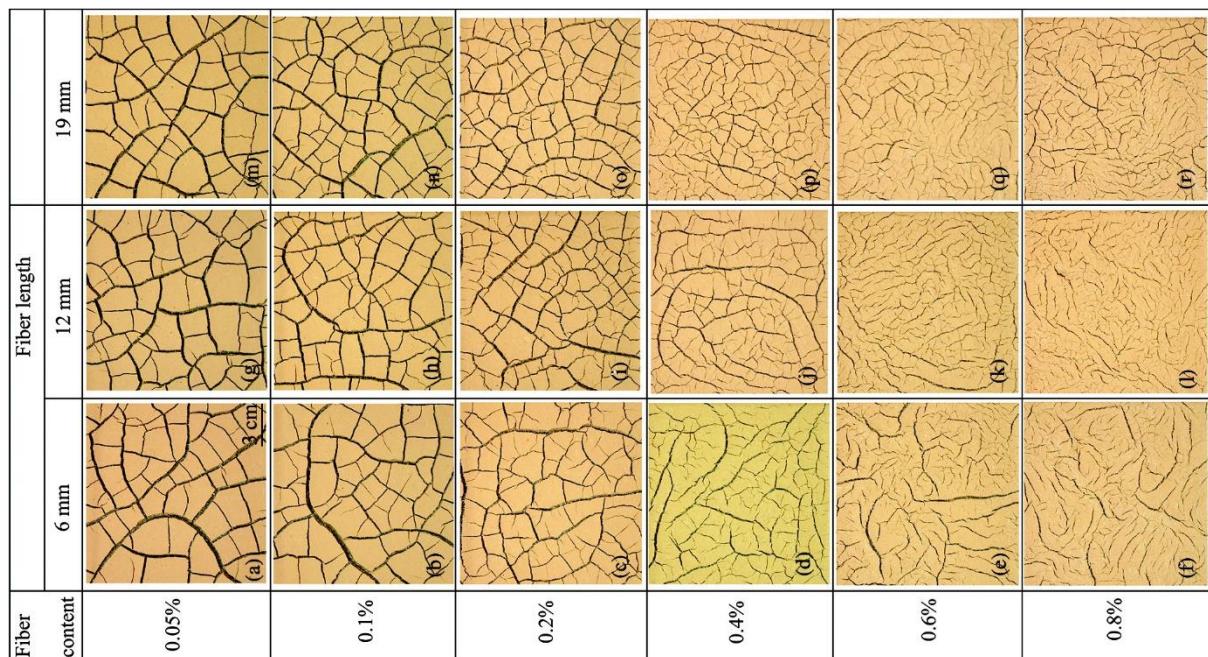


Figure 2.25. Crack patterns of soils with different fibre contents (Tang et al. 2012).

This section has reviewed observations of soil desiccation cracking, its mechanism and the effect of different factors on soil cracking. Generally, cracks may start from the surface or any point inside the soil layer due to tensile failure or a combination of tensile and shear failures. The development of cracks can also be attributed to development of capillary suction within the layer. All factors except wind velocity have been thoroughly investigated and their effect on desiccation cracking in soils has been well explained. However, in most experimental studies, only the development of cracks has been quantified while ignoring quantification of strain or stress development in soil samples during desiccation,

and thus further studies, in which the development of strain field or stresses are quantified are necessary to provide a comprehensive understanding of soil cracking.

2.4. Numerical Methods for Modelling Soil Curling and Soil Cracking

Numerical methods have been widely applied in many engineering fields as they can be used to predict behaviour of many phenomena and to provide further understanding. In this section, existing numerical methods used to simulate soil curling and soil cracking are reviewed. These methods are classified into two groups, continuum methods and discontinuum methods.

2.4.1. Numerical methods for modelling soil curling

To date, there has been only one attempt to model soil curling. In this study, Kodikara et al. (2004) utilised FDM to study soil curling occurring in a slurry sample subjected to drying. The simulated soil sample was assumed to be near saturation and therefore the elastic modulus was calculated based on the modulus with respect to suction, which in turn was calculated based on the suction and the shrinkage strain obtained from a shrinkage test. The shrinkage process of the numerical sample was implemented by changing the suction profile. Figure 2.26 shows the changes of suction in the upper section and lower section of the sample. Data presented in this figure were obtained by dividing the experimental sample horizontally and measuring the water content of each half. This water content was then converted to suction for both halves by using the soil water retention curve. It can be seen that, as drying time increased, difference in suction between the two halves decreased. Note that suction of the top half was larger.

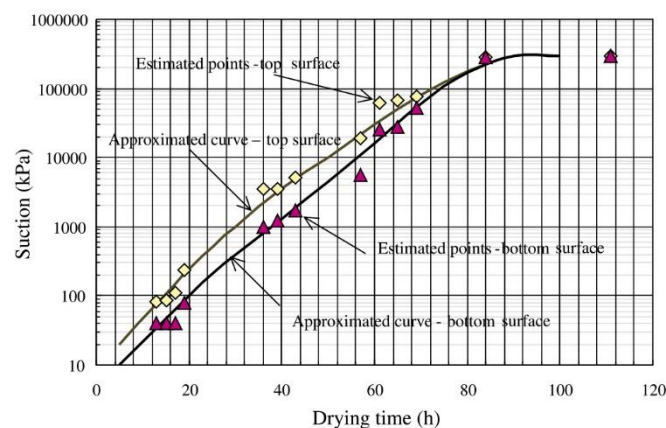


Figure 2.26. Estimated suction curves for top and bottom halves of a specimen (Kodikara et al. 2004).

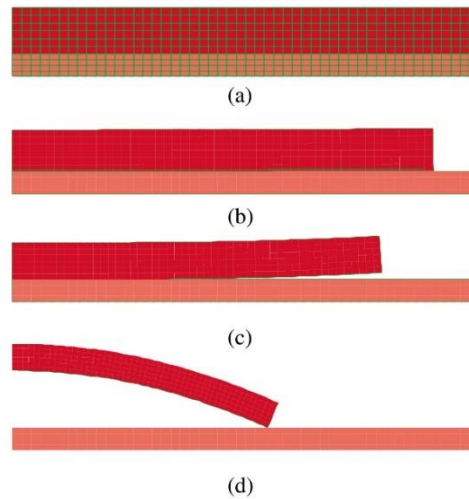


Figure 2.27. Numerical results of soil curling (Kodikara et al. 2004).

Predicted results of the soil curling process are shown in Figure 2.27. It can be observed that, at early stages of the drying process, the numerical sample deformed vertically and horizontally (Figure 2.27(b)). After that, the edges of the sample curled up to form concave-up curling (Figure 2.27(c)) and finally curved down to form convex-up curling (Figure 2.27(d)). Thus, the numerical method was able to describe the overall response of the soil curling in the experiment following the prescribed input boundary conditions. However, since FDM is a continuum-based numerical method and an elastic constitutive model was used, the FEM modelling approach did not reflect the true behaviour of slurry soils when they move from a slurry state to a semi-solid state during drying.

2.4.2. Numerical methods for modelling soil cracking

2.4.2.1. Continuum methods

Several continuum methods have been applied to model soil desiccation cracking, including FEM, FDM and SPH. FEM has been widely applied in many fields as it can handle complex conditions including complex geometry, boundaries and loads. In addition, this method also provides robust solutions, while requiring less computational costs. However, this method often suffers from mesh distortion issues when it deals with large deformations (Zienkiewicz et al. 1995) and cannot handle the occurrence and development of cracks without any treatment (Moës et al. 1999). Trabelsi et al. (2012) first implemented a new elasto-visco-plasticity model in the CODE_BRIGHT Finite Element program to simulate soil cracking. The Mohr-Coulomb criterion was modified to regulate the occurrence of cracks when tensile stress developed. As shown in Figure 2.28, the Mohr-Coulomb circle was achieved by considering the major principal stress as zero and the tensile stress as the minor principal stress. To allow cracks to propagate, after the Mohr-Coulomb criterion in each numerical element was satisfied, the viscosity of these elements had to be decreased. In addition, the drying process was implemented

by increasing suction. Figure 2.29 shows that cracks occurred in numerical samples. However, some did not connect to each other to form clear crack patterns.

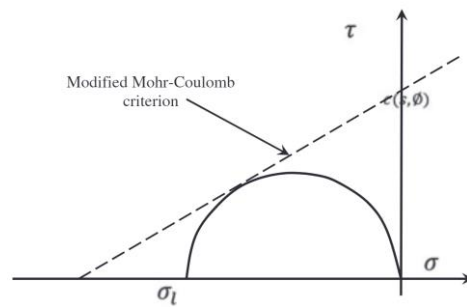


Figure 2.28. Modified Mohr-Coulomb criterion (Trabelsi et al. 2012).

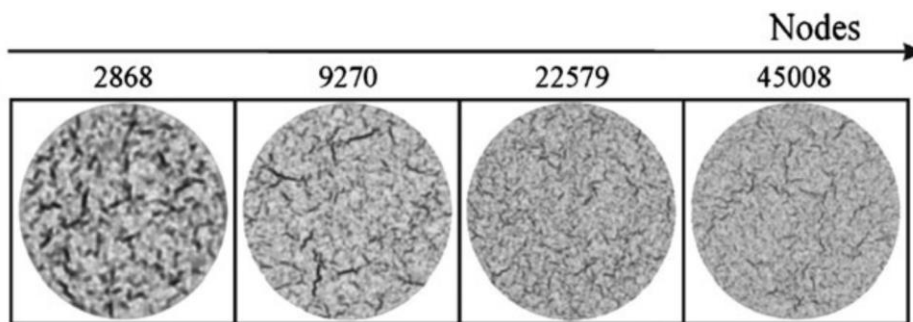


Figure 2.29. Typical crack patterns (Trabelsi et al. 2012).

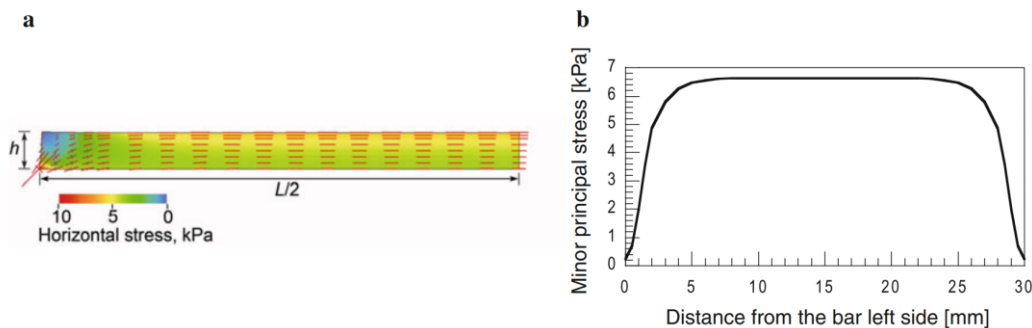


Figure 2.30. Minor principal stress developed in a numerical sample: (a) stress field in half of the sample; (b) stress profile along the sample surface (Peron et al. 2013)

FEM was also used by Peron et al. (2013) to provide further understanding of the process of desiccation cracking. In their study, a total stress analysis within the framework of the Biot theory of porous media was used. The drying process of numerical samples was implemented by simulating the redistribution of water after changing the water content on the boundaries and then calculating the shrinkage volumetric strain based on the new water content. This strain was then used to calculate the stress in the numerical samples. Although no crack occurred, this study shows that the distribution of the tensile stress developed in the numerical samples during drying was quite uniform (Figure 2.30), and thus cracks would occur simultaneously at some locations. However, this study did not

give a detailed framework for implementation of the model as well as calculation of input parameters.

To handle the initiation of cracks in the FEM simulation of soil desiccation cracking, Sánchez et al. (2014) introduced a technique known as “mesh fragmentation”. The key idea of this technique was to link standard finite elements by using high aspect ratio elements with a thickness of around 0.01mm. The tension damage model and the J2 damage model were adopted to describe the behaviour of soil-soil interface elements and soil-boundary interface elements respectively, while the elastic model was utilised to describe the behaviour of regular finite elements. The shrinkage process was activated by applying shrinkage strain only to regular finite elements. The technique was applied to study crack patterns developed in soils. The results showed that most of the behaviour observed in experiments during the desiccation process could be captured. For example, the number of vertical cracks decreased as thickness of samples increased (Figure 2.31). In addition, the occurrence of horizontal cracks in thick soil layers was also captured (Figure 2.32). However, the computational cost of the technique was very high due to an increase in the degrees of freedom.

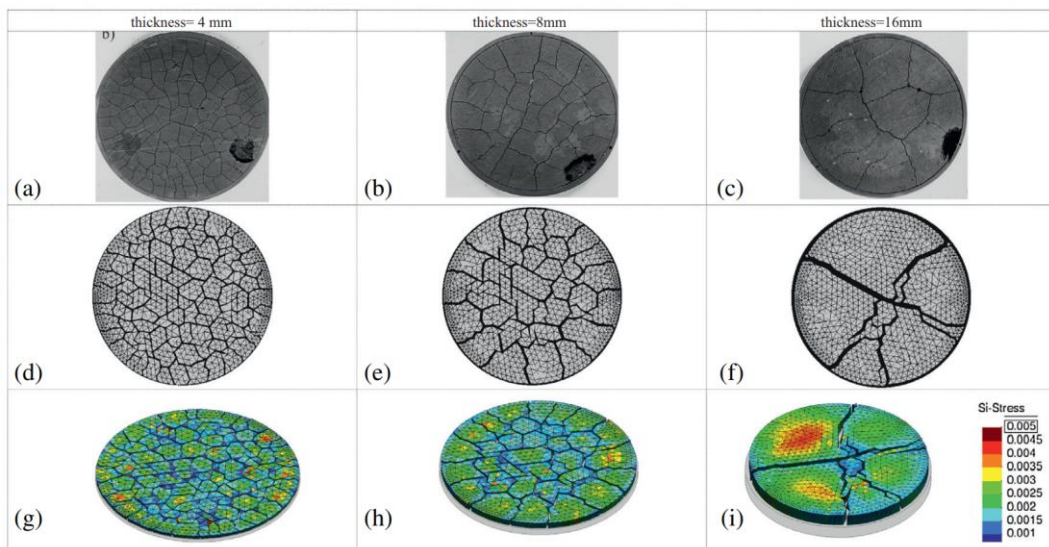


Figure 2.31. Crack patterns in soil samples with different thickness: (a-c) experimental results; (d-f) top views of the numerical samples; (g-i) distribution of the minimum principal stress on numerical samples (Sánchez et al. 2014).

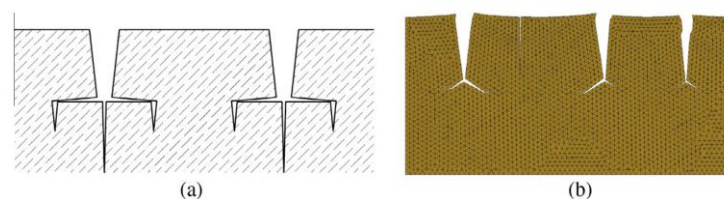


Figure 2.32. Cracks in thick layer: (a) field observation; (b) numerical result (Sánchez et al. 2014).

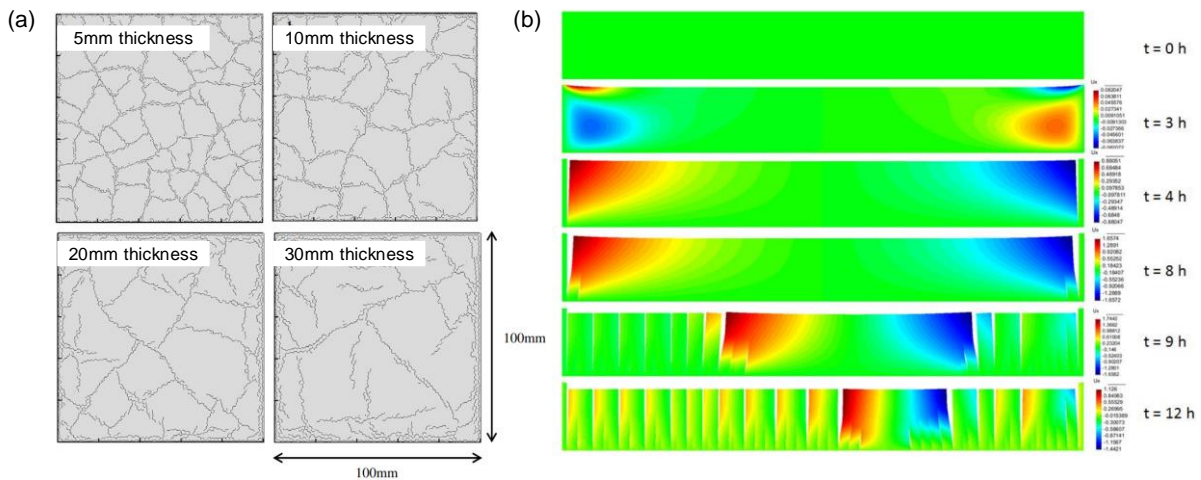


Figure 2.33. Numerical results with the coupled hydro-mechanical frameworks by FEM: (a) crack patterns in samples with different thickness (Hirobe and Oguni 2016); (b) development of cracks (Vo et al. 2017).

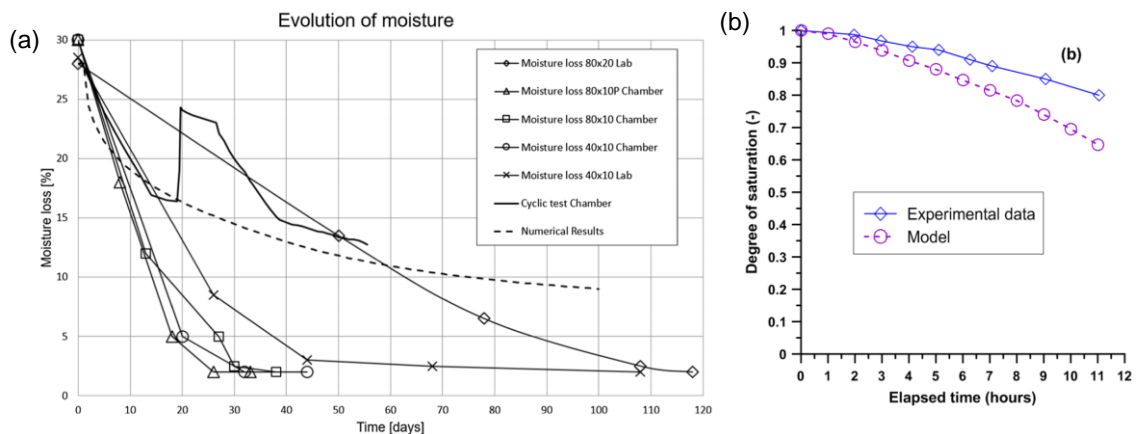


Figure 2.34. Numerical results with the coupled hydro-mechanical frameworks by FEM: (a) evolution of moisture during drying (Levatti et al. 2019); (b) evolution of degree of saturation during drying (Vo et al. 2017).

FEM was further extended to account for the hydraulic behaviour of soils when the mechanical behaviour of soils was simulated during drying in the studies of Hirobe and Oguni (2016), Vo et al. (2017), Vo et al. (2018) and Levatti et al. (2019). In their studies, the framework of the Biot theory of deformable porous media was used to simulate flows in soils, while the total stress framework was used to regulate mechanical behaviour of soils, and cohesive crack models were used to control development of fractures. In each numerical step, the hydraulic behaviour of soils was first solved to obtain the distribution of water in soils. This output was then converted to shrinkage strain and it was used to analyse the mechanical behaviour of soils. These studies showed that the initiation and development of desiccation cracks could be achieved (Figure 2.33). However, further developments are required to reasonably capture the hydraulic behaviour of soils as well as other phenomena occurring during drying such as soil curling. As illustrated in Figure 2.34, numerical and experimental results differed significantly.

Another continuum method, which has been used to simulate soil cracking, is FDM. Similar to FEM, FDM also requires interface elements to simulate the development of cracks and thus the crack patterns obtained significantly depend on the discretisation of the simulation domain. Stirling et al. (2017) conducted two-dimensional simulations to investigate the initiation of cracks by using this method with the help of the FLAC software. In this study, experimental tests were first conducted for compacted soil samples prepared in a long mould with semi-circular cross section. These tests were then simulated with consideration of both hydro behaviour and mechanical behaviour. Built-in material models were used. Input parameters were found from laboratory tests and field tests of the same soil. It was found that the crack patterns obtained in the experiments were reproduced well and more cracks occurred in soils with lower hydraulic conductivity (as shown in Figure 2.35). However, as the initiation and location of cracks depend on the interface elements, the method may be not capable of capturing complex crack patterns that normally occur in nature.

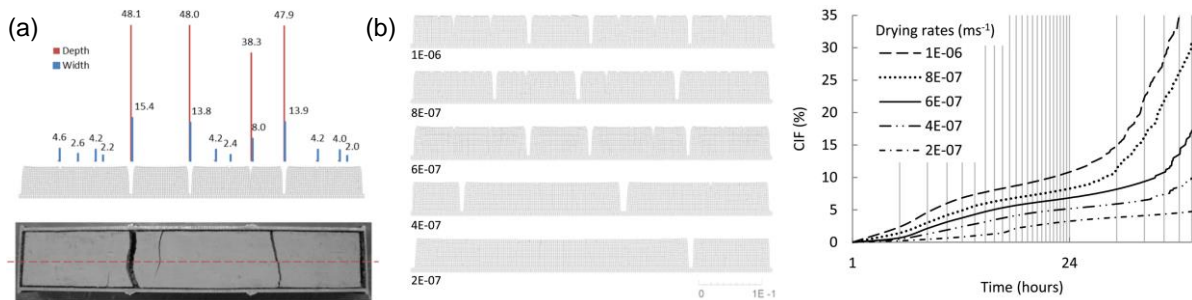


Figure 2.35. Numerical results of soil cracking with FDM: (a) crack patterns in experimental and numerical samples; (b) effect of hydraulic conductivity on soil cracking (Stirling et al. 2017).

Recently, a new framework developed based on SPH has been employed to study desiccation cracks in soils (Bui et al. 2015; Tran 2019). In this framework, both hydraulic behaviour and mechanical behaviour were considered. In addition, a rigorous cohesive model was implemented to solve issues associated with size dependence. Thanks to the nature of the method, fractures naturally occur and develop in numerical samples without using interface elements. Results demonstrate that this framework can capture well the occurrence of complex crack patterns (as shown in Figure 2.36). However, similar to other frameworks which couple hydraulic behaviour and mechanical behaviour, further work is required to reasonably capture the hydraulic behaviour of soils. As shown in Figure 2.37, the changes in water content in numerical samples were very different to those in experimental samples.

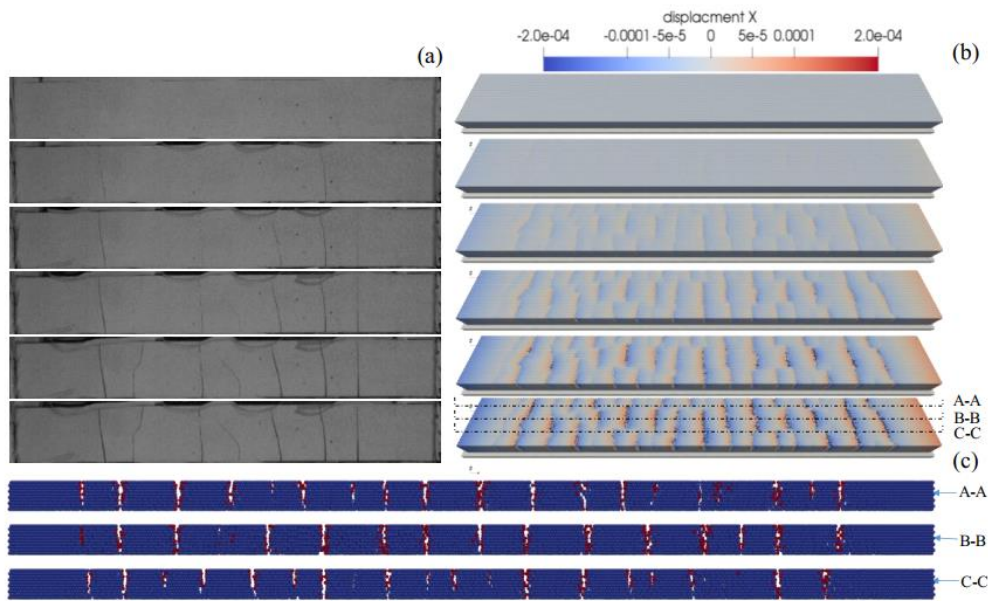


Figure 2.36. Development of cracks in experimental and numerical samples (Tran 2019).

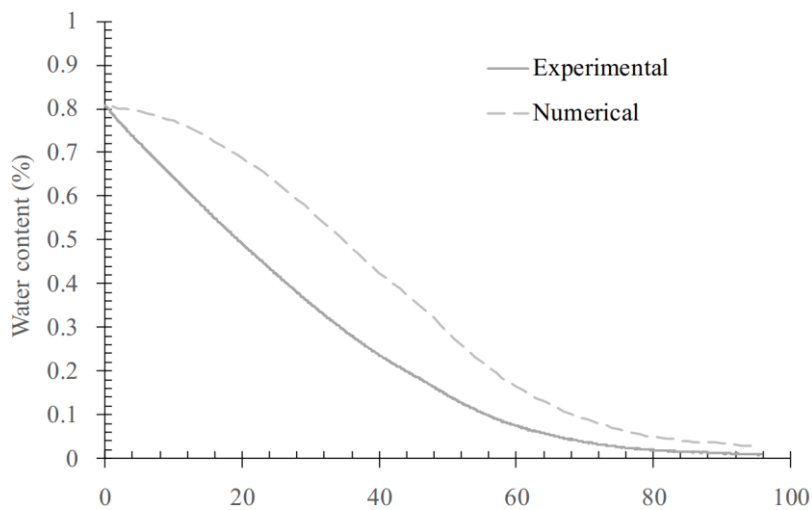


Figure 2.37 Evolution of water content in experimental and numerical samples (Tran 2019).

2.4.2.2. Discontinuum methods

Three discontinuum methods have been utilised to model soil desiccation cracking. The first method is the DEM. This method was introduced by Cundall and Strack (1979) and has been widely used to understand micro- and macro-behaviours of soils in geotechnical engineering (Bui et al. 2009; Lee et al. 2012; Tran et al. 2011a; Tran et al. 2011b; Tran et al. 2011c; Tran et al. 2012). In this method, soils are presented by assemblies of particles that interact with each other at contact points via springs, dashpots, dividers, sliders and rollers. Forces at contact points and the movement of particles are computed every time-step by using force-displacement laws and Newton’s second law (Cundall and Strack 1979).

Using DEM, Peron et al. (2009a) first conducted two-dimensional simulations to study desiccation cracks occurring in a long rectangular sample. In his approach, a group of DEM particles was used to represent clay aggregates. These particles were linked by bonds. The drying process of the numerical samples was implemented by changing the size of the DEM particles following Equations (2-1) and (2-2) for homogeneous and non-homogenous drying shrinkage, respectively.

$$R_t = R_0 \exp\left(-\frac{\alpha t}{\tau}\right) \quad (2-1)$$

$$R_t = R_0 \exp\left[\left(\alpha_1 \left(1 - \frac{y}{y_0}\right) + \frac{\alpha_2 y}{y_0}\right)\right] \quad (2-2)$$

where R_0 is the radius of a particle at time $t=0$; R is the radius of a particle at time t ; τ is the total drying time; y is the vertical coordination of the particle, y_0 is the reference height; and α , α_1 and α_2 are the shrinkage parameters, which can be calculated based on the volumetric shrinkage strain obtained from the experimental shrinkage test. For example, the shrinkage parameter α can be calculated based on the following relationship with volumetric shrinkage strain ϵ_v :

$$\epsilon_v = 1 - \exp\left(-\frac{2\alpha t}{\tau}\right). \quad (2-3)$$

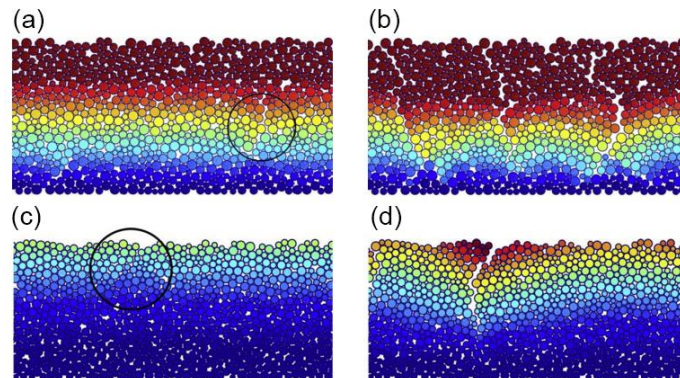


Figure 2.38. Initiation and development of cracks by using DEM (Peron et al. 2009a): (a) initiation of crack; (b) after a crack developed in the simulation with homogeneous shrinkage; (c) initiation of crack; (d) after a crack developed in the simulation with non-homogeneous shrinkage.

Typical results of this study are shown in Figure 2.38. For the homogenous shrinkage case, the first crack began anywhere along the height of the numerical sample and was not located at the centre of sample in the horizontal direction. For the non-homogenous shrinkage case, cracks began from points near the surface of the sample and they propagated towards the bottom boundary of the sample. However, cracks in both cases did not fully reach the bottom boundary of the sample due to zero displacement conditions applied to the bottom boundary (Peron et al. 2009a).

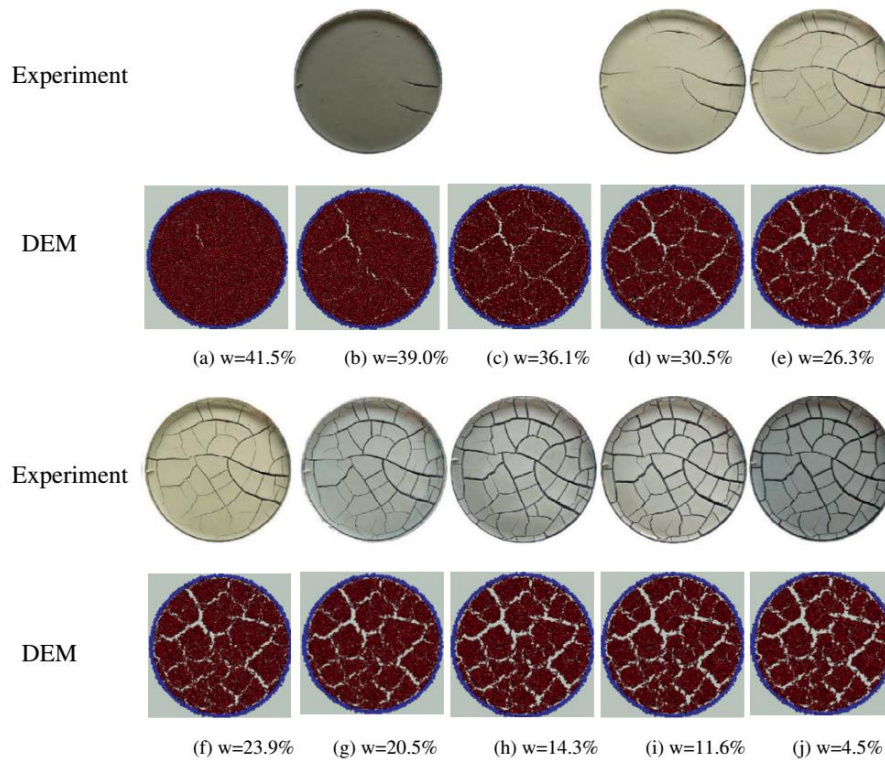


Figure 2.39. Development of crack patterns in experimental and numerical samples (Sima et al. 2014).

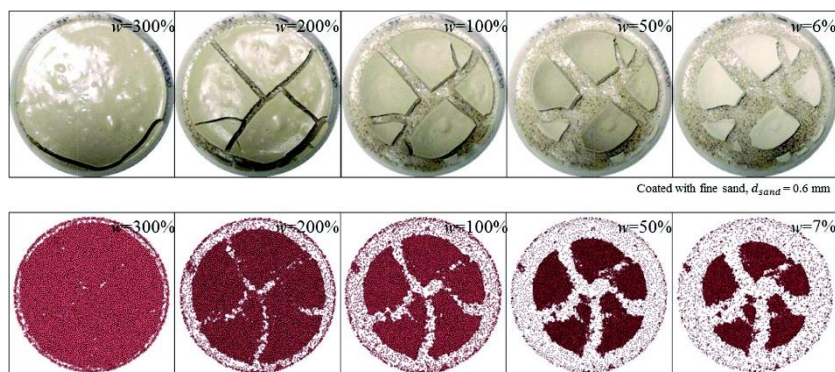


Figure 2.40. Development of the crack patterns in both experimental and numerical samples (Guo et al. 2017).

DEM was also used in studies of Sima et al. (2014) and Guo et al. (2017). In these studies, two groups of DEM particles were used to represent soils and moulds. Model parameters for soil-soil and soil-mould interfaces were calibrated by benchmarking numerical results with experimental results in uniaxial tensile tests or uniaxial compression tests. Typical results of these studies are plotted in Figure 2.39 and Figure 2.40. It can be seen that the numerical results qualitatively agree with experiments, suggesting that DEM could be a potential approach to model desiccation cracking in soils. Furthermore, the studies demonstrated that some factors affecting soil cracking such as thickness of samples, soil properties and soil-mould interface could be reasonably captured through DEM simulations. For example, the surface crack ratio decreased with an increase in the

normal stiffness of the soil-soil interaction, while with an increase in the normal stiffness of the soil-soil interaction, the water content when a first crack initiated (cracking water content) significantly increased (Figure 2.41). However, further work is required to couple hydro-mechanical behaviour when the soil cracking process is analysed.

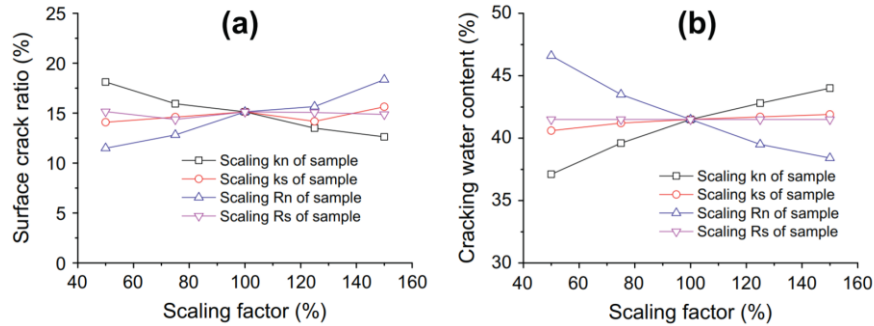


Figure 2.41. Effects of parameters for the soil-soil interaction on numerical results (Sima et al. 2014).

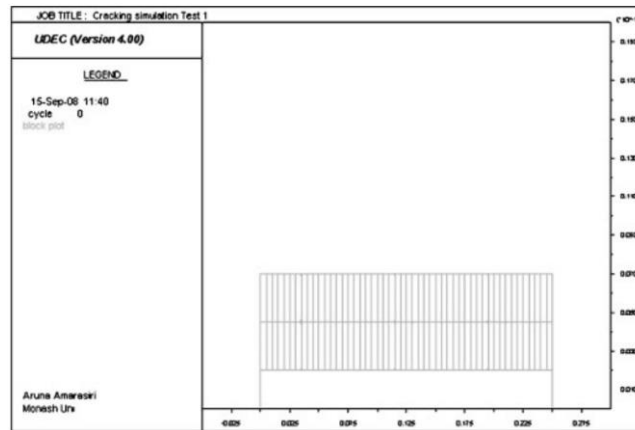


Figure 2.42. Discretisation of the numerical domain (Amarasiri et al. 2011b).

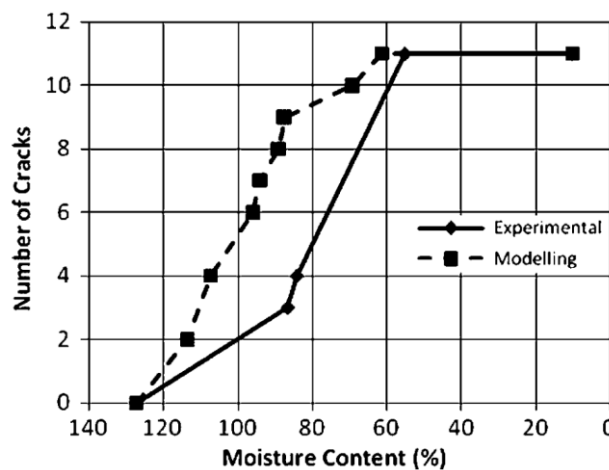


Figure 2.43. Development of cracks in experimental and numerical tests (Amarasiri et al. 2011b).

Another method in the discontinuum method group is the distinct element method. This method is similar to DEM, except that soil medium is represented by a group of discrete

blocks and each block can be subdivided into a group of finite different elements. In addition, motion of each block can be calculated at grid-points of the finite different elements, and then the material constitutive relation of blocks is used to obtain stresses within each block. The first studies of desiccation cracking in soils using the distinct element method were reported by Amarasiri et al. (2011b) and Amarasiri and Kodikara (2013). In these studies, an assembly of rectangular blocks was used to describe the soil domain (Figure 2.42). Properties of soil blocks (bulk modulus and shear modulus) were functions of water content and they were determined from laboratory tests, while properties of soil-mould interface and soil-soil interface were achieved from calibrations to match the numerical crack patterns to the experimental crack patterns. The soil block material behaved nonlinearly, while materials for soil-mould and soil-soil interfaces was regulated by a simple tensile strength criterion or a cohesive model with a softening law for the evolution of the tensile stress. The drying process was initiated by forcing isotropic shrinkage strain on each soil block. The studies showed that the method could quantitatively capture the development of cracks in an experimental sample (Figure 2.43). Gui et al. (2016) improved these works by using a voronoi tessellated mesh to discretise the soil domain and a mixed-mode cohesive fracture model to regulate the formation of cracks. Figure 2.44 shows that the randomness of crack development was fairly captured.

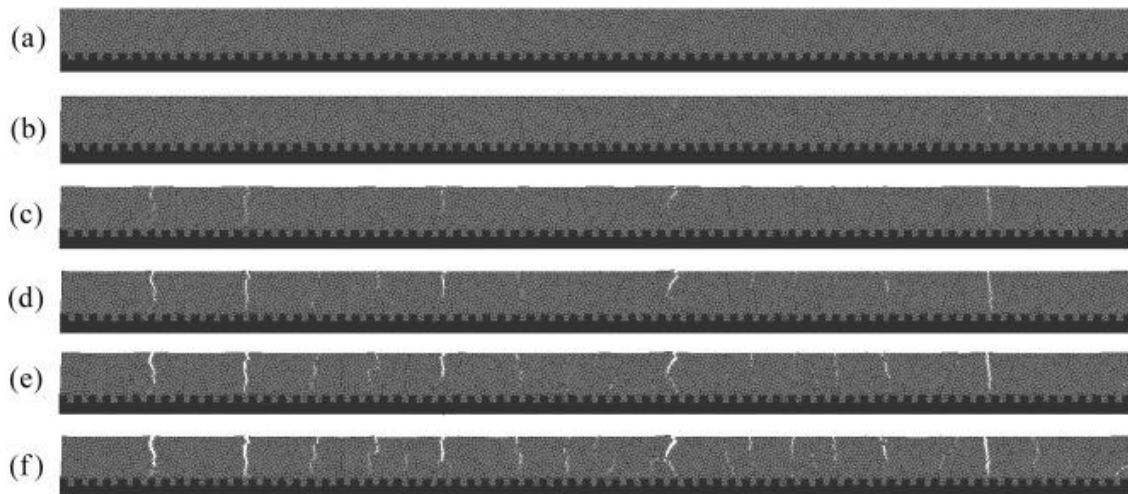


Figure 2.44. The development of cracks in a numerical soil domain (Gui et al. 2016).

The Distinct Lattice Spring Model (DLSM) is another discontinuum method that has been also used to study soil cracking. This method was developed recently and has been used in the study of soils and rocks (Zhao et al. 2011). Gui and Zhao (2015) used this method to investigate the behaviour of soil desiccation cracking. In their work, soil particles were modelled by spheres, which were linked by springs. The two-phase bond model (water bond and spring bond) was used to present the interaction of pore pressure with the soil matrix. During the shrinkage process, changes of suction were input in the model and spring bond forces were then calculated from volumetric shrinkage strain that was obtained from the suction, while the water bond forces were calculated from the suction.

These bonds broke when their forces reached their limits. This study shows that cracks developed in the numerical sample only when the limits of the water bond force was randomly distributed through the sample.

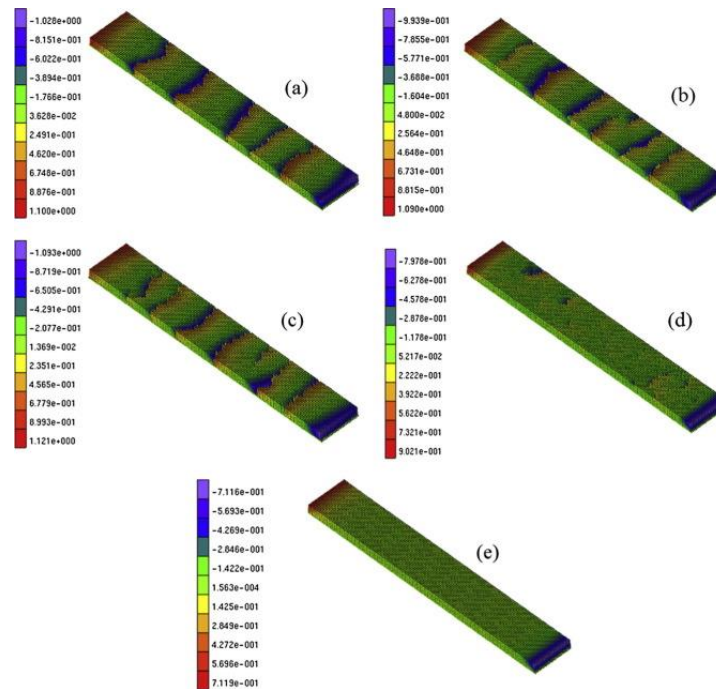


Figure 2.45. The development of cracks with different random ratios of properties: (a) random ratio = 5%, (b) random ratio =10%, (c) random ratio =30%, (d) random ratio =50%; (e) random ratio =0% (Gui and Zhao 2015).

This section has highlighted that both continuum and discontinuum approaches can be used to qualitatively capture most of experimental observations including crack patterns and curling behaviour. However, to allow development of cracks, treatments have to be used in the continuum approaches, while these treatments are not required in the discontinuum approaches. In addition, several attempts have been made to analyse coupled hydro-mechanical behaviour during desiccation cracking by using continuum approaches. However, the hydro behaviour of soils during desiccation has not yet been accurately captured.

2.5. Conclusions

This chapter has presented the review of the current knowledge on soil curling and desiccation cracking in soils and is summarised as follows:

1. Desiccation-induced soil curling and soil cracking are complex phenomena. They strongly influence the performance of soils and adjacent structures. Therefore, understanding the occurrence of these phenomena and predicting them are very important.

2. Soil curling may occur in concave-up form, convex-up form or even in a combination of first the concave-up form, and then the convex-up form. The occurrence of soil curling has been explained based on the differential shrinkage along the height of soil layers or the development of capillary force on the soil surface. However, these existing explanations were postulated by using only observations of the final stage of the desiccation process. Therefore, these explanations do not accurately cover the entire process of soil curling.
3. Soil curling is strongly influenced by various factors such as the drying temperature, distribution of soil particles and material properties. However, existing studies have only reported the general effect of these factors, while no attempt has been made to quantify how these factors affect soil curling or to provide quantitative relations of these factors to soil curling.
4. Soil cracking occurs due to moisture loss. During the cracking process, cracks may start from the surface of soil media, or any point inside the soil media and then propagate to divide the soil media into many small fragments. The development of cracks has been explained based on tensile failure, or a combination of both tensile and shear failures, or the intrusion of air into the soil media. These explanations were based on observations of the behaviour of the soil media during desiccation. Numerical studies have also been conducted to verify the proposed explanations for soil cracking. However, quantifying the behaviour of the soil media (i.e. quantifying the strain field) may provide further understanding of soil cracking.
5. Soil cracking is strongly influenced by various factors such as drying temperature, material properties and boundary conditions. Many studies have quantified how these factors affect soil cracking and reported quantitative relations between these factors and the behaviour of soil cracking. However, the effect of wind velocity on soil cracking has not yet been reported.
6. There has been only one study that reported the simulation of soil curling. In that study, a continuum-based method was used. Due to the nature of the continuum-based method, the link between the micromechanical processes and the macro-behaviour of soils was not fully captured. Therefore, a computational model capable of capturing both micro- and macro-behaviour of the desiccation cracking process in soils should be developed.
7. Many attempts have been made to simulate soil cracking using either continuum-based or discontinuum-based computational approaches. It has been reported that both approaches could qualitatively capture most experimental observations such as crack patterns and the effect of drying rate

on soil cracking. However, DEM has been shown to be the most promising method, owing to its ability to consider true physical processes at the grain scale level. In addition, soil cracking is a phenomenon that is associated with the evaporation process, and thus it is essential to consider the coupled hydro-mechanical behaviour in order to simulate this phenomenon accurately and provide further understanding of the behaviour of this phenomenon.

Chapter 3. Experimental Investigation of Soil Curling

3.1. Introduction

Clayey soils are encountered in various disciplines such as geotechnical engineering, soil science, agricultural science, engineering geology and environmental science. Due to their properties, the type of soils shrinks significantly when losing moisture, leading to the development of soil curling. As reviewed in Chapter 2, although many studies have been conducted (Allen 1986; Berney et al. 2008; Bradley 1933; Kindle 1917, 1923; Kodikara et al. 2004; Longwell 1928; Minter 1970; Style et al. 2011; Ward 1923; Zielinski et al. 2014), the mechanisms and factors affecting soil curling are still poorly understood.

The literature review presented in Chapter 2 also shows that concave-up curling (\cup) and convex-up curling (\cap) can be encountered in both field and laboratory tests for slurry and compacted clays, and have been explained from a macro-view, where differential water loss and non-homogeneous distribution of soil particles along the height of the soil sample are considered as the main cause of differential contraction (Allen 1986; Bradley 1933; Kindle 1917, 1923; Kodikara et al. 2004). This differential contraction leads to the development of a bending moment, thus this moment bends soil layers to form concave-up curling or convex-up curling (Kodikara et al. 2004; Style et al. 2011). This concept was verified in an empirically-based numerical study, in which explicit expressions of the suction-water content relationship and differential water loss along the height of soil layers were required (Kodikara et al. 2004). Although this numerical approach can capture concave-up curling, it cannot explain the mechanisms of curling in soils that experience both concave-up curling and convex-up curling. Considering concave-up curling from a micro-view, it has been explained that the non-uniform distributions of the vertical component of the surface tension and the gravity force on the soil surface can cause non-uniform settlement of soil particles on the surface layer, thus facilitating an initial curling (Zielinski et al. 2014). As drying continues, water starts evaporating from the sides, enhancing concave-up curling. However, a comprehensive explanation of how a soil sample lifts off remains elusive. In addition, most previous studies used the final stage of the desiccation process to infer the entire curling mechanism (Allen 1986; Bradley 1933; Kindle 1917, 1923; Kodikara et al. 2004; Longwell 1928; Minter 1970; Style et al. 2011; Ward 1923), and this may result in misinterpretation of the curling process, especially for soils that experience concave-up curling first and then convex-up curling. Although a recent study utilised time-varying observations of soil curling to explain this mechanism, only curling of the top-soil surface was captured (Zielinski et al. 2014). In the author's point of view, to fully understand soil-curling mechanisms, continuous time-varying

observation of the behaviour of both the top and bottom faces of a soil layer is required during drying and this has not been reported to date in the literature.

Previous studies on soil curling have also reported that soil curling is governed, amongst others, by the non-homogenous distribution of soil particles, clay minerals, boundary conditions, and the existence of salt and its distribution in a soil mass (Bradley 1933; Kindle 1917, 1923; Minter 1970; Zielinski et al. 2014). For example, Bradley (1933) reported that the edges of polygonal plates curl toward the layer with the finest grains. This means that concave-up curling occurs in soil layers with soil particles distributed from fine particles at the top to coarse particles at the bottom, and convex-up curling takes place when the particle distribution is reversed. Similarly, if the surface of clayey soil media dries faster, concave-up curling can be observed, while, convex-up curling occurs if the bottom layer dries faster (Bradley 1933; Minter 1970). Some studies have also revealed that the existence of salt in the soil media changes the curling behaviour of mud from concave-up curling to convex-up curling (Bradley 1933; Kindle 1917, 1923). Curling characteristics (e.g. the curvature and lift-off height) are strongly influenced by non-homogenous distribution of soil particles (Bradley 1933; Zielinski et al. 2014), evaporation rate (Bradley 1933; Longwell 1928), material types (i.e. clay, silt, fine sand) and soil layer thicknesses (Longwell 1928). However, how these factors and the state of soil media influence the soil curling process has not been comprehensively discussed.

This chapter aims to provide a more comprehensive explanation of the soil curling mechanism and its influencing factors (i.e. clay type or clay minerals, drying temperature, initial water content and sand content) by making time-dependent observations of a soil-layer undergoing drying. This chapter starts with brief explanations of the material properties, the experimental set-up and procedure. Next, the soil curling process and its mechanism are discussed in detail. Finally, the effects of the factors on the soil curling process are also presented and discussed.

3.2. Materials and Methods

3.2.1. Materials

Three clayey soils, Werribee clay, Altona North clay and Kaolin NY clay, were used in this study. The physical properties of these clayey soils were explained in detail (Nahlawi 2004; Nahlawi and Kodikara 2006; Shannon 2013) and hence are not repeated here. Only the key physical properties of these soils are presented to provide background for further explanation of the soil curling mechanism in subsequent sections. Table 3.1 summarises the key physical properties of these materials, and the soil water retention curves (SWRCs) and particle size distributions are plotted in Figure 3.1. The fitting curves for SWRCs are also plotted using equations proposed by Fredlund and Xing (1994) for

Werribee clay (Nahlawi 2004), and by van Genuchten (1980b) for other clays (Shannon 2013).

Table 3.1. Typical soil properties (Nahlawi 2004; Shannon 2013).

Properties	Werribee clay	Altona North clay	Kaolin NY clay
Liquid limit (%)	127.0	70.2	54.8
Plastic limit (%)	26.0	21.8	26.0
Plasticity index (%)	101.0	48.4	28.8
Linear shrinkage (%)	22.0	16.0	6.9
Shrinkage limit (%)	13.0	-	29.4
Soil classification	CH	CH	CH
Specific gravity	2.66	2.61	2.62
Hydraulic conductivity (m/s)	2.2×10^{-10}	3.4×10^{-10}	3.6×10^{-9}
Percentage sand (%)	4.4	3.7	0.1
Percentage silt (%)	28.2	33.1	29.1
Percentage clay (%)	67.4	63.2	70.8

CH: Clay of high plasticity

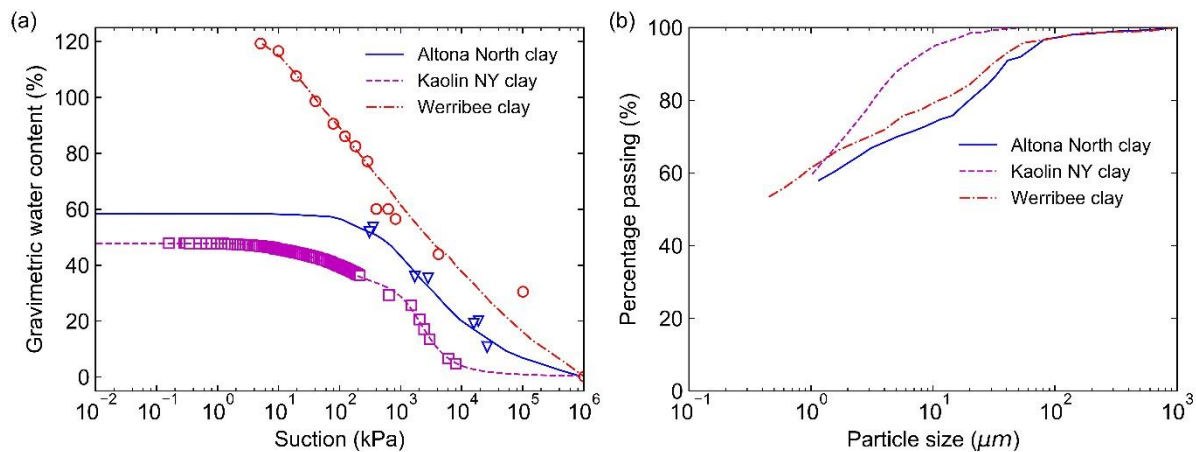


Figure 3.1. (a) SWRCs of Werribee, Kaolin NY and Altona North clay (the volumetric water content is roughly converted to the gravimetric water content in the case of Altona North clay); (b) particle size distribution (Nahlawi 2004; Shannon 2013).

The first type of clayey soil used in this study was Werribee clay, which was obtained at the Aquatic Centre site in Werribee, Victoria, Australia. It is a highly reactive residual soil, which consists of 42% Smectite, 30% Quartz, 8% Feldspars (albite), 10% Illite and 10% Kaolinite. The liquid limit and plastic limit of this clay are 127% and 26%, respectively, suggesting that this clay is extremely reactive with high potential for shrinkage and swelling. The second clayey soil was Altona North clay, which was obtained at a depth of 0.4 m - 2.0 m from the surface in Altona North, Victoria, Australia. Compared to Werribee clay, this soil is a highly plastic basaltic clay soil. The mineral composition of this clay is 31% Smectite, 59% Quartz, 2% Kaolinite, 3% Orthoclase, 2% Feldspars, and 3% Calcite. These two clays are quite similar in clay components with a dominant Smectite content.

However, the liquid limit and plasticity index of Werribee clay are much higher than those of Altona North clay, which may be attributed to the difference in the percentage of clay minerals. The last clayey soil was Kaolin NY clay, which is a commercial material produced at Granville, New South Wales, Australia. It is classified as clay of high plasticity (CH). The main chemical compositions of this clay are 46.7% Silica, 36.1% Aluminium Oxide and 14.0% loss on Ignition. Compared to the two previous clays, this soil has the lowest liquid limit, plastic index and linear shrinkage. Finally, mixtures of various amounts of Quartz sand with Werribee clay were also used to investigate the effect of sand content or of the non-homogenous distribution of soil particles. Quartz sand has a uniform size distribution with particle diameters ranging from 0.5 mm to 0.6 mm and medium angular shapes. The specific gravity is 2.62.

3.2.2. Methods

Four series of tests were conducted in this study, each exploring the soil curling mechanism and the effects of the main factors on the soil curling process. All tests were conducted for slurry clayey soils contained in the same Perspex mould with internal sizes of 251 mm long, 25 mm wide and 12.4 mm deep. The size of the mould was chosen to facilitate the development of soil curling in a two-dimensional view, ensuring that soil samples could resist crack developments within the samples when they were undergoing soil curling. To allow soils to shrink freely, a thin layer of grease was applied to the sidewalls and base of the mould. To prepare specimens, the natural clayey soils were dried, crushed and sieved through a 0.425 mm sieve. For each type of clay, the material passing through the 0.425 mm sieve was thoroughly mixed with distilled water in a cup at the designated water content. The amount of soil used to create slurry was slightly higher than required to ensure that the sample had the designated water content. The resulting clayey slurry was then poured into the mould and vibrated for 5 minutes to eliminate air trapped in the sample. The sample was covered, kept in a small box and stored in a cool and damp place for 24 hrs to achieve uniform distribution of moisture. Prior to testing, the sample was placed on a balance with 0.01 g precision, which was connected to a computer to automatically record the weight of the specimen every 10 min to 20 min. The time interval to log weight depended on the drying temperature and soil material. A camera was fixed to face the long side of the sample to monitor the soil curling process as shown in Figure 3.2. Photographs were taken at the same time intervals as the weight. A sensor was placed close to the sample to record temperature and relative humidity. The experiment was carried out in an air-conditioned room with a temperature of 20-22°C. 500W and 1000W lamps were used with different lamp distance (i.e. the distance from the sample's surface to the lamp) to generate drying temperatures. To verify the repeatability of experiments, each drying test except the case for kaolin clay was conducted twice. Details of the test program and experimental conditions are summarised in Table 3.2. The gravimetric water content is presented in this chapter.

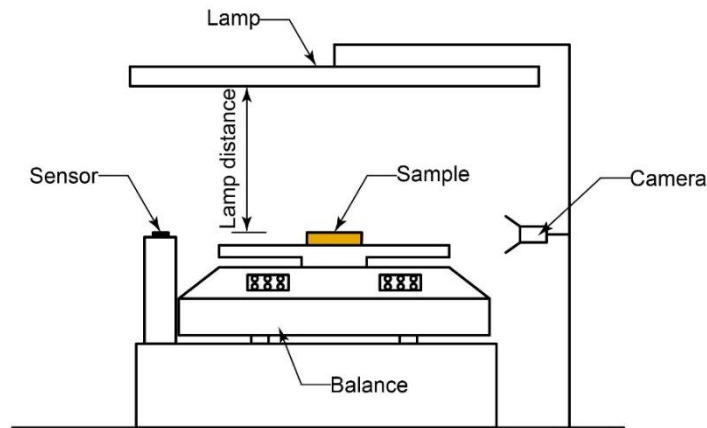


Figure 3.2. Experimental set-up (side view).

Table 3.2. Experimental program and conditions.

Test ID	Soil type	Initial water content (%)	Average temperature (°C)	Average relative humidity (%)
CL1_1, W3_1, T2_1	Werribee clay	191.67	28.6	22.57
CL1_2, W3_2, T2_2	Werribee clay	192.26	27.8	25.2
CL2_1	Altona North clay	104.11	29.8	34.8
CL2_2	Altona North clay	106.18	30.1	37.5
CL3_1	Kaolin NY clay	86.62	26.8	32.1
CL3_2	Kaolin NY clay	86.96	28.7	32.3
W1_1	Werribee clay	130.76	27.3	26.6
W1_2	Werribee clay	131.47	26.5	25.2
W2_1, S1_1	Werribee clay	174.48	28.2	24.1
W2_2, S1_2	Werribee clay	172.47	28.1	25.5
T1_1	Werribee clay	193.34	24.5	48.3
T1_2	Werribee clay	192.92	24.4	45.1
T3_1	Werribee clay	195.45	38.6	11.1
T3_2	Werribee clay	189.94	39.0	12.8
S2_1	Werribee clay+10% sand	172.76	26.2	26.9
S2_2	Werribee clay+10% sand	172.92	26.3	26.8
S3_1	Werribee clay+20% sand	174.35	26.9	28.8
S3_2	Werribee clay+20% sand	171.76	27.1	27.8
S4_1	Werribee clay+30% sand	165.33	27.2	25.6
S4_2	Werribee clay+30% sand	166.65	27.1	30.4

The first series of tests were designed to explore the soil curling mechanism and the effect of clay type or clay minerals on soil curling behaviour. Samples were prepared with three clays (i.e. Werribee clay (CL1), Altona North clay (CL2) and Kaolin NY clay (CL3)) at 1.5 times their liquid limit ($1.5 \times LL$). These samples were dried at a temperature of $28 \pm 2^\circ\text{C}$. The second series of tests was performed to explore the influence of initial water content on soil curling. Werribee clay samples were prepared with three different water contents: $1.0 \times LL$ (W1), $1.35 \times LL$ (W2) and $1.5 \times LL$ (W3). These values were chosen to facilitate the preparation of homogenous clay samples and to eliminate flaws created during sample preparation. In fact, these values have been commonly used in previous studies (Bradley

1933; Kindle 1917; Kodikara et al. 2004; Zielinski et al. 2014). After these samples were prepared they were dried at a temperature of $28\pm 2^{\circ}\text{C}$ and relative humidity of $24\pm 2\%$. The third series of tests explored the effect of temperature on soil curling. Six samples were prepared by mixing Werribee clay with distilled water with water contents of $1.5\times\text{LL}$, and then dried under three different temperature conditions with average temperatures of 24.5°C (T1), 28.2°C (T2) and 38.8°C (T3). Finally, for the fourth series of tests, quartz sand was washed, dried and sieved. The sand, which passed a 0.6 mm sieve and was retained by a 0.5 mm sieve, was mixed with Werribee clay and distilled water at $1.35\times\text{LL}$ of Werribee clay. The sand/clay ratios were 0% (S1), 10% (S2), 20% (S3) and 30% (S4). These samples were dried at a temperature of $28\pm 2^{\circ}\text{C}$. These series of tests were prepared to study the effect of sand content or the non-homogenous distribution of soil particles on soil curling behaviour.

3.3. Curling Process of Werribee, Altona North and Kaolin NY Clays

3.3.1. Water evaporation

The process of water evaporation of soil layers is controlled by environmental conditions (which mainly depend on air temperature, humidity, wind velocity and radiation) and properties of soil layers such as water content and hydraulic conductivity (Hillel 2003). Since the soil samples were dried under a lamp in an air-conditioned room, the main factors controlling the drying process were drying temperature, relative humidity and soil properties. Figure 3.3(a) presents a typical time history of temperature and relative humidity during the drying period of Werribee clay samples in the first series of experiments (tests CL1_1 and CL1_2). The temperatures induced by the lamp in two tests were close to each other and remained almost constant during the tests ($28^{\circ}\text{C}\pm 2^{\circ}\text{C}$ for both samples). Relative humidity followed the same trend as the temperature except for two short periods (at approximately 75 hrs and 150 hrs) where the relative humidity condition for test CL1_2 was noticeably higher than that for test CL1_1. Therefore, the two tests were subjected to almost the same boundary loading conditions.

The evolutions of water content and evaporation rate in different clay samples in the first series of tests are plotted in Figure 3.3(b)-(d). The water content of three clays decreased rapidly until reaching approximately 13%, 9% and 2.5%, then gradually decreased to residual values corresponding to 5.4%, 5.5% and 1.7% for Werribee clay, Altona North clay and Kaolin NY clay, respectively. The evolution of the evaporation rate showed a similar trend to that of water content. It declined greatly and then gradually approached zero with increasing drying time. However, there was a sudden change of slope in the evolution of the evaporation rate after the drying process started at approximately 40 hours, 25 hours and 30 hours, corresponding to water contents of 24%, 31% and 14% for Werribee clay, Altona North clay and Kaolin NY clay, respectively. The evaporation rate

then decreased much more rapidly than previously, corresponding to a minor decrease in water evaporation. This may be attributed to a significant decrease in the hydraulic conductivity as soils change from the plastic stage to the semi-solid stage. The reduction of hydraulic conductivity hinders liquid and vaporised water from transferring to the faces on which evaporation occurs.

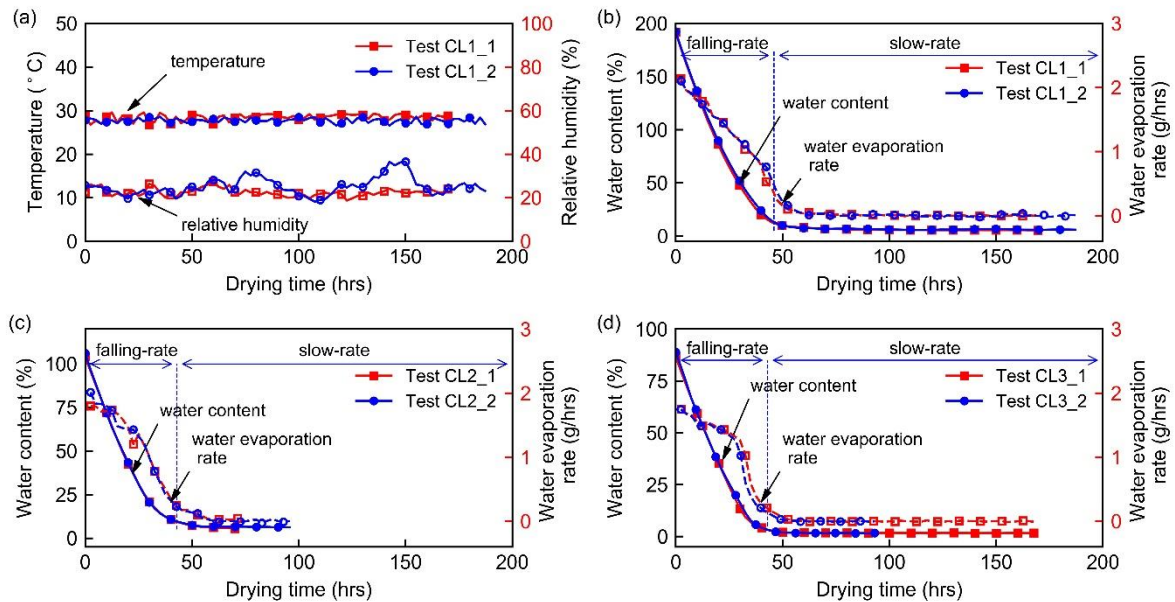


Figure 3.3. (a) typical drying conditions; (b) water content and water evaporation rate of Werribee clay; (c) water content and water evaporation rate of Altona North clay; (d) water content and water evaporation rate of Kaolin NY clay.

Based on the evolutions of water content and evaporation rate, the drying processes of the clays in the first series of tests can be classified into two main stages: a falling-rate stage and a slow-rate stage. A constant evaporation rate stage, which was reported in previous studies (Hillel 2003; Tang et al. 2011b; Tang et al. 2011c), was not observed in the current tests. This may be attributed to the influences of small sample sizes, drying conditions, soil properties and soil surface conditions (Hillel 2003; Kayyal 1995).

3.3.2. Curling process

The shrinkage processes of tested specimens were recorded by taking side-view pictures of soil samples. Figure 3.4 presents the progressive development of shrinkage deformation of a typical Werribee clay sample (test CL1_2) during drying. During desiccation, the sample shrank and concave-up curling occurred. After a certain time, concave-up curling gradually reduced and then convex-up curling began. To quantitatively measure shrinkage, the boundary of the soil sample was tracked and it is plotted in Figure 3.5. This process can be described as follows. Upon drying, water in the sample evaporated, causing shrinkage deformation of the soil specimen. Initially, the sample shrank significantly along its height and then detached from the left and right sides

of the mould when water content decreased from 192.26% to 166.57%. After this point, the specimen continued to shrink in three directions. However, the longitudinal shrinkage deformation was dominant after water content reached around 145%. The edges of the sample started lifting at water contents of 91.90% and 80.39% for the right and left edges, respectively, forming concave-up curling. With further drying, the left and right edges of the sample continued to curl up and reached their maximum elevations at a water content of approximately 47%. The curled edges then started to retreat downwards and touched the base of the mould. During this period, the edges fluctuated vertically and the sample continued to shrink. From a water content of 32.72% corresponding to a suction of approximately 18MPa (determined from SWRC plotted in Figure 3.1(a)), the centre of the sample was lifted from the mould, forming convex-up curling. The elevation of the centre fluctuated vertically until the water content was 22.98%. After this point, this elevation continuously increased and the sample's curvature therefore continuously increased. Convex-up curling stopped after the water content reached 7.61% and the sample remained static despite further drying. In the present study, the lift-off height is defined as the distance from the base of the mould to the highest point of the bottom face of the sample. Figure 3.4 and Figure 3.5 show that in this sample, the lift-off height after convex-up curling stabilised was around ten times greater than that for concave-up curling.

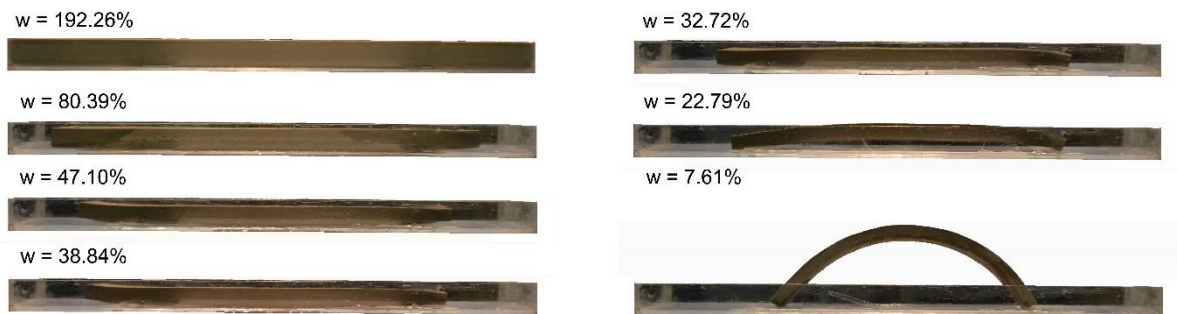


Figure 3.4. Time-lapse of shrinkage process of Werribee clay sample – test CL1_2.

Figure 3.6 presents the shrinkage process of an Altona North clay specimen (test CL2_1). Concave-up curling then convex-up curling were observed. The Altona North specimen initially detached from the mould and started curling up when its water contents were approximately 85% and 45%, respectively. The edges of the sample then moved up to maximum elevations when the water content of the sample was close to 26%. The curled edges then moved downwards and the centre section started moving up to form convex-up curling when the water content reached 20.61%, corresponding to a suction of 10MPa determined from Figure 3.1(a). The centre section continued to lift and ceased lifting while maintaining its elevation when the water content was 7.23%. The Altona North sample experienced the same behaviour as the Werribee clay sample. This may be attributed to the similarity of their mineral compositions. Further discussion is presented in the next section.

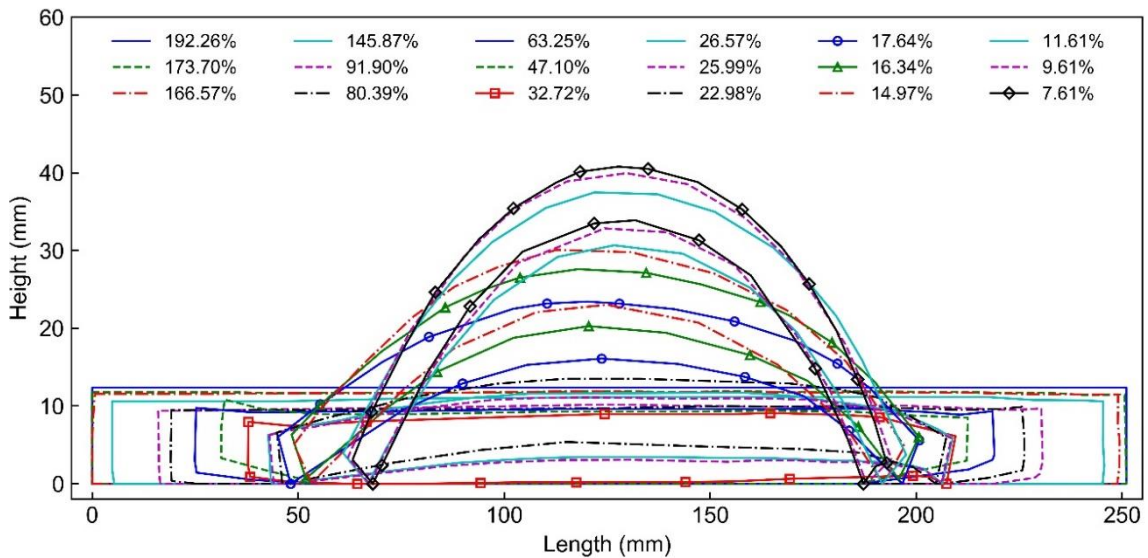


Figure 3.5. Shrinkage process of Werribee clay sample (test CL1_2).

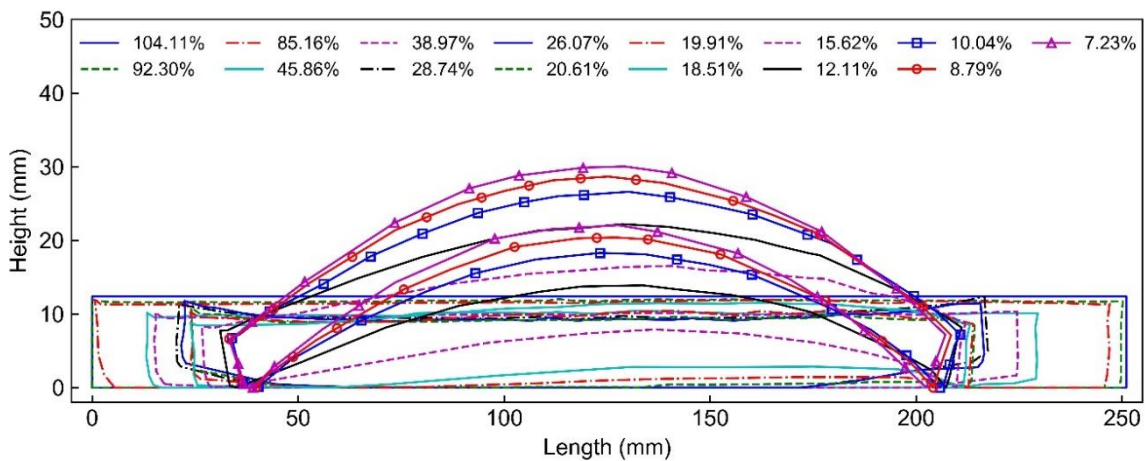


Figure 3.6. Shrinkage process of Altona North clay sample (test CL2_1).

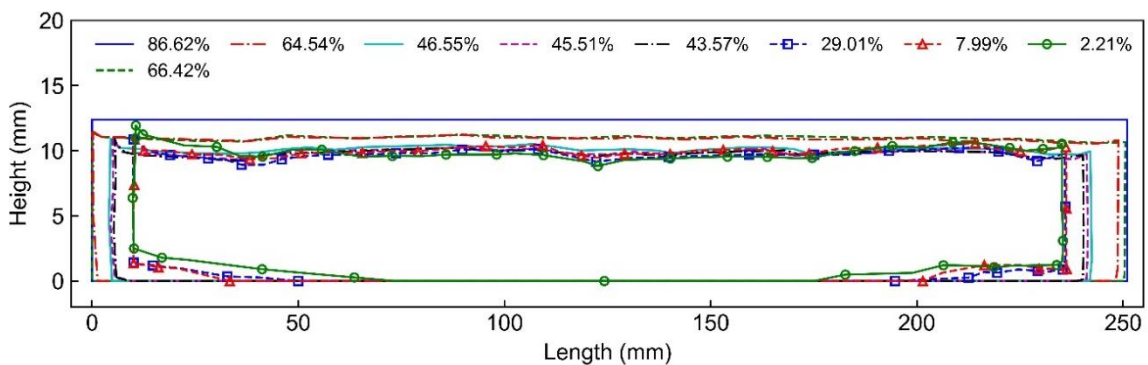


Figure 3.7. Shrinkage process of Kaolin NY clay sample (test CL3_1).

Figure 3.7 shows the behaviour of the Kaolin NY clay sample undergoing drying. The sample started to detach from the mould and concave-up curling started developing when the water contents were around 64% and 43%, respectively. The process progressively

developed until the water content was 29%. After that, the sample experienced a temporary stable period until the water content was 7.99%, in which the sample retained its shape. After this temporary period, the edges of the sample continued to curl up again until the water content reached 2.2%. With further drying, the sample retained its shape. Figure 3.7 also shows that this sample did not experience convex-up curling that was observed in the samples made of Werribee and Altona North clays. This different behaviour may be due to differences in material properties, especially in the clay mineral composition. The Kaolin sample also showed smaller lift-off height in comparison with the two other clays. The curling behaviour of the Kaolin NY clay sample is consistent with that reported by Zielinski et al. (2014) who conducted drying tests of another type of Kaolin clay, except a temporary stable period. This temporary stable period was not recorded in the study of these researchers could be because the sample was not be frequently measured.

Figure 3.4 to Figure 3.7 demonstrate that in these samples, concave-up curling starts when the water content of these samples is close to their liquid limits, while convex-up curling begins when the water content of these samples is slightly higher than their plastic limits. Both concave-up curling and convex-up curling continue to develop even when the water content is much lower than their shrinkage limits. According to these observations, the curling process in clayey soils can be summarised as follows. When a clayey soil sample is dried from its upper surface, concave-up curling occurs in two stages (stages I and II), while convex-up curling occurs in four stages (stages I, II, III and IV). These stages are:

- I. The sample shrinks in all directions. Soil particles settle down and the sample detaches from the mould. The dominant deformation direction of the sample shifts from vertical to longitudinal and lateral directions.
- II. The sample continues shrinking and its edges start curling up, forming concave-up curling. This process progressively develops until the curled edges reach their maximum elevations. During the development of soil curling, the sample may experience a temporary stable period, in which the sample retains its shape.
- III. The curled edges retreat downwards and reach the base of the mould. The soils then shrink dominantly in longitudinal and lateral directions.
- IV. The sample lifts off approximately at the centre to form convex-up curling and this process continues until the water content is near residual value.

By combining the findings from this study and previous studies (Allen 1986; Berney et al. 2008; Bradley 1933; Kindle 1917, 1923; Kodikara et al. 2004; Longwell 1928; Minter 1970; Style et al. 2011; Ward 1923; Zielinski et al. 2014), it is suggested that concave-up and

convex-up curling of clayey soils in nature occur following the same process described above. However, in stage I, instead of the detachment of a soil sample from the mould, vertical cracks occur and divide the soil media into many polygons. In stage II, horizontal cracks occur and the edges of soil polygons start curling up. The lift-off height and the curling shape of these polygons depend on their size and shape.

3.3.3. Curling water content

Water content is an important physical factor that governs the strength and mechanical characteristics of soils (Mitchell and Soga 2005). It is also important in the drying testing of clay soils, as it can affect the evaporation rate, soil deformation and the initiation of cracking and of soil curling. In all specimens studied, the evolution of water content followed the same trend. That is, the water content first significantly decreased and then slowed down before reaching a residual value. The water content at the point when concave-up curling and convex-up curling initiated, defined as w_{ccs} and w_{cvs} , were investigated. Furthermore, the water content when the edges of samples detached from the mould (w_{dt}), when concave-up curling reached its maximum elevation (w_{ccm}) and when convex-up curling continuously developed (w_{cvcd}) were also considered. These water contents are listed in Table 3.3 for all tests. In all experiments, the edges of soil samples detached from the mould very early, i.e. when the water content was very close to initial values. For samples with initial water contents higher than the liquid limit, w_{dt} was higher than the liquid limit. For example, the edges of the samples in tests CL1_2 and CL2_1 detached from the mould when the water contents were close to 166.57% and 85.15%, respectively, while their initial water contents were 192.26% and 104.11% respectively. It should be noted that the liquid limits of clayey soils used in tests CL1_2 and CL2_1 were 127% and 70.2%, respectively. These observations imply that the soil samples were still saturated and even in slurry conditions when the edges of the samples detached from the mould.

Regarding the stage at which the edges of a sample started curling up, the results show that the water content at this stage was slightly lower than the liquid limit and much larger than the plastic limit (presented in Table 3.1). For example, w_{ccs} of tests CL1_2 and CL2_1 was approximately 80%-92% and 39%-46% respectively, while the liquid limits of these soils were 127% and 70.2%, and the plastic limits of these soils were 26.0% and 21.8%. This implies that concave-up curling initiated when the soils were almost fully saturated. Previous studies have shown that concave-up curling was observed at the edges of cracks (Allen 1986; Bradley 1933; Kindle 1917, 1923; Longwell 1928; Minter 1970; Style et al. 2011; Ward 1923; Zielinski et al. 2014), and it initiated shortly after the appearance of cracks (Zielinski et al. 2014). Some studies have also revealed that during drying of slurry soils, the first crack is observed when water content is quite high, i.e. close to or higher than the liquid limit (Costa et al. 2013; Tang et al. 2011b; Tang et al. 2011c) and

soils are fully saturated (Shin and Santamarina 2011; Tang et al. 2011b; Tang et al. 2011c). Therefore, it is rational to conclude that in nature, concave-up curling initiates and develops when soils are almost saturated. Concave-up curling continued to develop in the Kaolin NY clay sample, while this curling reduced after the water content reached 43%-85% and 26%-30% in the samples made of Werribee clay and Altona North clay, respectively. These values were much higher than their plastic limits. Therefore, when concave-up curling reached its maximum elevation in Werribee clay and Altona North clay samples, the soils were almost saturated.

Convex-up curling started developing in the middle of samples when the water content reached around 30%-50% and 20% in Werribee clay and Altona North clay samples respectively, while it did not occur in the Kaolin NY clay sample (refer to Figure 3.7 and Table 3.3). These water contents were close to their plastic limits. The convex-up curling process of Werribee clay samples experienced a period in which their lifted edges fluctuated until the water content was around 9%-20%.

In summary, when clayey soils undergo a drying process from the surface, water in the soils evaporates and soil particles re-arrange. Consequently, concave-up curling may occur. Its occurrence takes place when soil media are almost saturated. In clayey soils, where only concave-up curling occurs, this curling process continues, and then it experiences a short period without changing the curling shape. After that, this process develops again to reach the maximum elevation until the soil media reach their residual water content. On the other hand, in soils, where both concave-up curling and convex-up curling occur, concave-up curling occurs close to saturation and then gradually reduces before convex-up curling occurs. At the stage when convex-up curling begins, the water content of the soil media is close to its plastic limit. Convex-up curling develops until the soil residual water content is reached. Note that this discussion of curling water content is based on the evolution of average water content measured in the whole specimen. This is reasonable, as the formation of curling can be viewed as a macro-process, which is induced by the accumulation of local suction/stress gradients. The authors acknowledge that the evolution of local water content also influences the curling process. However, the measurement of the local water content is very difficult and it is even more complicated to identify appropriate locations that trigger soil curling behaviour, which is beyond the scope of this thesis.

Table 3.3. Summary of drying tests.

Test ID	Water content at the stage of (%)								Maximum lift-off height (mm)		
	Detaching left edge (W_{dt})	Detaching right edge (W_{dt})	Starting concave-up left edges (W_{ccs})	Starting concave-up right edge (W_{ccs})	Concave-up peak left edge (W_{ccm})	Concave-up peak right edge (W_{ccs})	Starting convex-up (W_{cvs})	Increasing convex-up continuously (W_{cvcd})	Concave-up curling left edge	Concave-up curling Right edge	Convex-up curling
CL1_1, W3_1, T2_1	171.44	173.39	78.58	86.37	47.78	53.94	28.76	20.57	2.99	2.21	33.90
CL1_2, W3_2, T2_2	166.57	173.70	80.39	91.90	47.10	63.25	32.72	22.98	3.30	3.08	32.51
CL2_1	85.15	92.30	38.97	45.86	26.07	28.74	20.61	20.61	4.11	4.96	22.04
CL2_2	91.17	91.17	38.90	43.55	26.29	29.65	20.23	20.23	5.11	5.75	24.17
CL3_1	64.51	66.42	45.41	43.57	2.21	2.21	N/O	N/O	2.50	1.51	N/O
CL3_2	66.49	64.69	41.56	37.63	2.54	2.54	N/O	N/O	1.95	1.88	N/O
W1_1	123.98	126.37	108.53	117.17	69.71	85.3	35.32	24.52	3.53	3.77	42.70
W1_2	N/A	127.22	108.92	119.08	N/A	83.17	36.11	25.82	N/A	3.60	41.97
W2_1, S1_1	163.27	163.27	47.50	79.90	44.51	75.27	32.89	23.23	1.80	1.78	33.63
W2_2, S1_2	154.40	163.46	56.96	86.64	46.15	46.15	30.93	21.08	3.11	3.66	36.42
T1_1	162.55	170.32	57.95	61.22	53.58	54.70	30.58	9.63	0.29	2.38	18.69
T1_2	169.33	171.69	63.73	74.72	43.07	51.90	26.43	9.83	0.54	2.71	13.15
T3_1	183.15	172.09	105.49	92.00	62.89	62.89	54.03	54.03	11.32	7.99	54.44
T3_2	162.53	179.65	114.24	89.92	57.45	57.45	46.69	46.69	10.17	8.13	53.96
S2_1	N/A	N/A	N/A	N/A	N/A	N/A	27.22	21.52	N/A	N/A	31.86
S2_2	141.43	159.48	90.57	90.57	49.333	49.87	28.66	21.09	3.74	6.85	32.29
S3_1	146.77	154.79	130.93	89.36	45.69	45.69	25.16	17.05	14.61	5.4	16.43
S3_2	N/A	N/A	N/A	N/A	41.97	41.97	23.58	18.02	14.12	17.67	15.63
S4_1	135.23	138.24	118.30	122.51	69.50	72.16	N/O	N/O	25.73	28.77	N/O
S4_2	128.30	137.74	119.31	122.35	72.66	72.66	N/O	N/O	25.64	24.47	N/O

Note: N/A: no data due to the computer restarted; N/O: not occur

3.4. Curling Mechanism

The observed process of curling formation and development of a slurry clay layer is illustrated in Figure 3.8. The process starts with a significant deformation in the vertical direction as shown in Figure 3.8(a). The edges of the sample then detach from the mould and deformation becomes dominant in the longitudinal direction (Figure 3.8(b)). After sufficient drying, the edges of the soil layer start curling up to form concave-up curling (Figure 3.8(c)). This curling develops until the curled edges reach the maximum elevation on each side of the sample (Figure 3.8(d)). These curled edges then start moving downwards (Figure 3.8(e)) and finally, convex-up curling may begin and develop in some clays (Figure 3.8(f)). These processes can be explained using the concept of capillary force development as follows.

At the beginning of drying, water evaporates from the surface of the sample. Menisci form between clay particles located on or near the surface, causing the development of capillary forces. At this stage, capillary forces mainly come from surface tension, and their vertical component is therefore much greater than the horizontal forces. As a result, soil particles settle down and move towards the centre of the sample, and the vertical deformation is much larger than the horizontal deformation (Figure 3.8(a)). With further drying, the curvature of menisci increases, leading to an increase in capillary forces and vertical deformation. After sufficient drying time, clay particles on the surface of the sample and near the mould gradually detach from the mould. Water can then evaporate sideways, enhancing longitudinal deformation, and the sample disconnects from the sides of the mould (Figure 3.8(b)). This process continues with the dominant deformation in the horizontal direction because capillary forces now also exist on the sides of the sample.

As drying continues, water evaporates further and the soil surface dries faster. Therefore, liquid bridges start forming between soil particles that are on or near the surface. Liquid bridges then gradually develop between soil particles in the sample. The formation of liquid bridges causes a significant increase in capillary forces, especially the horizontal component, causing the sample to deform more in the horizontal direction. As the soil surface is drier, capillary forces between soil particles near the surface are larger, leading to a non-uniform distribution of horizontal forces along the height of the sample, with a larger value on the top and a smaller value at the bottom. This non-uniform force distribution forms an upward bending moment, which lifts the edges of the sample off to form concave-up curling as can be seen in Figure 3.8(c). As the drying time increases, capillary forces and this moment continue to increase. Consequently, the edges of the sample reach their maximum elevations (Figure 3.8(d)).

Stages	Global view	Particle scale view	Horizontal force distribution, moment	Notes on the curling process
(a)				<ol style="list-style-type: none"> 1. Water evaporates from the surface. 2. Menisci form between clay particles. 3. The capillary force increases. 4. Soil particles settle down. 5. Non-uniform distribution of horizontal component of the capillary force generates an upward bending moment.
(b)				<ol style="list-style-type: none"> 1. Sample detaches from the sides of the mould at water content w_{dt} 2. Water can evaporate sideways. 3. The capillary force and upward bending moment increase.
(c)				<ol style="list-style-type: none"> 1. Liquid bridges form between soil particles. 2. The upward bending moment lifts the edges of the sample off. 3. Concave-up curling initiates at water content w_{ccs} 4. Water can evaporate from the bottom of the sample
(d)				<ol style="list-style-type: none"> 1. Liquid bridges form inside the sample 2. The capillary force and upward bending moment increase. 3. Concave-up curling develops. 4. Edges of the sample reach maximum elevation at water content w_{cm}.
(e)				<ol style="list-style-type: none"> 1. Distribution of horizontal component of the capillary force is relatively uniform. 2. The capillary force increases and the upward bending moment decreases 3. The curled edges move downwards
(f)				<ol style="list-style-type: none"> 1. The capillary force increases and the upward bending moment decreases 2. The sample starts buckling. 3. Convex-up curling begins at water content w_{cvs} and continuously develops at water content w_{cvcd}

Note: - $M4 \gg M3 \gg M2 \gg M1$, and $M4 \gg M5 \gg M6$
 - $P6 \gg P5 \gg P4 \gg P3 \gg P2 \gg P1$

Figure 3.8. Soil curling mechanism: (a) soils start settling down; (b) soils detach from the mould; (c) concave-up curling starts; (d) concave-up curling reaches maximum elevations; (e) curved edges retreat; (f) convex-up curling begins and develops.

After the maximum elevation is reached, water evaporates more from the bottom surface, causing capillary forces to increase significantly on this surface. As a result, the total magnitude of capillary forces increases significantly. In addition, thanks to the water transfer inside the soil sample, the distribution of the horizontal force component along the height of the sample shifts from a non-uniform distribution to a relatively uniform distribution, causing a reduction in the upward bending moment. The reduction of the bending moment, in addition to the self-weight of clay particles, forces the curled edges to move downwards (Figure 3.8(e)). It is noted that, because of the shrinkage process, the stiffness of the clay layer gradually increases, hindering the downward movement of the curled edges. In particular clays, this process continues to form convex-up curling, as seen in Werribee and Altona North clays, and the mechanisms associated with this

behaviour are not well understood. One possible explanation for convex-up curling may be the buckling of the clay sample. This is reasonable, because, after the curled edges retreat downwards and touch the base, the horizontal force distribution along the sample height is relatively uniform, causing the sample to shrink along the horizontal direction. As drying continues, the magnitude of the horizontal component of the capillary force is sufficiently large to cause the sample to buckle (Figure 3.8(f)). The middle section of the clay layer then lifts off from the mould to form convex-up curling. With further drying, the lift-off height increases as water can now fully evaporate from the bottom of the sample, leading to an increase in capillary forces on this surface, thus facilitating the upward curling process. This explains why the lift-off height in convex-up curling is significantly larger than that in concave-up curling. Convex-up curling stops when the water content reaches its residual value. The other possible explanation can be attributed to the reverse of the bending moment that may occur due to the redistribution of capillary forces, which may be induced by the heterogeneous distribution of water content and the time-dependent evolution of stresses in the sample. The curling behaviour may also be explained based on the different shrinkage strain along the height of the sample, i.e. the sample bends towards the face that shrinks more.

In summary, concave-up curling in clayey soils can be attributed to the bending moment caused by the non-uniform distribution of capillary forces along the sample height, while convex-up curling may be caused by buckling of the sample under a high compression force generated by capillary forces. However, the authors acknowledge that alternative explanations exist for this mechanism, as discussed earlier. To fully understand this curling mechanism, future studies with modern techniques are required and these are postponed to future work. In the following sections, the mechanisms associated with the bending moment and buckling will be used to explain the influence of several factors on the soil curling process.

3.5. Factors Influencing Soil Curling

3.5.1. Effect of clay types

The shrinkage process of Werribee, Altona North, and NY Kaolin clays was presented in the previous section. Both Werribee and Altona North clays displayed similar curling processes where concave-up curling occurred first, followed by convex-up curling. By contrast, for Kaolin NY clay, only concave-up curling occurred. In addition, both Werribee and Altona North clays displayed a higher lift-off height than that of Kaolin NY clay in the case of concave-up curling, while Werribee clay showed a higher lift-off height than Altona North clay in the case of convex-up curling.

Differences in the curling process of these clays can be explained based on the curling mechanism discussed in the curling mechanism section, in combination with soil water

retention curves (SWRCs) and particle size distributions, which are presented in Figure 3.1. There was a significant difference in suction for the three clays at any given water content and the suction of Kaolin NY clay was always lower than that of other clays. For example, the suctions of Werribee and Altona North clays at 30% water content were approximately 23.5 MPa and 4 MPa, respectively, while that of Kaolin NY clay was around 0.85 MPa. In addition, Werribee and Altona North clays were less uniformly graded than Kaolin NY clay (Figure 3.1(b)), and the hydraulic conductivity of Werribee and Altona North clays was approximately ten times lower than that of Kaolin NY clay, as shown in Table 3.1. Therefore, when these soils are subjected to drying, water in the Kaolin NY clay sample can move more easily from the bottom surface to the top surface than in the other two clays. Therefore, the difference in water content along the sample height is lowest for Kaolin NY clay layer. This causes the distribution of the horizontal component of capillary forces along the height of Kaolin NY clay layer to be more uniform than the other two clays. Together with a lower magnitude of capillary forces, the upward bending moment caused by the horizontal component of capillary forces along the height has the lowest value for Kaolin NY clay layer. In addition, the compressibility of Werribee and Altona North clays is higher than that of Kaolin NY Clay (Shannon 2013). For these reasons, although concave-up curling occurs in all clays due to the upward bending moment, the maximum lift-off height of concave-up curling is smaller in the Kaolin NY clay sample. Convex-up curling occurs because of sample buckling under high compression forces, as discussed in the curling mechanism section. Convex-up curling takes place in both Werribee clay and Altona North clay samples at suction of approximately 10 MPa-18 MPa. For Kaolin NY clay, these suction levels correspond to a water content of around 2.5%-3.0%. At this water content, the Kaolin NY clay sample has a concave-up shape. Therefore, concave-up curling continues to develop due to sample buckling, while convex-up curling does not occur.

Differences in the curling process for the three clays may also be attributed to their mineral compositions. In particular, the main mineral component in both Werribee and Altona North clays is Smectite, while that in Kaolin NY clay is Kaolinite. The specific surface area of Smectite is much higher than that of Kaolinite (Mitchell and Soga 2005). According to the research literature (Elbert Walter LeFevre 1966; Muhunthan 1991), clays with larger specific surface areas often have higher plastic indices and liquid limits. This suggests that Werribee and Altona North clays have higher plastic indices and liquid limits than clays with Kaolinite, and these findings are consistent with the experimental data reported in Table 3.1. Clays with higher liquid limits develop larger suction and a wider range of SWRCs (Black 1962; Zapata et al. 2000), which is again consistent with the experimental data reported in Figure 3.1(a). Therefore, it can be concluded that the mineral composition significantly influences the soil curling process. Clays composed

predominantly of Smectite can experience both concave-up curling and convex-up curling, while those mainly consisting of Kaolinite experience only concave-up curling.

3.5.2. Effect of initial water content

The effect of initial water content on soil curling was investigated by conducting drying tests on samples made of Werribee clay with initial water contents of 1xLL, 1.35xLL and 1.5xLL (approximately 130%, 172%, 192%). Figure 3.9 shows the evolutions of the water content and water evaporation rate of these samples. The water contents and evaporation rates of all samples followed the same trend, which rapidly decreased and reached stable values. At the end of drying, these samples reached the same residual water content, although they started with very different initial water contents. There was a slight difference in the slope of the water content evolution curve, revealing that water evaporated faster in the sample with higher initial water content. Again, the constant-rate stage could not be observed in this series of tests, and this may be attributed to the drying conditions as discussed above.

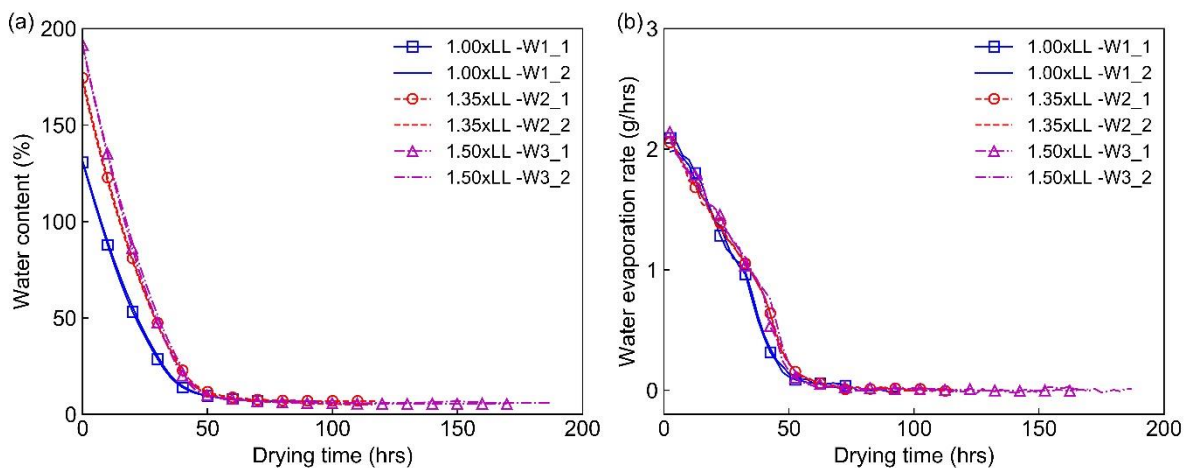


Figure 3.9. Effect of initial water content on water evaporation: (a) changes of water content during drying; (b) changes of drying rate during drying.

Figure 3.10 presents the water content at certain stages during the desiccation process and the maximum lift-off height of concave-up curling and convex-up curling. It can be observed that all samples underwent both concave-up and convex-up curling, regardless of the differences in initial water content. An increase in initial water content caused the sample to detach from the mould at a higher water content. However, the water content decreased for shrinkage stages at which concave-up curling initiated (w_{ccs}) and reached maximum elevations (w_{ccm}). The water content decreased slightly for shrinkage stages relating to convex-up curling (i.e. water content when convex-up curling initiated $w_{cvs} = 32.8\%$ and convex-up curling continuously developed $w_{cvcd} = 23.0\%$) and its difference is negligible. Figure 3.10(b) shows a similar trend for the lift-off height in both kinds of soil curling, suggesting that the lift-off height decreased with an increase in initial water

content. However, the lift-off height of convex-up curling was much greater. For example, the average lift-off height in the case of convex-up curling was 42.33 mm and 33.2 mm for specimens with an initial water content of 130% and 192%, respectively.

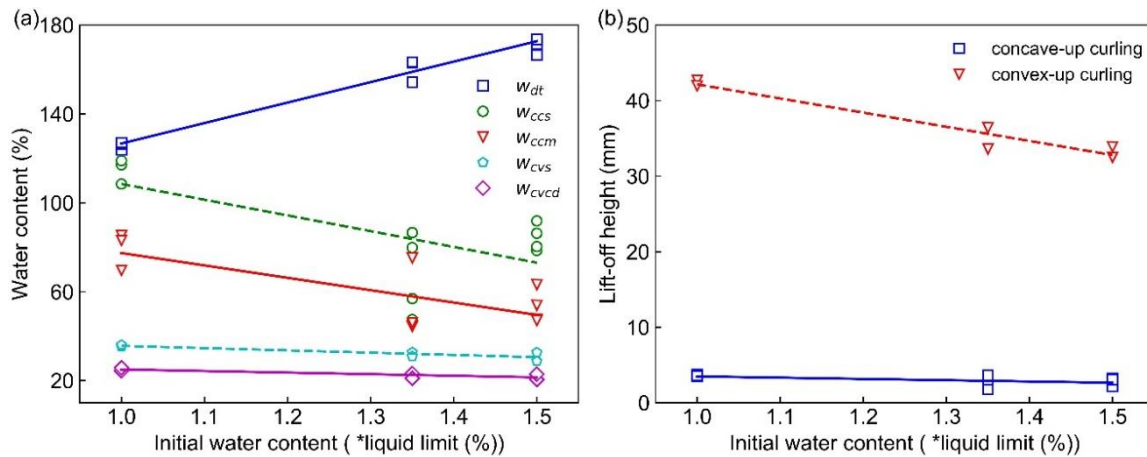


Figure 3.10. Effect of initial water content on soil curling: (a) water contents at particular stages; (b) the maximum lift-off height.

Different soil curling behaviours can be explained by using the general explanation given in the curling mechanism section. When samples are dried from their surface, the soil surface dries faster. In samples with lower initial water content, hydraulic conductivity is lower, and water in lower layers is therefore hindered from moving to the soil surface where water evaporates. Samples with lower initial water content have a less uniform water content profile, with a lower value on top and a larger value on the bottom. Samples that exhibited this non-uniform water content profile also strongly exhibited non-uniform profile of the lateral capillary force components along the height of samples, with a larger value on top and a smaller value on the bottom.

Samples with lower initial water content generated a higher upward bending moment, leading to concave-up curling occurring earlier, and the final water content and lift-off height of this curling process were larger. Convex-up curling is governed by the buckling of samples which mainly depends on the magnitude of the compression force and the sample's size (Timoshenko and Gere 1985). Compared to samples with higher water content, samples with lower initial water content shrank less, and their length was therefore slightly longer, corresponding to larger capillary forces for the same water content. However, all samples have similar a slenderness ratio regardless of initial water content. Therefore, samples with lower initial water content buckle earlier, corresponding to higher values of water content when convex-up curling initiates and when convex-up curling continuously develops (w_{cvs} and w_{cvcd}). The lift-off height of convex-up curling is also higher for samples with lower initial water content and this can be explained by the higher magnitude of capillary forces and the sample's greater length.

3.5.3. Effect of drying temperature

The effect of drying temperature on soil curling was investigated by testing Werribee clay samples under three drying conditions with temperatures of 24.5°C, 28.2°C and 38.8°C. Changes in the water content and water evaporation rate of these samples are shown in Figure 3.11. As the figure indicates, the evolution of the water content in these samples exhibited a similar trend with a strong decline followed by a gradual decrease to residual values. However, the water content dropped more quickly for samples with a higher drying temperature, which corresponded to a higher evaporation rate. The residual water content of these samples decreased with an increase in drying temperature. Under a high drying temperature, the suction applied to the samples is larger (Fredlund and Rahardjo 1993), requiring the samples to achieve lower water content to balance the suction on their boundaries. In this study, the suction applied on the samples was around 320 MPa, 200 MPa and 120 MPa when the drying temperature was around 38.8°C, 28.2°C and 24.5°C, respectively. These values were computed by using the thermodynamic relationship between soil suction and the partial pressure of the pore-water vapour (Fredlund and Rahardjo 1993). Figure 3.11(b) shows that in the first 16 hrs of drying, samples dried at 38.8°C had the highest evaporation rate. After 16 hrs, these samples changed to have the lowest evaporation rate, and samples dried at the second highest temperature became the samples with the highest evaporation rate. Later, samples with the lowest drying temperature became the samples with the highest evaporation rate. This phenomenon is caused by the increase of saturated vapour pressure (Neriah et al. 2014) and the hydraulic conductivity of soils (Cho et al. 1999) when temperature increases, resulting in the higher water evaporation rates and shorter drying periods of the samples subjected to high temperatures. Figure 3.11(b) shows that only samples dried at 24.5°C experienced a constant-rate stage. This again confirms our observation and discussion regarding the occurrence of the constant-rate stage in the previous section on the water evaporation in the first series of tests.

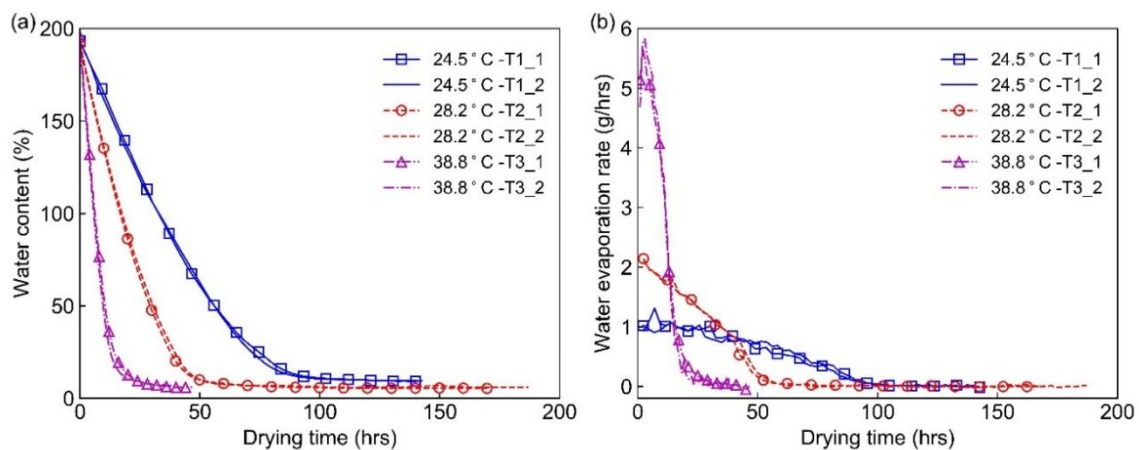


Figure 3.11. Effect of drying temperature on water evaporation: (a) changes of water content during drying; (b) changes of drying rate during drying.

The temperature also has a significant influence on the shrinkage deformation of clayey samples. Figure 3.12 shows the shrinkage strains at the top and bottom surfaces of samples dried at different temperatures. Negative values in the strains demonstrate the shortness of the sample length. In all samples, the shrinkage strains significantly increased during their drying process. The shrinkage strain at the top surface was larger for the samples dried at higher temperatures, but this tendency was reversed after the formation of convex-up curling. On the other hand, the strain at the bottom surface was always larger for the samples dried at higher temperatures (Figure 3.12(a)). Considering the shrinkage strains at the top and bottom surfaces, for the samples dried at relatively low temperatures (i.e. 24.5°C and 27.8°C), these strains were very similar until convex-up curling started developing as shown in Figure 3.12(b) and Figure 3.12(c). This suggests that the shrinkage strain difference between the top and bottom surfaces may not be the key factor causing the sample to form convex-up curling. The shrinkage strain at the bottom surface subsequently accelerated and overcame that at the top surface, and this may be a consequence of the convex-up curling whereby the water evaporated more at the bottom surface. For the sample dried at the highest temperature (i.e. 39.0°C), the shrinkage strain at the top surface developed faster than that at the bottom, even after convex-up curling had formed for a certain period (Figure 3.12(d)). This suggests that the shrinkage strain difference may not be a reasonable explanation for the formation of convex-up curling. On the other hand, the buckling mechanism appears to be a reasonable explanation for this mechanism and this is further evidenced by Figure 3.13, where the transition from concave-up curling to convex-up curling of the sample at 39.0°C (T3-2) is shown. Nevertheless, the authors acknowledge that this is not yet strong evidence to support the bucking explanation and the shrinkage strain difference should therefore still be considered as an alternative explanation. Further studies are required to provide a solid understanding of the convex-up curling mechanism when drying a soil sample from its surface.

Overall, when drying a clayey soil sample from its upper surface, concave-up curling occurs first, following by convex-up curling. The drying temperature has a significant influence on the water content at particular stages (e.g. detaching from the mould and beginning concave-up curling) and the lift-off height (Figure 3.14). The average water contents when the edges of samples detached from the mould (w_{dt}), concave-up curling initiated (w_{ccs}), the curled edges reached their maximum elevations (w_{ccm}), convex-up curling initiated (w_{cvs}) and continuously developed (w_{cvcd}) increased with an increase in the drying temperature. In addition, w_{ccs} , w_{cvs} and w_{cvcd} are significantly dependent on the drying temperature. When the drying temperature increased from 24.5°C to 39.0°C, the average w_{ccs} increased from 64.4% to 100.4%, and the average w_{cvs} increased from 28.5% to 50.4%. The increase of water content with an increase in the drying temperature corresponds to faster development of soil curling. Figure 3.14(b) shows that the lift-off

heights of both concave-up and convex-up curling were higher with a higher drying temperature. However, the lift-off height of convex-up curling was more dependent on the drying temperature and it was always much larger than the lift-off height of concave-up curling regardless of the drying temperature. The dependence of the lift-off height on the drying temperature observed in this study is consistent with the results reported in previous studies for concave-up curling (Bradley 1933; Longwell 1928). In addition, the lift-off height is also linked to the difference in the strains at the top and bottom surfaces of the samples. For the sample dried at a higher temperature, this strain difference was larger (Figure 3.12) and the lift-off height was higher (Figure 3.14(b)).

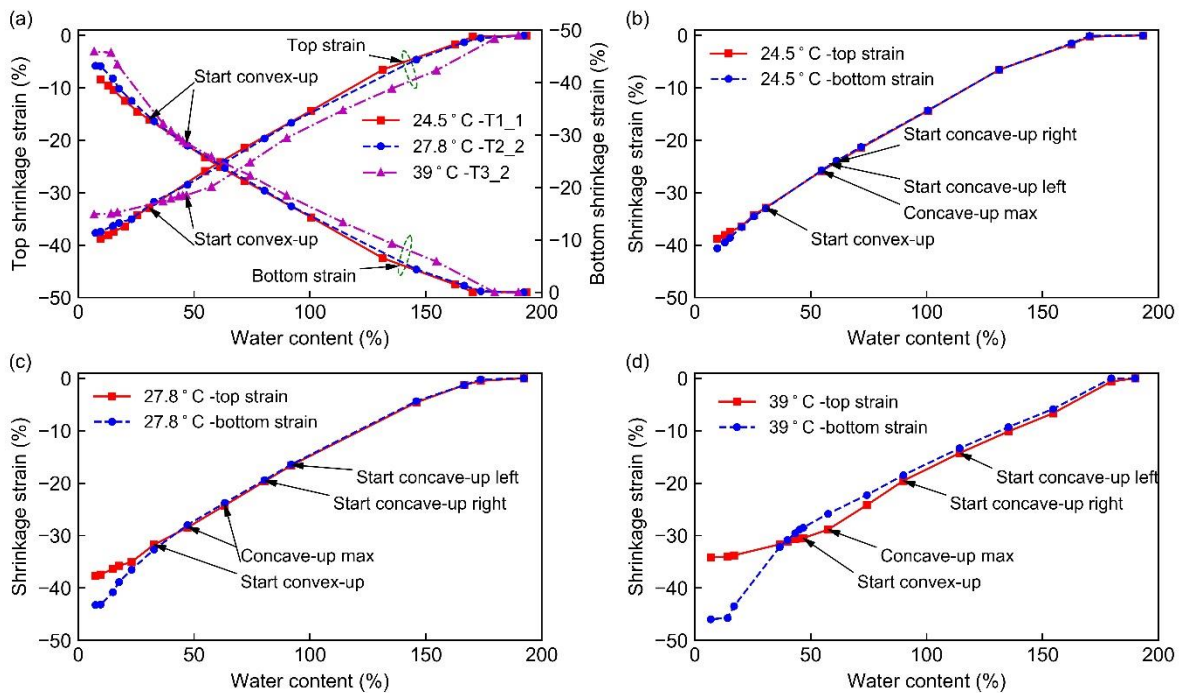


Figure 3.12. Top and bottom strains of samples dried at different temperatures: (a) strains of samples dried at different temperatures; (b) strains of sample dried at 24.5°C (T1_1); (c) strains of sample dried at 27.8°C (T2_2); (d) strains of sample dried at 39.0°C (T3_2).

(a) w=57.45%



(b) w =46.69%



(c) w=43.28%



(d) w=36.59%



Figure 3.13. Transition period from concave-up curling to convex-up curling in sample dried at 39.0°C (T3_2): (a) concave-up with highest edges positions, w=57.45%; (b) convex-up curling started but edges still curled up, w=46.69%; (c) convex-up developed but edges still curled up, w=43.28%; (d) only convex-up curling, w=36.59%.

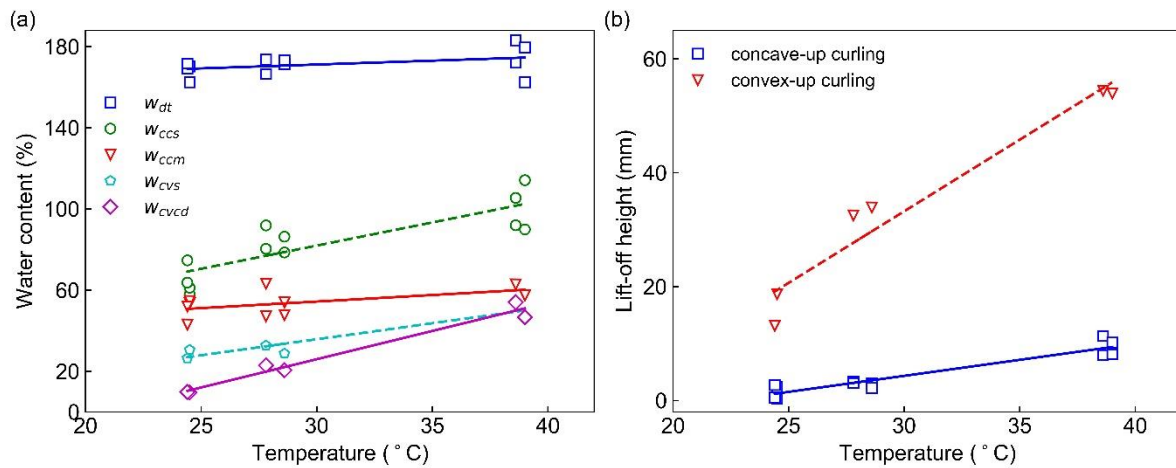


Figure 3.14. Effect of drying temperature on soil curling: (a) water contents at particular stages; (b) maximum lift-off height.

When the soil sample is subjected to drying, a very limited amount of water in lower layers can be transported to the surface layer as clayey soils have very low hydraulic conductivity. Consequently, with a high drying temperature, the soil surface dries faster and it is drier while the lower layers retain water, resulting in very non-uniform distribution of the lateral component of capillary forces. In addition, at a high temperature, the rate of water evaporation is larger (Figure 3.11(b)), resulting in a higher rate of suction increase, where generally higher loading rates have been shown to increase compressed deformation of soils (Huat et al. 2006). Plum and Esrig (1969) reported that an increase in the temperature of soils causes a significant increase in their compressibility. Therefore, when soil samples are dried at a higher temperature, the samples detach from the mould, and concave-up curling and convex-up curling occur early. The lift-off heights of both concave-up curling and convex-up curling of these samples are also expected to be higher.

3.5.4. Effect of sand content

Several studies have revealed that the soil fabric governs the physical properties of soils including their shear wave velocity and compressibility (Lee et al. 2012; Truong et al. 2010) and shear strength (Tran et al. 2012). The soil fabric is mainly governed by the mineral composition, the grain size distribution and the arrangement of particles. Therefore, different soil fabrics were created by mixing Werribee clay and Quartz sand with 0, 0.1, 0.2 and 0.3 of sand/clay fractions at a water content of 171.5%. These samples were then subjected to the same drying conditions. It was found that, for all sand/clay fractions, the evolution of water content and evaporation rate of all samples consisted of a period of significant decrease and a period of stabilization. In addition, an increase in the sand/clay fraction caused a slight decrease in the residual water content of the sample after the drying process and an increase in the rate of evaporation of the sample (Figure 3.15).

The shrinkage processes of samples were significantly influenced by the sand/clay fraction. All samples except those with a 30% sand/clay fraction experienced both concave-up and convex-up curling. In samples with a 30% sand/clay fraction, only concave-up curling was observed and this occurred before and after the samples were broken (Figure 3.16). This implies that for a certain sand/clay fraction, the slurry of the sand-clay mixture significantly changes curling behaviour. Figure 3.17(a) shows that with an increase in the sand/clay fraction, the average water content when the edges of samples detached from the mould (w_{dt}), and when convex-up curling initiated (w_{cvs}) and continuously developed (w_{cvcd}) significantly decreased, while the average water content when concave-up curling initiated (w_{ccs}) and when concave-up curling reached its maximum elevation (w_{ccm}) increased. The decrease of w_{dt} , w_{cvs} and w_{cvcd} and increase of w_{ccs} and w_{ccm} demonstrate that as the sand/clay fraction increases, the samples need more drying time to detach from the mould and to develop convex-up curling, while the drying time is shorter for concave-up curling to begin and reach its maximum elevation. Figure 3.17(b) shows that the lift-off height of concave-up curling increased substantially with an increase in the sand/clay fraction, increasing by around ten times when the sand/clay fraction increased from 0% to 30%. The lift-off heights of convex-up curling decreased as the sand/clay fraction increased. For example, they were 35mm and 16mm for samples with 0% and 20% sand/clay fractions, respectively. Note that the lift-off heights of samples with 30% sand/clay fraction were measured before the samples were broken. The observed effect of sand content on the lift-off height of concave curling was similar to the observations made by Bradley (1933) and Zielinski et al. (2014). In addition, Zielinski et al. (2014) reported that with a non-uniform texture created by mixing sand and clay, soil curling of the sample is irreversible as larger particles hinder retraction. This phenomenon also occurred in the present study (Figure 3.16). For mixtures with sand/clay fractions of 20% and 30%, the curled edges could not fully retreat downwards before the formation of convex-up curling in the middle of the samples.

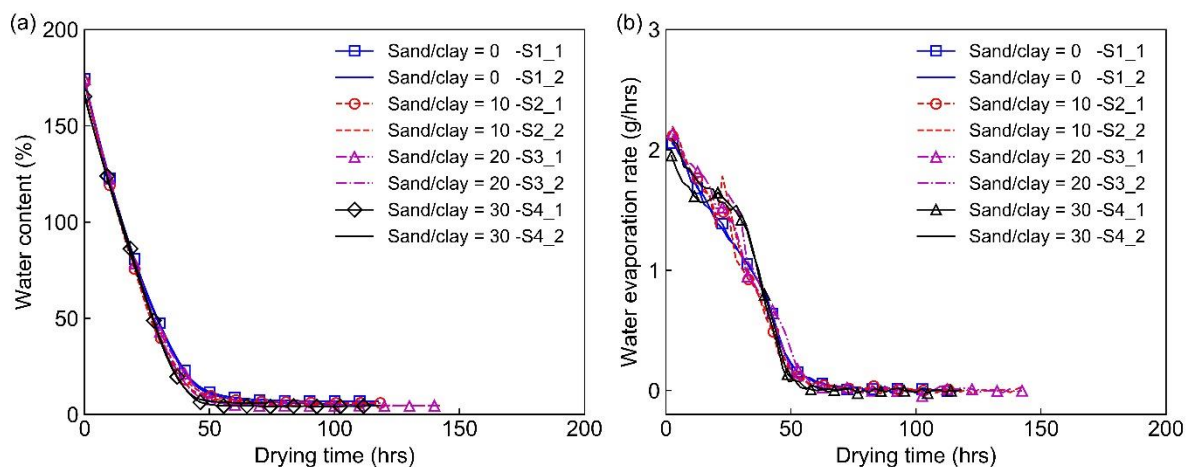


Figure 3.15. Effect of sand on water evaporation: (a) changes of water content during drying; (b) changes of drying rate during drying.

It can be seen from Figure 3.16 that, along the height of samples prepared of mixtures of sand and clay at a high water content ($1.35 \times LL$ of Werribee clay), the soil particles were distributed from coarse particles at the bottom to fine particles at the top. Even for samples with a high sand/clay fraction, a thin layer of mainly sand was formed at the bottom. When samples are subjected to drying, capillary forces develop inside the samples and their magnitude is significantly lower for samples consisting of large particles. Therefore, w_{dt} significantly decreases with an increase in the sand/clay fraction. An increase in the sand/clay fraction affects capillary forces such that the distribution of capillary forces is very non-uniform and thus causes a larger upward moment. This causes the sample to have higher values of w_{ccs} and w_{ccm} , and the lift-off height of concave-up curling increases, as illustrated in Figure 3.17. The formation of convex-up curling depends on the buckling behaviour of soil samples, which is controlled by the compression force and the stiffness of the sample. When the sand/clay fraction increases, the magnitude of the capillary forces of the sample decreases, while the stiffness increases (Cordero et al. 2017). As a result, when convex-up curling initiates and progressively develops, samples with a higher sand/clay fraction have a lower water content, resulting in higher capillary forces, which cause these samples to buckle. The lift-off height of convex-up curling decreases with an increase in the sand/clay fraction.

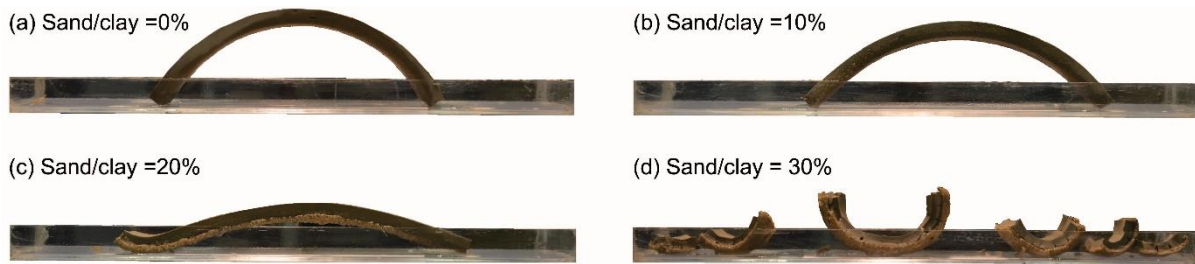


Figure 3.16. Soil curling of samples with different sand/clay fractions at the end of their drying processes: (a) sand/clay fraction of 0%; (b) sand/clay fraction of 10%; (c) sand/clay fraction of 20%; (d) sand/clay fraction of 30%.

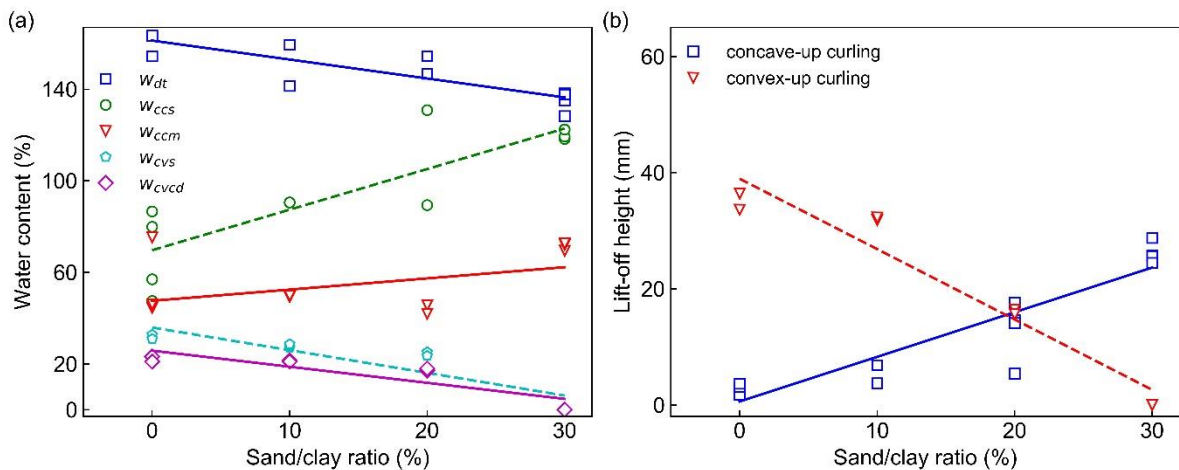


Figure 3.17. Effect of sand on soil curling: (a) water contents at particular stages; (b) maximum lift-off height.

3.6. Conclusions

In this chapter, the soil curling process and its influencing factors, including clay minerals and clay type, initial water content, drying temperature and sand/clay fraction, have been investigated. The key findings are summarised as follows:

1. The concave-up curling process has two stages. In stage I, a soil sample shrinks and detaches from the mould. In stage II, the edges of the sample lift off and concave up curling gradually develops. During this stage, the soil sample may have a short period without changing the sample shape. Initiation of concave-up curling takes place when the soil sample is almost saturated.
2. The convex-up curling process has four stages, with the two stages of the concave-up curling process followed by two others (stages III and IV). In stage III, the curled edges retreat downwards to the base of the mould. In stage IV, convex-up curling starts in the middle of the sample and develops until the sample dries. Convex-up curling commences when the water content is close to the plastic limit.
3. The concave-up curling process can be explained by the development of the bending moment due to the non-uniform distribution of horizontal forces generated by the development of capillary forces (or suction) and different water contents along the height of the sample, while convex-up curling may be caused by the buckling of the sample subjected to capillary forces.
4. Soil curling is strongly influenced by clay minerals, initial water content, drying temperature and sand/clay fraction. These factors significantly affect the magnitude of capillary forces and development of the non-uniform distribution of the horizontal component of capillary forces. The water content at which concave-up curling and convex-up curling initiate and develop decreases with an increase in initial water content. The lift-off height also decreases with an increase in initial water content. Furthermore, the water content and lift-off height increase significantly when the drying temperature increases. When the soil has a higher sand/clay fraction, the water content at which concave-up curling begins and the lift-off height of concave-up curling are higher. For a given sand/clay fraction (in this study, 30%), the soil curling behaviour of the soil media changes completely. For clays composed predominantly of Smectite minerals, both concave-up curling and convex-up curling occur, while for clays with more Kaolinite mineral only concave-up curling occurs.
5. This chapter provides complete time-varying observations of soil curling for different types of clayey soils and different initial conditions. It also provides a conceptual model for the soil curling mechanism. The proposed model is capable

of explaining the soil curling process and the effect of clay minerals, initial water content, drying temperature and sand/clay fraction on the soil curling process. Nevertheless, further studies are required to confirm the buckling hypothesis used to explain the convex-up curling mechanism.

Chapter 4. Experimental Investigation of Soil Cracking

4.1. Introduction

As reviewed in Chapter 2, desiccation cracking occurs in both slurry and compacted clays during drying, following a certain sequence: 1) at the beginning of the drying process of a soil medium, soil shrinks in all direction, cracks then initiate and develop until intersecting with each other or reaching the soil medium boundaries; 2) as evaporation continues, more cracks may begin at existing cracks and propagate until they reach other existing cracks; 3) after sufficient drying, no new cracks occur, while the width of cracks increases (Corte and Higashi 1960; Costa et al. 2013; Tang et al. 2011c). The occurrence and development of desiccation cracking is strongly influenced by various factors such as mineral composition; drying temperature; relative humidity; wetting-drying cycles; thickness and size of soil layers; presence of salt, polypropylene fibre; and surface plant cover (Corte and Higashi 1960; Costa et al. 2013; Ghazizade and Safari 2016; Lakshmikantha et al. 2012; Rodríguez et al. 2007; Shin and Santamarina 2011; Tang et al. 2011a; Tang et al. 2010; Tang et al. 2012; Tang et al. 2008; Tollenaar 2017). However, the effect of wind velocity on desiccation cracking has not been studied.

Formation and development of desiccation cracks have been explained from a macro-view, where the development of tensile stresses inside clay layers is mainly considered (Corte and Higashi 1960; Konrad and Ayad 1997; Morris et al. 1992; Peron et al. 2009b). Once the tensile stress reaches the tensile strength, cracks form. This theory has been proven by using observations of crack locations when soil samples were subjected to a drying process. Nahlawi and Kodikara (2006) and Peron et al. (2009b) reported that cracking normally occurs at the midpoint of long and thin soil layers when they were dried. The stress concentration at the midpoint of the soil layers has also been reported when the evaporation process of soil layers was analysed by conducting 2D simulations (Amarasiri et al. 2011b; Peron et al. 2013; Vo et al. 2017). However, by looking at principal strain directions after the formation of cracks, Wei et al. (2016) reported that desiccation cracks may occur due to the effects of tensile stresses, shear stresses or both tensile stresses and shear stresses developing inside the soil layers. Considering desiccation cracking from a micro-view, the formation of cracks has been described by the development of capillary suction. Shin and Santamarina (2011) and Tang et al. (2011c) postulated that after a sufficient drying time, air starts invading the largest pores in the soils and the capillary force generated by the air-water interface membranes causes soil particles to move away from each other. This process continues, causing the development of cracks. Although there have been several studies that made use of the latest imaging techniques such as laser scans, particle image velocimetry (PIV), digital

image correlation (DIC) and ground-penetration radar (Costa 2009; Levatti et al. 2017; Sanchez et al. 2013; Shannon 2013; Wang et al. 2018b; Wei et al. 2016) to investigate the mechanism of the desiccation cracking process, further studies are necessary to provide a comprehensive understanding of this phenomenon.

This chapter presents an examination of the desiccation cracking process by looking at the development of strain fields measured at the sample surface during drying. The effect of wind velocity on formation and development of desiccation cracks was also studied through drying tests under different wind velocities. This chapter begins with a description of the soil material and experimental techniques. The soil cracking process and the development of strain fields are then presented and discussed in depth. Finally, the influence of wind on soil desiccation cracking is established.

4.2. Material and Methods

4.2.1. Material and sample preparations

In this study, specimens were prepared with Werribee clay obtained at the Aquatic Centre site in Werribee, Victoria, Australia. It is highly reactive, with a dominance of Smectite. The soil has a high potential for shrinkage and swelling. Its liquid limit and plastic limit are 127% and 26%, respectively. This clay was also used for the test specimens in the investigation of soil curling presented in Chapter 3. More details of this clay can be found in Section 3.2.

The specimens were prepared by first drying the Werribee clay, then crushing and sieving it through a 0.425 mm sieve. The material passing through the 0.425 mm sieve was then thoroughly mixed with distilled water in a cup at a water content of approximately 160%. This water content was higher than the liquid limit of the clay to ensure that the prepared mixture was easy to place in Perspex moulds. The amount of soils for preparing the mixture was slightly higher than the required amount of soils for filling moulds to ensure that samples had the designated water content. The resulting clayey slurry was then poured into moulds and vibrated for 5 minutes to eliminate any air trapped. The samples were then covered, kept in a small box and stored in a cool and damp place for 24 hrs to achieve uniform moisture distribution.

Rectangular and circular Perspex moulds were used in this work. The rectangular mould had internal dimensions of 251 mm long, 25 mm wide and 12.4 mm deep, while the circular mould had an internal diameter of 140 mm and two different thicknesses of 5 mm and 10 mm.

4.2.2. Wind tunnel design

A miniature wind tunnel was designed and fabricated to generate laminar wind flows based on the suggestions of Cattafesta et al. (2010) and Hernández et al. (2013). Figure 4.1 presents the detailed design of the wind tunnel and Figure 4.2 shows the body of the fabricated wind tunnel. The wind tunnel consists of five main sections. The first section is settling chamber, which is used to reduce the turbulence and to increase the uniformity of the incoming wind flow before it enters the contraction. Normally, screens or honeycombs are used to achieve this purpose. As the screens can significantly reduce wind turbulence, especially when a series of two or three screens are used (Cattafesta et al. 2010; Hernández et al. 2013), a series of three screens with 0.5 mm diameter wires and 10 mm holes were used in the current design.

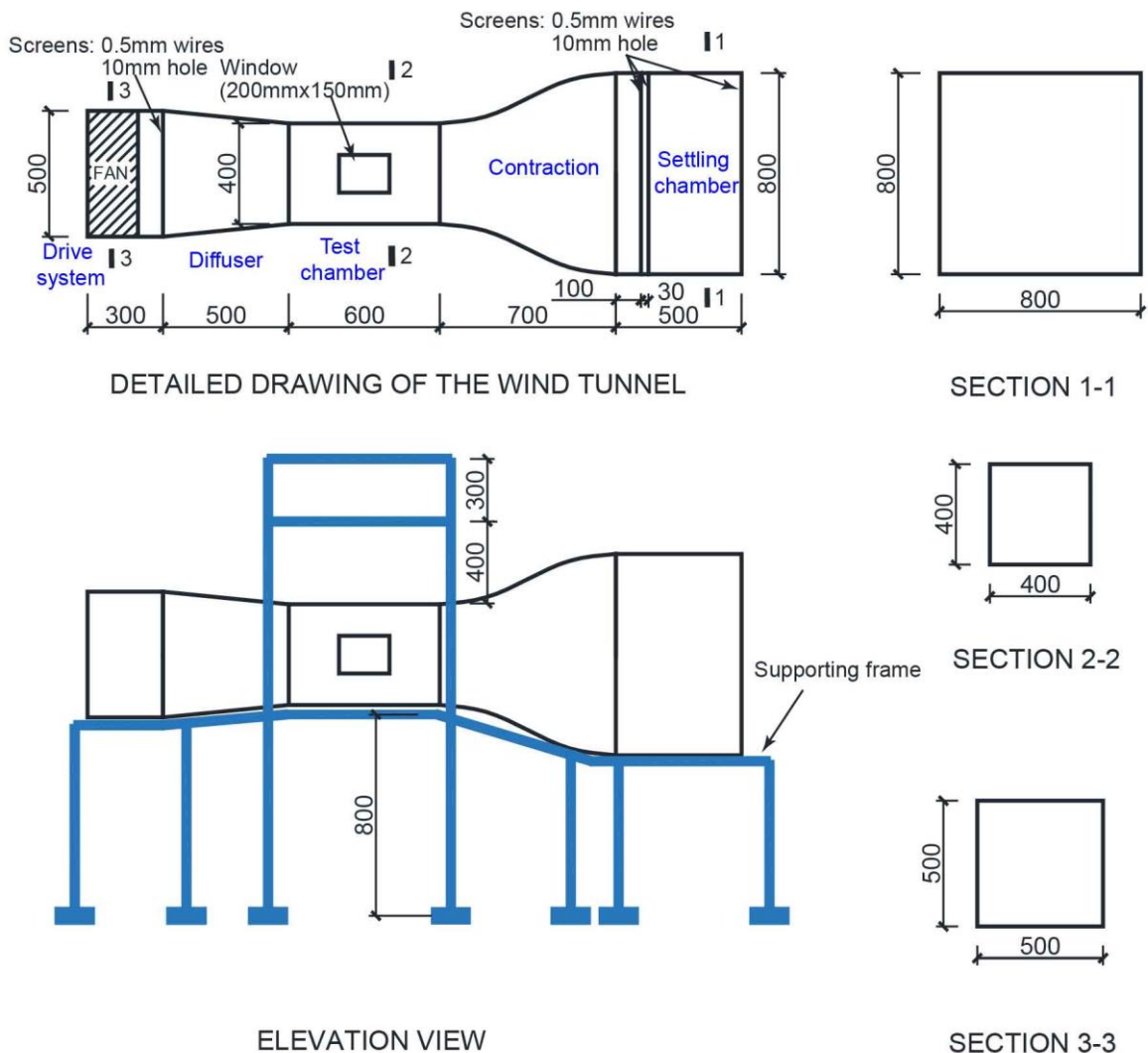


Figure 4.1. Design drawing of the miniature wind tunnel used in this study.

The second section is the contraction that is used to accelerate and align the flow coming from the settling chamber. The contraction also contributes to the reduction of flow turbulence and heterogeneities that depend on the contraction ratio, N , which is

determined based on areas of the entrance and exit sections. The larger the contraction ratio, the better the flow quality. For civil and industrial applications, the contraction ratio can range from 4 to 6 (Hernández et al. 2013). In this work, the contraction ratio is equal to 4, so the contraction of the current design is 700 mm long with the entrance section area of 800 mmx800 mm and the exit section area of 400 mmx400 mm. These dimensions were selected to ensure laminar flow coming into the test chamber and the maintenance of reasonable overall dimensions of the wind tunnel.



Figure 4.2. Wind tunnel body after fabricated.

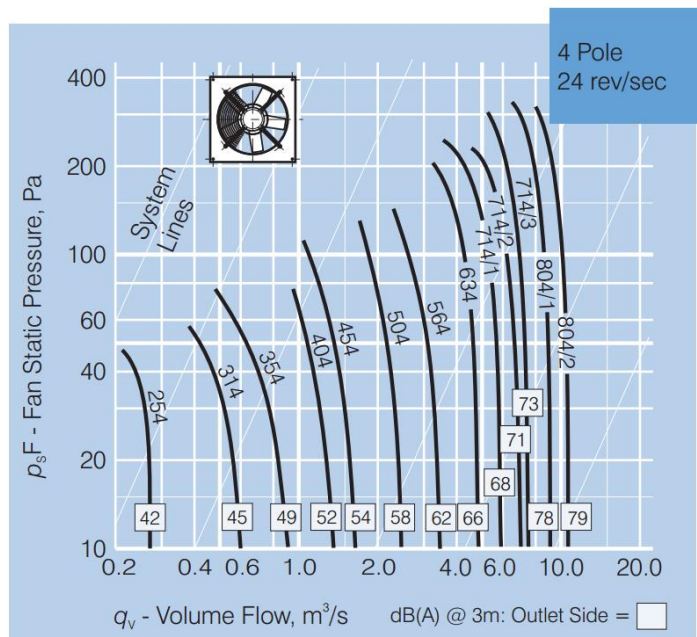


Figure 4.3. Performance curve of fans (Fantech 2008).

The next section is the test chamber, in which samples are placed. This section has been recommended to have a rectangular cross-section with a ratio of 1.4-1 and a blockage ratio of less than 10% (Cattafesta et al. 2010; Hernández et al. 2013). In this work, samples were dried from the surface and they were not located inside the test chamber. Thus, a test chamber with cross-section of 400 mm high and 400 mm wide was big enough for the maximum sample size (i.e. 251 mm). The length of the test chamber was 600 mm, which was also longer than the maximum sample length. The next section is the

diffuser, which is placed right behind the test chamber to recover the static pressure and reduce the load of the fan (Cattafesta et al. 2010). The last section is the drive system, in which a fan is installed to generate a constant speed flow and to compensate all the losses (Cattafesta et al. 2010; Hernández et al. 2013). In the current wind tunnel, an exhaust fan model CPE0354F supplied by Fantech Pty. Ltd was installed in this area and its performance is plotted in Figure 4.3.

4.2.3. Test procedures

After keeping the samples for 24 hrs to achieve uniform distribution of moisture, the samples were dried under a lamp or by using the wind tunnel in an air-conditioned room with a temperature of around 22°C. Two series of tests were conducted, exploring the soil cracking process, the strain development on the sample surfaces, and the effects of wind velocity on soil desiccation cracking.

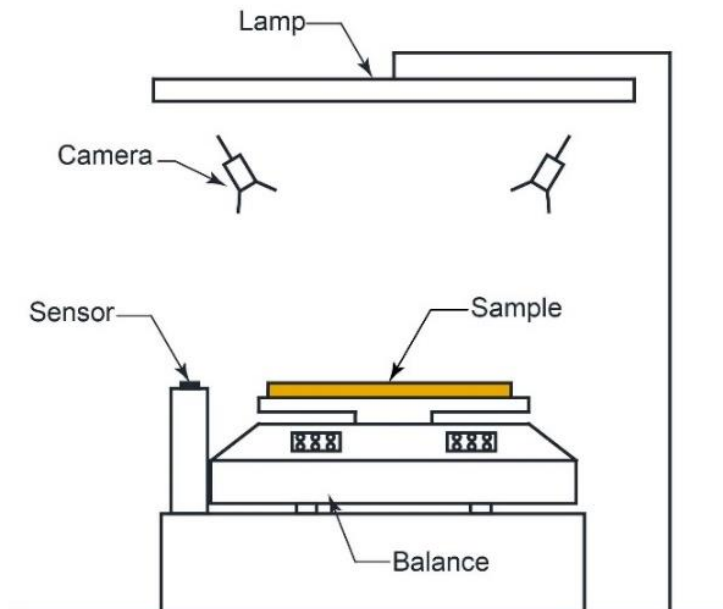


Figure 4.4. Experimental setup for exploring the soil cracking process and strain development on the sample surfaces.

The first series of tests were conducted for the rectangular samples and 5 mm deep circular samples following the set-up illustrated in Figure 4.4. In this setup, a balance with 0.01 g precision connected to a computer automatically recorded the weight of the specimens every 10 minutes. Two cameras equipped with high resolution lenses were fixed above the samples to monitor the sample surface. These cameras were connected to a controller box and controlled by a computer through ISTR4 4D software. The time interval for taking photographs varied from 1 minute to 30 minutes, depending on the development speed of cracks in the samples. A sensor was placed close to the samples to record temperature and relative humidity. A 500W lamp was used to generate drying temperatures. Additional LED lights were also used to ensure the samples were properly

lit. Prior to testing, white and black paints were randomly sprayed on the surfaces of the samples to generate random speckles for image processing. The speckles were very small and were sparsely distributed on the sample surface (as shown in Figure 4.5). Thus, their effect on the water evaporation and desiccation processes of the samples can be ignored. After generating random speckles on the sample surface, the cameras were adjusted to set the region of interest at the centre of both cameras. The cameras were then calibrated following the calibration procedure described in the ISTRA 4D software manual (Dantec 2017). The samples were then placed on the balance and the tests started.

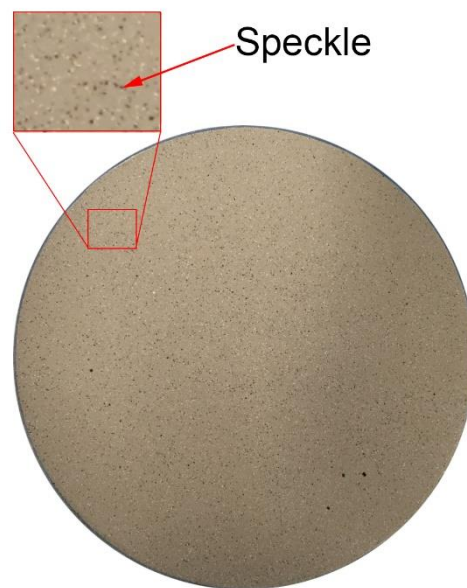


Figure 4.5. Typical sample surface for DIC analysis.

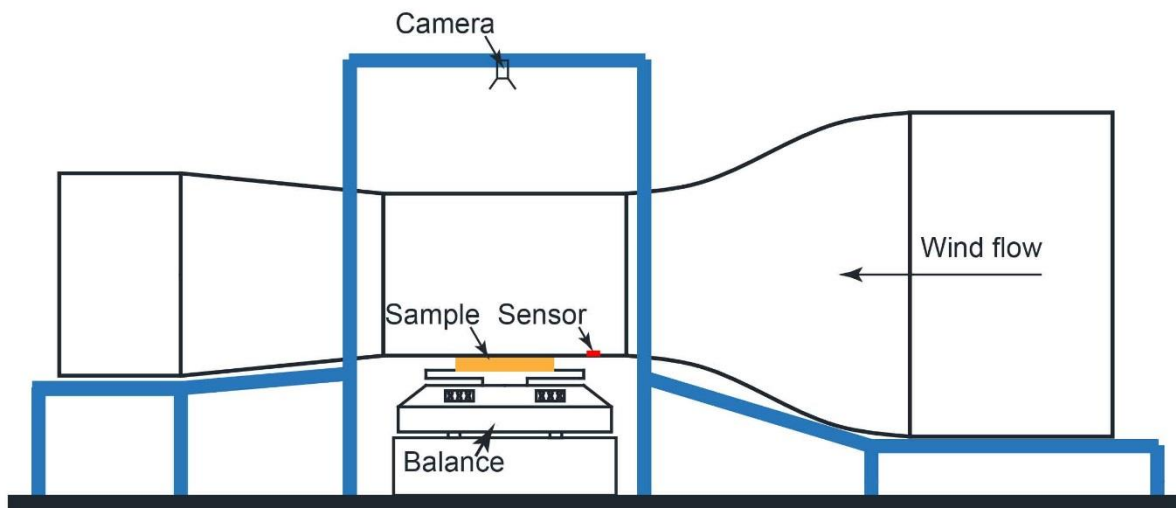


Figure 4.6. Experimental set-up for exploring the effect of wind velocity on soil cracking.

The second series of tests were conducted to explore the influence of wind velocity on soil desiccation cracking. Circular samples 10 mm thick were dried in the wind tunnel.

The test set-up is shown in Figure 4.6. In this setup, the same balance used in the first series of tests was used. Different wind velocities were generated by changing the speed of the fan. A camera was fixed on the top of samples to take pictures of the sample surface. A sensor was located inside the wind tunnel to measure temperature and relative humidity. This sensor's location did not influence the wind flow on the sample surface. To verify the repeatability of the tests, each drying test was conducted twice. Details of the experimental program and conditions are summarised in Table 4.1.

Table 4.1. Experimental program and conditions

Test ID	Mould shape	Initial water content (%)	Average temperature (°C)	Average relative humidity (%)	Wind velocity (m/s)
SR1	Rectangular mould	159.6	23.9	35.9	NA
SR2	Rectangular mould	160.7	22.3	45.1	NA
SC1	Circular mould, 5 mm thick	156.7	22.6	33.0	NA
SC2	Circular mould, 5 mm thick	158.3	22.6	37.4	NA
Wind 1-S1	Circular mould, 10 mm thick	158.8	22.8	30.4	0
Wind 1-S2	Circular mould, 10 mm thick	157.2	22.6	32.4	0
Wind 2-S1	Circular mould, 10 mm thick	160.7	23.7	35.1	0.89
Wind 2-S2	Circular mould, 10 mm thick	158.5	23.8	30.9	0.89
Wind 3-S1	Circular mould, 10 mm thick	161.8	23.5	30.8	1.89
Wind 3-S2	Circular mould, 10 mm thick	162.7	23.5	34.3	1.89

Note: NA is not applied

4.2.4. Digital image correlation technique

In this study, the digital image correlation technique (DIC) was employed to obtain the strain development of the samples. The technique was first introduced by Peters and Ranson (1982), and further developed by Sutton et al. (1983). This technique has been widely applied to obtain surface deformations in various engineering fields, including mechanical engineering, structural engineering and geotechnical engineering (Ha et al. 2017, 2018; Ha et al. 2015; Sutton et al. 2009; Wang et al. 2018b; Wei et al. 2016). The main idea of the technique is to compare images of the sample surface at different loading states to a reference image to detect the motion of each image point during loading, then calculate displacement and strain fields. The image comparing work starts by defining a square-grid system and square subsets centred at grid points in the reference image (Figure 4.7(a)). The locations of these subsets in other images recorded during loading are then calculated by using a cross-correlation criterion or sum-squared difference correlation criterion (Figure 4.7(b)). Finally, the displacements of these grid points are found based on differences in locations of the subsets in the reference image and other images (Figure 4.7(c)), and the strain field can be achieved (Figure 4.7(d)) (Sutton et al. 1983).

The DIC techniques are generally classified into two groups including 2D DIC and 3D DIC (3D full field DIC). In the 2D DIC technique, only one camera is used to capture the images of the sample surface during loading. Thus, this technique is limited to in-plane displacement measurement of the sample and to objects with planar surfaces. While in the 3D DIC, two or many synchronized cameras are used, and thus full-field displacements can be measured (Sutton et al. 1983). In this study, the DIC system including cameras, a controller box and ISTR4 4D software supplied by Dantec dynamics were utilised to control the cameras and record images of the sample surface. This software was also used to analyse the taken pictures to obtain displacement and strain fields. Subsets with size of 17x17 pixels and grid with spacing of 17 pixels were used. In following Sections, engineering principal strain 1 (ε_1), engineering principal strain 2 (ε_2) and tangential shear strain (ε_{12}), of the sample surface are chosen to present and discuss.

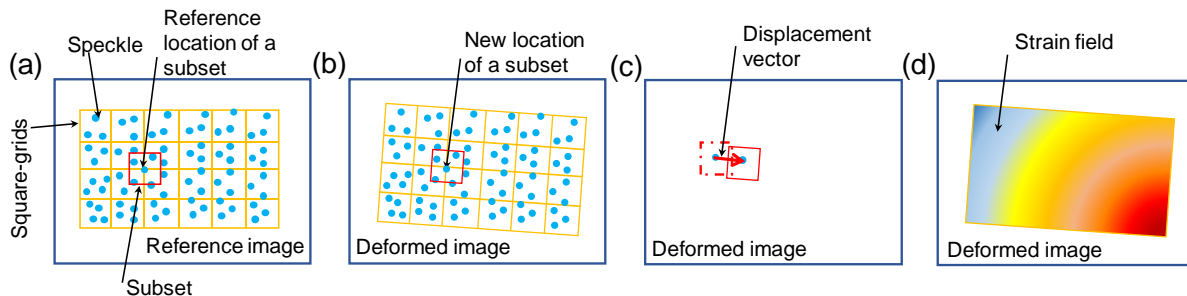


Figure 4.7. Main steps in image comparing work: (a) defining a square-grid system and subsets in the reference image; (b) finding locations of subsets in the deformed image; (c) obtaining displacement after matching deformed image with reference image; (d) calculating the strain field.

4.3. Desiccation Cracking and Development of Strain Fields

4.3.1. Rectangular sample

4.3.1.1. Desiccation cracking

The changes in water content of the rectangular samples during their drying process are plotted in Figure 4.8. As the drying time increased, the water content of two samples significantly decreased and gradually approaching a stable value. During the first decrease period, the relationship between the water content and the drying time was almost linear. In addition, the changes in water content of both samples showed good agreement, demonstrating repeatability. Note that in this chapter, the gravimetric water content is used.

Figure 4.9 shows development of the crack network occurred in sample SR1. Cracks shown in this figure were labelled based on their order of appearance. It can be seen that as the desiccation process started, the sample started shrinking. After a certain period,

edges of the sample started detaching from the mould. When the water content reached 133%, the first crack initiated from one long edge of the sample, then propagated transversely and reached the other long edge when water content was approximately 129%. This first crack was located at middle of the specimen and was classified as the primary crack. As the desiccation process continued, the sample continuously shrank, the first crack became wider, while more cracks initiated and developed following the same behaviour of the first crack. When the water content was 91.8%, four more cracks appeared in the sample. Among these cracks, cracks 2 and 3 were classified as secondary cracks because they appeared between main cracks, while cracks 4 and 5 were tertiary cracks because they were between secondary and main cracks. With further drying, the sample continued shrinking, the existing cracks became wider and crack 6 appeared. However, this crack did not cross entire sample though it appeared when the water content was at the high value of 52.1%. With further drying, no more crack existed, while the width of the existing cracks still developed and the sample continued shrinking until the water content reached the soil shrinkage limit (i.e. 13%).

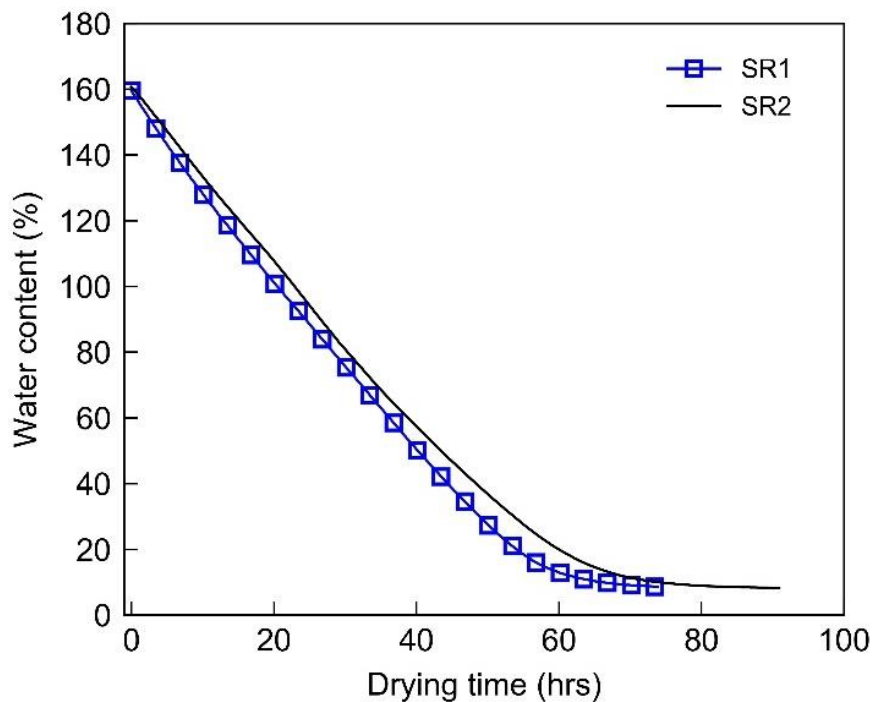


Figure 4.8. Evolution of water content in the rectangular samples during drying.

Figure 4.9 also shows that the crack lines were curved, but perpendicular to the edge where they stopped. In addition, the distribution of cracks along the longest edge of the sample was not uniform. The shape of crack lines may be attributed to the adhesion of the sample to the mould, while the random distribution may be because the sample was not homogeneous even though it was prepared from the slurry state. Figure 4.9 reveals that when the first crack initiated, the water content was very high, even higher than the liquid limit of the soil. Other cracks also developed at a high water content, which was

close to the liquid limit. Therefore, it can be concluded that the sample was saturated when cracks developed. This finding agrees well with results of previous studies for other clayey soils (Costa et al. 2013; Shin and Santamarina 2011; Tang et al. 2011c).

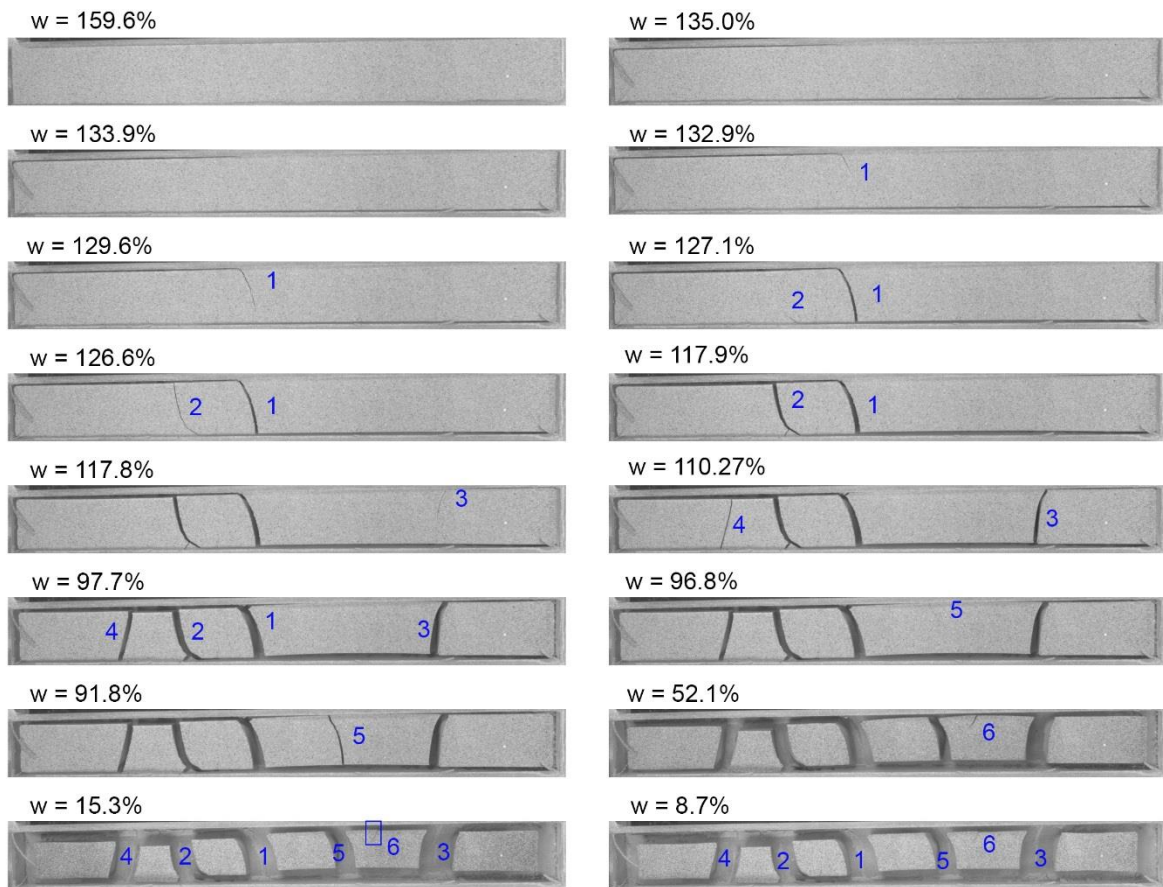


Figure 4.9. Development of the crack network on sample SR1.

4.3.1.2. Development of strain fields

The development of ε_1 on the surface of sample SR1 is plotted in Figure 4.10. At some stages, additional figures with smaller scale bars are utilised to clearly illustrate the strain concentration. In this figure, colour indicates the strain magnitude, while lines indicate strain directions. The strain heterogeneously developed on the sample surface even before the development of cracks. Both tensile and compressive ε_1 appeared and they formed bands distributed alternately along the longest sample edge. After the formation of cracks, the zones near crack lips and tips underwent very high tensile strain. The existence of tensile strain could be attributed to differential shrinkage. This differential shrinkage occurred along the sample due to soil structure and heterogeneity of the sample, and interface friction between sample and mould. Figure 4.10 also shows that direction of ε_1 was parallel to the long edge of the sample, except regions near cracks and near the ends of the sample. In regions near cracks, ε_1 was perpendicular or parallel to the cracks, while in the regions near the ends of the sample, the strain met the edges of the sample at an angle of approximately 45° .

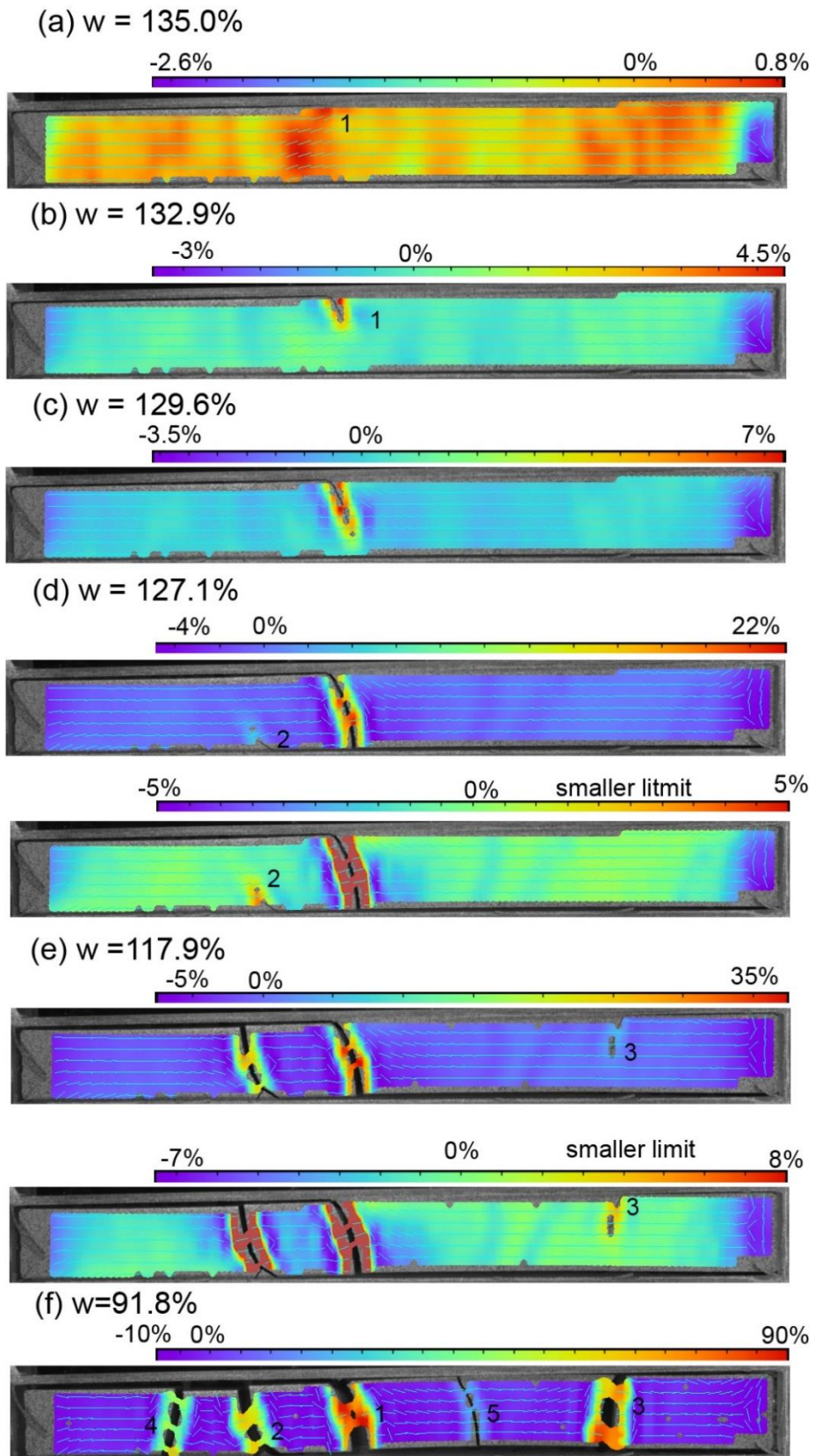


Figure 4.10. ϵ_1 developed on the surface of sample SR1.

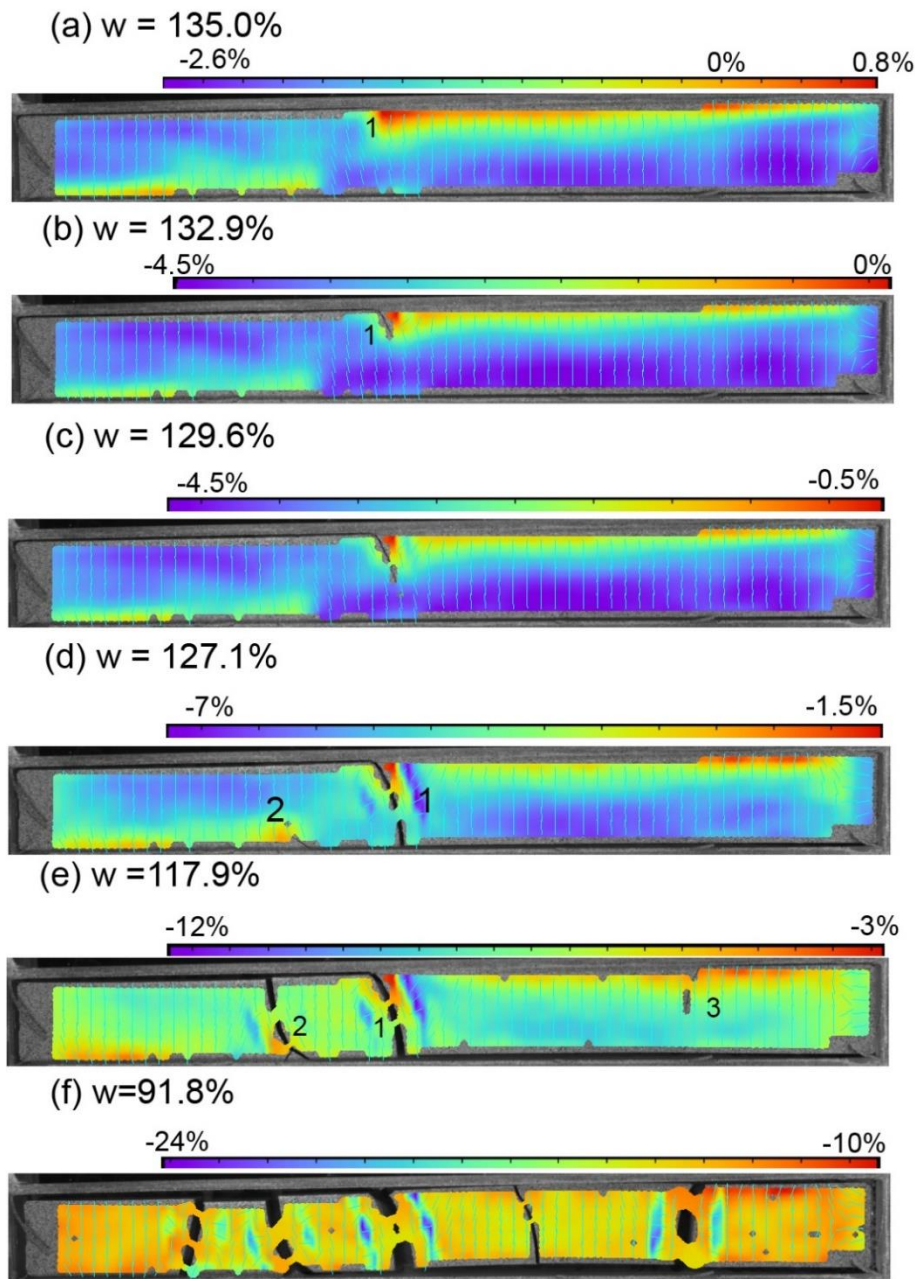


Figure 4.11. ϵ_2 developed on the surface of sample SR1.

Figure 4.11 shows the development of ϵ_2 . It can be observed that tensile strain also developed and concentrated at some locations near the long edges of the sample. However, the magnitude of this tensile strain was negligible compared to compressive strain. The appearance of tensile strains may be due to adhesion of the sample to the walls of the mould. This adhesion hindered the movement of soil particles. As a result, this tensile strain occurred only when the sample did not fully detach from the mould. As shown in Figure 4.11(e), when the water content was 117.9%, there was no tensile ϵ_2 on the surface of the sample. Figure 4.11 also reveals that the direction of ϵ_2 at most locations was parallel to the short edge of the sample, except near cracks and ends of the sample.

In these areas, ε_2 was parallel or perpendicular or met the edges of the sample at an angle of around 45° .

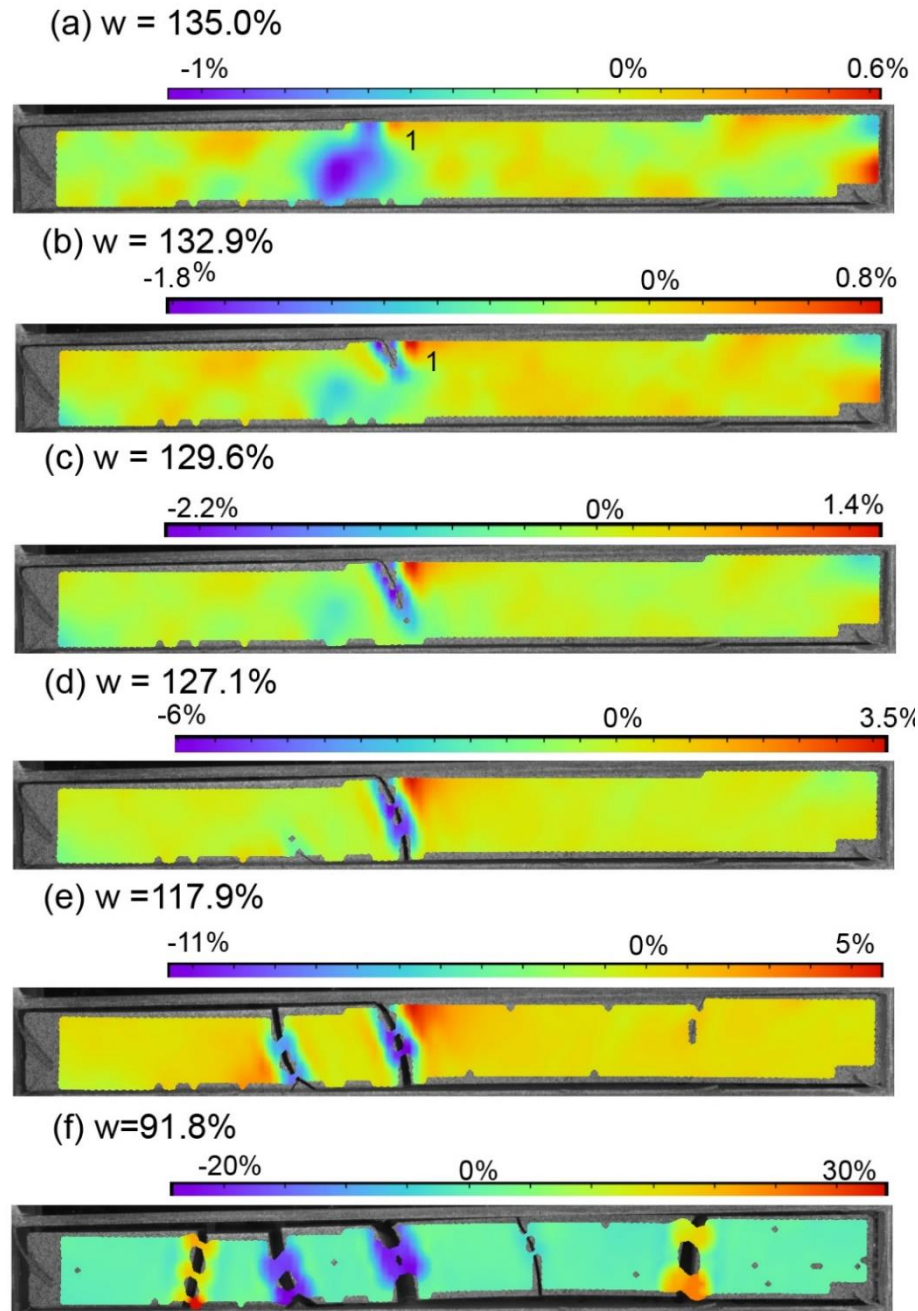


Figure 4.12. ε_{12} developed on the surface of sample SR1.

Figure 4.12 shows ε_{12} developed in the rectangular sample. Both tensile and compressive strains were observed during shrinkage of the sample. With a decrease in water content, the magnitude of engineering tangential shear strain increased. In addition, during drying, the strain was concentrated at the crack lips and crack tips. However, there was no obvious pattern in distribution of engineering tangential shear strain.

When initiation and propagation of desiccation cracks 1, 2 and 3 are examined, it can be observed that crack 1 started at the point where tensile ε_1 , ε_2 and compressive ε_{12} were concentrated. This crack then propagated along the boundary of the zone where direction of ε_1 was not parallel to the long edges of the sample. Appearance of this crack changed strain directions at its vicinity. For example, on its left side, near the sample edge, ε_1 became parallel to the long edges of the sample, while near the crack tip, ε_1 was perpendicular to the crack. Based on this observation, it can be inferred that the development of crack 1 first follows the shear and tensile failure mode, and then the tensile failure mode. Similarly, crack 3 also appeared at the location experiencing a high tensile ε_1 , while the crack 2 appeared where there was no strain localisation. When these cracks appeared, at their vicinity, the strain directions were also changed. Based on the directions of the principal strains, crack 2 followed the shear and tensile failure mode, and then the tensile failure mode, while crack 3 occurred following the tensile failure mode.

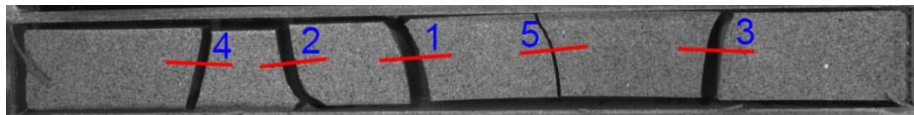


Figure 4.13. Locations for strain measurements.

To provide further understanding how strains developed in the sample during desiccation, strains at locations where cracks occurred were analysed. The locations were adjacent to five main cracks as shown in Figure 4.13. Figure 4.14 shows the development of strains at these locations. Five additional points were added into this figure to illustrate the time when these cracks initiated. When the sample was subjected to a drying process, the sample started to shrink. When the drying time was less than 7 hours, strains were negative at locations 1, 2 and 5, while they were positive at locations 3 and 4. These results demonstrate that soil at some locations (i.e. 1, 2 and 5) experienced a compression, while soil could undergo the tension at other locations (i.e. 3 and 4). This tensile behaviour may be due to the heterogeneous material and the adhesion between soils and the mould base, leading to differential shrinkage of soil elements along the longitudinal direction. With further drying, for location 1 the strain increased and become positive and then when crack 1 initiated this strain again significantly increased. For locations 2, 4 and 5, the strain magnitude increased and then significantly increased after the initiation of cracking at 2, 4 and 5. When these cracks began to appear, strains were compressive at these locations. For location 5, the strain also increased, then slightly decreased before increasing again when crack 5 began. However, this strain was still positive when crack 5 began. From these discussions, it can be inferred that some cracks may start at some points below the soil surface and then propagate towards the soil surface. Corte and Higashi (1960) postulated that cracks may also initiate for points

around the centre of soil layers and propagate either upwards to the soil surface or downwards to the bottom by looking at fracture markings on sides of cracks.

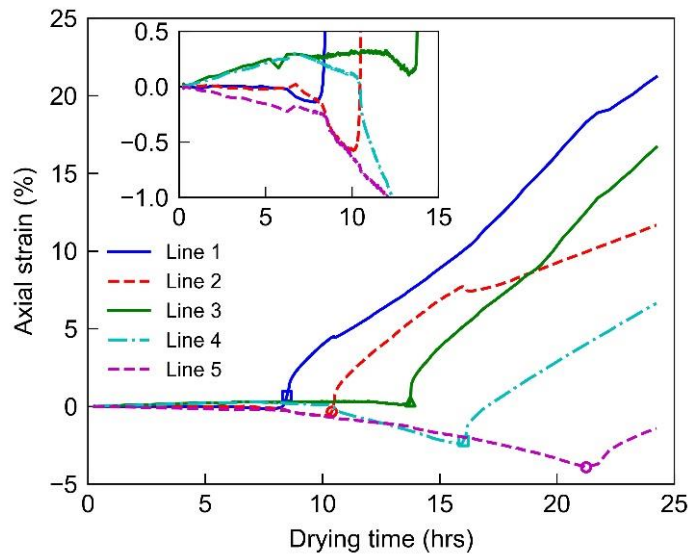


Figure 4.14. Development of axial strains of the selected locations.

4.3.2. Circular sample

4.3.2.1. Desiccation cracking

The evolution of water content of circular samples during their drying process is plotted in Figure 4.15. It can be seen that water content of two samples decreased almost linearly until reaching approximately 20%, and then gradually approached stable value, which was around 5%. The results of two samples agreed well with each other.

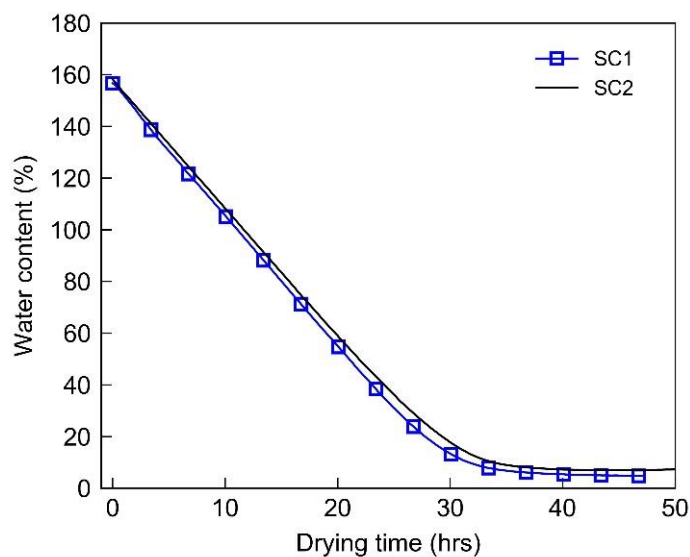


Figure 4.15. Changes in water content of circular samples.

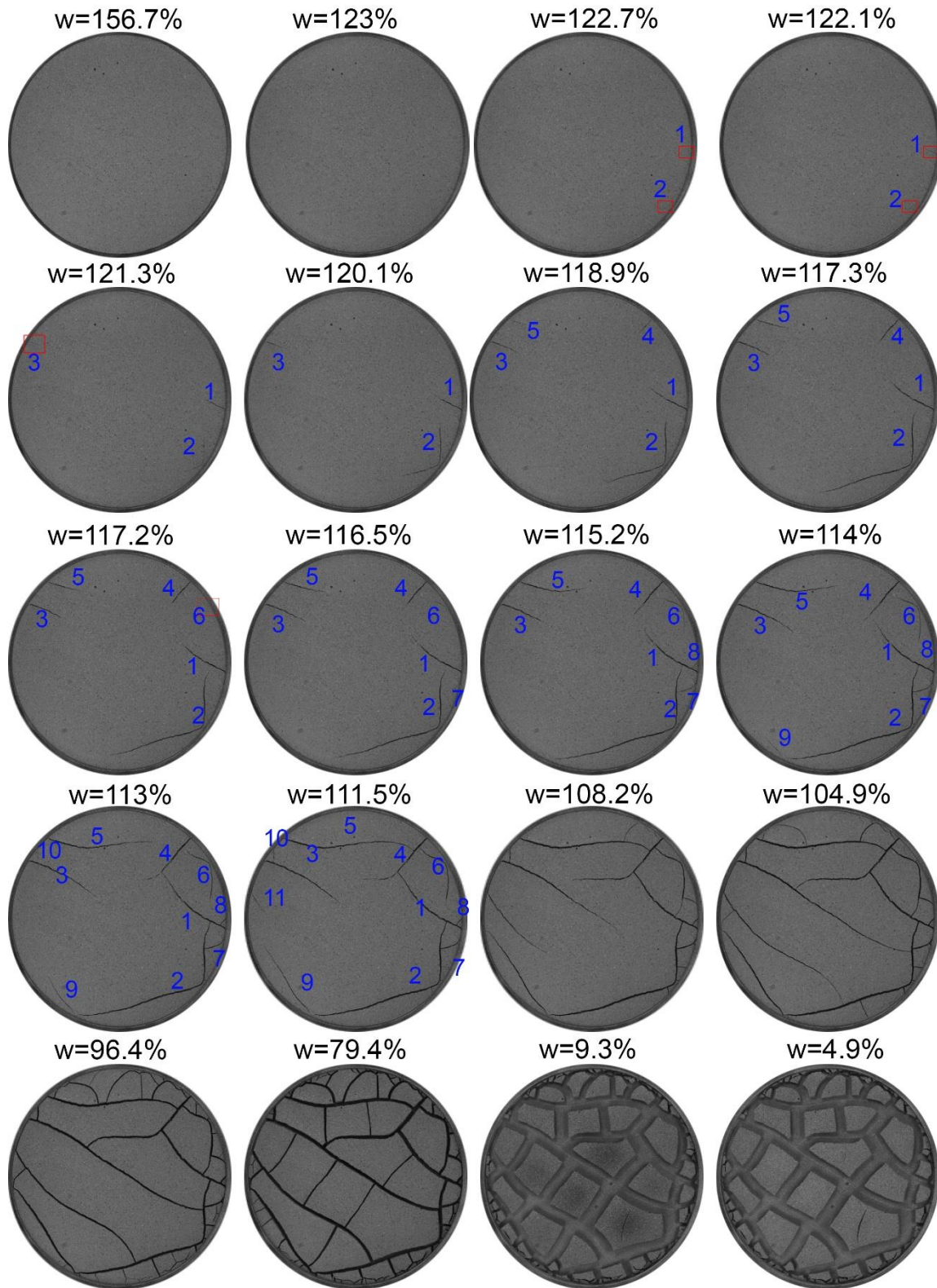


Figure 4.16. Development of the crack network on sample SC1.

The development of the crack network occurred in sample SC1 is plotted in Figure 4.16. As drying began, the sample started shrinking and detached from the mould. When the water content was around 122.7%, the first cracks started developing from points near the boundary of the sample. After the water content reached 115.2%, six more cracks initiated. Among these cracks, some (crack No. 3 and 4) propagated radially, while others

(crack No. 1, 2 and 5 to 8) propagated somehow circumferentially. As drying continued, these cracks continued to develop until reaching the mould or intersecting with each other, and more cracks developed. Once the water content was 111.5%, there were 11 cracks. With further drying, the sample continued to shrink, the existing cracks became wider and more cracks initiated from the boundary or existing cracks. These new cracks propagated until reaching the existing cracks or the boundary to subdivide the sample into many cells.

Once the water content reached 79.4%, no more new cracks occurred until the water content reached 9.3% that was lower than the shrinkage limit of the soil (i.e. 13%), while the width of all cracks continued to increase. After this period, two more cracks appeared. These two cracks initiated from the centre of two biggest cells and propagated towards existing cracks. However, these cracks did not reach existing cracks at the end of drying. Based on the definition of the crack type introduced by Corte and Higashi (1960), these first 11 cracks were primary cracks, the cracks developed when the water content was between 111.5% to 79.4% were secondary cracks and the two last cracks were tertiary cracks. Figure 4.16 also shows that all cracks were curved. Most cracks intersected with each other at right angles.

4.3.2.2. Development of strain fields

The development of ε_1 on the surface of sample SC1 is plotted in Figure 4.17. For the strain field when water content was 113%, an additional picture with a smaller scale bar is added to highlight the strain concentration. In this figure, colour indicates the magnitude of strains, while lines indicate strain directions. ε_1 heterogeneously developed on the sample surface. Tensile strain bands occurred near the boundary of the sample, while compressive strain bands occurred near the centre of the sample. At some locations near the boundary, tensile strains were very high. In addition, at locations near the boundary the direction of ε_1 was parallel to the boundary, while at locations inside the sample, the direction of ε_1 was random. After cracks occurred, the tensile strain was highly concentrated at crack tips and small zones along crack lips. The direction of this tensile strain was perpendicular to the crack lips, except locations that were near the initiation points of the cracks. Both tensile and compressive ε_1 appeared and they formed bands distributed alternately along the longest sample edge. The zones near the ends of the sample and crack lips experienced a very high compressive strain, while the zones at crack tips showed a very high tensile strain. The existence of tensile strain could be attributed to the differential shrinkage. This differential shrinkage occurred along the sample due to soil structure, inhomogeneity of the sample, and interface friction between the sample and the mould.

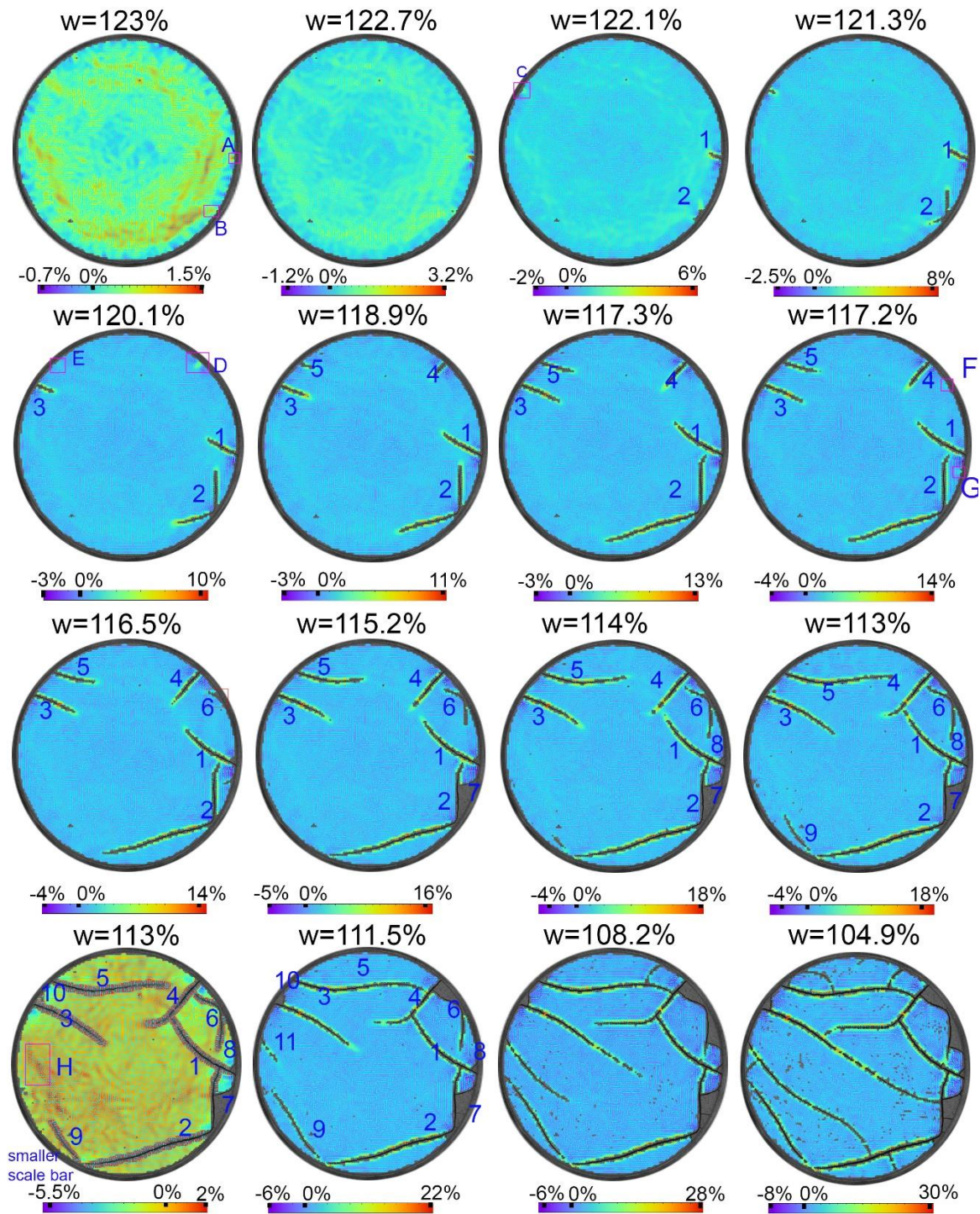


Figure 4.17. ϵ_1 developed on the surface of sample SC1.

The development of ϵ_2 is plotted in Figure 4.18. It can be observed that the compressive strain was highly concentrated at the edge of the sample. When cracking began, the compressive strain was highly concentrated at the crack lips. Figure 4.18 also shows that the tensile strain also developed inside the sample. However, the magnitude of this tensile strain was negligible when compared to the compressive strain when the water content reached around 115.2%. After this period, the magnitude of the tensile strain increased, but remained less than the compressive strain. Before the formation of the cracks, at

locations near the edge of the sample, ε_2 was perpendicular to the edge of the sample, while at other locations, the direction was random. After cracks appeared, ε_2 was parallel to the crack lips at locations around the crack lips, except locations that were near the initiation points of the cracks.

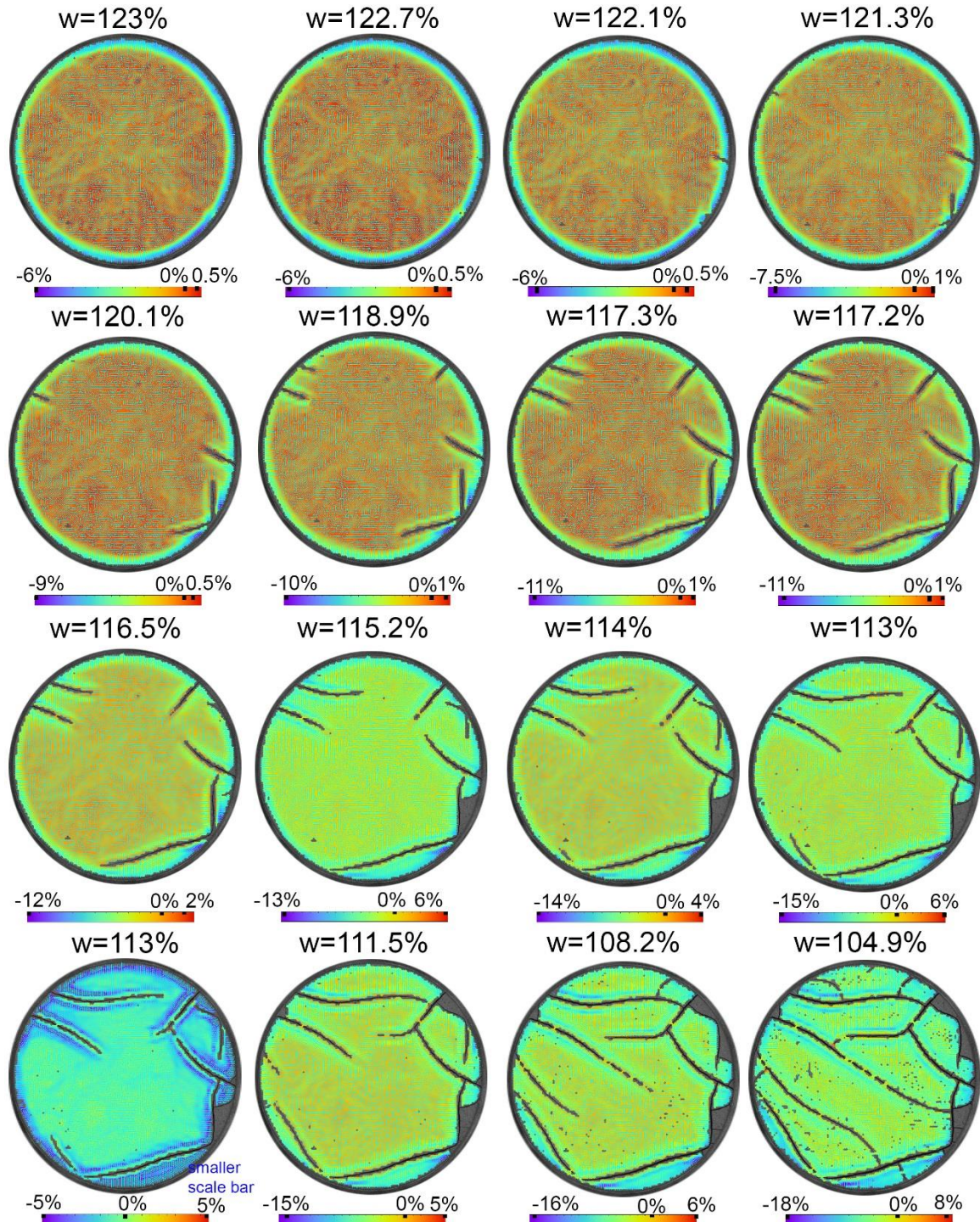


Figure 4.18. ε_2 developed on the surface of sample SC1.

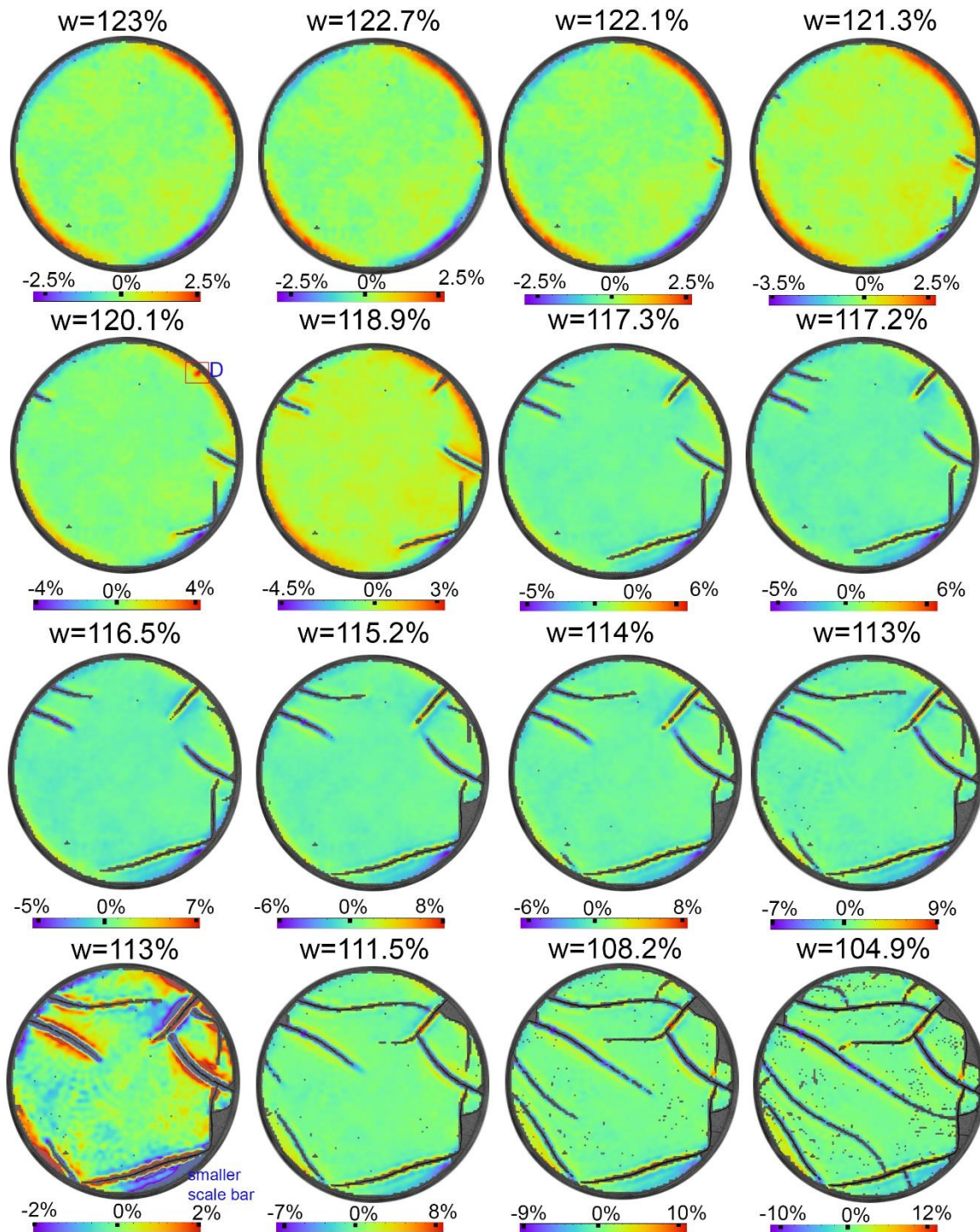


Figure 4.19. ϵ_{12} developed on the surface of sample SC1

The development of ϵ_{12} is plotted in Figure 4.19. Both tensile and compressive strains were observed during the shrinkage process of the sample. These strains highly concentrated at some locations near the edge of the sample, crack lips and crack tips. However, there was no obvious pattern in the distribution of ϵ_{12} . In addition, as the water content decreased, the magnitude of ϵ_{12} increased.

When initiation and propagation of the first 11 cracks are examined, it can be observed that all these cracks initiated at the points where ϵ_1 and ϵ_{12} highly concentrated. In

addition, ε_1 at these points were tensile. These cracks then propagated along the zones where the tensile value of ε_1 were highly concentrated. In addition, cracking changed the distribution of strains at their adjacent zones. For example, tensile ε_1 was highly concentrated at the crack lips and crack tips and its direction was perpendicular to the cracks except locations where the crack initiated (Figure 4.20). Based on the observation on the strain distribution and direction where the cracks occurred, it can be inferred that the first 11 cracks occurred due to the shear and tensile failure mode, and then these cracks propagated due to the tensile failure mode.

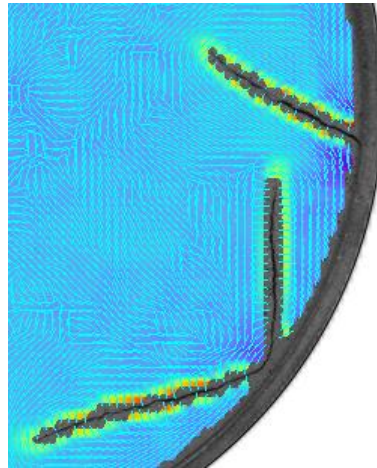


Figure 4.20. ε_1 at the zone near cracks 1 and 2 when water content was 118.9%.

4.4. Effect of Wind on Desiccation Cracking

The effect of wind on desiccation cracking was investigated by drying Werribee clay samples under three drying conditions with three different wind velocities of 0 m/s, 0.9m/s and 1.9m/s, and constant temperature and relative humidity. In this section, the drying conditions and effect of wind on water evaporation and desiccation cracking are discussed and analysed.

4.4.1. Drying conditions and changes of water content

The drying conditions of these tests are plotted in Figure 4.21. The temperature and relative humidity in these tests were kept approximately fixed, while the wind velocity was varied, with speeds of 0 m/s, 0.89 m/s and 1.89 m/s for tests labelled as wind 1, wind 2 and wind 3, respectively. These values were measured at the centre of the test chamber and 200 mm above the sample surface, and the values of 0.89 m/s and 1.89 m/s were the minimum and maximum wind speeds produced by the wind tunnel. Figure 4.21(b) also shows that the wind speed profiles along the height of the test chamber were almost uniform.

The water content of these samples during drying is plotted in Figure 4.22(a). The water content decreased greatly and linearly from an initial water content of approximately 160% to 20%, and then gradually decreased to residual values. On the other hand, the water content decreased faster for samples dried under a higher wind velocity. For example, more than 75 hours were required for the samples dried with zero wind velocity (wind 1) to reach its residual water content, while it took 16 and 11 hours for the samples dried with wind 2 and wind 3 respectively. This significant difference in drying time is due to the increase in ability to remove water vapour from the sample surface with wind speed, resulting in quicker drying (Hillel 2003). Note that the temperature and relative humidity during the drying process of these samples were kept almost constant (as shown in Figure 4.21).

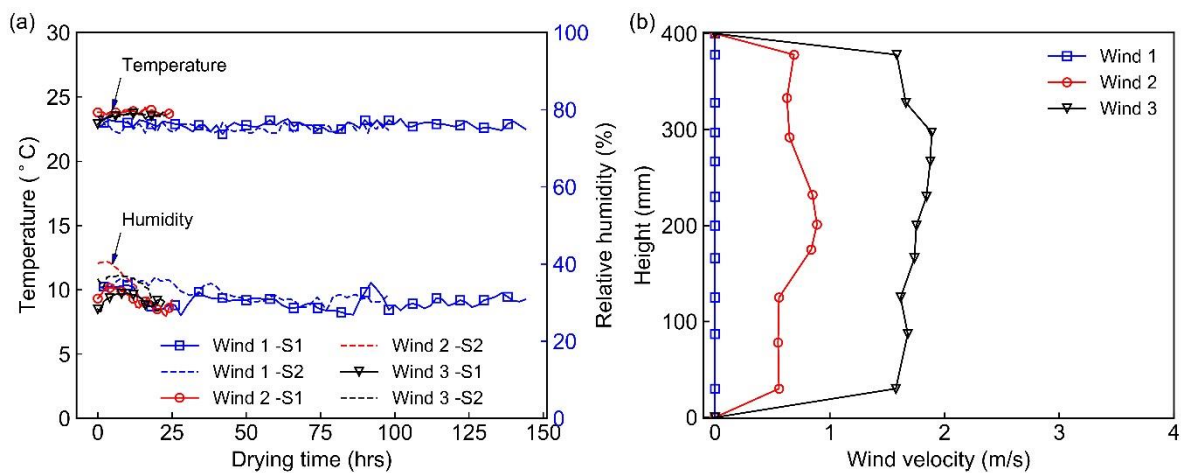


Figure 4.21. Drying conditions: (a) drying temperature and relative humidity; (b) wind velocity.

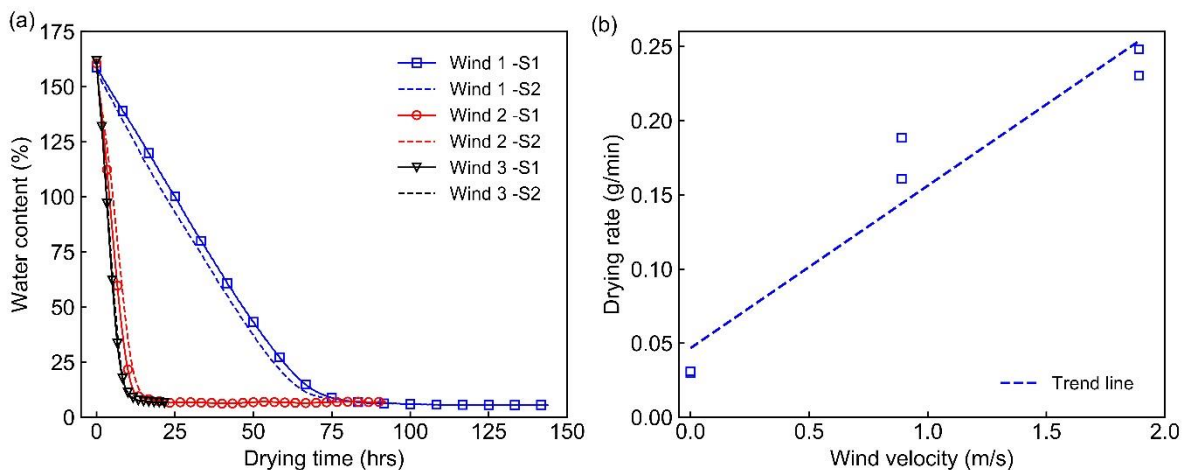


Figure 4.22. Effect of wind on water evaporation: (a) changes in water content; (b) relationship between initial drying rate and wind velocity.

The initial average drying rate calculated during the linear reduction stage of the water content is plotted in Figure 4.22(b). A significant increase in the initial average drying rate

with an increase in wind velocity is observed. This initial average drying rate was approximately 0.03 g/hrs; 0.18 g/hrs and 0.24 g/hrs for the samples dried with wind velocities of 0 m/s, 0.89 m/s and 1.89 m/s, respectively. Figure 4.22(b) shows that a linear relationship between the initial average drying rate and drying wind velocity was achieved. This finding is consistent with that reported by Davarzani et al. (2014), who conducted both experimental and numerical tests to study the effect of wind speed on evaporation of a porous medium prepared by silica sands.

4.4.2. General observations of crack networks

Figure 4.23, Figure 4.24 and Figure 4.25 present the development of crack networks on the surface of the specimens dried under wind 1, wind 2 and wind 3, respectively. These results were obtained from tests Wind 1-S1, Wind 2-S1 and Wind 3-S1. It can be observed that the development of crack networks shows a similar trend, following main features summarised in Section 4.3, but differed slightly with changes in wind speed. First, primary cracks began from a point inside sample Wind 1-S1, or from the edges of samples Wind 2-S1 and Wind 3-S1, and developed towards the centre of the specimens. This observation illustrates that these primary cracks occurred in sample Wind 1-S1 may be attributed to the significant development of tensile stresses due to restrained shrinkage. This stress exceeded the tensile soil strength, resulting in cracking. However, the initiation of the primary cracks in Wind 2-S1 and Wind 3-S1 may result from differential shrinkages along edges of the samples.

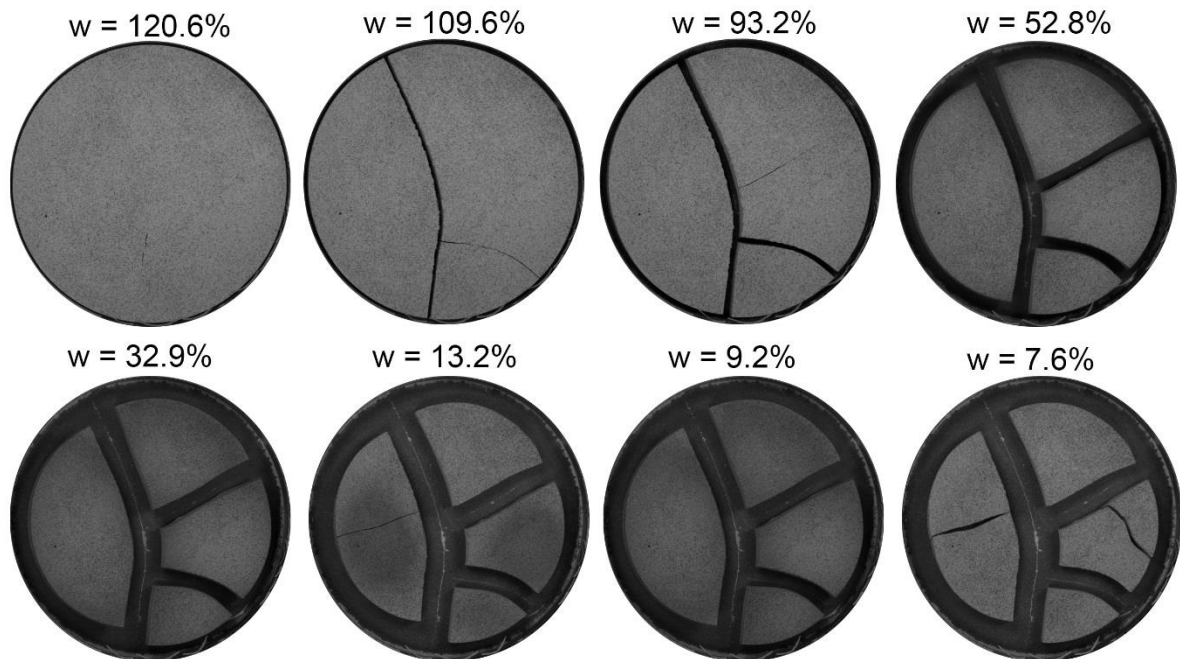


Figure 4.23. Development of the crack network on the specimen dried under wind velocity of 0 m/s (Wind 1 -S1).

Close to termination of primary cracks, secondary cracks initiated. Some secondary cracks started at the primary cracks, while others started at the edges of the samples. For the sample dried under wind 1, these cracks propagated and terminated once reaching sample edges when the water content was very high ($w > 52.8\%$). In this sample, these secondary cracks were almost perpendicular to the primary cracks, suggesting that these secondary cracks may have been caused by tensile failure. For samples dried under wind 2 and wind 3, some secondary cracks did not terminate despite the water content being very low (e.g. 13.2%). In these samples, some angles created by primary cracks and secondary cracks were around 45° , thus some secondary cracks may fail due to a combination of shear and tensile stresses. These observations suggest that the fracture mode may depend on the drying wind velocity. Considering tertiary cracks, it can be seen that these cracks appeared in all samples when the samples were very dry ($w \approx 9\%$) and these cracks developed until the tests finished.

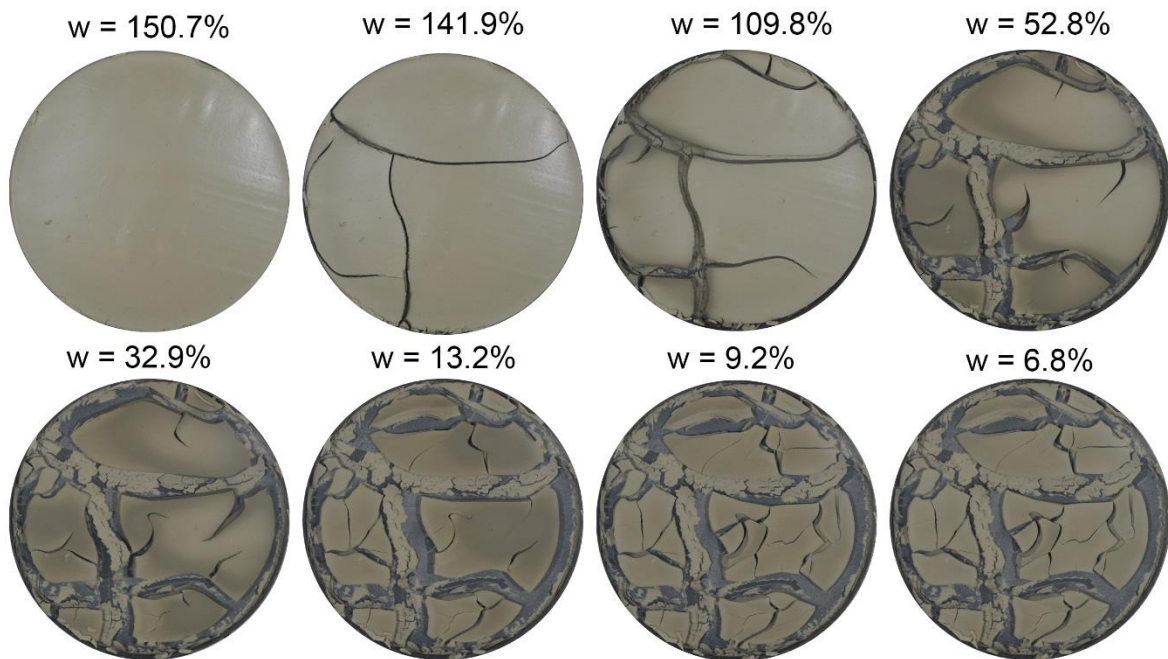


Figure 4.24. Development of the crack network on the specimen dried under wind velocity of 0.89 m/s (Wind 2 -S1).

Figure 4.23, Figure 4.24 and Figure 4.25 also show that when the sample was dried under higher wind velocity, cracking occurred more often and the sample was also divided into more cells, while the area of soil cells decreased. For example, for the sample dried under a wind velocity of 0 m/s, there was only one primary crack, two secondary cracks and two tertiary cracks, while for the sample dried under a wind velocity of 0.89 m/s, there were three primary cracks, seven secondary cracks and more than 10 tertiary cracks. These changes in the number of cracks and cells, and in the area of soil cells can be explained by the evaporation speed and changes in suction inside the sample. As the sample is dried under a higher wind velocity, water evaporates faster, causing a

signification reduction in the water content (as shown in Figure 4.22). Consequently, the rate of suction increase is higher (Kayyal 1995), the sample shrinks faster and the tensile stress inside the sample may develop faster. This tensile stress exceeds the soil tensile strength in a shorter time, causing more cracks, more cells, and smaller cell areas. In addition, Tollenaar (2017) reported that under a higher loading rate, soils were more brittle and loading rate had no effect on the tensile strength, thus it is expected that the number of cracks and cells will increase when the sample is dried under a higher wind velocity.

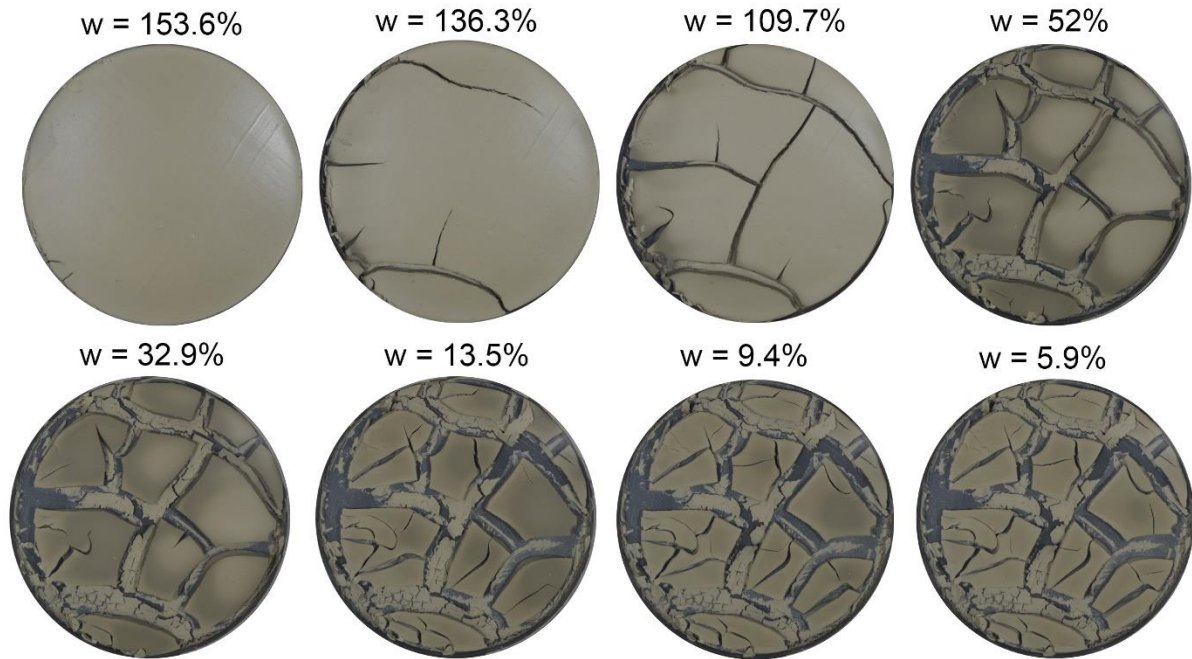


Figure 4.25. Development of the crack network on the specimen dried under wind velocity of 1.89 m/s (Wind 3 -S1).

4.4.3. Crack density factor and number of cracks

As discussed above, soil desiccation cracking significantly influences the performance of soils, especially the hydraulic and mechanical performance. Therefore, quantifying the development of geometric feature of cracks is crucial because it provides further understanding on how cracks develop, so proper measures can be introduced to prevent the occurrence of catastrophes associated with desiccation cracking. In this study, the crack density factor (CDF) defined as the ratio of total crack and shrinkage area to the initial area of the drying sample (Lakshmikantha et al. 2012), and the number of cracks were measured during the desiccation process of all samples. To calculate the area of cracks or shrinkage area, the image processing technique was employed with support of the software PCAS developed by Liu et al. (2013). The main idea of the technique is to convert colour images of the sample surface (Figure 4.26(a)) recorded during drying to binary images using only white and black (Figure 4.26 (b)). During this process, white and black spots located within the soil cells and cracks are removed by using the seed

filling algorithm (Liu et al. 2013). Finally, the seed filling algorithm is utilized to identify soil cells (Figure 4.26(c)) and the crack area is calculated as a summation of black pixels.

Figure 4.27(a) shows changes in the crack density factor of all samples during the desiccation process. It can be observed that the CDF of all samples followed the same trend. It first increased significantly as the water content decreased and then gradually stabilized after the water content reached 15%. During the period of increase in the CDF, at any given water content, the CDF of the samples dried under a wind velocity of 0 m/s was always smaller than that of the samples dried under wind velocities of 0.89 m/s and 1.89 m/s. However, the difference between the CDF of the samples dried under high wind velocities (i.e. 0.89 m/s and 1.89 m/s) was small. After the water content was less than 15%, all samples gave a similar CDF value even though new cracks continued appearing in the samples dried under high wind velocities (as shown in Figure 4.24, Figure 4.25). For example, at a water content of 75%, the CDF values were around 23%, 32% and 33% for the samples dried under wind velocities of 0m/s, 0.89m/s and 1.89m/s, respectively, while at a water content of 8% the CDF was around 53%, 54% and 56%. The increase in the CDF values with an increase in the drying wind velocity may be attributed to a faster suction increase rate resulting from a higher evaporation rate and Huat et al. (2006) reported that a faster loading rate caused an increase in the deformations of a soil sample. For the samples dried under wind velocities of 0.89 m/s and 1.89 m/s, the CDF values were close to each other as these velocities resulted in a small difference between the evaporation rates of these samples (as shown in Figure 4.22).

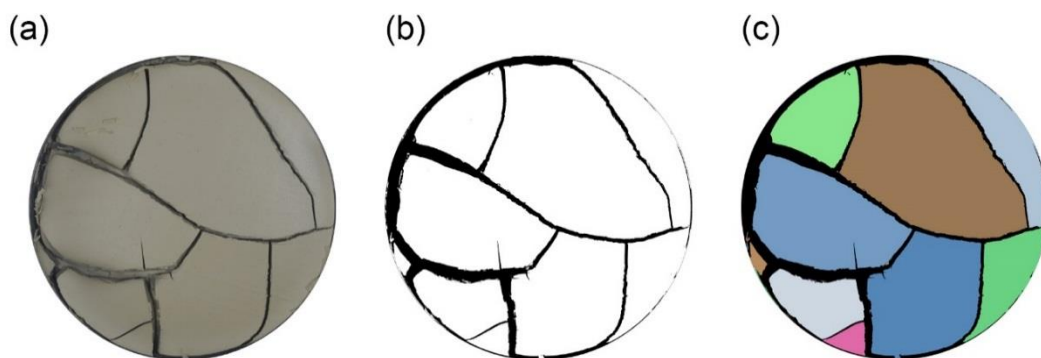


Figure 4.26. Image processing technique to calculate the area of cracks: (a) initial image of the sample surface; (b) binary image; (c) image after identifying soil cells.

Figure 4.27(b) presents the evolution of the number of cracks of all samples during drying. The changes in the number of cracks can be divided into three main stages. In the first stage, after the initiation of cracks, the number of cracks increased rapidly with a decrease in the water content. This stage lasted until the water content reached around 100%. During this stage, all primary cracks and some secondary cracks appeared (refer to Figure 4.23, Figure 4.24 and Figure 4.25 for more details). In the second stage, the

number of cracks gradually increased. In this stage, more secondary crack initiated. This stage ended when water content decreased to approximately 25%, and then the third stage began. In this stage, the number of cracks increased greatly as the water content continued to decrease due to many tertiary cracks existing. At the end of this stage, the number of cracks was twice more than that at the end of the second period. Figure 4.27(b) also shows that the number of cracks strongly depend on drying wind velocity. At any given water content during the drying process, the higher the drying wind velocity, the larger the number of cracks. Figure 4.23, Figure 4.24, Figure 4.25 and Figure 4.27(b), support the conclusion that the increase in the CDF values was mainly caused by the primary and secondary cracks.

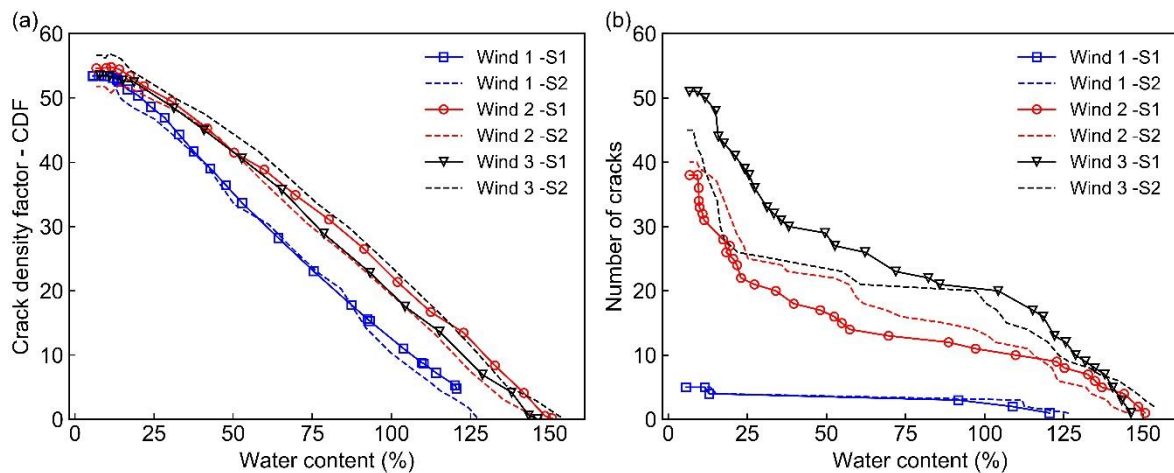


Figure 4.27. (a) evolution of the CDF; (b) evolution of number of cracks.

4.4.4. Cracking water content

Water content is an important parameter that reflects the mechanical behaviour of soils (Mitchell and Soga 2005). In this work, the cracking water content defined as the average water content of the sample when the first crack initiated was quantified. This is justified because the formation of cracks is due to the development of stresses that is caused by the shrinkage deformation of the whole sample. This average water content was also utilised in various studies (Costa et al. 2013; Shin and Santamarina 2011; Tang et al. 2010; Tang et al. 2011c). Figure 4.28 shows the influence of the drying wind velocity on the cracking water content. It is can be seen that this cracking water content increased with an increase in the drying wind velocity. For example, this water content was around 123% and 148% for the samples dried under wind velocities of 0 m/s and 0.89 m/s, respectively. In addition, the cracking water content of all samples was close to or greater than the soil liquid limit (i.e. 127%), especially for the samples dried under a high wind velocity. These results revealed that these samples were saturated when the first crack initiated. This finding is consistent with results reported by Costa et al. (2013), Shin and Santamarina (2011) and Tang et al. (2011c) when they conducted desiccation cracking

tests for other types of clayey soils. The dependence of the cracking water content on the drying wind velocity can be explained based on the development of the suction inside these samples. As water evaporates faster due to a greater drying wind velocity, suction develops faster, causing cracks to initiate earlier. In addition, an increase in loading rate changes the soil behaviour from ductile to brittle behaviour (Tollenaar 2017), so cracking occurs more easily. Note that the increase in the cracking water content was also reported in studies where soil samples were dried under a higher temperature (Tang et al. 2010).

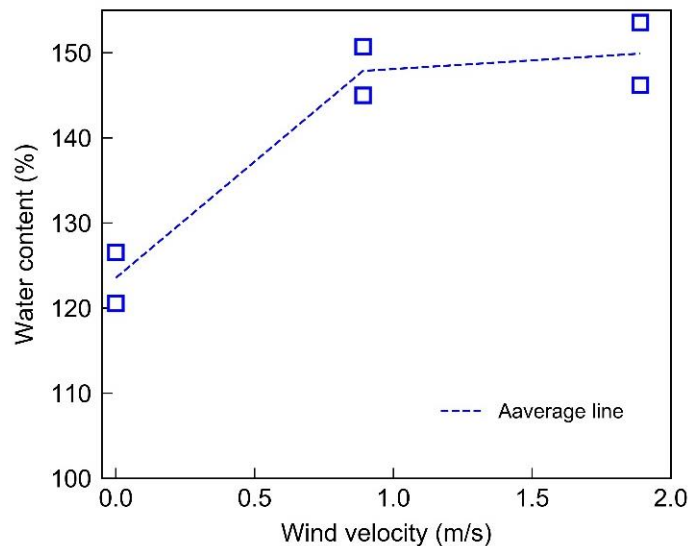


Figure 4.28. Water content when the first crack initiated.

4.5. Conclusions

This chapter has presented the initiation and development of desiccation cracks and the development of the strain fields measured on the sample surface during drying. Circular and rectangular samples were tested. During testing, the digital image correlation technique was employed to measure and analyse the development of the strain fields. The effect of wind velocity on desiccation cracking was also examined by conducting drying tests under different wind velocity generating by a miniature wind tunnel. The key findings are summarised as follows:

1. During drying, the water content of samples significantly decreased then gradually stabilized. The soil samples shrank significantly and cracks occurred.
2. Soil samples with different shapes had different types of crack networks. For rectangular samples with a high aspect ratio, the cracks were almost parallel to the short side of the samples. For circular samples, the cracks met each other at right angles.
3. Both tensile and compressive strains heterogeneously developed on the sample surface, concentrated at crack tips and libs. The development of strains indicated

the appearance and the failure mechanism of cracks. Cracks initiated and propagated in the regions where the tensile strain highly concentrated. In addition, cracks initiated due to a combination of the shear and tensile failure modes, while these cracks propagated further due to the tensile failure mode.

4. Wind velocity significantly influenced the water evaporation in clayey samples. The higher the wind velocity, the faster the water evaporation. Besides, wind velocity also strongly affected soil desiccation cracking. For samples dried under a faster wind velocity, cracks initiated earlier, and the crack network was more complex with more cracks. In addition, during the drying process of these samples, the CDF was also larger. However, when the samples were almost completely dried, difference in the CDF was negligible regardless of the difference in wind velocity.

Chapter 5. A Micromechanics Approach to Model Curling of Slurry Soils

5.1. Introduction

Clayey soils are abundant throughout the world. This type of soils adsorbs and retain a high volume of water. When they lose water, they shrink considerably and soil curling may occur. As reviewed in Chapter 2, existing studies on soil curling conducted by carrying out field observations and laboratory tests within the context of soil desiccation cracking (Allen 1986; Berney et al. 2008; Bradley 1933; Kindle 1917, 1923; Style et al. 2011) or the shrinkage test (Kodikara et al. 2004; Zielinski et al. 2014), reveal that that this phenomenon can be grouped into three main patterns: 1) concave-up curling (\cup); 2) convex-up curling (\cap) and 3) concave-up curling (\cup) followed by convex-up curling (\cap). These patterns are encountered in both slurry and compacted clayey soils (Allen 1986; Berney et al. 2008; Bradley 1933; Kindle 1917, 1923; Kodikara et al. 2004; Style et al. 2011; Zielinski et al. 2014), and are governed by various factors such as the distribution of soil particle size, clay type, temperature, initial water content, drying boundary conditions, and gradient of salt concentration (Bradley 1933; Kindle 1917, 1923; Minter 1970; Zielinski et al. 2014). Occurrence of soil curling has been explained by differential shrinkage along the height of the sample during water evaporates (Allen 1986; Bradley 1933; Kindle 1917, 1923; Kodikara et al. 2004; Style et al. 2011), thereby generating a bending moment (Allen 1986; Bradley 1933; Kindle 1917, 1923; Kodikara et al. 2004; Style et al. 2011). Behaviour at the micro-level, considering the non-uniform distribution of the vertical component of capillary forces on the surface layer, has also been proposed to explain this phenomenon (Zielinski et al. 2014). Furthermore, the curling mechanism has been inferred from observations of the final stage of the desiccation process (Allen 1986; Berney et al. 2008; Bradley 1933; Kindle 1917, 1923; Style et al. 2011), therefore overlooking the entire soil curling process. To comprehensively understand this phenomenon, time-varying observation of both top and bottom surfaces of a soil layer is recommended.

Numerical studies can assist to provide further understanding of the soil curling process. However, up to now, there has been only one attempt to study soil curling by using a numerical approach. In this study, Kodikara et al. (2004) used FDM to study the desiccation process of a slurry, assuming that the soil behaved elastically and remained almost saturated during drying. The measured suction profile was the primary input for the model. This approach was able to describe fairly well the overall response of the sample upon desiccation, including observed soil curling in experiments. However, a

discrete model can be instrumental to bridge micro- to macro-behaviour and to gain a better understanding of desiccation and soil curling processes, including the complex response of clayey soils when they evolve from the initial slurry condition to a semi-solid-state during water evaporation.

DEM introduced by Cundall and Strack (1979) has been widely used to understand micro- and macro-behaviours of soils in geotechnical engineering (Bui et al. 2009; Cui et al. 2017a, b; Lee et al. 2012; Peron et al. 2009a; Sima et al. 2014; Tran et al. 2012; Yao and Anandarajah 2003). In this method, soils are presented by assemblies of particles that interact with each other at contact points via springs, dashpots, dividers, sliders and rollers. Forces at contact points and the movement of particles are computed every time-step by using force-displacement laws and Newton's second law (Cundall and Strack 1979). For clayey soils, Yao and Anandarajah (2003) showed that numerical simulation results of an oedometer test of slurry clay in DEM agreed well with experimental data. Peron et al. (2009a) and Sima et al. (2014) also used DEM to study soil desiccation cracking. In their studies, clayey soils were treated as an assembly of aggregates that represented groups of several clay particles. These aggregates were linked together by a contact bond model. The drying process was simulated by changing the sizes of aggregates. These numerical studies captured fairly well cracking characteristics (i.e. the surface crack ratio, crack length per unit area and average crack width) of clays during drying. Although this approach may be used to simulate soil curling, it cannot correctly capture physical behaviour of slurry clays. These include the transition process from the slurry state (i.e. high water content) to the semi-solid state (i.e. when water almost evaporated) due to drying; rearrangement of non-deforming solid particles/aggregates during drying; and free movement of fluid phase during drying. Therefore, it is necessary to develop a new approach capable of describing physical behaviour of slurry clays at the micro-level to capture macro-behaviour of the material.

This chapter aims to develop a new water particle approach in DEM to properly describe the entire desiccation process inducing soil curling of slurry clays, in which the material undergoes the transition process from a slurry state to a semi-solid state. Different models have been proposed to simulate the effect of capillary forces in unsaturated soils behaviour (Jiang et al. 2004; Lambert et al. 2008; Scholtès et al. 2009a; Scholtès et al. 2009b). The range of application of this type of model is limited to a relatively low degree of liquid saturation (Jiang et al. 2004; Lambert et al. 2008; Scholtès et al. 2009a; Scholtès et al. 2009b). This concept is extended in this paper to higher saturations, including almost fully saturated soils, introducing the 'DEM water particle concept'. To demonstrate capabilities of the proposed DEM water-particle approach, challenging tests conducted on clay slurries that exhibit curling upon drying are selected.

This chapter is organised as follows. Section 5.2 describes development of the proposed numerical approach. This is followed by validation of the proposed approach in Section 5.3. Section 5.4 presents applications of the proposed approach where influences of evaporation rate and sample thickness on soil curling are investigated.

5.2. Proposed Numerical Approach

A brief overview of DEM is presented first, followed by the main components and mathematical description of the proposed approach are presented and discussed.

5.2.1. DEM overview

DEM treats soil samples as assemblies of rigid particles that can overlap each other at contact points. Behaviour at contact points can be modelled by a system of springs, dashpots and sliders, as illustrated in Figure 5.1. The motion of each particle i is governed by Newton's 2nd law (Cundall and Strack 1979):

$$\ddot{\vec{x}}_i = \frac{\vec{F}_i}{m_i} + \vec{g} \quad (5-1)$$

$$\dot{\vec{\omega}}_i = \frac{\vec{M}_i}{I_i} \quad (5-2)$$

where $\ddot{\vec{x}}_i$ and $\dot{\vec{\omega}}_i$ are the translational and rotational acceleration vectors of a particle i respectively; m_i is the total mass of the particle i ; \vec{g} is the acceleration vector of gravity; I_i is the moment of inertia of the particle i and the force vector (\vec{F}_i) and moment vector (\vec{M}_i) acting on particle i can be calculated as follows:

$$\vec{F}_i = \sum_{c=1}^N F_c^n \vec{n} + \sum_{c=1}^N F_c^s \vec{s} + \sum_{c=1}^N D_c^n \vec{n} + \sum_{c=1}^N D_c^s \vec{s} \quad (5-3)$$

$$\vec{M}_i = \sum_{c=1}^N F_c^s \vec{s} \vec{l}_c + \sum_{c=1}^N D_c^s \vec{s} \vec{l}_c \quad (5-4)$$

where F_c^n and F_c^s are the contact forces at contact c in normal (\vec{n}) and shear (\vec{s}) directions, which can be computed using Equations (5-5) and (5-6)); D_c^n and D_c^s are, respectively, normal and shear dashpot forces or damping forces (which can be calculated using Equations (5-7) and (5-8)); N is the total number of contacts of particle i ; \vec{l}_c is the vector from the centre of particle i to contact c .

$$F_c^n = \begin{cases} K_n u_n & \text{if } u_n \geq 0 \\ 0 & \text{if } u_n < 0 \end{cases} \quad (5-5)$$

$$F_c^s = \begin{cases} \sum K_s \Delta u_s & \text{if } F_c^s < \mu F_c^n \\ \mu F_c^n & \text{if } F_c^s \geq \mu F_c^n \end{cases} \quad (5-6)$$

$$D_c^n = -2\beta_n \sqrt{m_c K_n} \dot{\delta}_n \quad (5-7)$$

$$D_c^s = -2\beta_s \sqrt{m_c K_n} \dot{\delta}_s \quad (5-8)$$

$$m_c = \frac{m_1 m_2}{m_1 + m_2} \quad (5-9)$$

where u_n is the overlap of two particles, and Δu_s is the relative tangential (shear) displacement increment; μ is the friction coefficient; K_n and K_s are the normal and tangential (shear) contact stiffnesses, respectively; β_n and β_s are the normal and shear critical damping ratios, respectively; $\dot{\delta}_n$ and $\dot{\delta}_s$ are the relatively normal and shear contact velocities, respectively and m_c is the effective system mass that can be calculated by using Equation (5-9).

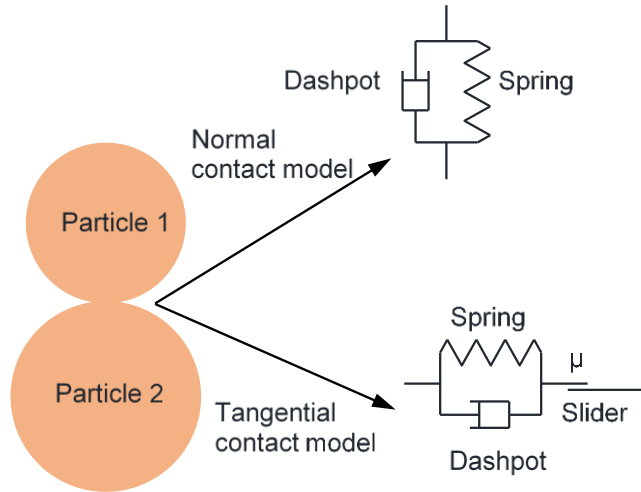


Figure 5.1. Basic contact model in DEM.

5.2.2. A water particle approach

In absence of external loads, clay particles in slurries tend to interact with each other via inter-particle forces such as van der Waal force, double layer force, Born's repulsive force, or a combination of them (Mitchell and Soga 2005). These forces are behind the suspension of clay particles in water. When these slurries undergo a drying process, water evaporates, causing capillary forces to develop. These forces pull particles towards each other, causing the rearrangement of both solid and fluid phases. A DEM water particle concept is proposed in this study to capture this behaviour at the micro-scale level in the simulations. The key ideas of the proposed approach are summarized below:

- 1) Slurry clayey soils are modelled by two different sets of particles, namely, clay and water (as shown in Figure 5.2(a) and Figure 5.2(b)). These particles interact with each other through a set of contact forces.
- 2) Liquid bridge or viscous force always exists between two particles when water evaporates, regardless of their nature, provided that they are in a wet condition and located within a predefined contact distance. To account for this phenomenon, a liquid bridge force model (Figure 5.2(c)) is modified to extend its working range to a higher degree of saturation. This assumption is essential to describe the shrinkage process of soils subjected to the drying process.

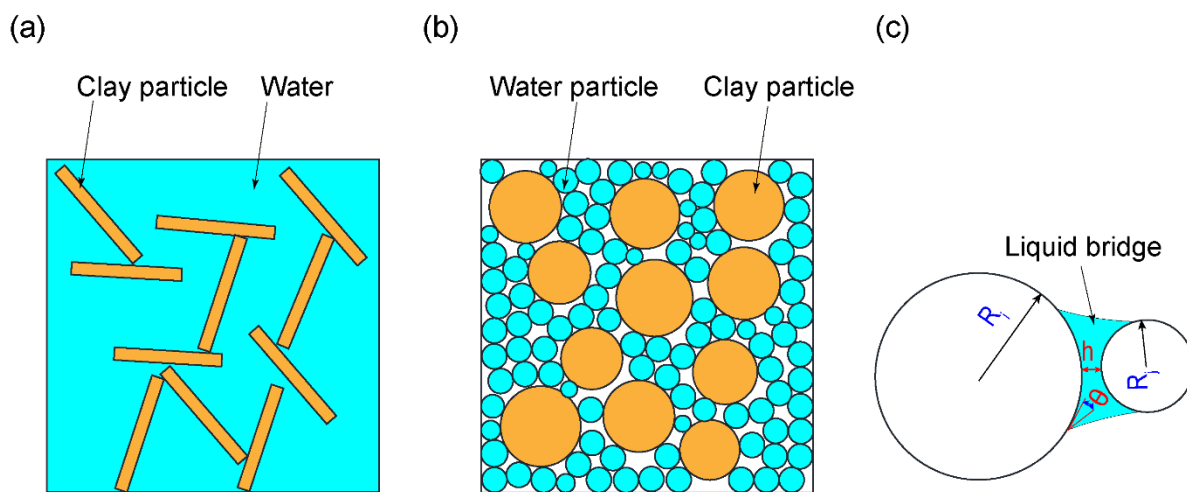


Figure 5.2. Water particle concept in DEM: (a) slurry clayey soils; (b) DEM model of slurry clayey soils; (c) liquid bridge model.

The concept shown in Figure 5.2 requires water particles to be smaller than the minimum size of the clayey particles adopted in the simulation so that water particles can fill the void spaces among clayey particles. The numbers of water and clayey particles in a numerical specimen are computed to satisfy the initial water content of the experiment, and to ensure that all particles are in contact with each other without overlapping to eliminate stress-locking effects. The density of water and clayey particles is also scaled up to account for large voids that occur in DEM simulations and also to ensure that the effect of density on the numerical specimen is similar to that in the experiment. As clayey particles are plate-shaped and interlocking between them may also occur in real soils, clayey particles have a limited rotation capability compared to that of spherical particles. Therefore, angularity and interlocking should be considered in DEM simulations when spheres are used to represent clayey particles. To capture the effects of angularity and interlocking in DEM simulations, two alternative approaches have been widely applied: 1) to incorporate a rolling resistance model that required contact between DEM particles (Ai et al. 2011; Iwashita and Oda 1998; Jiang et al. 2015); and 2) to randomly hinder the rotation of a selected fraction of the total particles (Cha and Santamarina 2014; Cha and

Santamarina 2016). The first method is not applicable to the material selected in this research, because contact between soil particles cannot be guaranteed when modelling slurries and clays samples with high water content. Therefore, the second approach is selected hereafter. The fractions of soil particles with hindered rotation (HR) investigated in this paper are 0%, 20% and 50%. This mechanism is activated during the evaporation process only.

The interaction between water-water and water-soil particles is formulated to mimic their physical behaviour. In compression mode, a penalty spring force model is adapted to calculate the interaction between these particles. This effect can in turn represent hydraulic forces acting on submerged particles under fully saturated conditions, or the compressibility of the bulk unsaturated soil. In the tension mode, on the other hand, a liquid bridge force is assumed to be always present between two particles. This mechanism represents either a viscous force between water molecules under the fully saturated condition, or a suction force under unsaturated conditions. Lambert et al. (2008) suggested the following equation to estimate the effect of the capillary force under unsaturated conditions:

$$F_{cap} = -\frac{2\pi R\gamma\cos\theta}{1 + (h/2d_{sp})} \quad (5-10)$$

$$d_{sp} = \left(\frac{h}{2}\right) [-1 + \sqrt{1 + 2V_{lb}/(\pi R h^2)}] \quad (5-11)$$

$$R = \frac{2R_i R_j}{R_i + R_j} \quad (5-12)$$

where F_{cap} is the capillary force between two spheres; V_{lb} is the volume of the liquid bridge; θ is the water contact angle; γ is the surface tension of water; h is the distance from surface to surface of two spheres; R_i and R_j are the diameters of spheres i and j , respectively. Afterwards, this equation was upgraded by Jiang et al. (Jiang et al. 2004) to capture the scaling effect associated with particle size, by multiplying F_{cap} times a scaling factor (n), which is calculated as the ratio between DEM and real particles' radii. This factor ensures the same stress condition between two samples with the prototype and scaling particles (Jiang et al. 2004).

As discussed in previous sections, the above equations are valid for low water content. This work proposes an extended equation able to account for water-related-links between particles at higher saturations, as follows:

$$F_{w_int} = f(w) n F_{cap} \quad (5-13)$$

where F_{w_int} represents the interaction forces associated with the presence of water in soils and $f(w)$ is a function of the water content added to the approach to extend the liquid bridge forces model to higher water contents. This type of link between particles always exists, even when the sample is almost saturated and it can be associated with viscous and/or surface tension effects (Mitchell and Soga 2005).

This function can be determined by mapping the experimental soil water retention curve (SWRC) to the one obtained from a DEM simulation involving the representative volume element (RVE) of the material. The mapping requires the calculation of the suction from a DEM simulation that incorporates capillary forces, which in turn can be obtained by considering the net stress associated with the RVE of an unsaturated DEM soil sample. This concept can be initially defined as (Scholtès et al. 2009b):

$$\sigma_{pq}^{net} = \sigma'_{pq} + \sigma_{pq}^{cap} \quad (5-14)$$

$$\sigma_{pq}^{cap} = \frac{1}{V} \sum_c F_{p,c}^{w_int} x_q^{i,j} \quad (5-15)$$

where σ_{pq}^{net} is the net stress; σ'_{pq} is the effective stress; σ_{pq}^{cap} is the capillary stress induced by the capillary force; V is the volume of the RVE; $F_{p,c}^{w_int}$ is the water interaction force at a contact c oriented along the direct direction p ; $x^{i,j}$ is the vector pointing from particle i to particle j through the contact c . The net stress can be written in the alternative form as (Houlsby 1997):

$$\sigma_{pq}^{net} = \sigma'_{pq} - S_r \psi \delta_{pq} \quad (5-16)$$

where ψ is the suction; S_r is the degree of saturation; δ_{pq} is the Kronecker Delta.

By comparing Equations (5-14) and (5-16), the suction can be expressed as follows:

$$\psi = -\frac{1}{3S_r V} \sum_c F_{p,c}^{w_int} x_q^{i,j} \quad (5-17)$$

Equation (5-17) can be used to derive a SWRC from DEM simulations, which (for a given soil) can be then benchmarked against experimental data to determine the water content shifting function.

This process also implicitly accounts for variation of the volume of the liquid bridge between two soil particles when the water content changes. Therefore, a reference volume of the liquid bridge between two particles is adopted at the beginning of the

simulation, and $f(w)$ accounts for subsequent changes (more details are provided in the next section).

Finally, the force associated with water-interactions between particles is included in the calculation of the contact force (\vec{F}_c) between two particles as:

$$\vec{F}_c = F_c^n \vec{n} + F_c^s \vec{s} + D_c^n \vec{n} + D_c^s \vec{s} + F_{w_int} \vec{n} \quad (5-18)$$

which can then be used to update the motions of both clay and water particles in the DEM simulation.

In the following sections, the proposed DEM approach is first examined against experimental data and then used to study the effects of both soil-layer thickness and drying rate on the soil drying and curling processes.

5.3. Validation of the Proposed Water Particle Approach

The proposed approach is validated by simulating the free shrinkage test of sample prepared by the kaolin slurry (CL3_1) that has been reported in Chapter 3. Modelling and experimental results are compared and discussed. In this section, preparation of the numerical sample and input parameters, including water evaporation process, are first outlined and discussed. Then, the calibration process adopted to obtain the input parameters for the modified capillary force model is presented. Finally, the proposed water-particle approach is employed to simulate the drying process of the experimental sample and comparisons are made between the simulations and experiments.

5.3.1. Sample preparation and input parameters

The numerical specimen was prepared by generating two groups of particles to represent both, clay and water. The sample preparation process followed the requirements discussed in Section 5.2.2. The clayey and water particles were computed based on their weight fraction in accordance with the corresponding experimental sample. To reduce computational time, the initial water content of the numerical specimen was set at 46.5%, which was lower than the initial water content of the experimental sample (86.6%), but higher than the water content at which soil curling initiated (43.5%). A range of particle size between 1 μ to 3 μ was considered in this study based on the reported Kaolin size-particles distribution, with around 80% of the particles in this range (Shannon 2013). However, the actual size of particles was scaled up with a scaling factor of 1000 to reduce both computational cost and numerical errors that would occur due to the very small particle size (Jiang et al. 2004). Water particles were taken to be uniformly distributed from 0.8 mm to 1.2 mm. The sample preparation process began with generation of a

predefined number of clayey particles in a rectangular mould created by faceted boundaries, after which the sample with only clayey particles was simulated for several steps to avoid significant overlapping among these particles. After that, a predefined number of water particles were generated, and then the entire numerical sample was run to obtain the equilibrium condition. All particles were then allowed to settle under gravity. During the sample preparation process, the capillary force model was not activated, and the friction coefficients of all particles and facets were set equal to zero. The friction coefficient of 0.5 was then assigned to soil particles and facet boundaries before the water evaporation process was activated. No friction was considered for the interaction between soil and water particles or between water particles. Note that during the entire simulation process the normal and shear stiffnesses of particles were assumed equal to 1×10^7 N/m and 5×10^6 N/m, respectively.

5.3.2. Water evaporation process

Existing DEM approaches utilise a single type of particle to represent both, solid and fluid phases when modelling wet granular materials. Accordingly, the water loss in DEM simulations is normally simulated by reducing the radii of DEM particles regardless of their nature. In this work, in contrast, only the radii of water particles are reduced during the drying process, while the radii of clayey particles remain unchanged during the simulation. This concept allows the proposed modelling approach to closely replicate the water evaporation process of slurry soils in the physical experiment because actual soil particles are not shrinkable. To reduce the radii of water particles during the drying process, the following equation proposed by Peron et al. (2009a) is adopted:

$$R_w = R_{w0} e^{\left[-\alpha_1 \left(1 - \frac{z}{z_0} \right) - \alpha_2 \frac{z}{z_0} \right] \frac{t}{\tau}} \quad (5-19)$$

where R_{w0} and R_w are the radius of a water particle at time $t = 0$ and t , respectively; τ is the total duration of the experiment; z is the vertical coordinate of the water particle; z_0 is the reference height; and α_1 and α_2 are shrinkage parameters.

Equation (5-19) allows a description of the differential shrinkage process in the numerical specimen, in which the water would evaporate more quickly on the upper surface and more slowly at the bottom of the specimen. The shrinkage parameters for this model can be determined from the water content curve obtained from the laboratory experiment, instead of using volumetric strain and void ratio as proposed by Peron et al. (2009a). This approach alleviates difficulties associated with the measurements of strains and void ratio that are required in the previous model (Peron et al. 2009a; Sima et al. 2014). To derive the shrinkage parameters from the experimental water content curve, the water content of the DEM sample at time t is required, which can be computed as follows:

$$w = \frac{\rho_w \sum_{i=1}^{n_w} R_{w(i)}^3}{\rho_s \sum_{j=1}^{n_s} R_{s(j)}^3} \quad (5-20)$$

where ρ_s and ρ_w are the densities of clayey and water particles, respectively; n_s and n_w are the number of clayey and water particles, respectively; R_s and R_w are the radius of clayey and water particles at t , respectively.

The ratio between water contents w_1 and w_2 at time t_1 and t_2 , respectively, can be rewritten by considering that the shrinkage parameters are the same for all water particles:

$$\frac{w_1}{w_2} = \frac{\sum_{i=1}^{n_w} R_{w(i)1}^3}{\sum_{i=1}^{n_w} R_{w(i)2}^3} = \frac{e^{-3\alpha_2(0.75\frac{t_1}{\tau})}}{e^{-3\alpha_2(0.75\frac{t_2}{\tau})}} = e^{2.25\alpha_2\frac{t_2-t_1}{\tau}} \quad (5-21)$$

in which the ratio between α_1 and α_2 was taken to be 0.5 as used by Peron et al. (2009a).

Given the nature of the water content and evaporation rate curves of the slurry clay as shown in Figure 3.3(d), the shrinkage parameters in this study can be reasonably assumed to be constant during three main stages: i) when the water content dropped linearly from 46.5% to 13.5%; ii) when the water content changed from 13.5% to 3.5%; and iii) when the water content gradually changed from 3.5% to 1.8%. Furthermore, during the drying process, the liquid bridge model was activated.

5.3.3. Calibration of water content shifting function for DEM simulations

To derive the shifting function, a DEM simulation of an RVE slurry clay sample subjected to drying was conducted to obtain the soil water retention curve (SWRC). The RVE specimen is a 25mm sided cube and was prepared following the procedure described in Section 5.2.1. The water evaporation process described in Section 5.3.2 was then activated using the shrinkage parameters calculated from the water content curve of the soil curling test. During the evaporation process, the water content shifting function $f(w)$ was kept at 1.0 and the suction at a corresponding water content was measured within a spherical volume, with a diameter of 18mm located at the centre of the RVE specimen. The suction computed at multiple designated water contents (i.e. the simulated SWRC) was then benchmarked against the SWRC obtained from the experiment to obtain the water content shifting function $f(w)$. This function was subsequently used to repeat the simulation related to the RVE slurry clay sample to obtain a new SWRC. The new numerical SWRC was then compared again to the experimental SWRC, to check whether the water content shifting function $f(w)$ could satisfactorily reproduce the experiment results. The calibration process would be repeated until achieving reasonable agreement. Numerical results for the RVE slurry clay sample obtained with the water content shifting

function $f(w)$ of 1.0 and without hindered rotation (HR=0%) are plotted in Figure 5.3. Simulated water content agreed well with the experimental counterpart (Figure 5.3(a)), demonstrating that the assumption of constant shrinkage parameters during three stages of change in water content was satisfactory for the current DEM simulation. Nevertheless, the numerical SWRC significantly underpredicted the experimental one (Figure 5.3(b)), although they shared a tendency for the suction to increase as the water content decreases. This trend was sensible because the volume of the liquid bridge between two particles used in the current simulation was different from that in the experiment, note that no existing DEM simulation is capable of capturing the experimental SWRC using a capillary force model (Scholtès et al. 2009a; Wang et al. 2018a). The water content shifting function $f(w)$ was incorporated in the model to obtain a reasonable agreement between the DEM simulation and experiment.

Figure 5.4(a) shows the first water content shifting function $f(w)$ obtained as the ratio between the experimentally measured suction and the simulated one assuming $f(w) = 1$. This result allowed mapping of the simulation results to those of the experiment. Using the best-fit polynomial trend-line, the following sixth-order polynomial water content shifting function $f(w)$ could be derived with its parameters listed in Table 5.1:

$$f(w) = a_1w^6 + a_2w^5 + a_3w^4 + a_4w^3 + a_5w^2 + a_6w + a_7 \quad (5-22)$$

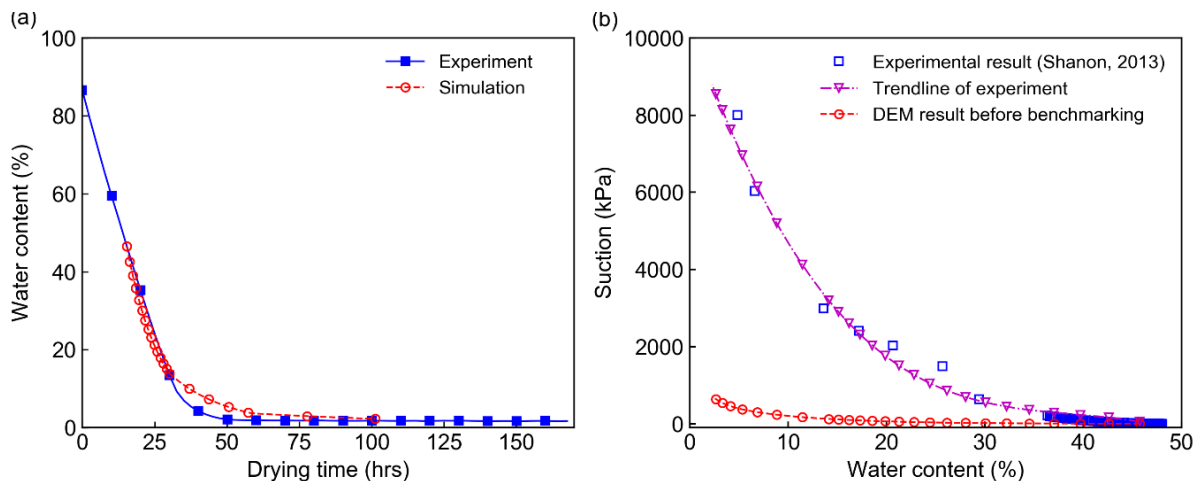


Figure 5.3. Numerical results of the RVE without hindered rotation (HR=0%) before benchmarking with experimental results: (a) changes in water content; (b) soil water retention curve (SWRC).

Numerical simulation of the RVE slurry clay sample was then repeated with the new function, $f(w)$, and HR=0%, with the new numerical SWRC plotted in Figure 5.4(b), together with the experimental SWRC. Now numerical and experimental SWRCs agreed well, suggesting that the water content shifting function $f(w)$ derived in (5-22) can be used for DEM simulations of soil curling without hindering rotation. A similar process was

repeated to derive $f(w)$ for cases with 20% and 50% of hindered rotation. It was found that Equation (5-22) can still be used for these cases with the parameters listed in Table 5.1.

Table 5.1. Parameters for the function $f(w)$

Hinder rotation (%)	a_1	a_2	a_3	a_4	a_5	a_6	a_7
HR=0%	-71596	109276	-68024	22103	-3979.8	417.43	4.7252
HR=20%	-17565	45784	-43070	19402	-4504.6	539.42	-0.1584
HR=50%	-1067.2	14786	-20878	11867	-3295.6	464	0.5726

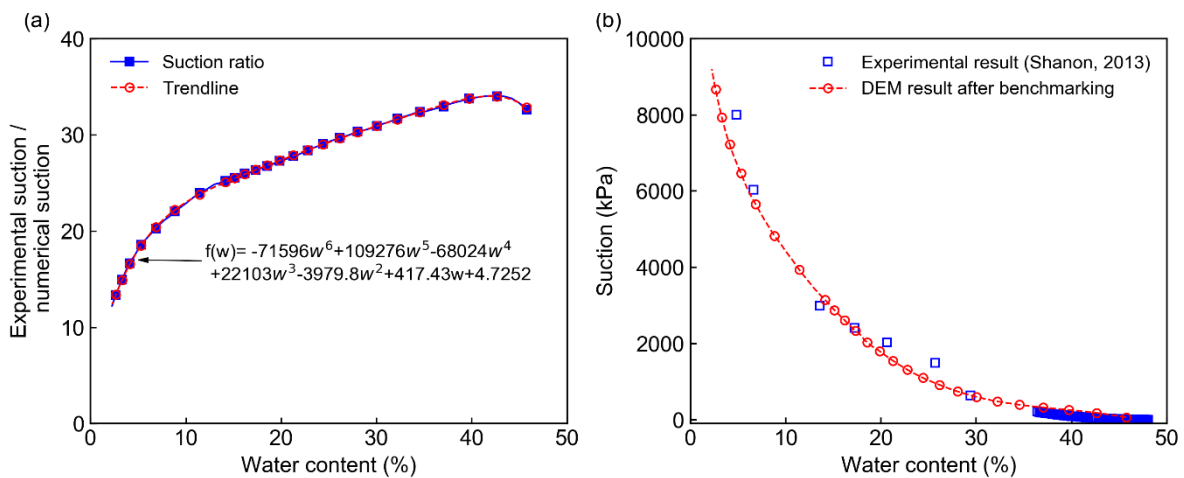


Figure 5.4. (a) suction ratio between the experiment and simulation with $f(w) = 1.0$ and HR=0%; (b) SWRC after using the water content shifting function $f(w)$.

5.3.4. Simulations of the desiccation process

The free shrinkage experiment for kaolin slurry reported in Chapter 3 was then simulated using the proposed approach with input parameters selected and obtained following the procedure described in Sections 5.3.1 to 5.3.3. Figure 5.5 shows the evolution of water content obtained in the numerical specimen without considering hindered rotation (HR=0%). Simulated water content agreed reasonably well with the experimental counterpart, confirming the suitability of the shrinkage parameters adopted in the water evaporation model.

The progressive development of the desiccation process in an experimental sample of kaolin slurry presented in Chapter 3 is again shown in Figure 5.6, while the numerical results of the numerical soil sample without considering hindered rotation (HR=0%) is illustrated in Figure 5.7. The results in Figure 5.6 show that the specimen initially shrank in three directions, with the vertical deformation being the largest one. After the water content decreased from 86.6% to 64.5%, the sample detached from the right and left sides of the mould. The horizontal deformation then became dominant. When the water

content decreased to 45.4% and then 43.5%, the sample started curling up at the left and right edges, respectively, forming concave-up curling. These edges continued to curl up and reached a temporary stable stage when the water content of the sample was 29.01%. The stable stage lasted until the water content reached approximately 7.99%, after that the edges curled up again and reached their maximum elevations at a water content of approximately 2.2%. The sample retained the curved shape upon further drying.

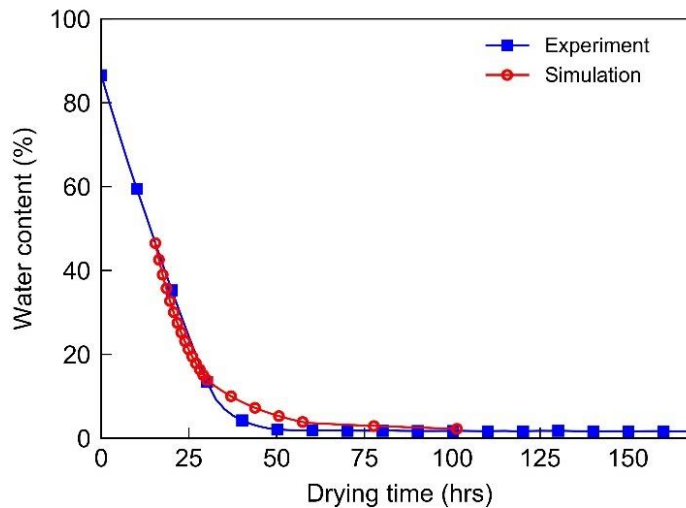


Figure 5.5. Water content of the sample in the simulation without hindered rotation (HR=0%).

The data presented in Figure 5.7 for the numerical sample show that the numerical specimen initially underwent shrinkage in all directions with the vertical deformation being dominant. It then detached from the mould and the horizontal shrinkage subsequently accelerated to trigger the curling process on the edges of the specimen. The upward curling initiated at water content of approximately 43.4%, which was very close to experimental values (43.5% - 45.4%). After soil curling initiated, the curled edges continued lifting up until reaching their maximum elevations at a water content of around 9.4%. After this stage, the edges began to retreat downwards to a stable location and the sample retained its curled shape. Compared to experimental results as shown in Figure 5.6, the proposed DEM model with HR=0% could qualitatively reproduce the progressive development of the curling process observed in the experiment, except for the retreating downward stage. This difference can be attributed to the use of spherical particles (HR = 0%) in the DEM simulation, thereby overpredicting motions of soil particles. In reality, clayey particles are non-spherical and do not rotate freely. As a result, the rearrangement capability of the clayey particles in the real sample during the evaporation process is limited compared to that of spherical ones used in the DEM simulation without hindered rotation (HR = 0%). In addition, if no hindered rotation was applied, DEM particles would rotate freely due to the presence of the tangential force at contact and this would result in a small bending stiffness of their assembly, which could cause DEM particles to move downwards easily under gravitational force. This mechanism results in over-prediction of

the lift-off height in the DEM simulation (HR = 0%) compared to the experiment and the downward retraction of the curled edges for a short period before the end of the evaporation process.



Figure 5.6. Shrinkage deformation and curling development of the Kaolin NY clay.

To address the above issue, the hindered rotation was employed in subsequent DEM simulations. Figure 5.8 shows a comparison of the lift-off height between the experiment and the DEM simulations for the three hindered rotation fractions of HR = 0%, 20% and 50%. The lift-off height in this study is defined as the distance from the base of the mould to the highest point of the bottom face of the sample. In the experiment, after soil curling initiated, the lift-off height in both samples increased as water content decreased, and then reached a temporary stable period when the water content decreased to approximately 29 and 25.5% for samples 1 and 2, respectively. After water contents of samples 1 and 2 decreased to around 5.8% and 3.85% respectively, the lift-off height increased again and reaches its maximum of 2.5mm at the end of the test. The numerical sample with HR=0% showed that the lift-off height followed a trend similar to that in the experimental test except for the retreating period, which brought the elevation of the

sample to 3.85mm after the water content decreased from 9.4% to 2.2%. No temporary stable period was recorded for the numerical sample with HR=0%. However, with the introduction of the hindered rotation, the retreating behaviour of the lift-off height in the numerical samples was not clearly observed. In addition, the hindered rotation significantly influenced the magnitude of the lift-off height, which decreased with an increase in the fraction of soil particles with hindered rotation. The trend and magnitude of the numerical lift-off height are reasonably matched with those observed in the experiments when the fraction of hindered rotation is 50%, except for the temporarily stable period of the lift-off height in the numerical samples, which occurred later than in the experiments. This difference can be attributed to the influence of plate-shaped clay particles in the experiments. Specifically, the platen shape could hinder both translational and rotational movements of particles in the experiments, whereas the hindered rotation technique employed in the simulations only limited the rotational motion of a certain number of particles. As a result, the numerical simulations underpredict the initiation of this temporary stable period of the lift-off height. Figure 9 also shows that the water content at which the soil curling initiated in all simulations was similar to that in the experiment, regardless of the difference in the level of hindered rotation. The reasonable agreement between the numerical and experimental results implies that the proposed approach could be used to study the behaviour of slurry clays during drying.

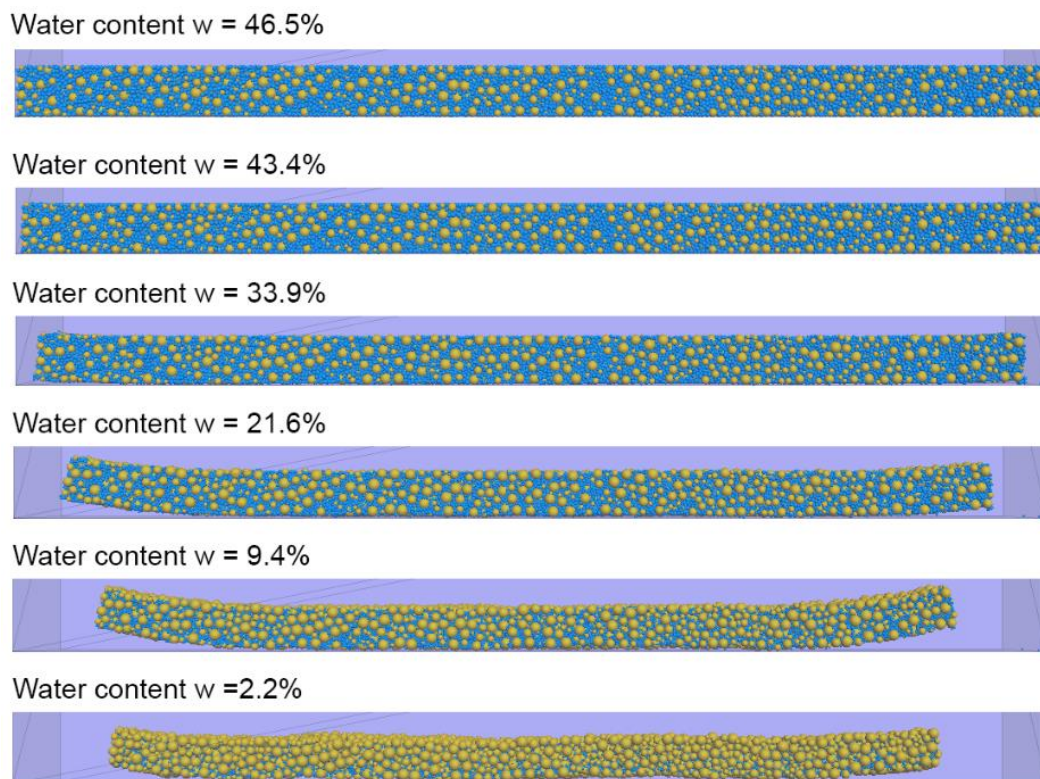


Figure 5.7. Shrinkage deformation of the sample in the simulation without hindered rotation (HR=0%).

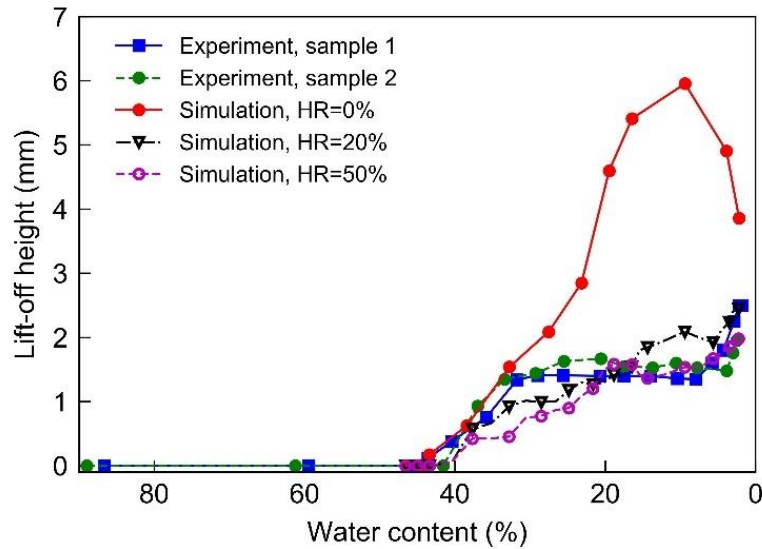


Figure 5.8. Lift-off height in the experimental and numerical tests.

5.4. Applications

This section employs the proposed DEM water-particle approach to investigate the influence of soil layer thickness and water evaporation rate on the desiccation process inducing soil curling. All numerical tests in this section are conducted with the hindered rotation of 50% (HR=50%) and the input parameters presented in Section 5.3.

5.4.1. Effect of soil layer thickness

The effect of soil layer thickness on the desiccation process was investigated by conducting two additional numerical simulations with the sample thicknesses of 8 mm and 10 mm. Figure 5.9 shows the evolution of water content during the drying process in all samples. Similar to what was observed in the experiment and the previous sections, the water content greatly decreased and then gradually stabilised. At every drying time, the water content of the samples with greater thickness was slightly greater than that of thinner ones, indicating that thicker samples are always wetter and they need more time to dry. This behaviour is consistent with that in experimental observations of drying tests of clayey samples with different thickness in the desiccation cracking study of Costa et al. (2013), suggesting that the proposed approach can physically model the water evaporation process in the experiment by applying the water loss rate to water particles.

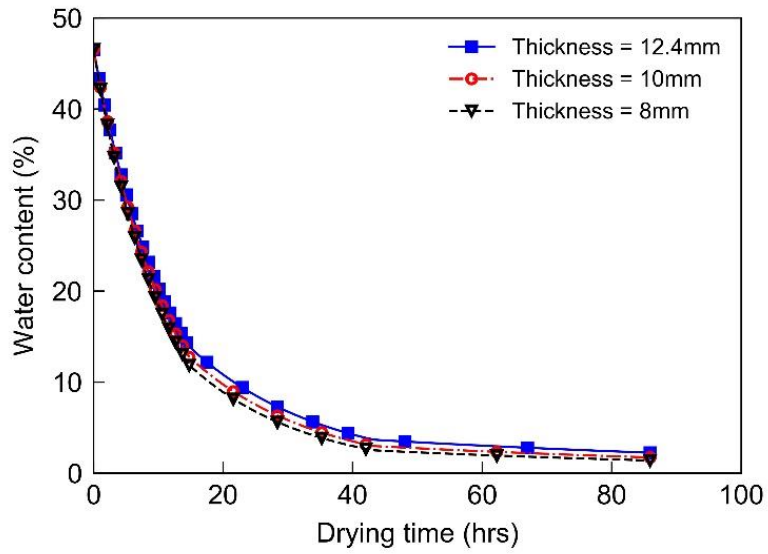


Figure 5.9. Variation of water content during drying (HR=50%).

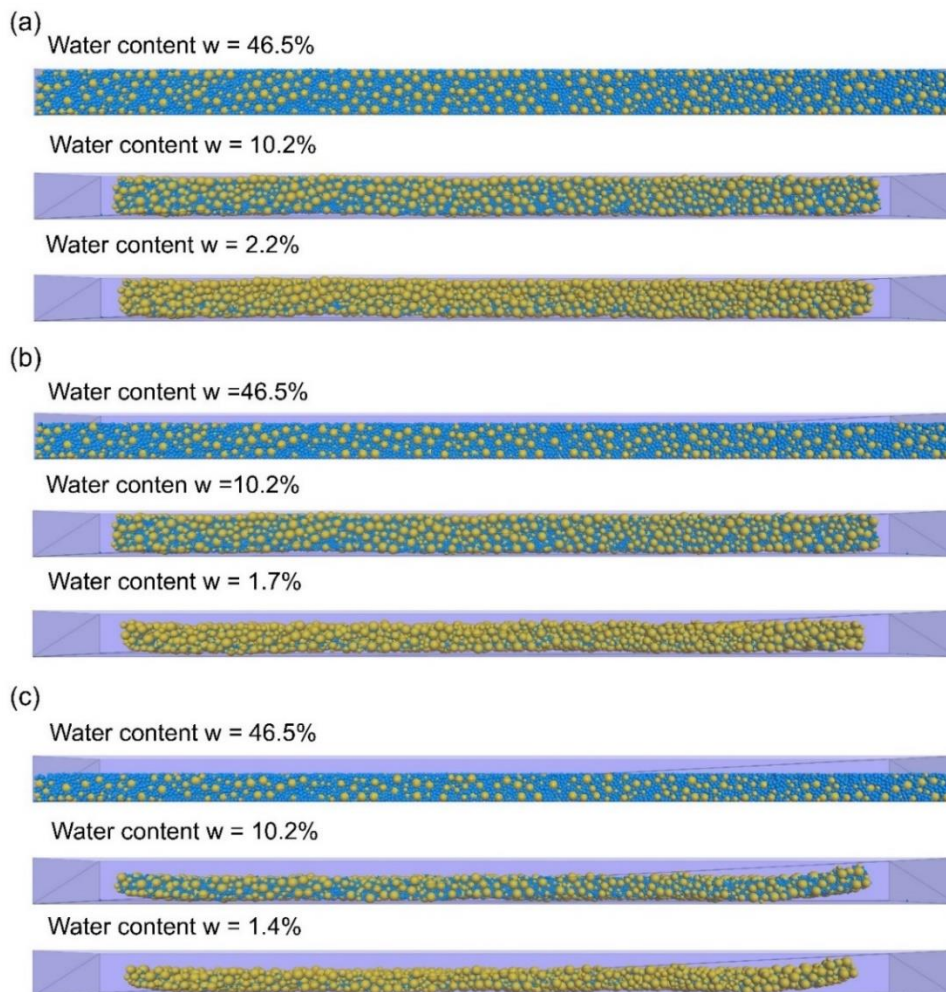


Figure 5.10. Numerical samples with different thickness at three drying stages (HR=50%): (a) sample with 12.4 mm thick; (b) sample with 10 mm thick; (c) sample with 8 mm thick.

The progressive development of shrinkage behaviour at three stages of drying in three numerical samples is plotted in Figure 5.10. It can be observed that soil curling occurred in all samples regardless of their thickness. The lift-off height developed more quickly and reached higher elevation in the thinner samples, suggesting that soil curling occurs more easily in thinner samples. This finding is consistent with field observations reported in previous studies (Kindle 1917; Longwell 1928), in which very thin soil layers could even form cylinders or cones due to excessive curling. The progressive development of the lift-off height with respect to different water contents is plotted in Figure 5.11 for the left edge of samples. The lift-off height significantly increased as water content decreased. Beyond a certain water content, samples with thickness of 12.4 mm and 10 mm experienced a temporary stable period, where the lift-off height remained almost constant, but no such period seemed to occur in the 8 mm thick sample. After this temporary stable period, the lift-off height of the 12.4 mm and 10 mm thick samples increased again. In addition, during the entire drying process, thinner samples reached higher elevations. For example, when the water content was around 10%, the lift-off height was around 3 mm for the 8 mm thick sample, while it was approximately 1.8 mm and 1.55 mm for the thicker 10 mm and 12.4 mm samples, respectively. This difference in lift-off height may be attributed to the fact that thinner samples evaporate faster, causing greater imbalance in forces within the sample, therefore facilitating the curling process (Bradley 1933; Longwell 1928). Further investigation is required to confirm this mechanism by conducting simulations with more particles. In the current application study, because of the relatively small number of particles adopted in the simulations to reduce the overall computational cost, the distribution of forces and their evolution during drying were not clearly observed in the numerical samples, and thus were not explored in depth.

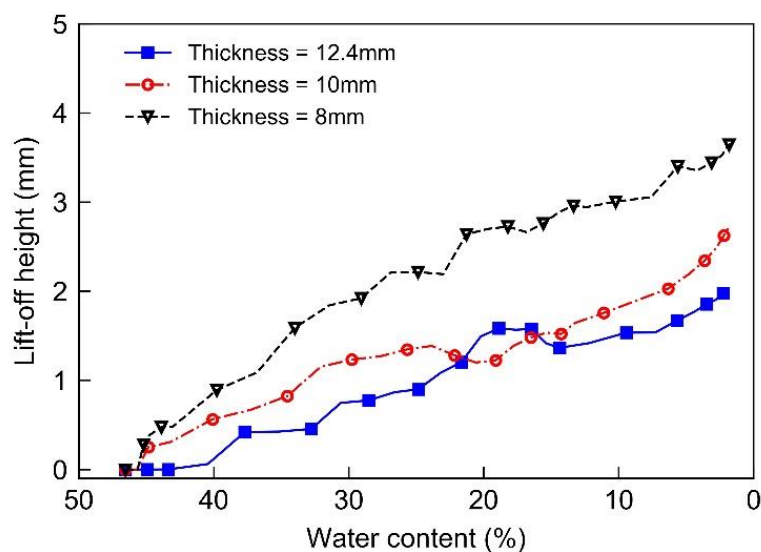


Figure 5.11. Effect of thickness of soil layer on lift-off height (HR=50%, left edge).

5.4.2. Effect of water evaporation rate

The water evaporation rate in clayey soils is one of the main factors significantly affecting soil behaviour. According to existing experimental observations (Bradley 1933; Longwell 1928), when soil layers are subjected to higher temperatures, water evaporates faster and soil layers curl more. In this study, the effect of water evaporation rate on the desiccation process, in particular, soil curling was investigated by conducting one additional numerical simulation with the evolution of water content shown in Figure 5.12(a), denoted “evaporation rate 2”. The water content dropped faster in this case, which corresponded to a higher evaporation rate than that presented in Section 5.3.4 (i.e. evaporation rate 1).

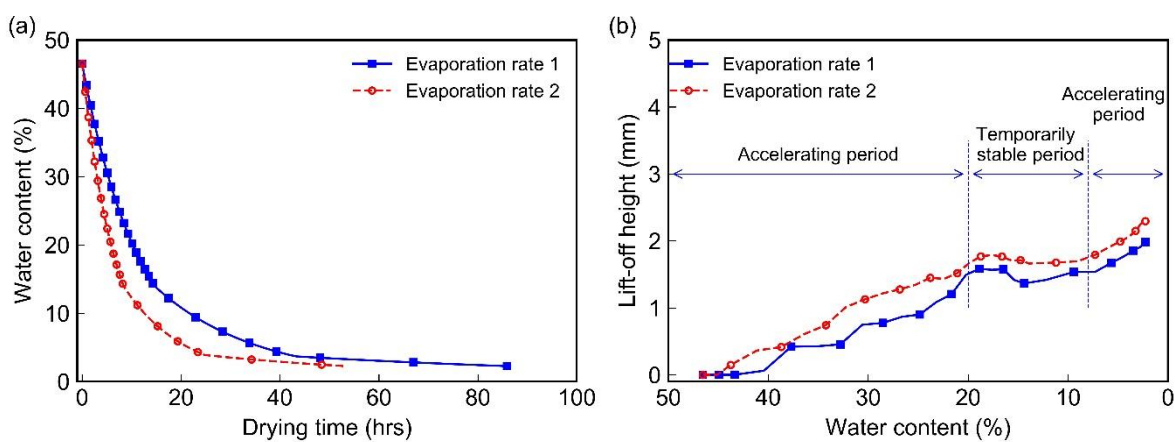


Figure 5.12. Effect of evaporation rate: (a) evolution of water content, (b) evolution of lift-off height (HR=50%, left edge).

Figure 5.12(b) shows the influence of evaporation rate on evolution of lift-off heights of the numerical samples. It can be observed that curling began earlier in the sample with higher evaporation rate, corresponding to higher water content at the beginning of soil curling. The lift-off height of these samples showed a similar trend, increasing significantly as the water content decreased after the soil curling began, and reaching a temporary stable period after the water content in the samples reduced to around 20%. The lift-off height then increased again until simulations stopped when the water content was less than approximately 8%. The trend of the lift-off height of these samples was similar to what was observed in the experiment presented in Figure 5.8 for evaporation 1. Figure 5.12 also shows that the lift-off height was always greater in samples with higher water evaporation rate. For example, after the drying of two samples finished, the lift-off heights were 1.98mm and 2.3mm for samples with evaporation rates 1 and 2, respectively. The effect of evaporation rate on soil curling in this study agrees well with observations in previous studies (Bradley 1933; Longwell 1928), where the final lift-off height of similar soil layers was reported to be more significant in summer.

The faster development of soil curling represented in the greater lift-off height of the sample with the higher water evaporation rate may be explained on the basis of capillary force development. As water evaporates faster, change in water content is larger, resulting in greater increase rate of the capillary force. Huat et al. (2006) reported that with higher loading rate, soils deformed significantly more. In addition, higher evaporation rate corresponded to greater water loss, creating more spaces for soil particles to move under the increasing capillary forces. Therefore, soil curling is more significant in this sample.

5.5. Conclusions

This chapter has presented a new DEM numerical approach for studying the desiccation process of slurry clays subjected to drying. In this approach, both soil and water are explicitly modelled using DEM particles. The interaction between two particles is modelled by a set of contact forces, which are formulated to closely represent the physical behaviour of clayey materials and to capture both the shrinkage deformation and curling behaviour of clays when they are still in the saturated condition. One key feature of the proposed approach is its ability to represent the slurry state of clays. Thus, it can describe suspended clay particles in water and capture the transition behaviour of clays from the slurry to semi-solid state as water evaporates. In addition, the new concept allows the physical drying process to be modelled by shrinking water particles with shrinkage parameters computed from experiments. The proposed approach is first validated against free shrinkage experiments conducted on Kaolin NY clay presented in Chapter 3. It is then utilised to study the influence of soil thickness and evaporation rate on soil curling. Key findings are summarised as follows:

- 1) The proposed approach can capture the shrinkage process and curling behaviour of clayey soils observed in the experiment, demonstrating its applicability to the study the curling behaviour of slurry clayey soils subjected to drying.
- 2) Sample thickness and evaporation rate have a significant influence on the soil curling process and lift-off height. This height increases with a decrease in sample thickness and with an increase in evaporation rate. The difference in lift-off height in these samples is more significant when samples are drier.
- 3) Simulation results show that the capillary forces within the sample that develop as water evaporates is the main cause behind soil curling.

This chapter reports for the first time an approach that can describe the transitional behaviour of soils from the slurry to semi-solid states, as illustrated by qualitatively capturing the curling behaviour of slurry clayey samples that underwent a desiccation process. The approach can also be employed to provide further insights into the

behaviour of saturated and unsaturated soils. However, the current study focused on demonstrating the capability of the proposed new concept for modelling soil curling. Therefore, a relatively small number of soil particles were used to reduce computational cost, and thus micromechanical insights into the soil curling process were not investigated. Further studies with a larger number of soil particles are recommended to establish a detailed mechanism of soil curling. However, these studies are out of scope of the current work. In addition, as water particles are required to have small sizes, when large scale simulations are conducted, the total number of DEM particles for both soil and water phases are huge and thus these simulations require high computational cost. Therefore, for large applications, a large-scale approach, requiring lower computational cost while still providing micromechanical insights, is necessary. In next chapters, when soil cracking is dealt with, a new large-scale approach is proposed.

Chapter 6. Modelling Unsaturated Flow through Discrete Pore-networks

6.1. Introduction

The flow through unsaturated porous media is extremely important in many fields including soil science, geotechnical engineering, agricultural engineering, environmental engineering and groundwater hydrology. In geotechnical engineering, unsaturated flow occurring in soils may result in significant changes in soil suction, water content and shear strength of soils. This can lead to significant changes in the performance of geo-infrastructure or even cause them damage. For example, the performance of soil covers used in mine tailings and waste landfills significantly deteriorates due to water evaporation; and slopes, embankments or building foundations may fail due to heavy rainfall, water evaporation or internal seepage erosion (Bui and Nguyen 2017; Hillel 2003). Thus, understanding the unsaturated flow behaviour through porous media has been an active research area over the years.

Early studies of water flow through unsaturated porous media were mainly based on the continuum methods in which the governing equations (i.e. Darcy's law and mass conservation equations (Celia et al. 1990; Hillel 2003)) were solved by using FDM, the FEM, the boundary element method (BEM), or the finite volume method (FVM) (Celia et al. 1990; Eymard et al. 1999; Feddes et al. 1988). These methods could produce reasonable results including flow paths, flow rates, and distributions of pore water pressure in the porous media. However, heterogeneous distributions of water and pore water pressure in the porous media, which occur due to random arrangement of granular particles in the porous system, cannot be achieved without ad-hoc treatments. For example, Le et al. (2012) and Le et al. (2019) combined a Monte Carlo analysis with FEM to model seepage through a heterogeneous embankment with a random porosity field. Zhang (1998) and Dagan (1993) adopted the hypotheses of an infinite flow domain and uniform mean head gradient, which rarely occur in practice, to derive solutions for unsaturated flow in heterogeneous porous media. Amir and Neuman (2001) formulated the solution of steady-state unsaturated flow in randomly heterogeneous porous media using the pressure head as a multivariate Gaussian function.

An alternative approach is DEM. This method was originally introduced by Cundall and Strack (1979) and has been widely used to investigate micro- and macro-behaviour of soils (Bui et al. 2009; Gan et al. 2013; Lee et al. 2012; Tran et al. 2011a; Tran et al. 2011b; Tran et al. 2011c; Tran et al. 2012). Subsequently, the method has been extended to simulate saturated flow through porous media by introducing a network of domains

connecting centres of solid particles (Duan et al. 2018; Itasca 2008; Shimizu et al. 2011). In this approach, water flow is assumed to occur through pipes connecting the centre of domains when there is a pressure difference between domains, and the water flow is governed by the Poiseuille equation (Duan et al. 2018; Itasca 2008; Shimizu et al. 2011). The approach has been widely used to study the micro- and macro-behaviour of permeable rocks in hydraulic fracturing applications (Duan et al. 2018; Itasca 2008; Shimizu et al. 2011). However, owing to its concept, this approach cannot be used to model unsaturated flow through porous media (Duan et al. 2018; Itasca 2008; Shimizu et al. 2011).

Recently, attempts have been made to model unsaturated flow through a discrete porous medium in DEM. In these attempts, the solid skeleton of a porous medium is represented by random packing of spherical particles (disks for 2D simulations) and the pore space of this medium is discretised as the “pore network” (Blunt et al. 1992; Kharaghani et al. 2012; Prat 2002) or “pore-scale finite volume” (Yuan and Chareyre 2017; Yuan et al. 2018). The pore network is a system of relatively large pores, connected by pipes that are segments having a minimum cross-section between pores, while the pore-scale finite volume network is a system of pore bodies that are the pore parts inside tetrahedrons generated with four vertex corners that are centres of four particles (Yuan and Chareyre 2017; Yuan et al. 2018). Water flow, which occurs between pores through pipes in the pore network or through facets of the tetrahedrons in the pore-scale finite volume network, is governed by the percolation theory (Blunt et al. 1992; Kharaghani et al. 2012; Prat 2002; Yuan and Chareyre 2017; Yuan et al. 2018). Although these attempts can provide the distribution of liquid and gas in a soil medium, they have certain limitations. For example, as the percolation theory is used, these approaches cannot model the transient unsaturated flow (Blunt et al. 1992; Kharaghani et al. 2012; Prat 2002; Yuan and Chareyre 2017; Yuan et al. 2018), which is very important in many fields mentioned above (Celia et al. 1990; Hillel 2003; Wang and Anderson 1995). Another limitation of these approaches comes from the way they define the flow network (i.e. pore network or pore-scale finite volume network). When the soil medium experiences large deformation, the flow network changes, and thus the information of liquid and gas in the new network should be updated based on the information in the initial pores and pipes. This update is a challenging and time-consuming process. As a result, up to now, to the best of our knowledge, there has been no attempt to resolve this issue, and thus these approaches are only applicable to undeformed porous media. Therefore, a robust numerical approach capable of modelling unsaturated flow through discrete porous media needs to be further developed.

In this chapter, a new approach is proposed based on DEM to simulate water flow through unsaturated discrete pore-networks. Accordingly, governing equations are derived based on the concept of water flow through the particle contact network. Thanks to this concept, the approach does not require any background mesh to model water flow, allowing the

proposed approach to handle problems involving large deformations of porous media. The illustration of these applications is presented in Chapter 7 when this approach is extended in the coupled hydro-mechanical framework for modelling soil cracking. The rest of this chapter is organised as follows. Section 6.2 presents the development of the new approach including assumptions and governing equations. This is then followed by the model validation in Section 6.3 and some modelling aspects of the proposed approach are discussed in Section 6.4. The chapter ends with the conclusions and recommendations for future work.

6.2. The Proposed Approach

In this section, general assumptions are first introduced for the water flow process through the pore network. The mathematical descriptions of this approach are then formulated together with discussions on model parameters and boundary conditions.

6.2.1. General assumptions

Consider a discrete porous medium subjected to an imbalanced flux boundary condition causing water flow through the pore network, as shown in Figure 6.1(a). At the microscopic scale, the water flow in this medium may occur through the following ways: i) flow in the pore system by air flow and vapour diffusion; ii) flow between pores and menisci, where vapour may evaporate from menisci and flow towards pores or condense towards water meniscus; iii) flow between menisci, in which water flows along the water films adhered to particles (Gili and Alonso 2002). Based on the above flow processes, the following assumptions are adopted to describe the unsaturated flow through a porous medium by DEM simulations:

- 1) The discrete porous medium (Figure 6.1(a)) can be represented by a set of solid particles, each has its own solid volume, carries the unsaturated flow information (e.g. hydraulic conductivity, volumetric water content) and occupies an equivalent continuum-space. This equivalent continuum-space can be approximated based on the volume of the solid particle and its surrounding porosity. For simplicity, solid particles are assumed to be spheres (or disks in 2D) in this article as shown in Figure 6.1(b), although this is not the key requirement.
- 2) Water flow between two particles (or two equivalent-continuum spaces) only occurs when there is a difference in their volumetric water content (or piezometric head). The flow path is assumed to take place through the contact point between two solid particles and directly from the centre of the particle with a higher water content to that of the particle with lower water content (Figure 6.1(c)). This assumption mimics the water flow process at the microscopic scale mentioned above. The author acknowledges this is a strong assumption, but it significantly

simplifies the calculation of unsaturated flow when being applied to problems involving large deformations of porous media.

3) The flow between two particles is governed by Darcy’s law (Hillel 2003):

$$\mathbf{q} = -\mathbf{K}(\theta) \cdot \nabla H = -\mathbf{D}(\theta) \cdot \nabla \theta \tag{6-1}$$

where \mathbf{q} is the water-flux vector; $\mathbf{K}(\theta)$ is the average hydraulic conductivity tensor between two particles or the macro-hydraulic conductivity; $\mathbf{D}(\theta)$ is the average diffusivity tensor between two particles or the macro-diffusivity tensor; θ is the volumetric water content and H is the piezometric head. Note that the effect of gravity is ignored when the water-flux vector is calculated based on the diffusivity and volumetric water content.

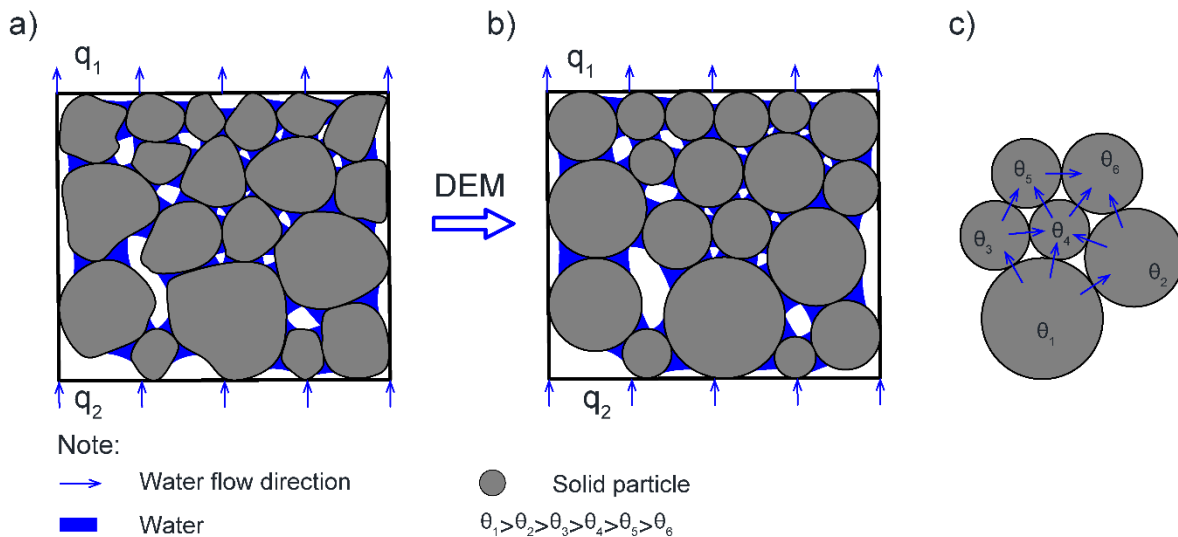


Figure 6.1. Concepts of the proposed approach: (a) porous medium and boundary conditions; (b) idealised system in DEM model; (c) water flow directions between some particles.

6.2.2. Governing equation

Considering particle i with inflows and outflows caused by the difference in volumetric water content (or piezometric head) between this particle and its neighbours (Figure 6.2). This particle has N contacts with other N particles and occupies an equivalent continuum volume V_i . By applying the mass conservation law to this particle (or the equivalent continuum volume occupied by the particle), the rate of change in the volumetric water content of this particle can be calculated as follow (Hillel 2003):

$$\frac{\partial \theta_i}{\partial t} = -\nabla \cdot \mathbf{q}_i \tag{6-2}$$

where t is the time and z denotes the vertical dimension, which is assumed to be positive in the upward direction. Equation (6-2) can be written in the hydraulic head (h) form, water content (θ) form or even in a mixed form of both hydraulic head (h) and water content (θ) (Celia et al. 1990). In this study, the governing equation in the form of water content (θ) is selected and Equation (6-2) can be rewritten by substituting Equation (6-1) into Equation (6-2) and ignoring the effect of gravity:

$$\frac{\partial \theta_i}{\partial t} = \nabla \cdot [\mathbf{D}(\theta_i) \cdot \nabla \theta_i] \quad (6-3)$$

The average water flux per unit equivalent continuum volume occupied by particle i can be expressed as follows:

$$\langle \nabla \cdot \mathbf{q} \rangle_i = \frac{1}{V_i} \int \nabla \cdot \mathbf{q}_i \, dV \quad (6-4)$$

By applying the Gauss divergence theorem, the volume integral on the right-hand-side of Equation (4) can be converted to a surface integral, so Equation (6-4) can be rewritten as:

$$\langle \nabla \cdot \mathbf{q} \rangle_i = \frac{1}{V_i} \int \mathbf{q}_i \cdot \mathbf{n}_i \, dS \quad (6-5)$$

where \mathbf{n}_i is the outward unit normal vector of the surface S of the equivalent continuum volume V_i .

Since the water flow into and out of particle is assumed to occur only through its contacts with neighbouring particles, Equation (6-5) can be written in a discrete form as follows:

$$\langle \nabla \cdot \mathbf{q} \rangle_i = \frac{1}{V_i} \sum_{j=1}^N \mathbf{q}_{ij} \cdot \mathbf{n}_{ij} \Delta S_{ij} = \frac{1}{V_i} \sum_{j=1}^N Q_{ij} \quad (6-6)$$

where N is the total number of neighbouring particles j , which are in contact with particle i at contact point c ; ΔS_{ij} is the cross-section area of the flow from particle i to particle j (or the common edge between two adjacent equivalent continuum domains); \mathbf{n}_{ij} is the outward unit normal vector of surface ΔS_{ij} ; \mathbf{q}_{ij} is the water-flux vector of particle i to particle j through their contacts c and Q_{ij} is the corresponding discharge rate of water flow from particle i to particle j .

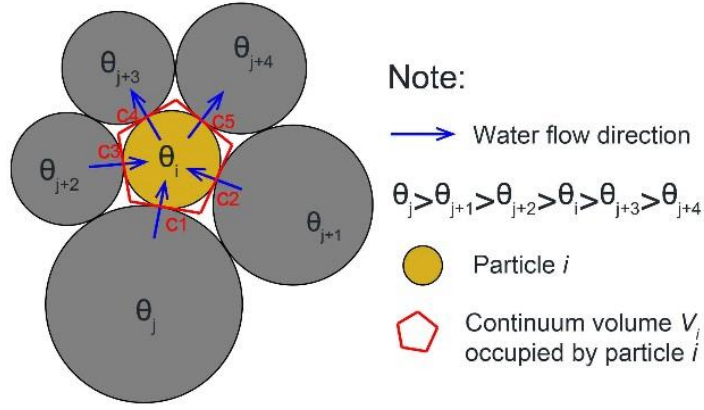


Figure 6.2. Inflows and outflows through particle i (or through an imaginary equivalent V_i continuum volume occupied by particle i).

The water-flux vector and discharge rate of particle i to its neighbours across the contact c that appear in Equation (6-6) can be calculated using Darcy's law as follows, respectively:

$$\mathbf{q}_{ij} = -d_{ij} \frac{\Delta\theta_{ij}}{L_{ij}\Delta S_{ij}} \mathbf{n}_{ij} \quad (6-7)$$

$$Q_{ij} = \mathbf{q}_{ij} \cdot \mathbf{n}_{ij} \Delta S_{ij} = -d_{ij} \frac{\Delta\theta_{ij}}{L_{ij}} \quad (6-8)$$

where $\Delta\theta_{ij}$ and d_{ij} are the water content difference and the inter-particle diffusivity between particles i and j respectively, and L_{ij} is the distance between the centres of two particles. The inter-particle diffusivity d_{ij} between particles i and j should be distinguished from the micro-diffusivity of each particle (i.e. d_i or d_j), which will be discussed in the next section.

By substituting Equations (6-6) and (6-8) into Equation (6-2), the rate of change in volumetric water content of particle i can be now calculated as follows:

$$\frac{\partial\theta_i}{\partial t} = \frac{1}{V_i} \sum_{j=1}^N d_{ij} \frac{\Delta\theta_{ij}}{L_{ij}} \quad (6-9)$$

The above equation can be solved using different numerical techniques. In this work, the forward finite-difference approximation scheme is applied and the volumetric water content $\theta_i^{t+\Delta t}$ of particle i at time $t + \Delta t$ can be computed as follows:

$$\theta_i^{t+\Delta t} = \theta_i^t + \Delta t \left(\frac{1}{V_i} \sum_{j=1}^N d_{ij} \frac{\Delta\theta_{ij}}{L_{ij}} \right) \quad (6-10)$$

To close this equation, the inter-particle diffusivity d_{ij} at time t between particles i and j is required and this is discussed in the following section.

6.2.3. The inter-particle diffusivity

In this section, mathematical equations that link the macro-diffusivity $\mathbf{D}(\theta_i)$ to the inter-particle diffusivity d_{ij} are derived. First, an equation for calculating the micro-diffusivity of particle i (d_i) is derived by considering an average water flux per unit equivalent continuum volume occupied by particle i . This average water flux can be calculated as follows:

$$\langle \mathbf{q} \rangle_i = \frac{1}{V_i} \int \mathbf{q}_i dV \quad (6-11)$$

By considering water flux from the particle centre to its points of contact with neighbouring particles (or from the centre of the equivalent continuum volume to its edges and vice-versa), the discretised form of the above equation can be rewritten as follows:

$$\langle \mathbf{q} \rangle_i = \frac{1}{V_i} \sum_{c=1}^N \mathbf{q}_{ic} \Delta S_{ic} l_{ic} \quad (6-12)$$

where l_{ic} is the distance from the centre of particle i to its contact c (see Figure 6.2); \mathbf{q}_{ic} is the water-flux vector of particle i through its contacts c . This flux can be computed if micro-diffusivity of particle i (d_i) and the water content difference between the particle centre and its interface at contact c ($\Delta\theta_{ic}$) are known:

$$\mathbf{q}_{ic} = -d_i \frac{\Delta\theta_{ic}}{l_{ic} \Delta S_{ic}} \mathbf{n}_{ic} \quad (6-13)$$

The water content difference ($\Delta\theta_{ic}$) can be computed based on the distance l_{ic} and the water content gradient $\nabla\theta_i$ as follow:

$$\Delta\theta_{ic} = l_{ic} \mathbf{n}_{ic} \cdot \nabla\theta_i \quad (6-14)$$

Substituting Equations (6-13) and (6-14) into Equation (6-12) the average water flux in particle i is:

$$\langle \mathbf{q} \rangle_i = -\frac{1}{V_i} \sum_{c=1}^N d_i \mathbf{n}_{ic} \otimes \mathbf{n}_{ic} l_{ic} \cdot \nabla\theta_i \quad (6-15)$$

By comparing the water flux vector in particle i calculated by using Equation (6-1) and Equation (6-15), to ensure this vector is equal, the following relationship between the micro-diffusivity and the macro-diffusivity of particle i can be obtained:

$$d_i \sum_{c=1}^N \mathbf{n}_{ic} \otimes \mathbf{n}_{ic} l_{ic} = \mathbf{D}(\theta_i) V_i \quad (6-16)$$

If the material properties at the equivalent continuum domain occupied by particle i are homogeneous and isotropic (i.e. $D(\theta_i)_{xx} = D(\theta_i)_{yy} = D(\theta_i)_{zz} = D(\theta_i)$), the following equation can be therefore derived from Equation (6-16):

$$d_i \sum_{c=1}^N l_{ic} = [D(\theta_i)_{xx} + D(\theta_i)_{yy} + D(\theta_i)_{zz}] V_i \quad (6-17)$$

The micro-diffusivity of particle i in 2D and 3D dimensions can be now computed as follows, respectively:

$$d_i = \frac{2D(\theta_i)V_i}{\sum_{c=1}^N l_{ic}} \quad (6-18)$$

$$d_i = \frac{3D(\theta_i)V_i}{\sum_{c=1}^N l_{ic}} \quad (6-19)$$

Finally, the inter-particle diffusivity d_{ij} between particles i and j associated with the contact c can be calculated by either the harmonic mean:

$$d_{ij} = \frac{2d_i d_j}{d_i + d_j} \quad (6-20)$$

or by the geometric mean and arithmetic mean, respectively:

$$d_{ij} = (d_i d_j)^{0.5} \quad (6-21)$$

$$d_{ij} = \frac{d_i + d_j}{2.0} \quad (6-22)$$

The geometric mean and arithmetic mean have been widely used to calculate the hydraulic conductivity and diffusivity between elements in the finite difference method or the finite element method (Berg 1999; Haverkamp and Vauclin 1979; Zaidel and Russo 1992) as these averages provide flexibility and precision for simulating unsaturated flow (Haverkamp and Vauclin 1979). However, only the harmonic mean can be derived from physical arguments (Berg 1999). Therefore, the inter-particle diffusivity d_{ij} calculated by the harmonic mean is employed in the remainder of this chapter, except for Section 6.4.1

where the other averages are also used to study the effect of the inter-particle diffusivity calculation methods on numerical results. In addition, as illustrated in Equations (6-18)-(6-22), the inter-particle diffusivity d_{ij} is a function of water content, and thus it is necessary to update this parameter every running step during simulations to calculate the corresponding volumetric water content $\theta_{t+\Delta t}$ at time $t + \Delta t$. To reduce the computational cost, the inter-particle diffusivity can be updated after every n computing cycles during m running steps ($n \ll m$). The effect of the updating cycles on numerical results is investigated in Section 6.4.2.

6.2.4. Numerical time-step

As discussed in the previous section, the water content ($\theta_i^{t+\Delta t}$) of particle i at time $t + \Delta t$ is calculated from the water content at time t (θ_i^t) by using the forward finite-difference approximation as presented in Equation (6-10), and thus the numerical time-step (Δt) should be less than or equal to a limited time-step to ensure the convergence of numerical solution. To find the limited time-step, we now consider a scenario in which a particle i with a water content of θ_i^t at time t is in contact with other N particles which have zero water content ($\theta_j^t = 0$). As the water content of particle i is higher than that of its neighbours, water flows from particle i to its neighbours, and thus the water content of particle i after one numerical time step from t to $t + \Delta t$ can be computed as follows:

$$\theta_i^{t+\Delta t} = \theta_i^t + \Delta t \left(\frac{1}{V_i} \sum_{j=1}^N \frac{d_{ij}}{L_{ij}} \Delta \theta_{ij} \right) = \theta_i^t - \Delta t \left(\frac{1}{V_i} \sum_{j=1}^N \frac{d_{ij}}{L_{ij}} \theta_i^t \right) \quad (6-23)$$

The water content of particle i at $t + \Delta t$ ($\theta_i^{t+\Delta t}$) must be always positive or equal zero if all water in this particle drains out to its neighbours. Accordingly, the following condition must be satisfied:

$$\theta_i^t - \Delta t \left(\frac{1}{V_i} \sum_{j=1}^N \frac{d_{ij}}{L_{ij}} \theta_i^t \right) \geq 0 \quad (6-24)$$

By rearranging Equation (6-24), the following limiting condition for the time-step is required to ensure the numerical stability of the approach:

$$\Delta t \leq \frac{V_i}{\sum_{j=1}^N \frac{d_{ij}}{L_{ij}}} \quad (6-25)$$

Accordingly, for a porous medium consisting of many particles, the numerical time-step should be the minimum value calculated by using Equation (6-25) for all particles.

6.2.5. Boundary conditions

Two different types of boundary conditions are used in modelling unsaturated flow, including: 1) Dirichlet type where the water pressure head is known and 2) Neumann type where the water flux is known (Wang and Anderson 1995; Zaradny 1978). In the proposed approach, these boundary conditions are directly applied to particles. For the Dirichlet type, the known pressure head is first converted to the water content by using the soil water retention curve. This water content is then applied to particles located on this boundary and its magnitude remains unchanged during the simulation process. For the Neumann type boundary, the water flux is simply converted to the discharge rate for each particle on the boundary taking into consideration of the equivalent continuum area occupied by each particle. This discharge rate can be calculated as follows:

$$Q_j = \frac{qSA_j}{\sum_{j=1}^M A_j} \quad (6-26)$$

where Q_j is the discharge rate of particle j on the boundary; q is the water flux on the boundary; S is the surface area of the boundary; M is the number of particles on the boundary; A_j is the area of the cross-section of particle j . The discharge rate Q_j is then applied to particle j by adding this discharge rate into equation (10) when this equation is solved.

6.2.6. Hydraulic properties

For simulations of water flow through unsaturated porous media, the soil water retention curve and hydraulic conductivity curve are commonly required (Celia et al. 1990; Hillel 2003). The soil water retention curve is used to calculate the volumetric water content θ when the pressure head h is known and vice versa (Celia et al. 1990; Hillel 2003), while both curves are used to estimate the hydraulic conductivity $K(\theta)$ and diffusivity $D(\theta)$ of the media at any pressure head h . In this chapter, these curves are employed when the inter-particle diffusivity d_{ij} used in Equation (6-10) is calculated. To facilitate the calculation process, the van Genuchten model (Van Genuchten 1980a) is adopted and is presented by the following equations:

$$S_e = \frac{\theta - \theta_r}{\theta_s - \theta_r} = \frac{1}{[1 + (\alpha|h|)^n]^{1-\frac{1}{n}}} \quad (6-27)$$

$$K(\theta) = K_s S_e^{\frac{1}{2}} \left[1 - \left(1 - S_e^{\frac{n}{n-1}} \right)^{1-\frac{1}{n}} \right]^2 \quad (6-28)$$

where S_e is the effective saturation; θ_s is the saturated volumetric water content; θ_r is the residual water content; h is the pressure head; α , n and m are curve fitting parameters;

$K(\theta)$ is the hydraulic conductivity at the pressure head or the water content and K_s is saturated hydraulic conductivity.

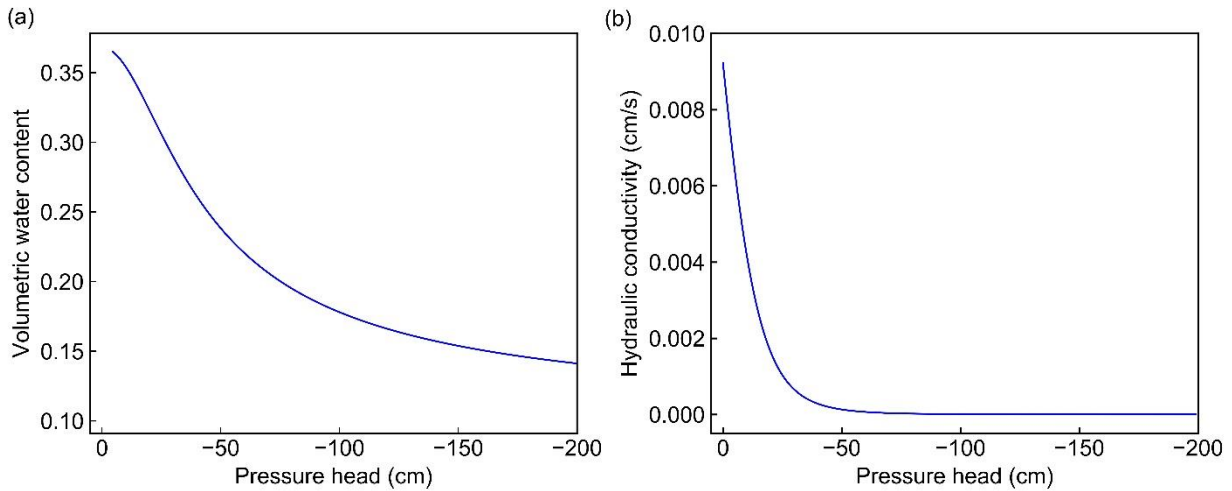


Figure 6.3. Hydraulic properties of an unsaturated porous medium: (a) soil water retention curve; (b) hydraulic conductivity curve.

The diffusivity $D(\theta)$ at the pressure head h or the water content θ is then calculated as the following equation (Van Genuchten 1980a):

$$D(\theta) = \frac{(1-m)K_s}{\alpha m(\theta_s - \theta_r)} S_e^{\frac{1}{2} - \frac{1}{m}} \left[\left(1 - S_e^{\frac{1}{m}}\right)^{-m} + \left(1 - S_e^{\frac{1}{m}}\right)^m - 2 \right] \quad (6-29)$$

Figure 6.3 shows an example of a soil water retention curve and hydraulic conductivity curve for a porous medium with a saturated volumetric water content θ_s of 0.368, a residual water content θ_r of 0.102, a saturated hydraulic conductivity K_s of 0.00922cm/s and curve fitting parameters α , n and m of 0.0335, 2.0 and 0.5, respectively.

6.3. Numerical Validation

In this section, the proposed approach is used to predict infiltration and evaporation of water from an unsaturated soil column under different boundary conditions. The results are compared against those obtained by the standard FDM.

6.3.1. Infiltration tests

The proposed approach is first examined by simulating water flow in a 2.0 cm unsaturated soil column subjected to vertical infiltration under different boundary conditions. The model geometry and boundary conditions are first presented, followed by the discussion of numerical results.

6.3.1.1. Model geometry and boundary conditions

Simulations of the water infiltration process were conducted on a 2cm tall soil column. Soils used in these tests were assumed to be homogenous and isotropic with an initial volumetric water content of $\theta_{int} = 0.15$, a saturated hydraulic conductivity of $K_s = 0.00922 \text{ cm/s}$, a saturated volumetric water content of $\theta_s = 0.368$ and a residual water content of $\theta_r = 0.102$. Their soil water retention and hydraulic conductivity curves were described by the Van Genuchten model as discussed in Section 6.2.6 with the curve fitting parameters α , n and m of 0.0335, 2.0 and 0.5, respectively (Celia et al. 1990).

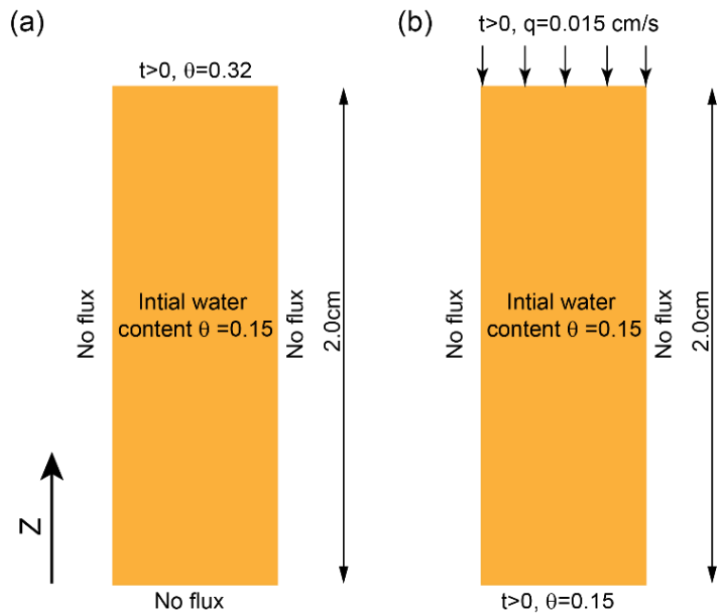


Figure 6.4. Boundary conditions of infiltration tests: (a) constant water content boundary; (b) constant flux boundary.

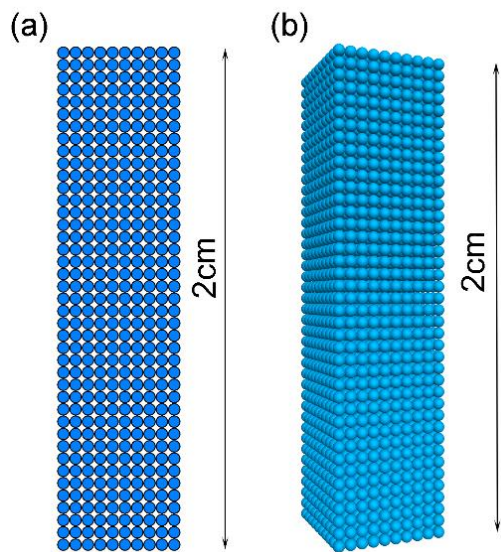


Figure 6.5. DEM model discretisation with cubic packing: (a) 2D model; (b) 3D model.

This soil column was tested for two different boundary conditions (i.e. constant water content and constant infiltration rate), which are commonly used in the literature (Haverkamp et al. 1977; Parlange 1971; Philip 1957). In the first constant water content infiltration test, an initial water content of 0.32 was prescribed at the top of the soil column and kept constant during the computation, while a zero flux condition was applied to the sides and bottom of the soil column (Figure 6.4(a)). In the second test, a constant flux of 0.015 cm/s was imposed on the top of the soil column, while a water content of 0.15 was maintained at the bottom of the column and a zero flux was applied to the sides (Figure 6.4(b)).

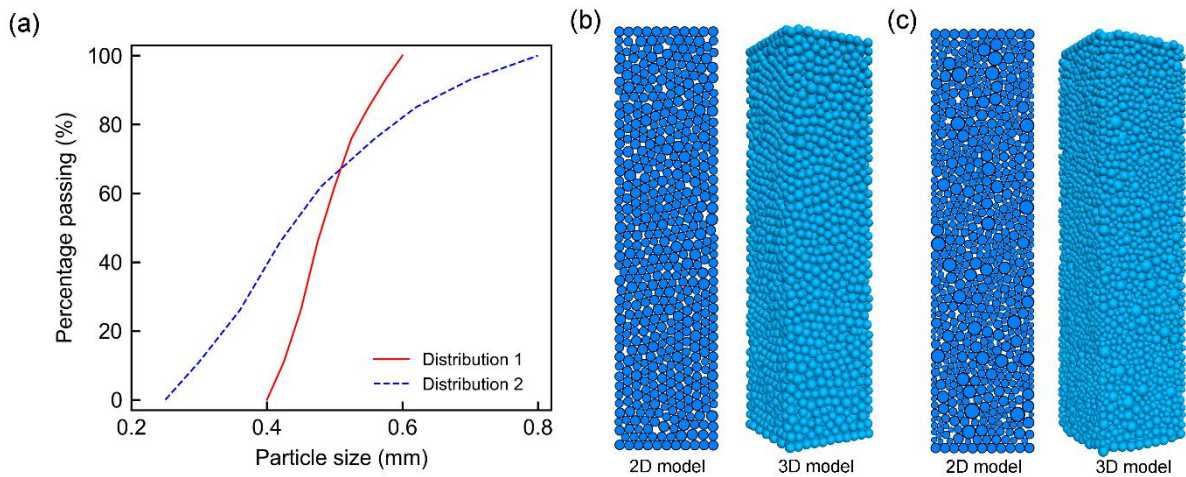


Figure 6.6. DEM model discretisation with random packing: (a) particle size distribution; (b) 2D and 3D models with the particle size distribution 1; (c) 2D and 3D models with the particle size distribution 2.

The infiltration process was then simulated using the proposed approach, hereafter called DEM simulations. The soil medium was first discretised by using two types of particle packing: uniform packing and random packing. The uniform packing was used for a detailed comparison with the results obtained by FDM, while the random packing was used to examine the effect of domain discretisation on the performance of the proposed approach. For the uniform packing, a square lattice of DEM particles with a uniform particle size of 0.5 mm was employed to create a numerical domain of 2 cm in height and 0.5 cm in other directions, which had no influence on the current 1D infiltration, as illustrated in Figure 6.5 for 2D and 3D DEM simulations. For the random packing, the same soil column was discretised with two different particle size distributions as shown in Figure 6.6(a). The total number of particles was 517 and 712 disks for distribution 1 and distribution 2 in 2D simulations, and 6242 and 10946 spheres for distribution 1 and distribution 2 in 3D simulations (Figure 6.6(b) and Figure 6.6(c)), respectively. All DEM simulations were then run with the boundary conditions described above and a time-step of 2.0×10^{-5} s corresponding to 50000 steps to achieve a testing time of 1 s. During 50000 running steps, the inter-particle diffusivity was updated only 2500 times. For FDM

simulations, the soil medium was first discretised with 0.5mm elements and they were then run with very small time-step to ensure stable and good results (Celia et al. 1990).

6.3.1.2. Results of infiltration test with the constant water content boundary

Figure 6.7(a) shows a comparison of the time-evolution of water content profile developed in the soil column obtained by FDM and DEM simulations with cubic packing. It can be observed that progressive development of the wetting front towards the bottom of the column was well described in all simulations. As the simulation progressed, the water content in the soil column along the vertical direction increased. For locations near the top surface, the water content increased immediately after initiation of the test, while for deeper locations, the increment of water content was slightly delayed. After approximately 10s, the water content at the bottom of the column started increasing and continuously developed until the end of the test. Figure 6.7(a) also shows that there was no difference in the 2D and 3D DEM simulation results and they agreed well with those obtained from FDM simulations. This confirms that the proposed approach works well for both 2D and 3D simulations and the approach can predict well unsaturated flow in 1D condition.

To highlight the difference between results of the two methods, the relative error was calculated and plotted in Figure 6.7(b). Greater error occurred mainly around the wetting front where the water content traversed the initial water content, while it was almost zero everywhere else. This error near the wetting front may be attributed to a significant difference in hydraulic conductivity in the wetting zone and lack of an iteration process. Note that error between two methods is always inevitable and can still be large when results of the FDM and FEM are compared (Gottardi and Venutelli 1993). By carefully looking at Figure 6.7(b), it can be observed that error of most locations along the soil column was negative, demonstrating that the proposed method slightly underestimates the water distribution in the unsaturated soil column. This may be attributed to the fact that the effect of gravity on flow in the proposed method is ignored as compared to that of FDM. However, the error was small and it significantly decreased as the simulation progressed. For example, the maximum value was 2.7% at 3s while it was 1.1% after 10s. This again confirms that the approach is able to predict water flow in unsaturated soils, in particular in an infiltration test with a constant water content boundary, with acceptable error.

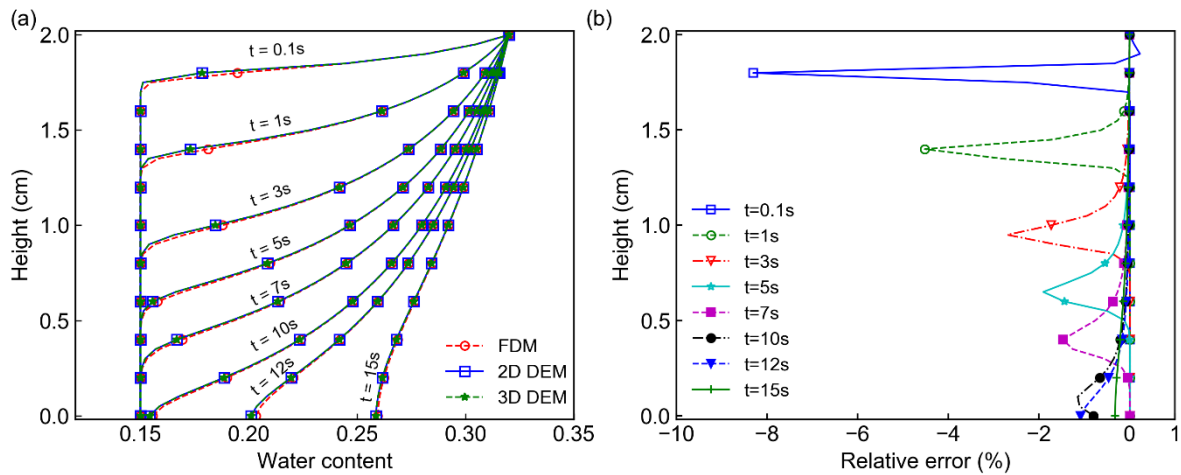


Figure 6.7. Numerical results obtained from the FDM simulation and DEM simulations with cubic packing for the test with the constant water content boundary: (a) water content profile of the soil column; (b) relative error.

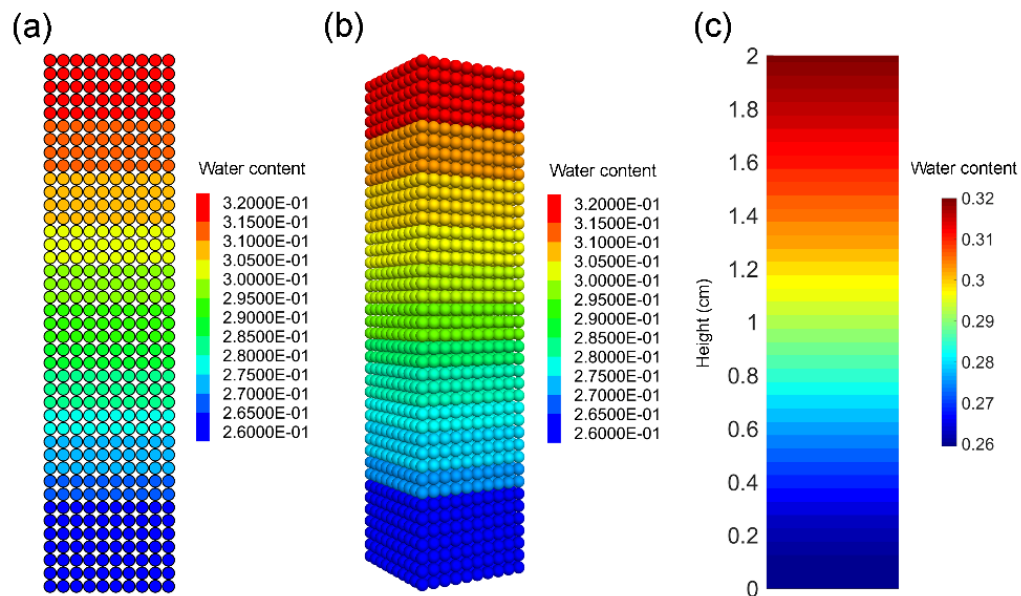


Figure 6.8. Water distribution in the soil column after 15s due to infiltration with the constant water content boundary: (a) 2D DEM simulation with cubic packing; (b) 3D DEM simulation with cubic packing; (c) FDM simulation.

Figure 6.8 shows a comparison between DEM and FDM for the distribution of water content in the soil column after 15s water infiltration. It can be observed that in all simulations, water content at every location increased from the initial value. However, the greater the depth, the lower the water content, revealing that water moved downwards from the soil surface. This was consistent with the boundary condition applied to the test, in which water was supplied from the soil surface. Figure 6.8 also shows that particles at the same depth in DEM simulations possessed the same water content, which can be attributed to the uniform arrangement of DEM particles with the same particle size in the simulations.

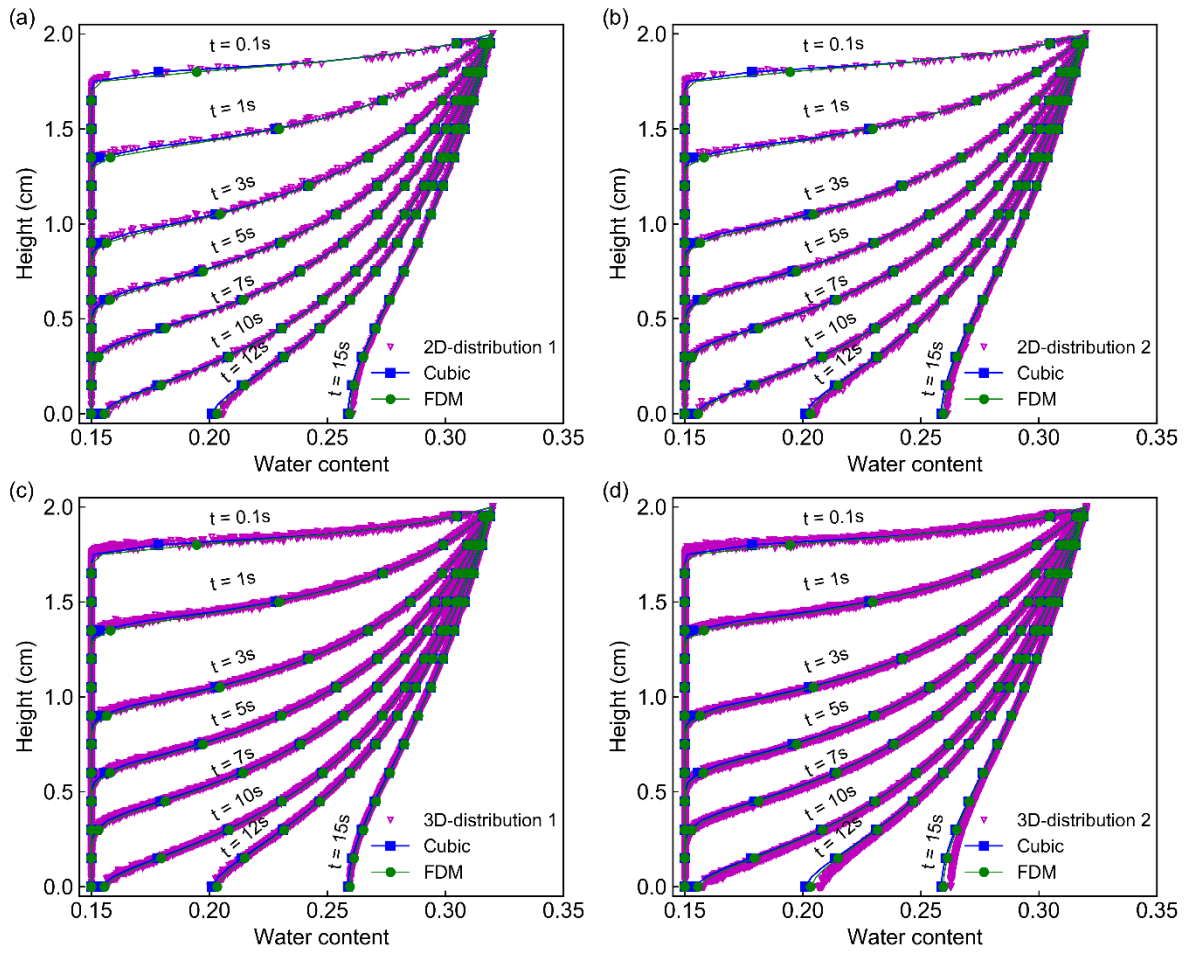


Figure 6.9. Water content profiles of the soil column due to infiltration with the constant water content boundary: (a) 2D DEM simulation with particle distribution 1, (b) 2D DEM simulation with particle distribution 2, (c) 3D DEM simulation with particle distribution 1, (d) 3D DEM simulation with particle distribution 2.

Figure 6.9 shows the water content profile of the soil column obtained from the DEM simulations for two particle-size distributions at several time intervals. These water content profiles were obtained by plotting the water content of every particle used to represent the simulation domain. Results of FDM and DEM simulations with cubic packing were also included for comparison. As the testing time passed, the water content increased and progressed towards the base of the soil column. This process started immediately at locations near the column surface, while it was slightly delayed for deeper locations. The DEM results were similar regardless of particle distributions and types of particle packing, and they agreed well with FDM results. This good agreement is because the SWRC and hydraulic conductivity curve are only main parameters influencing water flow, and in this work, these curves are kept the same in all simulations in order to examine the influence of spatial discretisation or particle arrangement on predicted results. The data presented in Figure 6.9 confirm the capability of the proposed approach in capturing unsaturated flow when the domain is described with different types of packing and particle distribution.

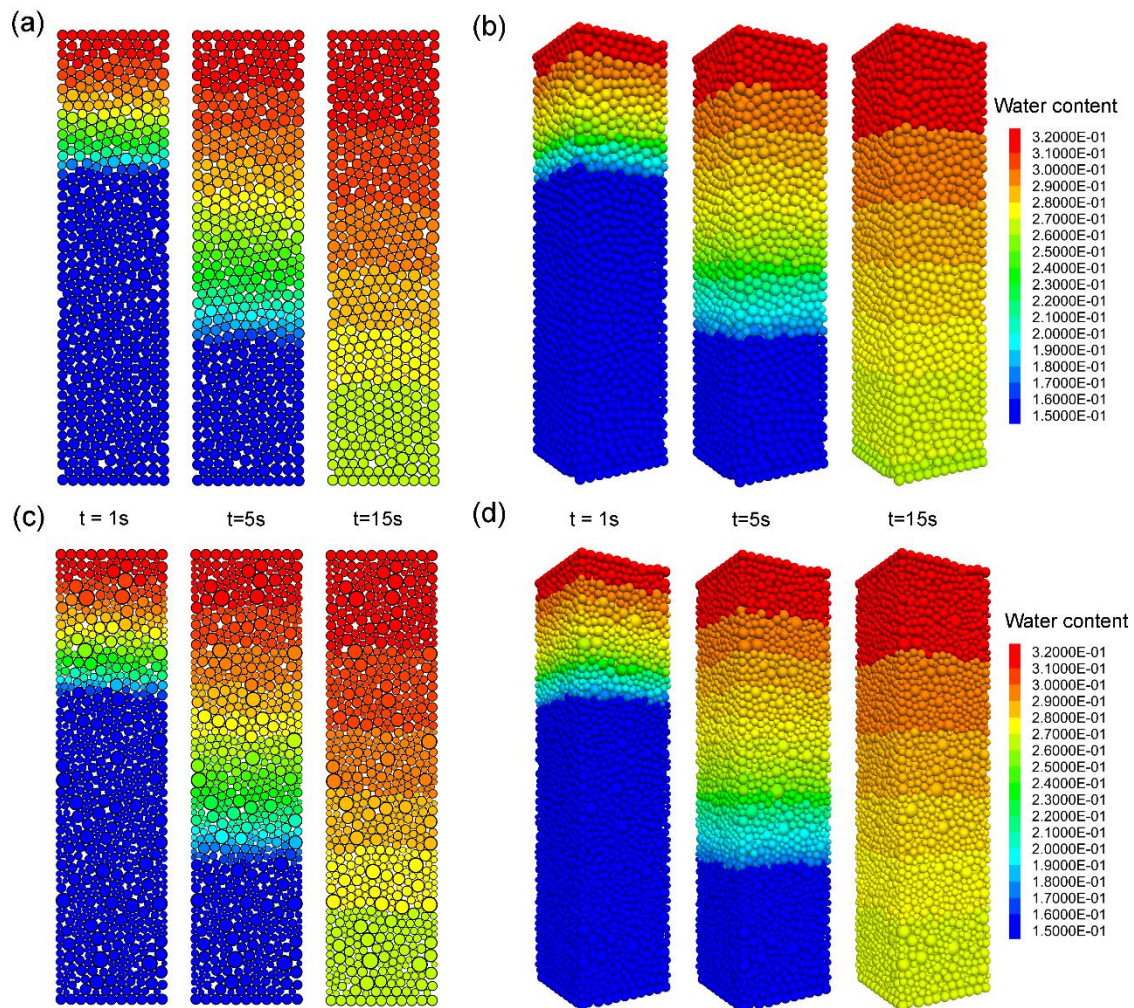


Figure 6.10. Water distribution in the soil column during infiltration with the constant water content boundary: (a) 2D simulation with particle distribution 1; (b) 3D DEM simulations with particle distribution 1; (c) 2D simulation with particle distribution 2; (d) 3D DEM simulations with particle distribution 2.

Figure 6.10 shows the progressive development of wetting front in the DEM specimens at several time intervals for cases of random packing with different particle-size distributions. The results showed a consistent wetting front propagation as well as the profile of water content between 2D and 3D simulations and between two types of particle-size distributions. As time passed, more water infiltrated to the soil column, causing the wetting front to propagate towards the base of the soil column. For example, after 1s of infiltration, the wetting front moved from the soil surface to one-third of the height of the soil column, while after 5s, the wetting front moved to two-thirds of the height. Consequently, water content increased at locations above the wetting front. After 15s, water content increased from 0.15 to around 0.32 at locations from the soil surface to around one-third height of the column and the water content increased from 0.15 to 0.26 at locations near the bottom of the column. Figure 6.10 also shows that at the same depth, the water contents in all simulations were similar because the same SWRC and hydraulic conductivity curves were used in the simulations. In addition, the water content

was randomly distributed along the width of the soil column, due to discretisation of the domain using particles in the proposed method. Figure 6.10 again confirms the capability of the proposed approach in predicting water flow through porous media.

6.3.1.3. Results of infiltration test with the constant flux boundary

Changes in water content at different depths in the infiltration test with the constant flux boundary are plotted in Figure 6.11(a). The DEM results plotted in this figure were obtained from simulations using cubic packing. It can be observed that these changes depended on both elapsed time and location. During the test, the water content at all locations increased, for example from 0.15 to around 0.323 at $z = 2\text{cm}$ and from 0.15 to approximately 0.18 at $z = 0.25\text{cm}$. However, the increase of water content at deeper locations was delayed. For example, the water content at $z = 1.7\text{cm}$ started increasing after approximately 1s, while it changed after 10s at 0.5cm. In addition, the water content at shallower locations was always larger. This behaviour results from the condition of the test where water is supplied from the soil column surface, and thus it takes more time for water to move to deeper locations. Figure 6.11(a) also shows that the 2D DEM results perfectly matched the 3D DEM results, while they were slightly different from the FDM results. To quantify the difference between the DEM and FDM results, the relative error is plotted in Figure 6.11(b). It can be seen that the maximum error was less than 4.5%, suggesting that the DEM results were very close to the FDM results. The error may be due to the ignoring of the effect of gravity on flow and the lack of an iteration process when equation (2) is solved in DEM.

Figure 6.12 presents the water content profiles of the soil column obtained from all DEM simulations and the FDM simulation. It can be seen that the proposed approach successfully captures the development of water content along the soil column regardless of the domain discretisation in DEM simulations. At the beginning of the test, the water content of particles near the soil surface increased significantly. This gradually slowed down after 10s elapsed time. However, the increase in water content at deeper locations was retarded. For example, water content at $z = 1.7\text{cm}$ started to increase after approximately 1s, while this increase at $z = 1\text{cm}$ occurred after 5s. Figure 6.12 also shows that during the test, the wetting front moved towards the bottom surface of the soil column, reaching the base after approximately 15s. In addition, all DEM simulation results were quite close to the FDM results regardless of the types of particle packing and particle distributions. The good agreement between DEM and FDM results again demonstrates that the proposed approach is a good method to predict water flow in unsaturated discrete porous media.

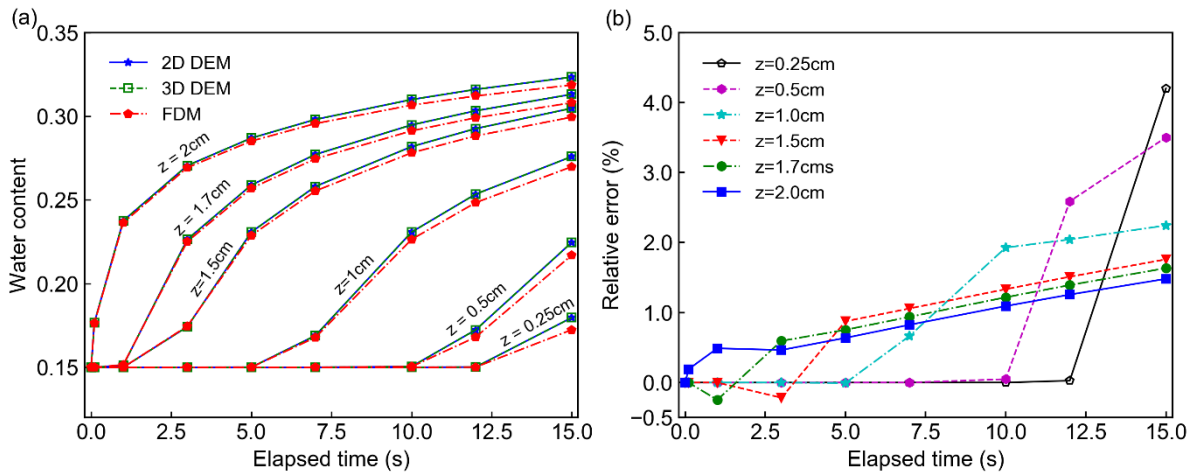


Figure 6.11. Numerical results obtained from the FDM simulation and DEM simulations with cubic packing for the infiltration test with the constant flux boundary: (a) water content at different depths; (b) relative error.

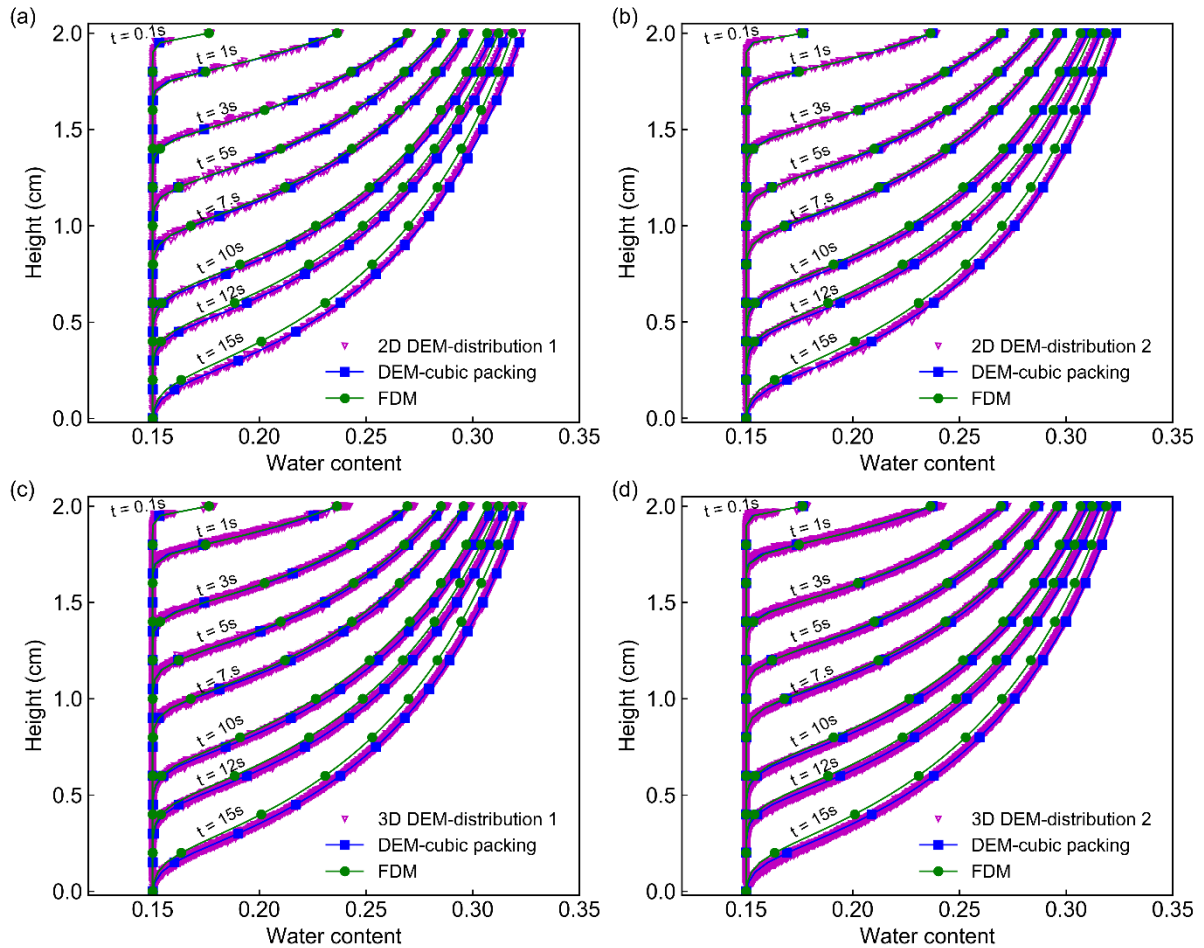


Figure 6.12. Water content profiles of the soil column due to infiltration with the constant flux boundary: (a) 2D DEM simulation with particle distribution 1, (b) 2D DEM simulation with particle distribution 2, (c) 3D DEM simulation with particle distribution 1, (d) 3D DEM simulation with particle distribution 2.

Figure 6.13 shows the water content distribution in the soil column after 15s due to infiltration with the constant flux boundary. It can be observed that all simulations showed a similar distribution of water. After 15s, the water content at every location increased from the initial value, except for the locations at the bottom of the soil column where the water content was kept constant. However, the shallower the locations, the higher the water content. This behaviour is due to water being supplied from the soil surface. Figure 6.13 also shows that at the same depth, water content along the width of the soil column obtained from the simulations with random packing was randomly distributed, while water content obtained from the DEM simulations with cubic packing was the same. These results again confirm the capability of the method in simulating of heterogeneous water flow.

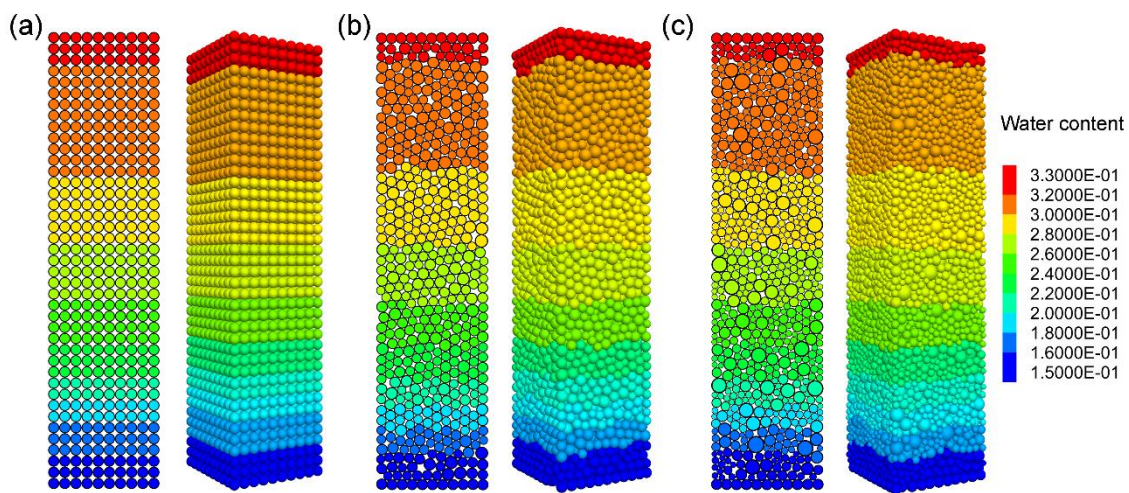


Figure 6.13. Water distribution in the soil column after 15s due to infiltration with the constant flux boundary: (a) 2D and 3D DEM simulations with cubic packing; (b) 2D and 3D DEM simulations with particle distribution 1; (c) 2D and 3D DEM simulations with particle distribution 2.

6.3.2. Evaporation test

In this section, performance of the proposed approach in the case of losing water was validated by conducting simulations for a water evaporation test of an unsaturated soil column. The soil column had a height of 2.0cm and an initial water content of 0.32. During the test, the soil column was dried from the surface with a constant flux of 0.01cm/s, while zero flux was maintained at other faces. The soil column was assumed to be homogenous and isotropic with identical properties used in the infiltration tests presented in Section 6.3.1. DEM simulations were carried out for the domain discretised by cubic packing of 0.5mm particles and random packing of particle-size distributions 1 and 2 for the infiltration tests.

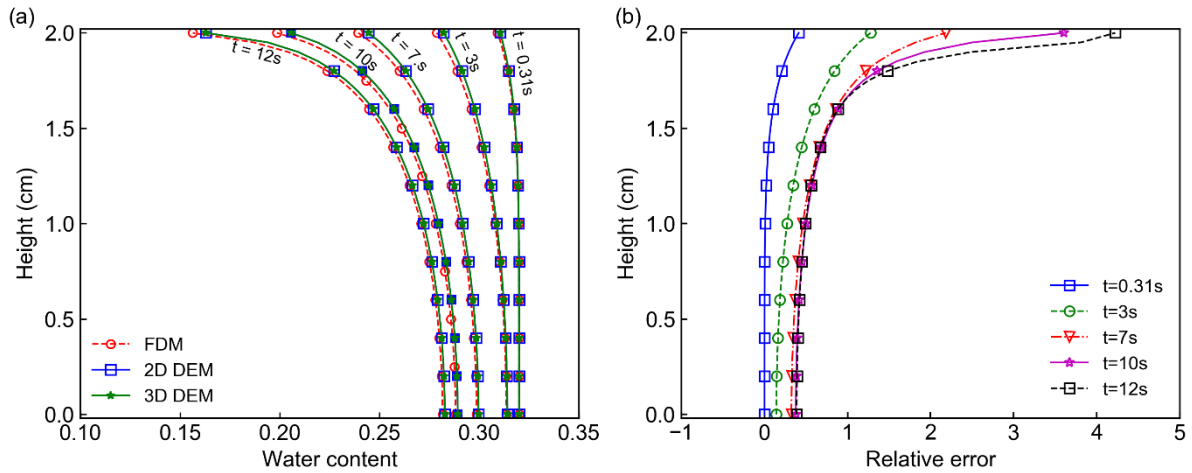


Figure 6.14. Numerical results of the evaporation test obtained from the FDM simulation and DEM simulations with cubic packing: (a) water content profile; (b) relative error.

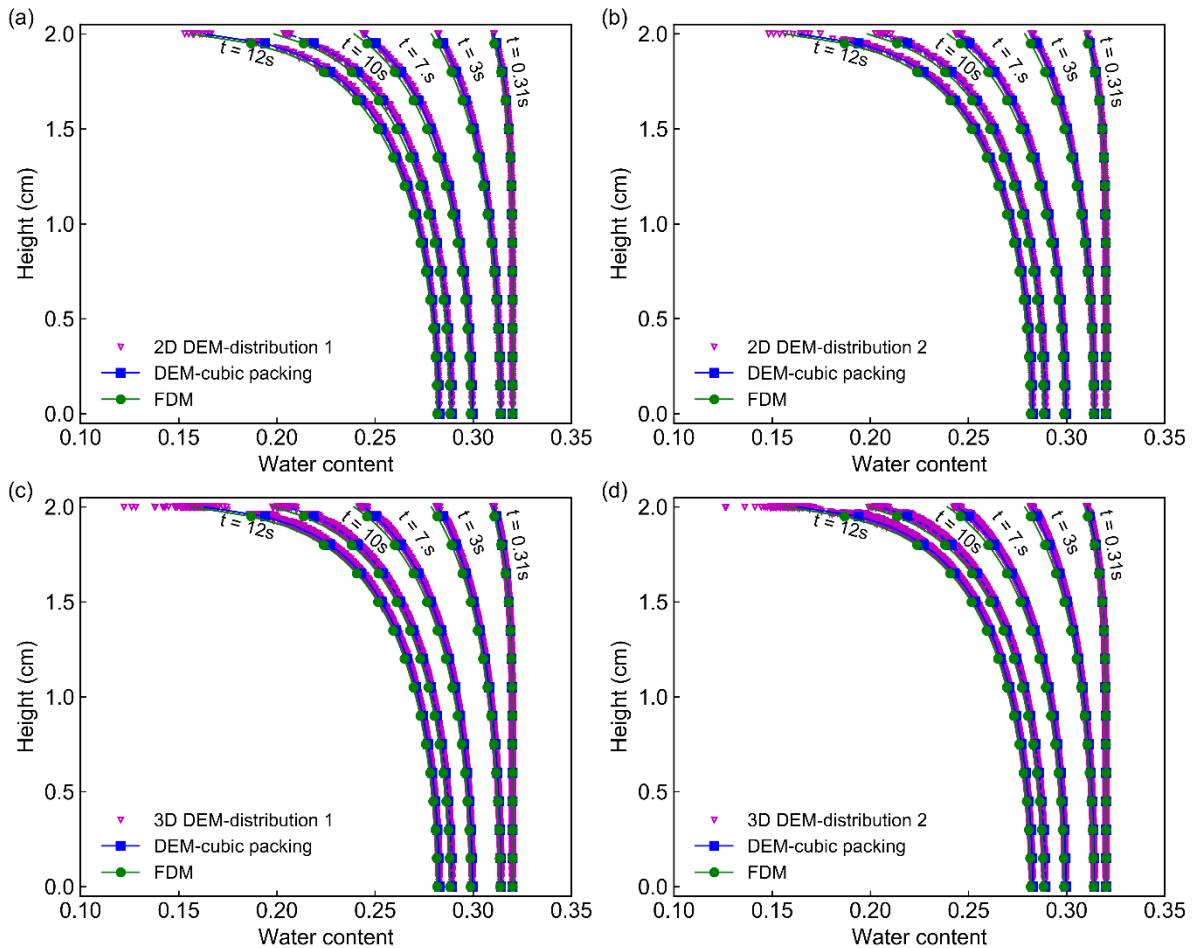


Figure 6.15. Water content profiles of the soil column due to water evaporation: (a) 2D DEM simulation with particle distribution 1; (b) 2D DEM simulation with particle distribution 2; (c) 3D DEM simulation with particle distribution 1; (d) 3D DEM simulation with particle distribution 2.

Water content profile of the soil column obtained from DEM simulations with cubic packing and FDM simulations is plotted in Figure 6.14(a). It can be observed that similar evolution

of water content over the depth of the soil column was captured in all results. Upon the beginning of the test, water content at locations near the surface started decreasing due to the loss of water, while more time was required to reduce the water content at deeper locations. For example, the decrease in water content on the surface started immediately after the test began, while it occurred at the bottom of the column after 0.31s. In addition, during the test, the decrease in water content at locations near the surface was more significant. For example, the water content at $z = 2.0\text{cm}$ decreased 0.12 after 10s, while it only decreased by 0.04 at $z = 1.0\text{cm}$. This behaviour indicated that during the evaporation process, water lost mainly occurred near the soil surface. This finding is consistent with previous experimental studies (Song et al. 2013; Wilson et al. 1994). Figure 6.14(a) also shows that 2D and 3D DEM results were identical, and these agreed well with FDM results. By looking at the relative error between DEM and FDM results plotted in Figure 6.14(b), it can be seen that error was greatest near the top surface when the evaporation process takes place. This may be caused by the large difference in the water contents, as well as the micro-diffusivity between particles near the soil surface. However, this error is relatively small, suggesting that the proposed approach is able to predict the water movement in soils during drying.

Figure 6.15 presents the DEM simulation results for the numerical domain described by particle-size distributions 1 and 2. The results obtained from the DEM simulations with cubic packing and FDM simulation are also included for comparison. It can be seen that all simulations showed the same trend in water loss over depth. As the test started, water content started decreasing. This process started for locations near the surface of the soil column, then for deeper locations. In addition, the decrease in water content was more significant for locations near the soil surface during the test, suggesting that the amount of water evaporated from the soil column was mainly contributed from these locations. This figure also shows that during the water evaporation process, the water content at every location in the soil column obtained from the DEM simulations was close the FDM simulations, except the water content on the soil surface after 12s obtained from the DEM simulations with random packing. The difference in the water content on the soil surface after 12s was clearer when the results of the 3D DEM simulations with random packing and the FDM simulation were compared. This difference is due to the heterogeneous distribution of water in the soil column after the initiation of the water evaporation process in the DEM simulations with random packing. This difference is also because locations near the soil surface mainly contribute to the evaporation flux. After a certain time, water is not supplied enough to some locations on the soil surface where water evaporates, thus the water content at these locations decreases more to keep the constant flux condition of the test. This behaviour can be observed in nature.

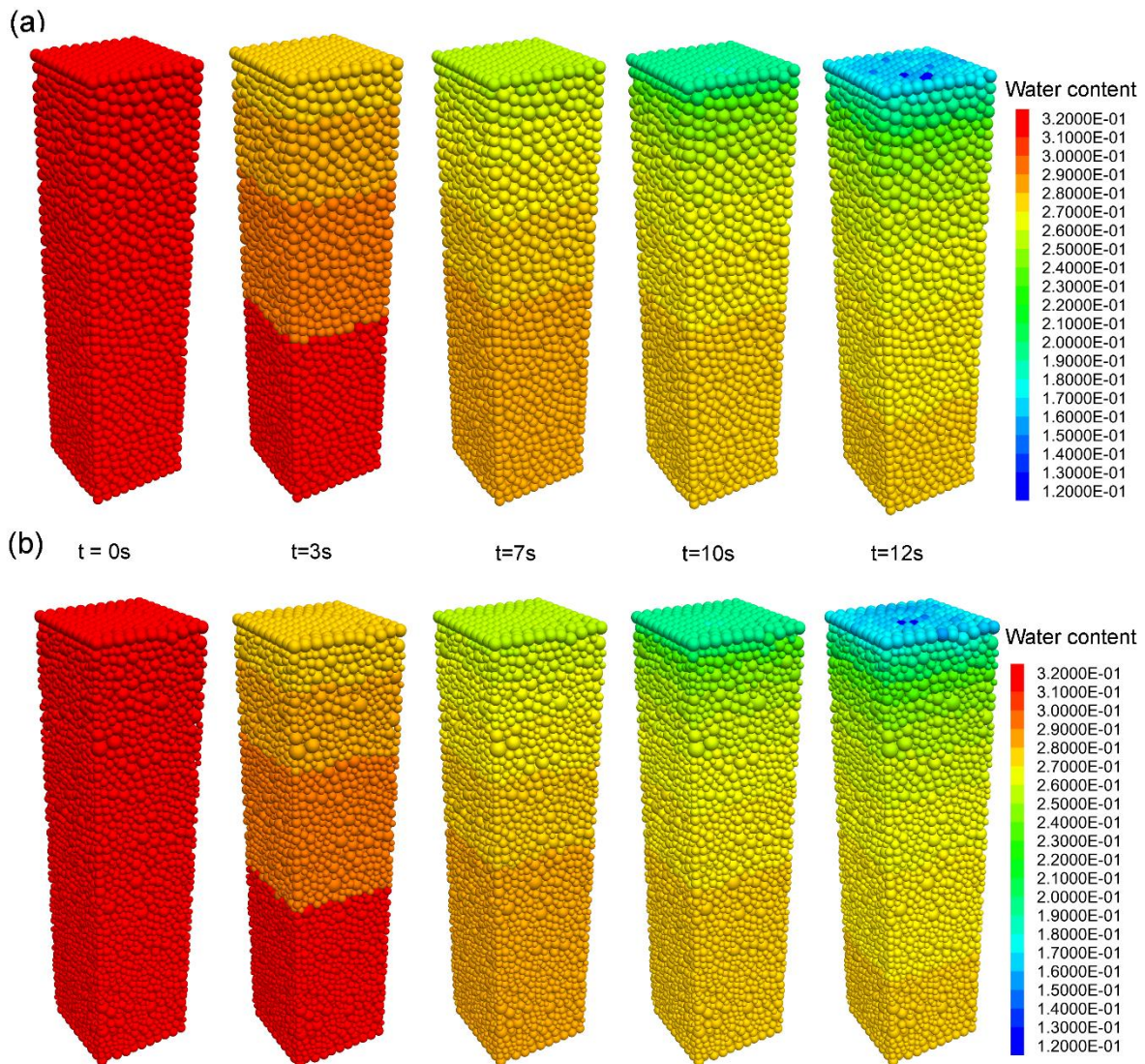


Figure 6.16. Water distribution in the soil column during water evaporation: (a) 3D DEM simulations with particle distribution 1; (b) 3D DEM simulations with particle distribution 2.

Figure 6.16 illustrates how water is distributed in the soil column during water evaporation. These results were obtained from 3D DEM simulations, in which the soil domain was described by particle distributions 1 and 2. It can be observed that as soon as the test started, water started evaporating from the column surface, causing a reduction in water content around this location, while this effect was delayed in deeper locations. In addition, decrease in the water at locations near the column surface was greater than at other locations, so the soil near the column surface was always drier. This is because of low hydraulic conductivity of the porous media, therefore requiring more time to transfer water from bottom to the surface. Consequently, the surface layer loses more water to balance the amount of water evaporating. Figure 6.16 also shows that the distribution of water in the soil column changes from a uniform distribution to heterogeneous distributions during the test. In addition, after 12s, the water content at some locations on the soil surface ranged from 0.12 to 0.15, which gave a clear view for the difference in the water content

of the DEM and FEM simulations presented in Figure 6.15. The data in Figure 6.16 again highlights the unique feature of the proposed method in naturally capturing heterogeneous water flow.

In conclusion, the proposed DEM-based approach has been shown to successfully predict water movement in an unsaturated soil column with different boundary conditions regardless of the discretisation of the numerical domain. In the next section, the effect of different inter-particle diffusivity calculation method and the number of updating cycles on the results of the proposed approach is checked and discussed.

6.4. Modelling Aspects of the Proposed Approach

In this section, effects of the inter-particle diffusivity calculation approach, the number of updating cycles and the particle size on predicted results of the proposed approach are investigated. To reduce computational cost, only 2D DEM simulations for the infiltration test with the constant water content boundary presented in Section 6.3.1 are considered.

6.4.1. The inter-particle diffusivity calculation approach

As discussed in Section 6.2.3, the inter-particle diffusivity can be calculated by using the harmonic, geometric or arithmetic means. These methods were examined in this section through DEM simulations of the infiltration test with the constant water content boundary. Figure 6.17(a) shows a comparison of predicted water content profiles between FDM and DEM using different means of calculating the inter-particle diffusivity, while the maximum value of relative errors with respect to the FDM result at each period is plotted in Figure 6.17(b). It can be observed that the DEM and FDM simulation results showed the same trend in evolution of water content along the height of the soil column, regardless of inter-particle diffusivity calculation approach used in DEM simulations. As testing time increased, water infiltrated into the soil column, causing water content of the column to increase. This process first started for shallow locations, then for deeper locations. Figure 6.17(a) also shows that the inter-particle diffusivity calculation approach used in DEM simulations slightly influenced the results. When the inter-particle diffusivity was calculated by using the harmonic mean, the DEM results were close to the FDM results, while the DEM results were slightly underestimated when the geometric or the arithmetic means were used. Figure 6.17(b) shows that the magnitude of the maximum relative error of all DEM simulations decreased significantly and then gradually decreased to small values as the testing time increased. In addition, the DEM simulation using the harmonic mean always gave the smallest maximum relative error, followed by the use of the geometric mean and then the arithmetic mean. Therefore, the harmonic mean will be used in the proposed approach to calculate the inter-particle diffusivity.

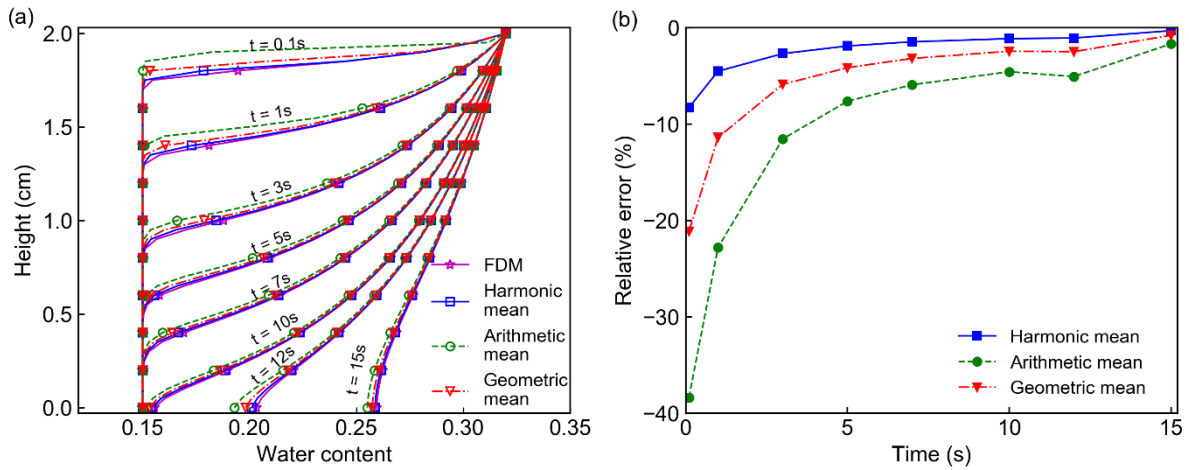


Figure 6.17. DEM simulation results with different inter-particle diffusivity calculation methods: (a) water content profile, (b) maximum relative error.

6.4.2. Effect of the number of updating cycles

To study the effect of the number of updating cycles on the accuracy of the proposed approach, DEM simulations were carried out with the inter-particle diffusivity updated every 200, 500, 1000 and 2500 times (cycles) per 1s physical testing time. The same numerical test of water infiltrating a 2cm soil column was repeated with constant water content boundary and that the inter-particle diffusivity calculated by the harmonic mean. The time-step was set to 2×10^{-5} s, corresponding to 50000 steps to achieve a physical time of 1s.

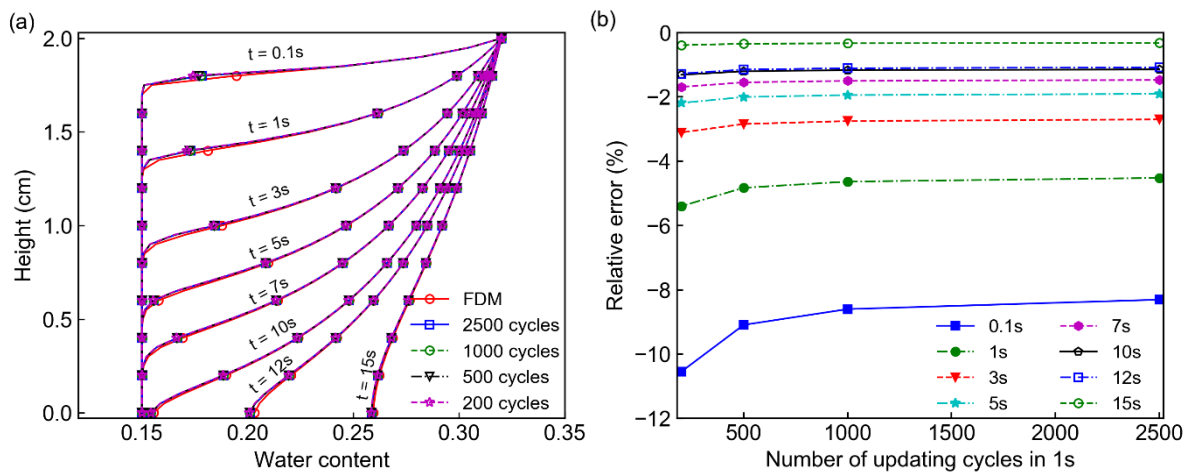


Figure 6.18. DEM simulation results with different numbers of updating cycles: (a) water content profile; (b) maximum relative error.

The predicted water content profiles are plotted in Figure 6.18(a). It can be seen that the evolution of water content along the height of the soil column in all simulations followed the same trend. At the beginning of the test, at locations near the soil surface, the water content increased significantly, while at deeper locations the initial value remained constant. This behaviour is because water is supplied from the soil surface and more time

is required for water to move to deeper locations. As testing time increased, water content at deeper locations started increasing which continued until the end of the tests. The wetting front in all simulations moved towards the bottom face of the column during the test. After around 10s, the wetting front reached the bottom face of the soil column. Figure 6.18(a) shows that the results of all DEM simulations with different numbers of updating cycles agreed well with the FDM results.

Figure 6.18(b) shows the maximum value of the relative error of the DEM results at different elapsed times. This was calculated from the water content obtained from each of the DEM and FDM simulations. It can be seen that this error depended on both the number of updating cycles and elapsed time, decreasing as the number of updating cycles and elapsed time increased. However, difference in error between simulations with a different number of updating cycles was insignificant. For example, at 1s physical testing time, the magnitude of this error was around 5.4% in the simulation with 200 updating cycles, while it was 4.5% in the simulation with 2500 updating cycles. This implies that the proposed approach is insensitive to the number of updating cycles. Accordingly, a small number of updating cycles can be used in order to reduce the computational cost.

6.4.3. Effect of the particle size

The effect of the particle size on the accuracy of the proposed approach was investigated by carrying out DEM simulations of water infiltrating a 2cm soil column with constant water content. The particle diameter used in these simulations was 1, 1.25, 1.6, 2 times and 4 times higher than the diameter (0.5mm) used in Section 6.3.1. The time-step in all simulation was set to 2×10^{-5} s, corresponding to 50000 steps for a physical time of 1s.

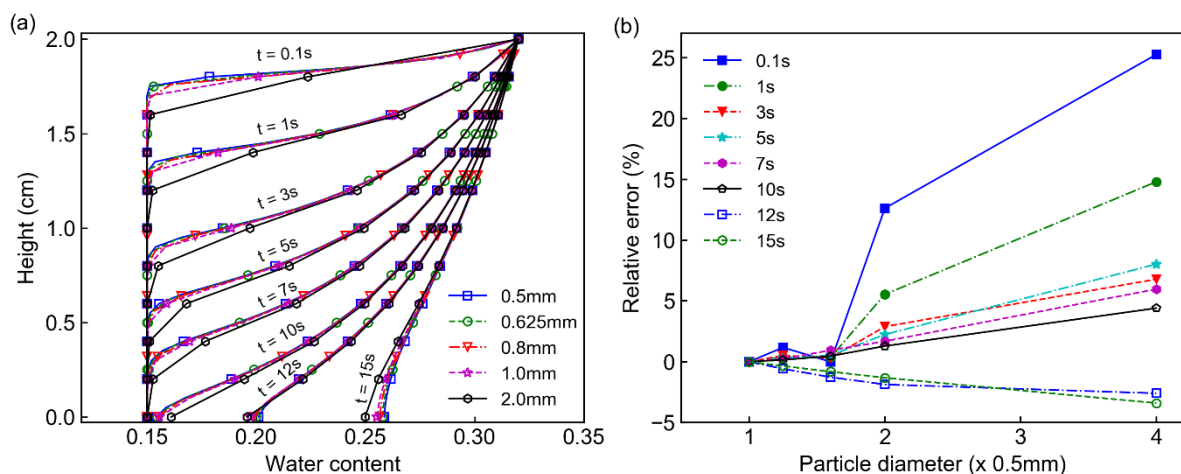


Figure 6.19. DEM simulation results with different particle size: (a) water content profile; (b) maximum relative error.

The predicted water content profiles are plotted in Figure 6.19(a). Change of water content along the height of the soil column in all simulations followed the same trend. As the test began, the water content started increasing at locations near the surface, while the initial value remained constant at deeper locations. With further testing time, water content at deeper locations started increasing. However, there was a difference in results of simulations with different particle size. This difference mainly occurred at the wetting front where the initial water content started changing.

To have a better view on the effect of particle size on numerical results, the maximum relative error, which was calculated based on the results at different elapsed times of each DEM simulation and the DEM simulation with particle size of 0.5mm, is plotted in Figure 6.19(b). It can be seen that error depended on both particle size and elapsed time, significantly increasing as particle size increased, while decreasing as elapsed time increased. However, the difference was not significant for simulations with particle size increasing up to 2 times. Effect of mesh size on numerical results has been reported for FDM and FEM (Celia et al. 1990; Eymard et al. 1999; Feddes et al. 1988).

6.5. Conclusions

This chapter has presented a new approach for predicting water flow in unsaturated porous media. In this proposed approach, an unsaturated porous medium is represented by a set of particles, each of which has its own solid volume, carries unsaturated flow information (i.e. water content, hydraulic conductivity or diffusivity) and occupies an equivalent-continuum space. Water flow in the porous medium is governed by Darcy's law and is assumed to flow through the contact network created by the DEM particles when there is a difference in the pressure gradient. This concept mimics the natural flow process at the microscopic scale, in which water flows along water films adhering to solid particles. These features in principle allow the approach to potentially predict unsaturated flow even when soil media experiences large deformations. The proposed approach is verified by conducting simulations of infiltration and evaporation of an unsaturated soil column and comparing the predicted results with those obtained by FDM. Very good agreement with FDM solutions is achieved, even for different types of particle packing and particle distributions, proves that the proposed approach is capable of predicting unsaturated flow through the discrete pore-networks. The proposed method is extended to model the coupling behaviour of fluid-solid interaction. This work is reported in the next chapter where soil cracking is modelled

Chapter 7. Micromechanics Modelling of Coupled Hydro-Mechanical Behaviour of Soil during Desiccation

7.1. Introduction

As discussed in previous chapters, soil desiccation cracking often occurs in clayey soils when they lose their moisture. When this process takes place, the soil strength significantly decreases, while the compressibility and hydraulic conductivity increase (Morris et al. 1992). These changes in the soil properties significantly affect the stability of adjacent structures and the performance of geoenvironmental applications. Therefore, understanding soil desiccation cracking and the effect of its influencing factors is very important.

Many experimental studies have reported that the desiccation cracking process of clayey soils generally takes place in three stages labelled as the primary stage, secondary stage and steady stage. In the primary stage, several cracks initiate and propagate in the soil until they reach each other. In the secondary stage, more cracks appear and divide the soil media into smaller fragments. These cracks normally start from the pre-existing cracks and terminate after reaching other pre-existing cracks. In the steady stage, only a few new cracks occur, while pre-existing cracks widen (Corte and Higashi 1960; Costa et al. 2013; Konrad and Ayad 1997; Nahlawi and Kodikara 2006; Peron et al. 2009b; Shin and Santamarina 2011; Tang et al. 2011c). During these three stages, cracks may start from any point on the surface of the soil or inside the soil, and then propagate towards either the surface or the bottom of the soil (Corte and Higashi 1960; Tollenaar 2017). Furthermore, approximately 90% of cracks occur when the soil is still fully saturated (Corte and Higashi 1960; Costa et al. 2013; Morris et al. 1992; Nahlawi and Kodikara 2006; Tang et al. 2011c).

The initiation and development of cracks have been explained based on the development of tensile stress inside soil layers during desiccation. As desiccation starts, water starts evaporating and the soil layers start shrinking. However, the movement of soil particles and the soil layers are hindered due to friction and adhesion, which occur between the soil and external boundaries or lower soil layers. As a result, tensile stress develops, and thus cracks occur when the tensile stress reaches the tensile strength of the soil (Corte and Higashi 1960; Kodikara and Costa 2013; Morris et al. 1992; Peron et al. 2009b). By looking at the direction of the horizontal strain, Wei et al. (2016) concluded that cracks may occur due to tensile failure or a combination of both tensile and shear failures. Another explanation for initiation and development of cracks is based on the intrusion

process of the air-water interface. This explanation was drawn from experimental observation of desiccation cracking by Shin and Santamarina (2011) and Tang et al. (2011c). As water evaporates, capillary suction develops. After a certain drying time, air starts intruding into the soil media and pushes soil particles away from each other and cracks initiate. This process repeats itself, and thus cracks continue to propagate in the soil media (Shin and Santamarina 2011; Tang et al. 2011c).

Numerical methods have also been applied to investigate soil desiccation cracking. Trabelsi et al. (2012) implemented the elasto-visco-plasticity model in a finite element program and used it to predict crack patterns in test samples during experiments. To allow for cracking, when the tensile stress in numerical elements reached the tensile strength, the Mohr-Coulomb criterion was modified and the viscosity of these elements was decreased. Although cracks occurred in numerical samples, width of the cracks did not change during desiccation and some cracks did not connect to each other to form clear crack patterns. Peron et al. (2013) used the total stress analysis within the framework of Biot theory in FEM to study soil cracking and reported that cracks would occur simultaneously at some locations. However, in Peron et al. (2013), the development of cracks could not be handled. To overcome this problem, Sánchez et al. (2014) introduced a technique known as “mesh fragmentation”. The drying process was simply implemented by assigning the volumetric strain to FEM elements. The results showed that most of the behaviour observed in laboratory and field tests during desiccation could be captured by using this technique. However, because of the mesh-based nature of the mesh fragmentation method, numerical solutions are highly influenced by the mesh orientation and further work is still required to fully capture the hydro-mechanical behaviour of soils during desiccation.

Hirobe and Oguni (2016), Vo et al. (2017) and Levatti et al. (2019) also proposed frameworks in FEM to couple the hydro-mechanical behaviour in simulations of soil cracking. In these studies, the framework of the Biot theory of deformable porous media was used to simulate unsaturated flow, while the total stress framework and cohesive crack models were used to analyse the mechanical behaviour of soils and to control the occurrence of fractures. These studies showed that cracks occurred vertically through prescribed vertical interface elements when the tensile stress in these elements reached the tensile strength. However, the hydraulic and mechanical behaviour of the experimental samples was not accurately captured (e.g. the predicted water content, crack patterns, crack development process were significantly different to that in experiments). Similarly, FDM and SPH have been also employed in studies of Bui et al. (2015), Stirling et al. (2017), Tran et al. (2019) and Tran (2019). In these studies, the framework of the Biot theory and total stress framework with embedded cohesive crack

models were also used. These studies show that both 2D/3D crack patterns of long samples were fairly reproduced. However, further improvement is required to capture complex crack patterns and hydraulic behaviour.

DEM, which has been widely used for studying macro- and micro-behaviours of soils (Bui et al. 2009; Lee et al. 2012; Tran et al. 2011a; Tran et al. 2011b; Tran et al. 2011c; Tran et al. 2012), has also been employed to study soil cracking by Peron et al. (2009a), Sima et al. (2014) and Guo et al. (2017). In these studies, bonded DEM particles were used to represent clay aggregates. The drying process of the numerical samples was implemented by changing the size of the DEM particles based on the changes in water content and volume strain of experimental samples. Other model parameters (i.e. the stiffnesses, tensile strengths and shear strengths for soil-soil and soil-mould interactions) were calibrated from experimental results obtained in uniaxial tensile tests, or uniaxial compression tests. Results of these studies demonstrate that the DEM is a potential approach for studying soil desiccation cracking as cracks naturally occurred without additional treatment and behaviour of soils during desiccation could be captured. However, these studies used the contact bond model, and thus the mixed-mode failure (the combination of tensile failure and shear failure), which occurs during the soil desiccation process (based on observations presented in previous chapters and the results of Wei et al. (2016)), could not be captured. Furthermore, none of the existing DEM works are capable of capturing the coupled hydro-mechanical process of soil desiccation cracking. Therefore, further studies are required to account for the coupled hydro-mechanical behaviour of soils and to properly capture the mixed-mode failure when soil desiccation cracking is analysed with DEM.

In this chapter, a coupled hydro-mechanical DEM framework is developed for studying soil desiccation cracking. The unique feature of this framework is its capability to simulate unsaturated flow through deformed porous media as well as to capture the mixed-mode failure of cracks in soil media during desiccation. The rest of the chapter is organised as follows. Section 7.2 presents the development of the hydro-mechanical framework. This is then followed by the validation of the framework in Section 7.3 and the conclusions in Section 7.4.

7.2. The Hydro-Mechanical Framework

In this section, general assumptions are first given to provide the theoretical basis for deriving the mathematical equations of the proposed framework. The approach presented in Chapter 6 is then extended to capture unsaturated flow through deformable porous media. The momentum equations for capturing the mechanical behaviour of soils are then

presented. Finally, constitutive relations and numerical algorithms for coupling the hydraulic behaviour and mechanical behaviour are established.

7.2.1. General assumptions

Previous studies have reported that in clayey soils, several clay particles gather together, following an edge-to-edge pattern, a face-to-face pattern or a combination of these two patterns to form aggregates. These aggregates are then linked together by water to form soil (Mitchell and Soga 2005; Wang and Xu 2007) (Figure 7.1(a)). As water evaporates, water content in a soil layer decreases, causing suction and soil strength to increase, so, the soil can carry tensile stresses. However, tensile stresses inside the soil developed due to the movement of soil particles is hindered by frictions and adhesion at the bottom of the soil layer, and thus cracks occur when the tensile stresses reach the soil strength (Corte and Higashi 1960; Kodikara and Costa 2013; Morris et al. 1992; Peron et al. 2009b). To model the mechanical behaviour of clayey soils during drying, the following assumptions are adopted:

- A soil medium is represented by a set of spherical discrete particles bonded together at their contacts and the behaviour at each contact is governed by a system of normal and tangential springs (Figure 7.1(b)). The forces of these springs represent the mechanical forces and suction forces in contact zones. In addition, these springs can bear tensile forces and break when the stresses in the contact zones satisfy a yield criterion. In addition, the tensile and shear strengths of these springs change, following changes in the water content of the soil medium.
- The desiccation process is facilitated by reducing the size of particles (Guo et al. 2017; Hirobe and Oguni 2016; Peron et al. 2009a; Sima et al. 2014). In this study, the equation that directly links size of particles to volumetric strain used in study of Guo et al. (2017) is adopted. At the beginning of a new time step, the volumetric strain at a particle is estimated, and the new radius of the particle is then computed using the following equation.

$$1 - \epsilon_{sk} = 1 - \frac{\Delta V}{V} = \frac{r_t^3}{r_0^3} \quad (7-1)$$

where V is the volume of the particle; ΔV is the change in volume of the particle; r_0 is the initial radius of the particle; r_t is the radius of the particle at time t and ϵ_{sk} is the volumetric strain of the soil skeleton. Its calculation is presented in the next section when the numerical validation is discussed.

To model unsaturated flow through deformable soil media, the approach presented in Chapter 6 is extended. The main assumptions of this approach are briefly summarised as follows:

- Each discrete particle has its own solid volume, carries unsaturated flow information (e.g. hydraulic conductivity and volumetric water content) and occupies an equivalent-continuum space, which can be approximated based on the solid volume and surrounding porosity (Figure 7.1(b)).
- Water flow is governed by Darcy's law and occurs through the contact point between two discrete particles. The flow travels from the centre of the particle with higher volumetric water content (or higher piezometric head) to that of the particle with lower volumetric water content (or lower piezometric head) (Figure 7.1(c)). This assumption attempts to mimic the water flow process at a microscopic scale, in which water flows along the water films that adhere to particles (Gili and Alonso 2002).

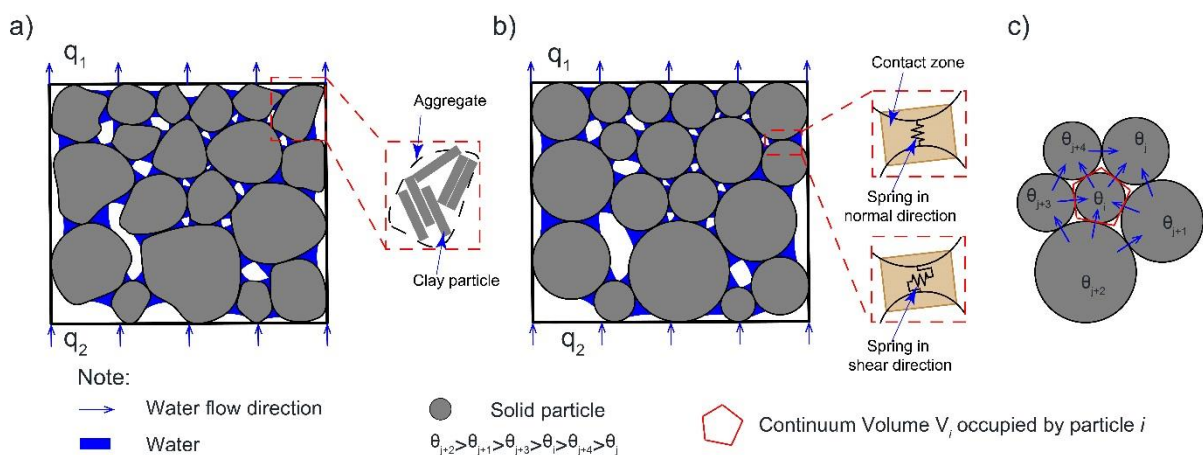


Figure 7.1. Concepts of the hydro-mechanical model: (a) clayey aggregates and boundary conditions; (b) idealised system in DEM model; (c) water flow directions between some particles.

7.2.2. Governing Equations

7.2.2.1. Mass balance equation for solid skeleton

A representative particle that occupies an equivalent continuum volume V is considered (Figure 7.1(c)). By applying the mass conservation law to this particle (or the equivalent continuum volume occupied by the particle), the rate of change in the solid mass of this particle can be calculated as (Bear and Cheng 2010):

$$\frac{\partial[\rho_s(1-n)]}{\partial t} = -\nabla \cdot [\rho_s(1-n)\mathbf{V}_s] \quad (7-2)$$

where ρ_s is the mass density of the solid phase; n is the porosity and \mathbf{V}_s is the velocity of the solid phase.

Expanding the right side of Equation (2-1), the rate of change in the solid mass of particle i can be calculated as follows:

$$\frac{\partial[\rho_s(1-n)]}{\partial t} = -[\rho_s(1-n)]\nabla \cdot \mathbf{V}_s - \mathbf{V}_s \cdot \nabla[\rho_s(1-n)] \quad (7-3)$$

Applying the material time derivative for the solid phase and expanding the left side of Equation (7-3), Equation (7-3) can now be written as follows:

$$\frac{1}{1-n} \frac{d_s(1-n)}{dt} + \frac{1}{\rho_s} \frac{d_s \rho_s}{dt} = -\nabla \cdot \mathbf{V}_s \quad (7-4)$$

In this work, clay particles are assumed to be incompressible and thus Equation (7-4) becomes:

$$\frac{1}{1-n} \frac{d_s(1-n)}{dt} = -\nabla \cdot \mathbf{V}_s \quad (7-5)$$

By introducing the volumetric strain of the solid phase, ε_{sk} , and rearranging the left side of Equation (7-5), the rate of change in the porosity can be calculated as:

$$\frac{1}{1-n} \frac{d_s n}{dt} = \frac{\partial \varepsilon_{sk}}{\partial t} \quad (7-6)$$

7.2.2.2. Mass balance equation for water phase

The mass balance for the water phase of the representative particle can be written as follows (Bear and Cheng 2010):

$$\frac{\partial(\rho_w n S)}{\partial t} = -\nabla \cdot [\rho_w S n (\mathbf{V}_w - \mathbf{V}_s)] - \nabla \cdot (\rho_w S n \mathbf{V}_s) \quad (7-7)$$

where ρ_w is the mass density of water; S is the degree of saturation and \mathbf{V}_w is the velocity of the water phase which can be found from the water flux vector, \mathbf{q} , through the deformed medium and the velocity of the solid phase, \mathbf{V}_s , based on the following equation:

$$\mathbf{q} = S n (\mathbf{V}_w - \mathbf{V}_s) \quad (7-8)$$

Substituting Equation (7-8) into Equation (7-7) and expanding terms in the right side of Equation (7-7), this equation can now be written as:

$$\frac{\partial(\rho_w n S)}{\partial t} = -\nabla \cdot [\rho_w \mathbf{q}] - \mathbf{V}_s \cdot \nabla(\rho_w S n) - \rho_w S n \nabla \cdot \mathbf{V}_s \quad (7-9)$$

Applying the material time derivative for the solid phase and expanding the left side of (7-9), this equation can be now expressed as:

$$\frac{d_s(\rho_w n S)}{dt} = -\nabla \cdot [\rho_w \mathbf{q}] - \rho_w S n \nabla \cdot \mathbf{V}_s \quad (7-10)$$

Expanding the left side of (7-10) and substituting Equation (7-5) into Equation (7-10), we obtain:

$$n S \frac{d_s(\rho_w)}{dt} + \rho_w S \frac{d_s(n)}{dt} + \rho_w n \frac{d_s(S)}{dt} = -\nabla \cdot [\rho_w \mathbf{q}] + \frac{\rho_w S n}{1-n} \frac{d_s(1-n)}{dt} \quad (7-11)$$

In this work, water is assumed to be incompressible, so the density of water does not change with respect to time. By applying this assumption and rearranging Equation (7-11), we obtain the following equation:

$$\frac{S}{1-n} \frac{d_s(n)}{dt} + n \frac{d_s(S)}{dt} = -\nabla \cdot (\mathbf{q}) \quad (7-12)$$

Assuming that $\left| \frac{\partial S}{\partial t} \right| \gg |\mathbf{V}_s \cdot \nabla S|$ (Bear and Cheng 2010) and after substituting Equation (7-6) into Equation (7-12), we obtain the following equation:

$$S \frac{\partial \varepsilon_{sk}}{\partial t} + n \frac{\partial S}{\partial t} = -\nabla \cdot (\mathbf{q}) \quad (7-13)$$

In unsaturated soil, the capillary pressure, p_c , is a function of the degree of saturation and this pressure is calculated based on water pressure, p_w , and air pressure, p_a , using the following equation:

$$p_c = p_a - p_w \quad (7-14)$$

For unsaturated flow, air pressure is normally assumed to be zero (Bear and Cheng 2010), so the rate of change in the degree of saturation of the representative particle can be calculated as follows:

$$\frac{\partial S}{\partial t} = \frac{dS}{dp_c} \frac{\partial p_c}{\partial t} = \frac{dS}{dp_c} \left(-\frac{\partial p_w}{\partial t} \right) = \frac{dS}{dp_w} \left(\frac{\partial p_w}{\partial t} \right) = \frac{dS}{dh} \left(\frac{\partial h}{\partial t} \right) \quad (7-15)$$

where h is the pressure head, which can link to the water pressure, p_w , and the gravitational acceleration, g , as follows:

$$p_w = hg\rho_w \quad (7-16)$$

Substituting Equation (7-15) into Equation (7-13), we obtain:

$$S \frac{\partial \varepsilon_{sk}}{\partial t} + n \frac{dS}{dh} \left(\frac{\partial h}{\partial t} \right) = -\nabla \cdot (\mathbf{q}) \quad (7-17)$$

where the water flux vector can be calculated as:

$$\mathbf{q} = -\mathbf{D}(\theta) \cdot \nabla \theta \quad (7-18)$$

where $\mathbf{D}(\theta)$ is the average diffusivity tensor between two particles or the macro-diffusivity tensor and θ is the volumetric water content.

Applying the chain rule and substituting Equation (7-18) into Equation (7-17), the mass balance equation considering the deformation of the solid skeleton can be obtained as follows:

$$C_w \left(\frac{\partial \theta}{\partial t} \right) = \mathbf{D}(\theta) \cdot \nabla \theta - S \frac{\partial \varepsilon_{sk}}{\partial t} \quad (7-19)$$

where $C_w = n \frac{dS}{dh} \frac{dh}{d\theta} = (1 - S \frac{dn}{d\theta})$.

The above equation allows the volumetric water content of the representative particle to be calculated once the hydraulic constitutive (i.e. soil water retention curve and hydraulic conductivity curve) is known. This constitutive is described later.

7.2.2.3. Momentum equations

As water is assumed to flow through the contact network created by an assembly of DEM particles, momentum equations are established only for DEM particles. At a time step t , the motion of the representative particle (e.g. particle i) can be described as follows (Cundall and Strack 1979):

$$\ddot{\vec{\mathbf{x}}}_i = \frac{\vec{\mathbf{F}}_i}{m_i} + \vec{\mathbf{g}} \quad (7-20)$$

$$\dot{\vec{\boldsymbol{\omega}}}_i = \frac{\vec{\mathbf{M}}_i}{I_i} \quad (7-21)$$

where $\ddot{\mathbf{x}}_i$ and $\ddot{\boldsymbol{\omega}}_i$ are the translational and rotational accelerations of particle i , respectively; m_i is the total mass of particle i ; g is the acceleration of gravity; I_i is the moment of inertia of particle i ; $\vec{\mathbf{F}}_i$ and $\vec{\mathbf{M}}_i$ the resultant force and moment acting on particle i , respectively. The force and moment can be calculated as follows:

$$\vec{\mathbf{F}}_i = \sum_{c=1}^N F_{i,c}^n \vec{\mathbf{n}} + \sum_{c=1}^N F_{i,c}^s \vec{\mathbf{s}} + \vec{\mathbf{F}}_i^{ext} + \vec{\mathbf{F}}_i^{damp} \quad (7-22)$$

$$\vec{\mathbf{M}}_i = \sum_{c=1}^N \vec{\mathbf{F}}_i \vec{\mathbf{l}}_{i,c} + \vec{\mathbf{M}}_i^{ext} \quad (7-23)$$

where $F_{i,c}^n$ and $F_{i,c}^s$ are the contact forces at contact c in the normal ($\vec{\mathbf{n}}$) and shear ($\vec{\mathbf{s}}$) directions (Figure 7.2), which can be computed using Equations (5-5) and (5-6). In this work, the contact force is the sum of mechanical forces and forces caused by suction. $\vec{\mathbf{F}}_i^{ext}$ and $\vec{\mathbf{M}}_i^{ext}$ are the external force and moment vectors acting on particle i , respectively; N is the total number of contacts of particle i ; $\vec{\mathbf{l}}_{i,c}$ is the vector from the centre of particle i to contact c ; and $\vec{\mathbf{F}}_i^{damp}$ is the damping force vector, which depends on the dissipation mechanisms used. In this study, local damping proposed by Cundall and Strack (1979) is selected, and thus the damping force vector can be calculated by using Equation (7-26).

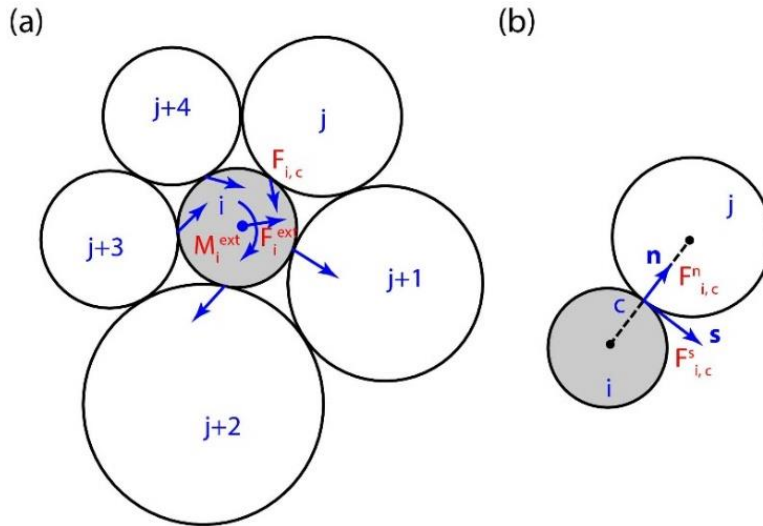


Figure 7.2. (a) forces and moments acting on a particle; (b) forces at a contact.

$$F_{i,c}^n = K_{c,n} u_{c,n}^e = k_{c,n} A_c u_{c,n}^e \quad (7-24)$$

$$F_{i,c}^s = \sum K_{c,s} \Delta u_{c,s}^e = \sum k_{c,s} A_c \Delta u_{c,s}^e \quad (7-25)$$

$$\vec{\mathbf{F}}_i^{damp} = -\alpha |\vec{\mathbf{F}}_i^*| \text{sign}(\dot{\mathbf{u}}_i) \quad (7-26)$$

where $u_{c,n}^e$ is the elastic displacement in the normal direction between two particles associated at contact c ; $\Delta u_{c,s}^e$ is the elastic relative shear (tangential) displacement increment between two particles associated at contact c ; $K_{c,n}$ and $K_{c,s}$ are the normal and shear contact stiffnesses at contact c , respectively; $k_{c,n}$ and $k_{c,s}$ are the normal and shear contact stiffnesses per initial unit area of the contact area at contact c , respectively; α is the damping coefficient; \vec{F}_i^* is the resultant force vector of all contact forces, external force and gravity force acting on particle i ; and A_c is the contact area at the time step t . When two particles in contact are under normal and shear forces, fractures may exist in the bond between these two particles. To reduce the ability of the bonding contact to carry tensile and shear stresses after the initiation of the fractures, the damage variable D_c is introduced, and the stiffnesses per initial unit area at any time step are calculated from the initial stiffnesses per initial unit area ($k_{c,n}^0, k_{c,s}^0$) as following equations:

$$k_{c,n} = \begin{cases} k_{c,n}^0(1 - D_c) & \text{for tensile force} \\ k_{c,n}^0 & \text{for compression force} \end{cases} \quad (7-27)$$

$$k_{c,s} = k_{c,s}^0(1 - D_c) \quad (7-28)$$

The contact area at contact c can be calculated based on the minimum radius, r , of two particles of the contact as follows:

$$A_c = \begin{cases} \pi r^2 & \text{for 3D simulations} \\ 2r & \text{for 2D simulations} \end{cases} \quad (7-29)$$

To complete the description of the momentum equations for DEM particles, a cohesive contact model that regulates the development of fracture in the bond between two particles is required and this will be presented in the next section.

7.2.3. Constitutive relations

7.2.3.1. Hydraulic constitutive relation

To complete the mass balance equations described in Section 7.2.2, the soil water retention curve (e.g. Figure 7.3) and hydraulic conductivity curve (e.g. Figure 7.3) have to be defined. These curves are used to link the volumetric water content, θ , or degree of saturation, S , the hydraulic conductivity, $K(\theta)$, and diffusivity, $D(\theta)$, when the pressure head is known. In this work, the van Genuchten model (Van Genuchten 1980a) is adopted to facilitate the simulation work. This model is presented as follows:

$$S_e = \frac{S - S_r}{1 - S_r} = \frac{\theta - \theta_r}{\theta_s - \theta_r} = \frac{1}{[1 + (\alpha|h|)^n]^{1-\frac{1}{n}}} \quad (7-30)$$

$$K(\theta) = K_s S_e^{\frac{1}{2}} \left[1 - \left(1 - S_e^{\frac{n}{n-1}} \right)^{1-\frac{1}{n}} \right]^2 \quad (7-31)$$

where S_e is the effective saturation; S is the degree of saturation; S_r is the residual degree of saturation; θ_s is the saturated volumetric water content; θ_r is the residual water content; h is the pressure head; α , n and m are curve fitting parameters; $K(\theta)$ is the hydraulic conductivity at the pressure head h or the water content θ and K_s is saturated hydraulic conductivity.

The diffusivity, $D(\theta)$, at the pressure head or the water content is then calculated as follows (Van Genuchten 1980a):

$$D(\theta) = \frac{(1-m)K_s}{\alpha m(\theta_s - \theta_r)} S_e^{\frac{1}{2} - \frac{1}{m}} \left[\left(1 - S_e^{\frac{1}{m}} \right)^{-m} + \left(1 - S_e^{\frac{1}{m}} \right)^m - 2 \right] \quad (7-32)$$

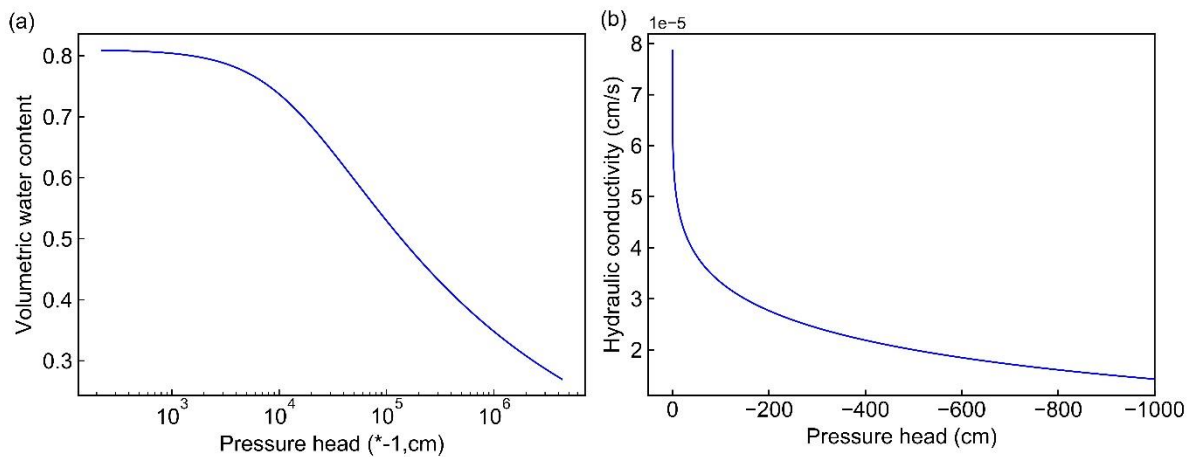


Figure 7.3. Hydraulic constitutive relation: (a) soil water retention curve; (b) hydraulic conductivity curve.

7.2.3.2. Mechanical constitutive relation

As discussed previously, during drying, water content of the soil decreases, leading to an increase in suction and capacity to carry tensile stresses of soil. During this process, tensile stresses inside the soil develop and thus cracks occur when the tensile stresses reach the soil strength. Previous studies have illustrated during the cracking process, soil experiences stress softening, plastic and ductile behaviour (Amarasiri et al. 2011a; Hasatani et al. 1992). In addition, the results presented in Chapter 4 reveal that cracks may occur due to both shear and tensile failures. To include the behaviour, a bonding model developed by Nguyen et al. (2017) was adopted in this work to regulate the soil-soil and soil-mould interactions. This model is capable of capturing both mixed-mode

failure and the stress softening, plastic and ductile behaviour of soil. In this subsection, main equations of the model are summarised.

First, to consider the irreversible displacement in a contact c , the displacement between two particles ($\mathbf{u}_c(u_{c,n}, u_{c,s})$) can be decomposed into elastic (\mathbf{u}^e) and plastic (\mathbf{u}^p) displacements as follows:

$$\mathbf{u}_c = \mathbf{u}_c^e + \mathbf{u}_c^p \quad (7-33)$$

The normal and shear stresses of this contact are calculated by using the following equations:

$$\sigma_{c,n} = \frac{F_{c,n}}{A_c} = \begin{cases} k_{c,n}^0(1 - D_c)(u_{c,n} - u_{c,n}^p) & \text{in tension mode} \\ k_{c,n}^0(u_{c,n} - u_{c,n}^p) & \text{in compression mode} \end{cases} \quad (7-34)$$

$$\sigma_{c,s} = \frac{F_{c,s}}{A_c} = k_{c,s}^0(1 - D_c)(u_{c,s} - u_{c,s}^p) \quad (7-35)$$

where $\sigma_{c,n}$ and $\sigma_{c,s}$ are the normal and shear stresses of the contact, respectively; $F_{c,n}$ and $F_{c,s}$ are the normal and shear contact forces, respectively; $k_{c,n}^0$ and $k_{c,s}^0$ are the initial normal and shear contact stiffnesses, respectively; $u_{c,n}$ and $u_{c,s}$ are the total displacements in normal and shear directions, respectively; and $u_{c,n}^p$ and $u_{c,s}^p$ are the plastic displacements in normal and shear directions, respectively.

The normal and shear contact stiffnesses per initial unit area can be found based on the effective modulus, E^* , and the normal-to-shear stiffness ratio, k^* , as follows (Itasca 2008):

$$k_{c,n}^0 = \frac{E^*}{r_i + r_j} \quad (7-36)$$

$$k_{c,s}^0 = k_{c,n}^0/k^* \quad (7-37)$$

The damage variable, D_c , can be calculated from the plastic displacements and softening parameters in normal and shear directions (u_n^c and u_s^c) as follows:

$$D_c = 1 - e^{-\left(\frac{u_{c,n}^p}{u_n^c} + \frac{u_{c,s}^p}{u_s^c}\right)} \quad (7-38)$$

The plastic displacements start developing when stresses in the contact satisfy a yield criterion. This yield criterion is defined as follows:

$$F(\sigma_n, \sigma_s, D_c) = \sigma_s^2 - [\sigma_s^0 \xi(D_c) - \sigma_n \tan \varphi]^2 + [\sigma_s^0 \xi(D_c) - \sigma_t^0 \xi(D_c) \tan \varphi]^2 = 0 \quad (7-39)$$

where σ_t^0 and σ_s^0 are the initial tensile strength and shear strength of the bonding contact, respectively; φ is the friction angle of the contact; $\xi(D_c) = 1 - D_c$. In addition, the incremental plastic displacements in normal and shear directions (δu_n^p and δu_s^p) are calculated based on the flow rule of plasticity theory by using a non-associate plastic potential function (G). The incremental plastic displacements and non-associate plastic potential function are given by:

$$\delta u_n^p = \delta \lambda \frac{G}{\sigma_n} \quad (7-40)$$

$$\delta u_s^p = \delta \lambda \frac{G}{\sigma_s} \quad (7-41)$$

$$G(\sigma_n, \sigma_s, D_c) = \sigma_s^2 - [\sigma_s^0 \xi(D_c) - \sigma_n \tan \psi]^2 + [\sigma_s^0 \xi(D_c) - \sigma_t^0 \xi(D_c) \tan \psi]^2 = 0 \quad (7-42)$$

where ψ is the dilatancy angle of the contact.

The evolution of stresses at a contact under tensile and shear displacements is plotted in Figure 7.4. It can be observed that, as the normal and shear displacements increase, the tensile and shear stresses increase linear-elastically, and then reach their peak values. At this stage, fractures initiate. After that, these stresses nonlinearly decrease. In addition, after the formation of fractures, plastic displacements occur.

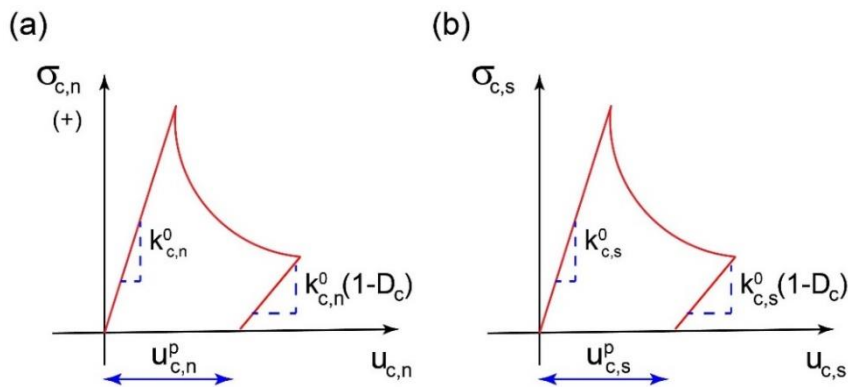


Figure 7.4. Stress-displacement behaviour: (a) tensile stress; (b) shear stress.

7.2.4. Numerical Solutions

In this section, numerical solutions for hydraulic and mechanical behaviour are derived. The coupled algorithm for hydro-mechanical behaviour is then established.

7.2.4.1. Numerical solution for the hydro behaviour

Consider a particle i with inflows and outflows caused by the difference in volumetric water content (or piezometric head) between this particle and its neighbours (Figure 7.5). This particle has N contacts with N other particles and occupies an equivalent continuum volume V_i . Following the framework presented in Chapter 6, the volumetric water content of particle i at time $t + \Delta t$ can be calculated as follows:

$$\theta_i^{t+\Delta t} = \left(\theta_i^t + \Delta t \left(\frac{1}{V_i} \sum_{j=1}^N d_{ij} \frac{\Delta \theta_{ij}}{L_{ij}} \right) - S_i \frac{\partial \varepsilon_{sk}^i}{\partial t} \right) \frac{1}{C_w^i} \quad (7-43)$$

where θ_i^t is the volumetric water content of particle i at time t ; $\Delta \theta_{ij}$ and d_{ij} are the water content difference and the inter-particle diffusivity between particles i and j respectively; L_{ij} is the distance between the centres of the two particles; S_i is the degree of saturation; ε_{sk}^i is the volumetric strain; and d_{ij} is the inter-particle diffusivity between particles i and j , which can be calculated from the micro-diffusivity of particles i and j (d_i and d_j) using the harmonic mean as follows:

$$d_{ij} = \frac{2d_i d_j}{d_i + d_j} \quad (7-44)$$

The inter-particle diffusivity between particles i and j can also be calculated by using either the geometric mean or arithmetic mean (illustrated in Equations (7-45) and (7-46)). However, as demonstrated in Chapter 6, the numerical results are more accurate when the inter-particle diffusivity is calculated using the harmonic mean, and thus Equation (7-44) is used to calculate the inter-particle diffusivity in this work.

$$d_{ij} = (d_i d_j)^{0.5} \quad (7-45)$$

$$d_{ij} = \frac{d_i + d_j}{2.0} \quad (7-46)$$

Following the same procedure that was presented in Chapter 6, the micro-diffusivity of particle i in 2D and 3D simulations respectively can be now computed as follows:

$$d_i = \frac{2D(\theta_i)V_i}{\sum_{c=1}^N l_{ic}} \quad (7-47)$$

$$d_i = \frac{3D(\theta_i)V_i}{\sum_{c=1}^N l_{ic}} \quad (7-48)$$

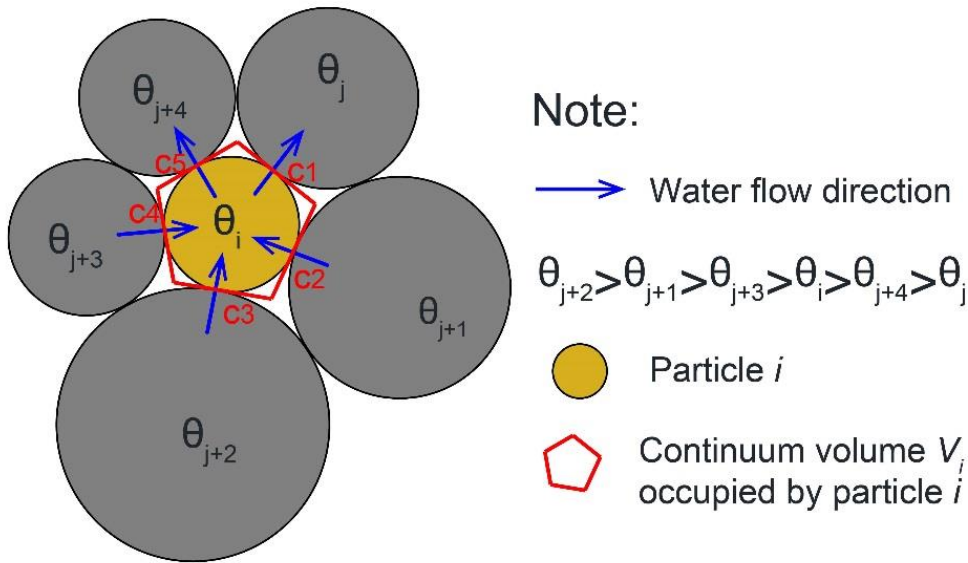


Figure 7.5. Inflows and outflows through particle i (or through an imaginary equivalent V_i continuum volume occupied by particle i)

7.2.4.2. Numerical solution for mechanical behaviour

The translational and rotational accelerations of particle i at time t can be calculated by using the central finite-difference approximation scheme as:

$$\ddot{\mathbf{x}}_i^t = \frac{1}{\Delta t} \left(\dot{\mathbf{x}}_i^{(t+\frac{\Delta t}{2})} - \dot{\mathbf{x}}_i^{(t-\frac{\Delta t}{2})} \right) \quad (7-49)$$

$$\ddot{\boldsymbol{\omega}}_i^t = \frac{1}{\Delta t} \left(\dot{\boldsymbol{\omega}}_i^{(t+\frac{\Delta t}{2})} - \dot{\boldsymbol{\omega}}_i^{(t-\frac{\Delta t}{2})} \right) \quad (7-50)$$

By substituting Equation (7-20) into Equation (7-49) and (7-21) into Equation (7-50) and rearranging these equations, the translational and rotational velocities of particle i at time $t + \frac{\Delta t}{2}$ can be now computed as:

$$\dot{\mathbf{x}}_i^{(t+\frac{\Delta t}{2})} = \dot{\mathbf{x}}_i^{(t-\frac{\Delta t}{2})} + \Delta t \left(\frac{\mathbf{F}_i^t}{m_i} + \mathbf{g} \right) \quad (7-51)$$

$$\dot{\boldsymbol{\omega}}_i^{(t+\frac{\Delta t}{2})} = \dot{\boldsymbol{\omega}}_i^{(t-\frac{\Delta t}{2})} + \Delta t \left(\frac{\mathbf{M}_i^t}{I_i} \right) \quad (7-52)$$

Finally, the position of the centre of particle i at time step $t + \Delta t$ can now be updated by using:

$$\mathbf{x}_i^{(t+\frac{\Delta t}{2})} = \mathbf{x}_i^t + \Delta t \left(\dot{\mathbf{x}}_i^{(t+\frac{\Delta t}{2})} \right) \quad (7-53)$$

7.2.4.3. Coupled algorithm for hydro-mechanical behaviour

To couple hydraulic behaviour with mechanical behaviour, one of two procedures is generally used. One is to analyse the hydraulic behaviour and mechanical behaviour at the same time, while the other is to first analyse the hydraulic behaviour and then the mechanical behaviour. In this study, the second procedure is selected.

For each time step, the information of the computation domain (i.e. locations of DEM particle, contact network, boundary conditions) is first obtained. The hydraulic behaviour is first analysed to update the water content of each particle in the computational domain. After that, the computation of the mechanical behaviour commences. The stiffnesses, tensile and shear strengths of every contact, and the radii of particles are updated based on the new water content of each particle. At each contact, the contact forces are then calculated and the yield criterion is checked to determine whether fracturing occurs. The calculation process in each time step ends by calculating and updating new locations of particles.

7.3. Numerical Validation

In this section, the proposed hydro-mechanical model is validated by simulating desiccation cracking tests presented in Chapter 4. The numerical results are then compared to the experimental results. This section starts with the description of the numerical samples, followed by the model parameters and results.

7.3.1. Model descriptions

In this study, numerical simulations were conducted for the experimental tests of rectangular samples with 12.4mm thick and circular samples with 5mm thick. Numerical samples were prepared by generating two groups of DEM particles, one represented soil, and the other represented the boundaries. The radii of all particles' varied uniformly from 0.45mm to 0.7mm. Accordingly, for the rectangular sample with dimensions of 251mm long, 25mm wide and 12.4 mm deep, 66468 and 27595 particles were used for soil and the boundaries, respectively, while for the circular sample with an internal diameter of 140mm and thickness of 5mm, 64751 and 38298 particles were used for soil and the boundaries, respectively. The boundary particles were fixed during the entire simulation process. In addition, interactions between soil-soil particles and soil-boundary particles were governed by the model presented in Section 7.2.3.2. Parameters for these interactions are discussed in next sections. Figure 7.6 shows the numerical samples. In this figure, the dark particles are the boundary particles, while the green particles are the soil particles.

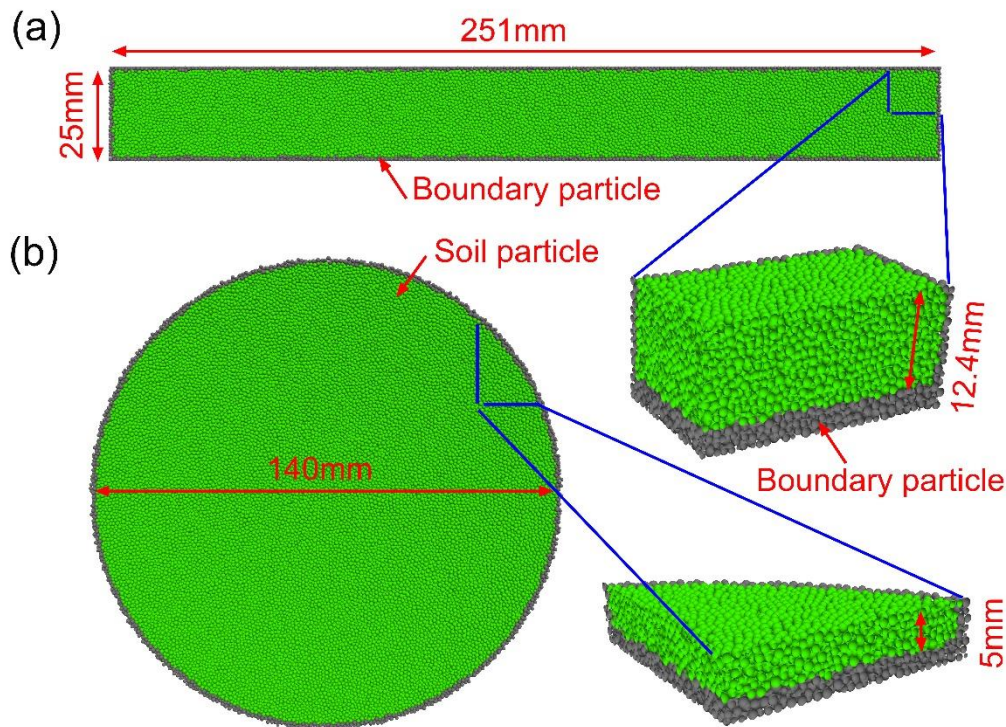


Figure 7.6. Numerical samples: (a) rectangular sample; (b) circular sample.

7.3.2. Model parameters

In this section, model parameters used in the simulations of soil desiccation cracking are presented. To obtain mechanical behaviour of samples during desiccation, mechanical parameters are obtained by calibrating the numerical results of three-point bending tests with experimental results, while to obtain hydraulic behaviour, hydraulic parameters and hydraulic boundary conditions are calculated from the literature and the experimental tests of rectangular and circular samples presented in Chapter 4. This section starts with the description of the mechanical parameters, followed by the hydraulic parameters and hydraulic boundary conditions.

7.3.2.1. Mechanical parameters

(a) Mechanical constitutive parameters for clays

The effective modulus, softening parameters, tensile strength and shear strength of contacts of soil particles were obtained by conducting numerical simulations three-point bending tests reported by Amarasiri et al. (2011a) for Werribee clay and benchmarking the numerical results against the experimental results.

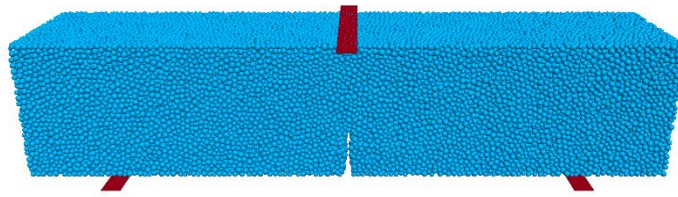


Figure 7.7. Numerical set-up of the three-point bending test.

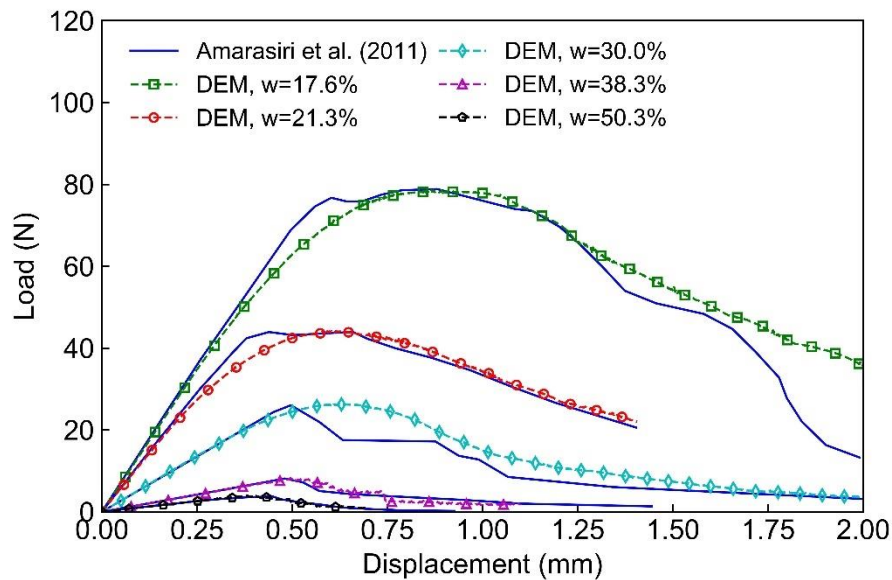


Figure 7.8. Load-displacement curves of three-point bending tests.

Figure 7.7 shows a typical numerical set-up. This setup was identical to the experimental set-up, in which the sample was supported by two small walls and was loaded by another wall that was located on the top surface at the centre of the sample. The distance between the two supports was 100mm. In addition, the numerical sample had the same dimensions and boundary conditions as the experimental sample, which was 140mm long, 30mm high, 30mm wide. A notch of 10mm height was at the middle of the sample. The numerical sample was created by an assembly of 98943 DEM particles with radii varying uniformly from 0.45mm to 0.7mm. This range was the same as the range used in the simulations of the desiccation cracking tests. The normal-to-shear stiffness ratio, friction coefficient, dilatancy angle and local damping were selected as 2.0, 0.5, 0.1 and 0.7, respectively. The shear strength was assumed to be equal to the tensile strength and the softening parameters were the same for both normal and shear directions (Nguyen et al. 2017).

The numerical and experimental results obtained from the three-point bending tests for samples at different gravimetric water content are plotted in Figure 7.8. It can be seen that after calibration, good agreement between the numerical and experimental results was obtained. All load-displacement curves showed linear behaviour at the beginning,

hardening behaviour until peak loads were reached and then softening behaviour. In addition, as gravimetric water content increased, initial stiffness and the peak load decreased.

Other mechanical constitutive parameters (i.e. the tensile strength, effective modulus and softening parameters of contacts) used in the simulations of the three-point bending tests are plotted in Figure 7.9. It can be seen that the tensile strength and effective modulus of contacts between DEM particles significantly increased with a decrease in gravimetric water content, while the softening parameters remained unchanged until gravimetric water content decreased to 38.3%. After that, these softening parameters strongly increased with a decrease in gravimetric water content. The increase in the mechanical constitutive parameters as the gravimetric water content decreased is attributed to an increase in suction as well as the capacity in binding particles (Lambert et al. 2008). To facilitate the process of estimating these parameters for the model during the simulation of soil cracking, the tensile strength, effective modulus and softening parameters of contacts were approximately formulated as functions of gravimetric water content (w in %) as follows:

$$\sigma_t^0 = 5 \times 10^7 \times w^{-1.435} \quad (7-54)$$

$$E^* = 2 \times 10^{12} \times w^{-3.056} \quad (7-55)$$

$$u_n^c \text{ or } u_s^c = \begin{cases} 4 \times 10^{-7} & \text{if } w \geq 38.3\% \\ -1.8 \times 10^{-5} \times w + 7 \times 10^{-4} & \text{if } w < 38.3\% \end{cases} \quad (7-56)$$

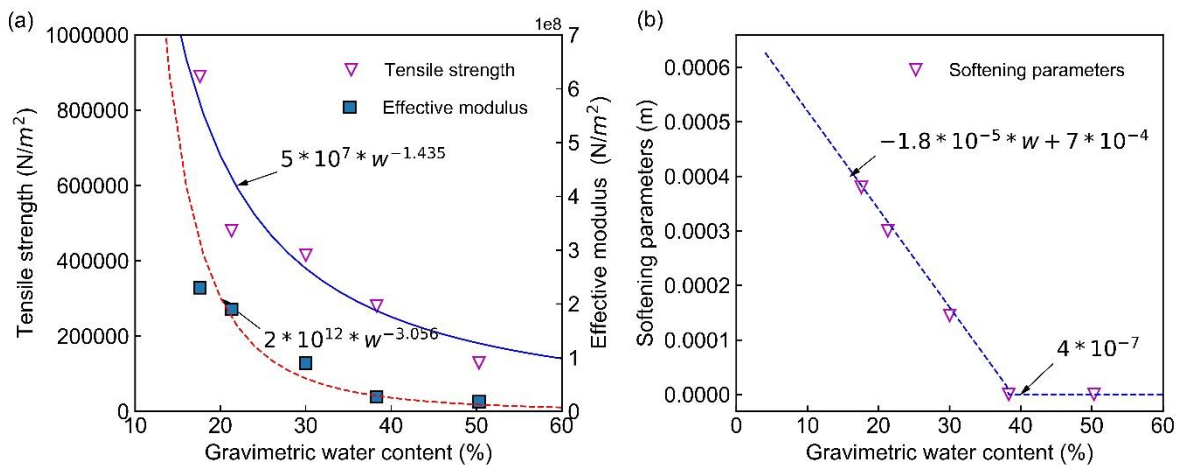


Figure 7.9. Mechanical constitutive parameters for DEM modelling.

In addition, as illustrated in Equation (7-1), the volumetric strain (ε_{sk}) is required to update radii of DEM particles in a given time step. In this study, this volumetric shrinkage strain

was linked to gravimetric water content by introducing the moisture shrinkage coefficient (α) given by (Kodikara and Choi 2006; Peron et al. 2009b):

$$\epsilon_{sk} = \alpha \Delta w \quad (7-57)$$

where $\Delta w = w_0 - w_t$ is the change of gravimetric water content; w_0 is the initial gravimetric water content, w_t is the gravimetric water content at time t and the moisture shrinkage coefficient, α , can be determined from free shrinkage tests.

To obtain the moisture shrinkage coefficient, a free shrinkage test was conducted for a circular sample 5mm thick. The sample was prepared from Werribee clay at water content of approximately 155%. The sample preparation was the same as that presented in previous sections. To allow the sample to shrink freely, grease was applied to all sides and the base of the mould. The test was conducted at room temperature following the testing procedure discussed in previous sections. During the test, the sample was monitored by a balance and two cameras. DIC techniques were used to analyse the strains.

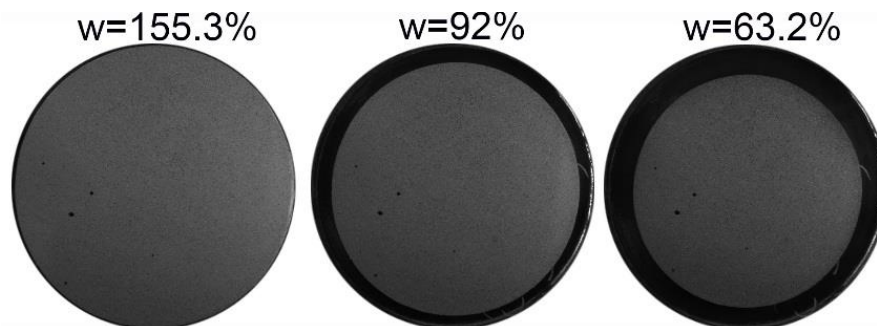


Figure 7.10. The shape of the sample during the free shrinkage test.

Changes in the shape of the sample during the free shrinkage test are plotted in Figure 7.10. It can be observed that the sample underwent uniform shrinkage in the radial and vertical directions. The evolution of gravimetric water content and volumetric water content of the sample during the free shrinkage test is plotted in Figure 7.11(a). It can be observed that change in water content followed the same trend during drying, first significantly decreasing with initial drying, then gradually approaching a stable value. The volumetric strain of the sample during drying was calculated. Calculated volumetric strain, prior to curling and cracking, is shown in Figure 7.11(b). It can be seen that volumetric strain increased linearly with an increase in the gravimetric water content change. This result is consistent with other studies, where free shrinkage tests were conducted for other materials with both slurry and compacted conditions (Kodikara and Choi 2006;

Peron et al. 2009b). Linear regression between volumetric strain and changes in water content yields a moisture shrinkage coefficient of 0.056.

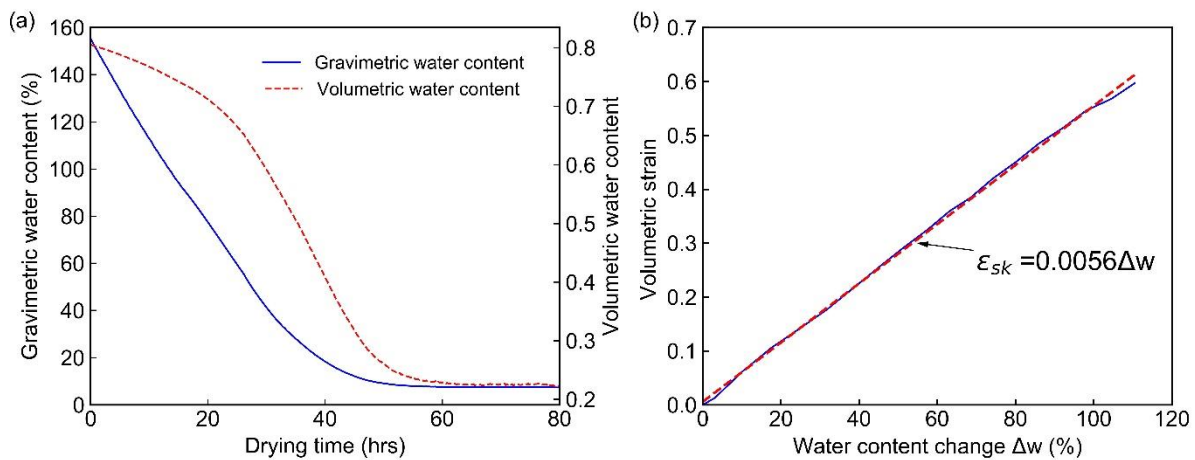


Figure 7.11. Results of the free shrinkage test: (a) changes in water content; (b) changes in volumetric strain.

(b) Constitutive parameters for the soil-mould interface

Previous studies have reported that the contact between soils and moulds significantly influences soil cracking. Corte and Higashi (1960) conducted experiments and reported that when the adhesion between soil and the bottom contact surface was large, more cracking occurred and the cracks were longer. Sima et al. (2014) and Gui et al. (2016) reported similar observations when 2D and 3D numerical simulations were conducted for rectangular samples and circular samples, respectively. However, the effect of the interface soil-mould contact on water content when the first crack occurred was negligible (Sima et al. 2014).

Previous numerical studies often selected contact parameters for soil-mould interaction by trial and error, in which many simulations with different sets of these parameters were conducted, and reported parameters that yielded a good agreement between numerical and experimental crack patterns. Sima et al. (2014) reported that reduction factors of 0.1 and 0.5 of the contact stiffness and bond strength gave good results when the desiccation cracking test of Romainville clay was simulated, while the parameters used in the study of Guo et al. (2017) for the desiccation cracking test of bentonite were 1 and 0, respectively. As the purpose of this study is to develop a hydro-mechanical model to study soil desiccation cracking as well as to understand the mechanism underlying the occurrence of cracks, there was no need to focus on calibrating these parameters. In this study, to take into account the weak interface between soil and the mould, the effective modulus, softening parameters and strengths of soil-mould contacts were selected as, respectively 0.25, 0.5 and 0.5 of the values of soil-soil contacts.

7.3.2.2. Hydraulic parameters and hydraulic boundary conditions

The initial volumetric water content of numerical samples was taken to be 0.809 for the rectangular sample and 0.807 for the circular sample, respectively. These values corresponded to the initial water content of the experimental samples, which are equivalent to gravimetric water contents of approximately 160% and 156%, respectively. The soil water retention data reported by Nahlawi (2004) for Werribee clay was adopted, which was used to determine the Van Genuchten model's parameters (Figure 7.12). The saturated hydraulic conductivity of 7.92×10^{-7} m/hrs was selected (reported in by Shannon (2013) for Werribee clay). Figure 7.1 shows that the fitted van Genuchten curve agreed fairly well with the experimental data reported by Nahlawi (2004). Note that fitting parameters used for the van Genuchten model were 0.81, 0.06, 8.0772×10^{-3} , 1.2176 for θ_s , θ_r , α and n respectively.

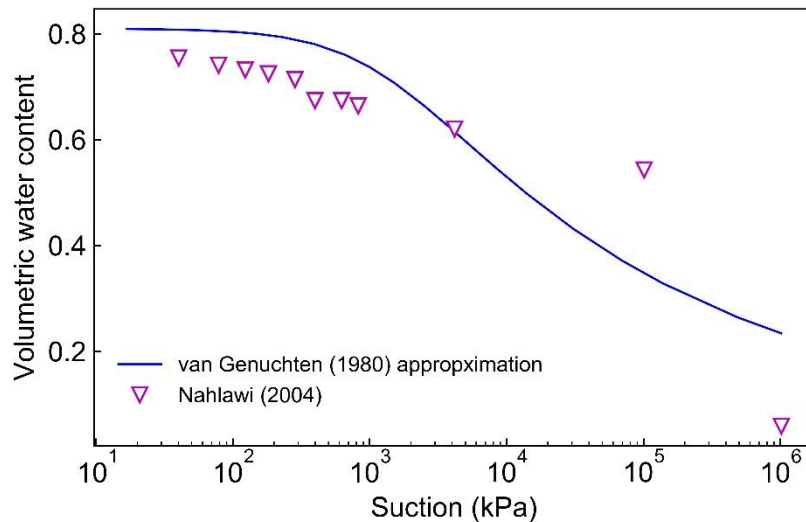


Figure 7.12. Soil water retention curve of Werribee clay.

For drying boundary conditions, flux was imposed only on the DEM particles that were on the sample surface and crack surfaces, while no flux was imposed on inside particles that were not exposed to the free surface (i.e. air environment). Note that the detachment of the samples from the mould was also considered as the occurrence of cracks for applying boundary conditions. In addition, the ratio between the flux through the sample surface and the flux through the crack surface was chosen to be 0.1, following the suggestion of Stirling et al. (2017). The reason for choosing this small ratio was due to the crack surface being shielded by atmospheric turbulence.

In this study, the flux on the numerical sample surface and crack surfaces was calculated based on the water evaporation rate of the experimental samples. Figure 7.13 shows the evolution of water evaporation rate of the experimental samples (SR1 and SR2 were

rectangular samples 1 and 2, while SC1 and SC2 were circular samples 1 and 2). This rate was calculated based on the initial area of the evaporative surface (A_{ss0}), which was 62.8cm^2 and 154cm^2 for the rectangular and circular samples, respectively. Figure 7.13 also shows that the water evaporation rate of the experimental samples almost remained unchanged until the drying time reached approximately 34 hrs for the rectangular samples and 24 hrs for the circular samples. After these times, water evaporation rate decreased significantly and then was almost zero when the drying time reached approximately 80h for the rectangular samples and 36.5 hrs for the circular samples. In addition, for each type of the sample shape, the evaporation rate of sample 1 was consistent with that of sample 2. The water evaporation rate E_t at a drying time t for the rectangular and circular samples can be approximately formulated as Equations (7-58) and (7-59), respectively. These equations were used to calculate the water evaporation rate at a given time. The values of these equations are also plotted in Figure 7.13 and are denoted as simulations.

$$E_t = \begin{cases} 1.6 \times 10^{-4} \frac{m}{hrs} & \text{if } t \leq 34 \text{ hrs} \\ -3.5 \times 10^{-6}t + 2.8 \times 10^{-4} \frac{m}{hrs} & \text{if } t > 34 \text{ hrs} \end{cases} \quad (7-58)$$

$$E_t = \begin{cases} 1.35 \times 10^{-4} \frac{m}{hrs} & \text{if } t \leq 24 \text{ hrs} \\ -1.0 \times 10^{-5}t + 3.75 \times 10^{-4} \frac{m}{hrs} & \text{if } t > 24 \text{ hrs} \end{cases} \quad (7-59)$$

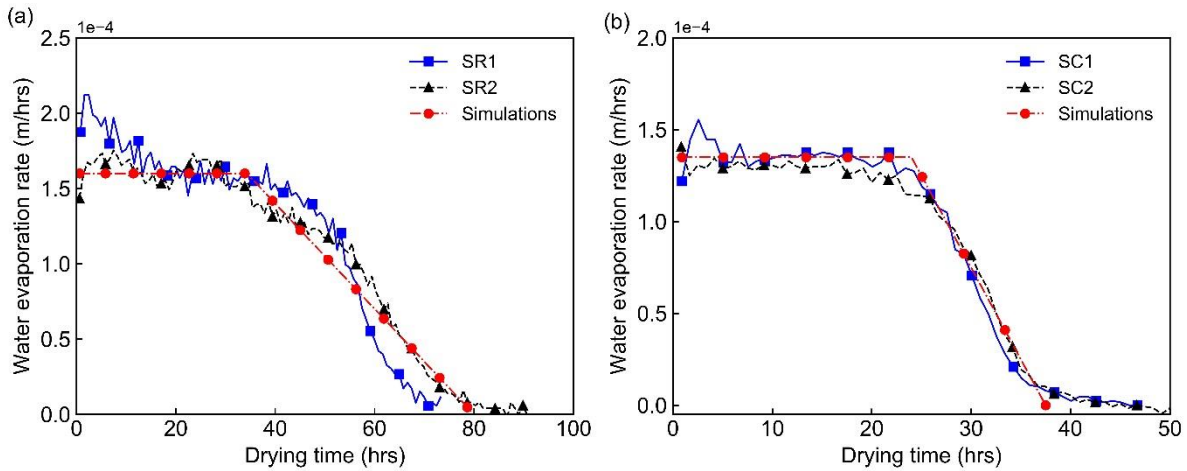


Figure 7.13. Water evaporation rates for the experimental data: (a) rectangular samples; (b) circular samples.

At a drying time t , if the area of the sample surface (A_{sst}) and the total area of the crack surface (A_{cst}) are known, the flux on the sample surface (E_{sst}) and the flux on the crack surface (E_{cst}) can then estimated as:

$$E_{sst} = E_t A_{ss0} / (A_{sst} + 0.1A_{cst}) \quad (7-60)$$

$$E_{cst} = 0.1E_{sst} \quad (7-61)$$

7.3.3. Numerical prediction of experimental results

In this section, the predicted results are presented and discussed. To evaluate the performance of the proposed framework in capturing hydraulic and mechanical behaviour of soil samples during desiccation, the predicted water content and cracking behaviour are compared to the measured and observed results. The behaviour of the numerical samples is then analysed and discussed to provide further understanding of soil desiccation cracking. This section starts with results of the rectangular sample, followed by results of the circular sample.

7.3.3.1. Rectangular sample.

Desiccation cracking of the rectangular samples was first simulated using the abovementioned parameters. The changes in water content of the numerical and experimental samples during drying are plotted in Figure 7.14. It can be seen that as the samples dried, the water content of all samples significantly decreased and gradually approached stable values. The water content of the numerical sample agreed well with the experimental counterpart, demonstrating that the proposed framework is able to capture unsaturated flow through deformed soil media.

The development of cracks in the numerical sample and experimental sample SR1 is shown in Figure 7.15. To highlight the development of cracks in the numerical sample, soil particles on the sample surface are shown as green and the remaining soil particles are red. It can be seen that the initiation and development of cracks in the numerical sample reflect with those observed in the experimental sample. At the beginning of the desiccation process, all samples started shrinking and detaching from the mould. The first crack then initiated from one long edge of the samples, propagated transversely and reached the other long edge when water content was approximately 127.1% and 124.2% for the experimental and numerical samples, respectively. As the desiccation process continued, the sample continuously shrank, the first crack became wider, while more cracks initiated and developed following the same behaviour as the first crack. When the water content was 117.6%, two more cracks appeared in both samples. With further drying, no more cracks occurred in the numerical sample, while two more cracked occurred in the experimental sample. In addition, the width of cracks in all samples continued to develop. Figure 7.15 shows that the water content when cracks occurred in

the numerical sample was slightly lower than that in the experimental sample. Furthermore, the number of cracks in the numerical sample was less than in the experimental sample. However, the location and sequence of the development of cracks were similar in both numerical and experimental samples, as well as cracks in both samples being curved.

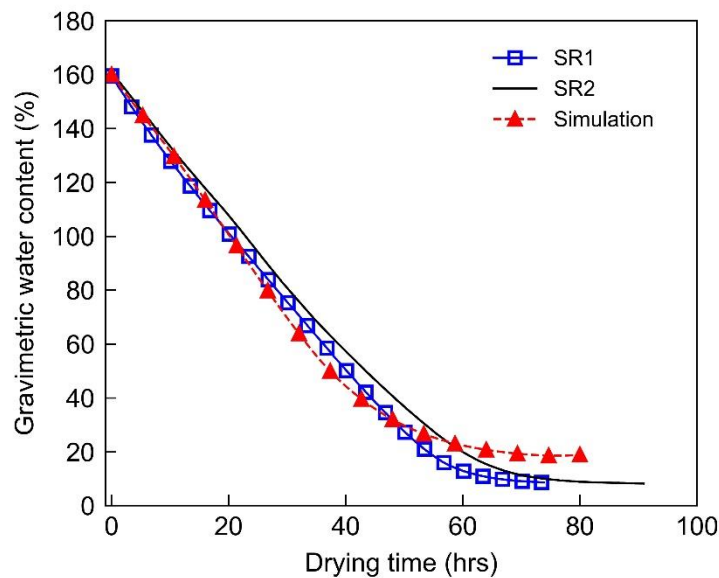


Figure 7.14. Evolution of water content during the simulation of the rectangular sample.

The slight differences in water content when cracks appeared and the number of cracks in the numerical and experimental samples were also reported in previous studies when numerical results were compared to experimental results (Guo et al. 2017; Sima et al. 2014; Stirling et al. 2017; Vo et al. 2017). These differences may be attributed to the heterogeneous properties and the occurrence of flaws inside samples. In this study, although the experimental samples were prepared from slurry clay with high water content (i.e. the initial gravimetric water content was 160%), these samples were not fully homogenous perhaps because air could be trapped inside or weak zones could be introduced in sample preparation. Therefore, in the experimental samples, cracks could occur earlier when the water content was high and the number of cracks could be higher. Note that differences in water content when cracks appeared and the number of cracks also occurred when two identical experimental samples SR1 and SR2 were dried under similar conditions (Figure 7.16). Based on the above discussion, it can be concluded that the proposed framework is capable of modelling soil desiccation cracking.

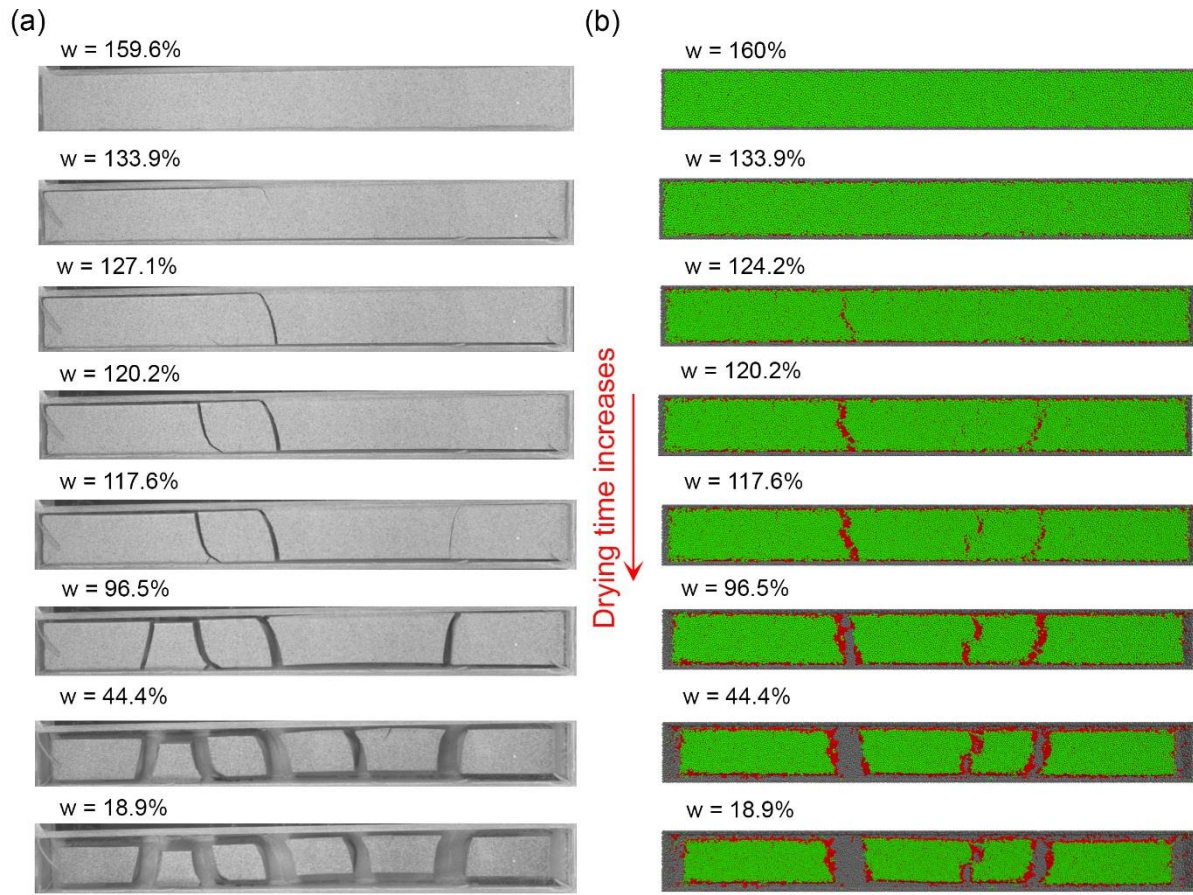


Figure 7.15. Development of cracks in rectangular samples: (a) experimental sample SR1; (b) numerical sample.

As discussed above in the numerical simulation, particles are bonded by a cohesive contact model representing the tensile strength clay due to suction and other inter-particle forces (e.g. van der Waal force) (Mitchell and Soga 2005). When the bonds are fully damaged ($D_c \approx 1$) and break, micro-cracks occur inside the specimen. Macro-cracks that connect these micro-cracks will eventually form in the specimen and progress with the moisture evaporation. Figure 7.17 shows the development and distribution of micro-cracks in the numerical sample. In this figure, dark small circles represent contact bonds that have been broken (i.e. a micro-cracks) in the specimen. To facilitate the discussion, these micro-cracks are also classified into soil-soil micro-cracks and soil-boundary micro-cracks, which represent breakage of soil-soil and soil-boundary contact bonds, respectively. It can be seen that as water evaporated, the sample started shrinking and micro-cracks developed. At a water content of 133.9%, micro-cracks developed around the sides of the sample, mostly consisting of soil-boundary micro-cracks, indicating the detachment of the sample from the sides of the mould. After that, as water content decreased, micro-cracks continued to develop. When water content was 124.2%, soil-boundary micro-cracks appeared at the base, around the two ends of the sample, while

soil-soil micro-cracks appeared inside the sample and they concentrated along a line indicating formation of the first macro-crack.

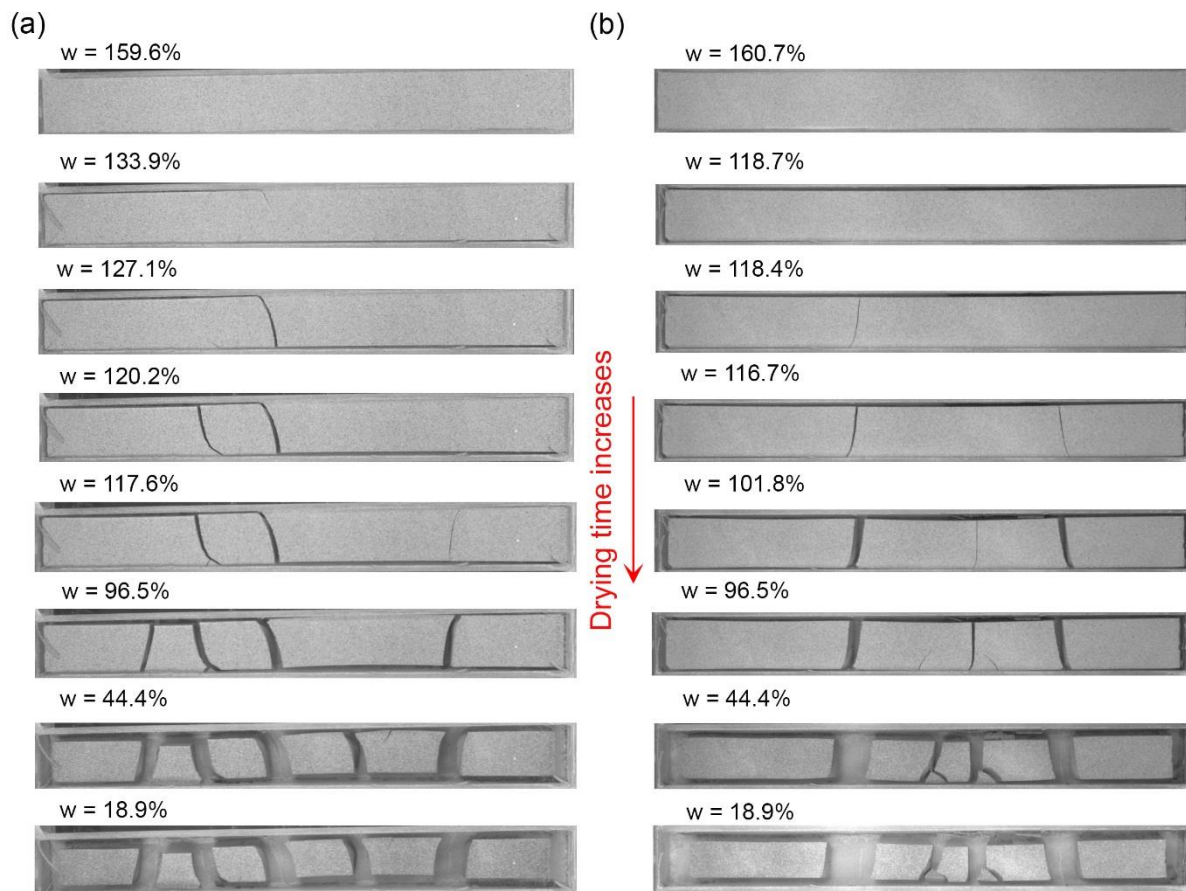


Figure 7.16. Cracks in two experimental samples: (a) sample SR1; (b) sample SR2.

After the formation of the first macro-crack, more soil-boundary micro-cracks appeared at the base, around the crack line, while more soil-soil micro-cracks concentrated at some locations inside the sample. When water content was 117.6%, soil-soil micro-cracks concentrated along three lines indicating the formation of three macro-cracks. After this period, soil-boundary micro-cracks appeared at the base, while soil-soil micro-cracks appeared randomly inside the sample. The development of micro-cracks agreed well with the shrinkage process of the experimental sample presented in Chapter 4. At the beginning of the process, water content decreased and the experimental sample shrank in all directions. After a certain water content was reached, the sample started detaching from the sides of the mould, indicating the development of soil-boundary micro-cracks. In addition, the strain of the sample was highly concentrated at the ends of the sample and at crack lips, indicating that micro-cracks could also develop at the interface between the soil sample and the base of the mould. This agreement confirms the validity of the proposed framework. In fact, this behaviour has been not captured in previous studies using DEM. For example, by looking at the evolution of the number of the micro-crack,

Sima et al. (2014) reported that the micro-cracks mainly occurred inside the numerical sample and soil-boundary micro-cracks appeared very late, after the formation of macro-cracks.

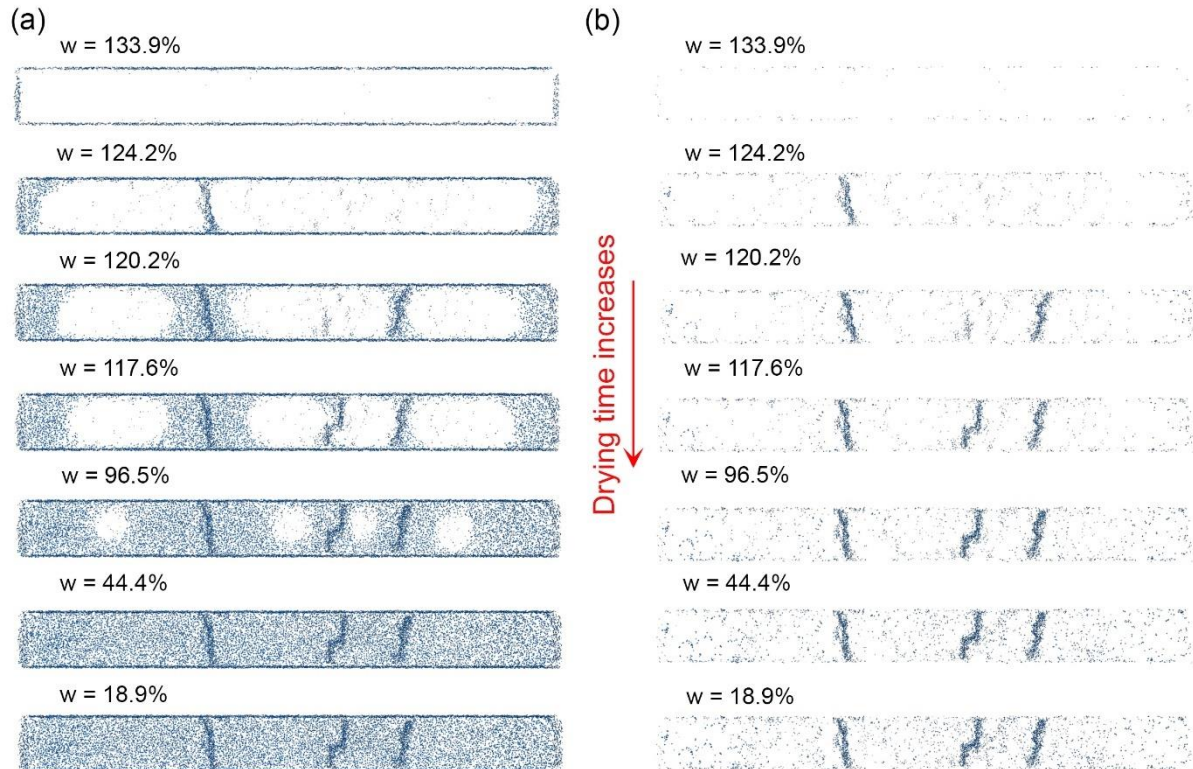


Figure 7.17. Development of micro-cracks in the rectangular sample: (a) all micro-cracks; (b) soil-soil micro-cracks.

The changes in the number of micro-cracks during drying of the numerical sample are plotted in Figure 7.18. It can be seen that soil-boundary micro-cracks started occurring after 3.7 hours of drying, while soil-soil micro-cracks started appearing after 5.8 hours of drying. The number of these cracks then increased significantly and gradually approached stable values. After 46.1 hours of drying the number of new micro-cracks for both types of micro-crack was negligible. During drying, the number of soil-boundary micro-cracks was much larger than that of soil-soil micro-cracks. For example, after 20 hours of drying, there were 11883 soil-boundary micro-cracks and 2896 soil-soil micro-cracks. Figure 7.18 also shows that soil-boundary micro-cracks and soil-soil micro-cracks appeared when the numerical sample was at very high water contents, 149.5% and 143.7%, respectively. As the water content decreased, the number of these cracks increased significantly until the water content reached approximately 100% and 120% for soil-boundary micro-cracks and soil-soil micro-cracks, respectively, and then gradually approached stable values.

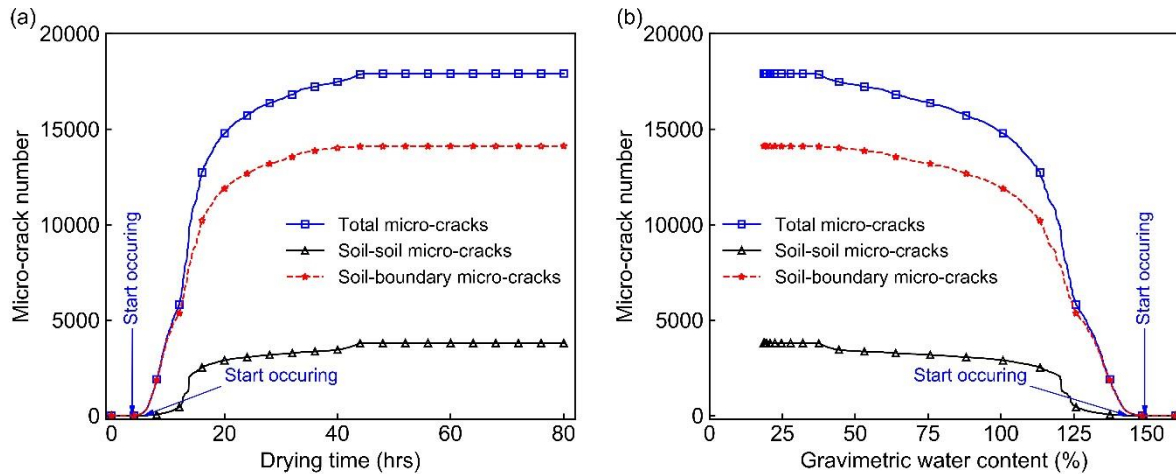


Figure 7.18. Evolution in the number of micro-cracks during the simulation of the rectangular sample: (a) the number of micro-cracks against drying time; (b) the number of micro-cracks against gravimetric water content.

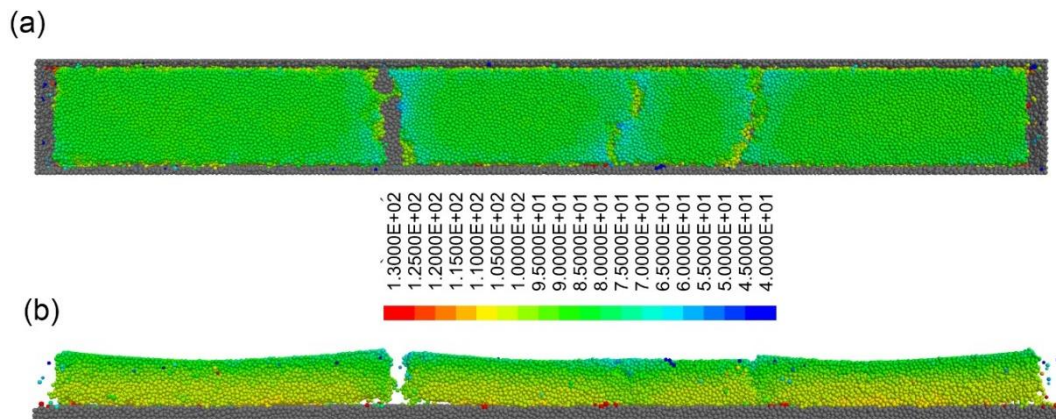


Figure 7.19. Distribution of gravimetric water content in the numerical sample with rectangular shape at an average water content of 96.5%: (a) top view; (b) side view.

The distribution of gravimetric water content in the numerical sample at an average water content of 96.5% is plotted in Figure 7.19. It can be observed that the water content was fairly uniform on the sample surface, except at/on crack lips where the water content was smaller. On the other hand, increased depth corresponded to higher water content. This distribution is consistent with that reported in literature. Nahlawi and Kodikara (2006) conducted desiccation cracking tests of slurry clayey soils and measured the water content of the top half and bottom half of samples. They reported that the water content of the top half was always less than that of the bottom half during testing. This agreement again confirms that the proposed framework can capture the hydraulic behaviour of samples during desiccation. Furthermore, concave-up curling occurred in the simulation (Figure 7.19), indicating that the increase in the number of soil-boundary micro-cracks after the appearance of all macro-cracks could also be attributed to the occurrence of concave-up curling.

7.3.3.2. Circular sample

In this second test, the proposed coupled hydro-mechanical DEM framework was applied to predict cracking in circular samples. Soil parameters presented in Section 7.3.2 were adopted. Figure 7.20 shows the changes in water content of the numerical sample and experimental samples with circular shape during drying Figure 7.20. It can be seen that the changes in water content of the numerical sample are consistent with those of the experimental samples. The water content in all samples during drying exhibited a strong decline period, followed by a gradual decrease to residual values. The results again demonstrate the capability of the proposed framework to model unsaturated flow through deformed soil media.

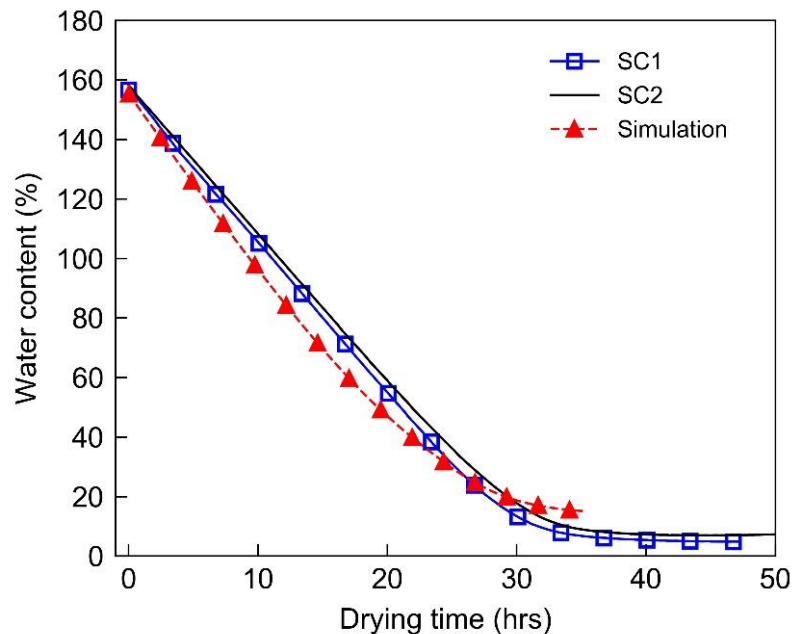


Figure 7.20. Evolution of water content during the simulation of the circular sample.

The development of cracks in the numerical sample and experimental sample SC1 is plotted in Figure 7.21. It can be observed that two cracks first initiated at a water content of 126.8% and 122.7% for the numerical and experimental samples, respectively. These cracks then propagated towards the centre and boundary of the sample and more cracks initiated. After the water content reached 53.4%, no new cracks initiated, while the existing cracks continued to widen until the end of drying. Figure 7.21 shows that the numerical results (i.e. water content when the first crack initiated, the cracking process and the crack pattern) are consistent with the experimental results, except that the rate of appearance of cracks in the numerical sample was faster than that in the experimental sample. This has been suggested to be due to the lack of plastic behaviour at bonds between DEM particles (Guo et al. 2017; Sima et al. 2014). As indicated in Equation

(7-38), the plastic behaviour of a bond between two particles depends on the softening parameters. In this study, these parameters, which were calibrated from the results of the three-point bending tests, were 4×10^{-7} when the water content was larger than 38.3%. A small value implies that the behaviour of the sample was still brittle, so the cracks appeared in the numerical sample faster.

The development and distribution of micro-cracks in the numerical sample with circular shape is plotted in Figure 7.22. At the beginning of drying, when the water content was very high (e.g. 128.2%), soil-boundary micro-cracks mainly occurred at the sides of the sample, indicating the detachment of the sample from the mould, while soil-soil cracking occurred randomly inside the sample. As the soil sample continued to shrink, soil-boundary micro-cracks continued to appear at the sample sides, while soil-soil micro-cracking occurred mainly within the sample, forming macro-cracks. When the water content was 115.3, soil-boundary micro-cracks appeared at the bottom surface of the sample, while soil-soil micro-cracks appeared at specific locations to form a macro-crack pattern. After this period, more soil-boundary micro-cracks continued to appear at the bottom surface of the sample, while more soil-soil micro-cracks appeared randomly inside the sample. The development of micro-cracks in the numerical sample can be summarised into three stages: 1) micro-cracks occurred at the sample sides, indicating the detachment of the sample from the mould; 2) micro-cracks occurred inside the sample to form a crack pattern; 3) micro-cracks occurred at the interface of the sample with the base of the mould.

Evolution of the number of micro-cracks during drying is plotted in Figure 7.23. It can be seen that as drying started, water started evaporating, causing the sample to shrink. However, the appearance of soil-boundary and soil-soil micro-cracks started appearing only when the drying time was 3.31 and 3.46 hours, respectively, corresponding to respective water contents of 135.3% and 134.5%. After this, water continued to evaporate and more of these cracks appeared, especially soil-boundary micro-cracks. After approximately 20 hours of drying, although the water content of the sample was very high (e.g. 47%) and water was still evaporating, only a few micro-cracks appeared. Figure 7.18 also shows that during drying, the number of soil-boundary micro-cracks was much larger than that of soil-soil micro-cracks.

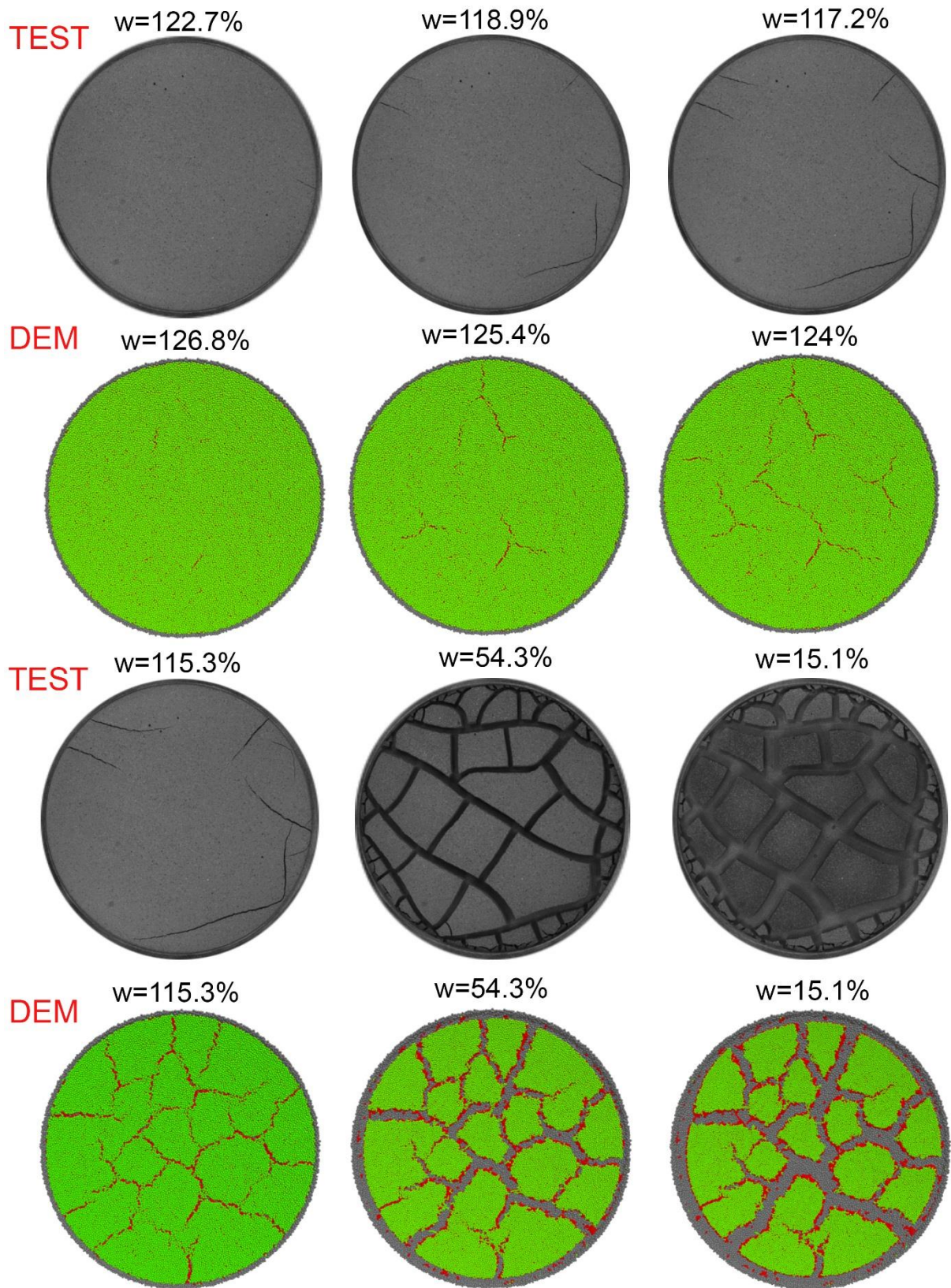


Figure 7.21. Development of cracks in the numerical sample and experimental sample (SC1).

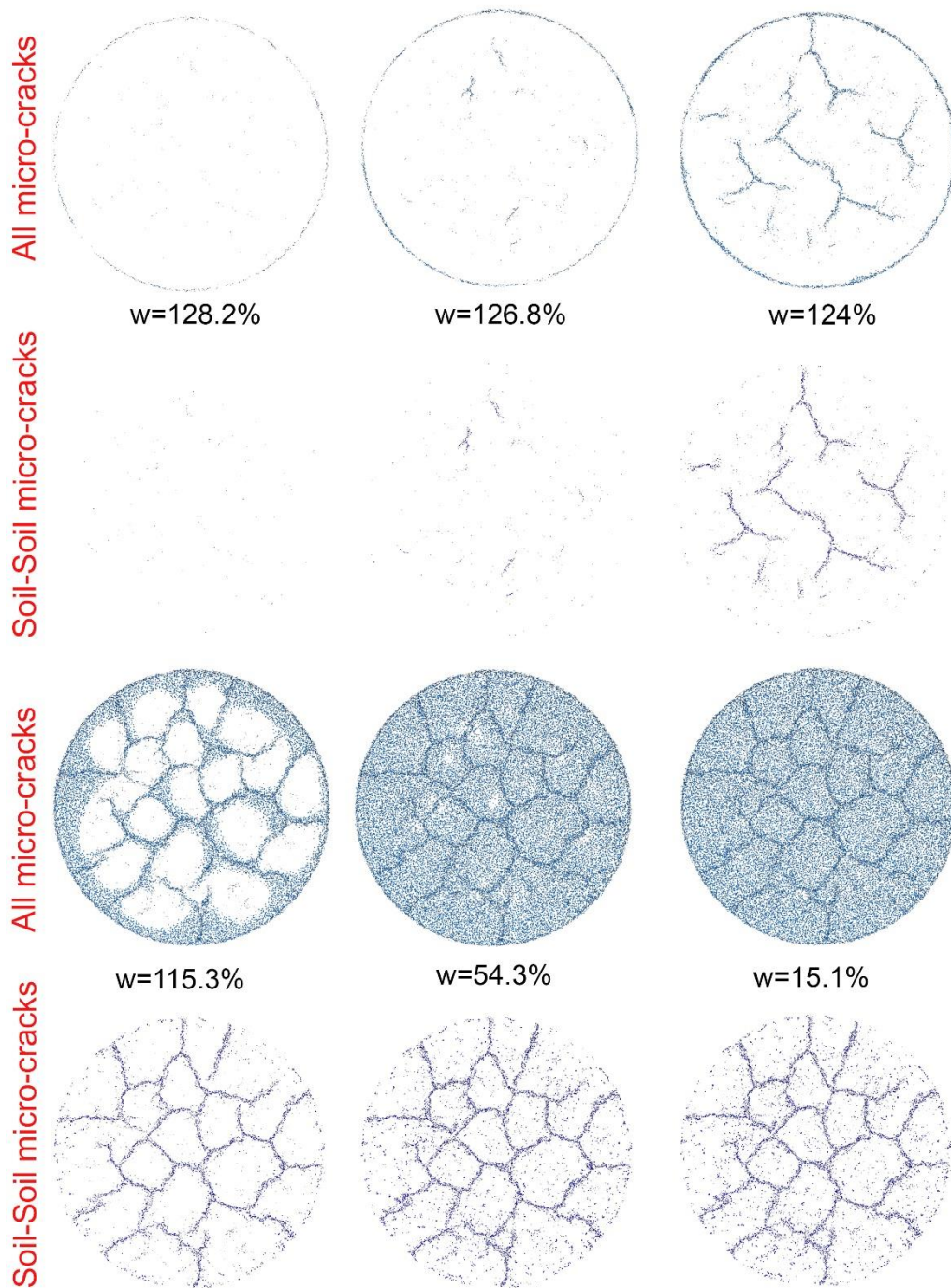


Figure 7.22. Development of micro-cracks in the circular sample: (a) all micro-cracks; (b) soil-soil micro-cracks.

The distribution of gravimetric water content in the numerical sample at an average water content of 71.6% is plotted in Figure 7.24. The water content was similar everywhere on the sample surface, except at/on crack lips where the water content was slightly smaller. In addition, along the height of the sample, the water content was smaller for locations near the sample surface. This behaviour was also reported in literature when drying tests were conducted for soil samples (Nahlawi and Kodikara 2006; Song et al. 2013). Figure

7.24 also shows the appearance of concave-up curling in the numerical sample. This type of soil curling was also observed in the experimental sample indicated in Figure 7.25.

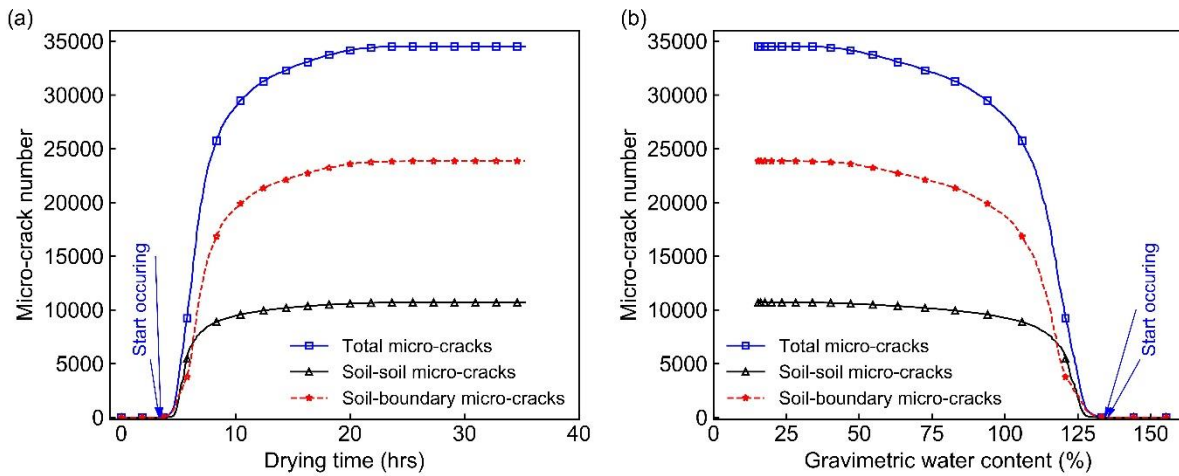


Figure 7.23. Evolution in the number of micro-cracks during the simulation of the circular sample: (a) the number of micro-cracks against drying time; (b) the number of micro-cracks against gravimetric water content.

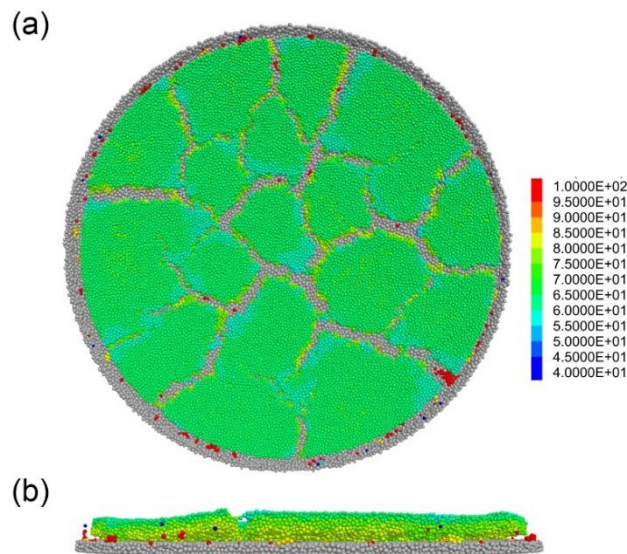


Figure 7.24. Distribution of gravimetric water content in the numerical sample with circular shape at an average water content of 71.6%: (a) top view; (b) side view.



Figure 7.25. SC1 sample after drying.

7.4. Conclusions

This chapter has presented a DEM-based hydro-mechanical framework for predicting soil desiccation cracking. In this framework, a soil layer is discretised into an assembly of DEM particles that are bonded together at their contacts. This feature allows the framework to capture the mechanical behaviour of clayey soils at a meso-level, in which several clayey particles gather together to form a clay aggregate, and clay aggregates are linked together by water to form soil layers that can carry compressive, tensile and shear forces. In addition, to capture mixed-mode failure (a combination of tensile failure mode and shear failure mode) during desiccation, a cohesive model is used to regulate the occurrence of fractures in the bonds. To capture the hydraulic behaviour of deformable soil layers, the approach proposed in Chapter 6 for modelling unsaturated flow through soil media is extended with consideration of the volumetric deformation of the soil skeleton in the governing equations of water flow. A numerical algorithm is proposed to link the hydraulic behaviour to the mechanical behaviour. The proposed framework is then used to model the soil desiccation cracking process occurring in the experimental samples with rectangular and circular shapes presented in Chapter 4. The numerical results are compared with the experimental results. Very good agreement was obtained for both hydraulic behaviour (e.g. the evolution of water content) and mechanical behaviour (e.g. the occurrence and development of cracks), suggesting that the proposed framework is able to accurately predict the behaviour of soil layers during desiccation as well as the formation of cracks. This framework can be applied to investigate the effect of various factors on soil desiccation cracking as well as the hydro-mechanical behaviour of soils in geotechnical applications.

Chapter 8. Conclusions and Recommendations

8.1. Conclusions

In this research, soil curling and soil desiccation cracking in clayey soils have been comprehensively investigated by conducting experimental tests on different types of soils and under different environmental conditions. Numerical frameworks have also been developed to predict the occurrence and development of these phenomena. The main conclusions drawn from this research are presented in the following sections.

8.1.1. Soil curling

Concave-up curling and convex-up curling that occurred in a soil sample during desiccation were investigated. It was found that during desiccation, concave-up curling follows two main stages. In the first stage, the soil sample shrinks and detaches from the mould. In this stage, the sample is saturated. In the second stage, the edges of the sample start lifting up to form concave-up curling when the sample is almost saturated. This lifting up process continues until the water content of the sample approaches the plastic limit of the soil. After that, the sample retains its shape until its water content is low. The edges of the sample then continue to lift off until the sample is almost dried.

Convex-up curling occurs following four main stages, the first two stages of which are similar to the first two stages of concave-up curling. However, the second stage of convex-up curling stops earlier and there is no temporary stable period. In the third stage, the curled edges retreat downwards and in the fourth stage, the middle of the sample lifts off to form convex-up curling when the water content is close to the plastic limit of the soil. This process continues to develop until the sample is almost dried.

In this work, it was also found that initiation and development of soil curling can be explained by considering the development of the capillary forces caused by the reduction of water content during desiccation. The horizontal component of this force causes the soil sample to detach from the mould, while the upward bending moment created by the non-uniform distribution of this component along the height of the sample lifts the edges of the sample to form concave-up curling. In addition, the continuous development of concave-up curling at low water content or the formation and development of convex-up curling may be caused by buckling of the sample due to a large capillary force.

The effect of clay minerals, initial water content, drying temperature and sand/clay fraction on soil curling was then investigated. The results revealed that in clays with a dominance of Smectite mineral, concave-up curling develops first and then convex-up curling, while

in clays with a dominance of Kaolinite mineral, only concave-up curling develops. For the same type of clayey soil, an increase in the initial water content causes the water content when concave-up curling or convex-up curling initiates and the lift-off height to decrease, while an increase in the drying temperature causes these values to increase.

For the effect of sand/clay fraction on soil curling, the results also demonstrated that as the sand/clay fraction increases, the water content when concave-up curling begins and the lift-off height of concave-up curling increase, while the water content when convex-up curling begins and the lift-off height of convex-up curling decreases. In addition, the soil curling behaviour of the sample completely changes for a given sand/clay fraction. For example, only concave-up curling occurs in the Werribee clay sample with a sand/clay fraction of 30%, while concave-up curling occurs first followed by convex-up curling in the Werribee clay sample with a sand/clay fraction of less than 30%.

8.1.2. Soil desiccation cracking

The mechanism underlying the desiccation cracking process was investigated in this study through measurement of the strain fields on the sample surface during experimental tests on samples with different shapes. The results show that cracks initiate and propagate in zones of high tensile strain. By considering the direction of principal strain developments, it can be concluded that cracks initiate due to a combination of shear and tensile loads (or mixed-mode loading) within the sample, while propagation of cracks is only due to tensile load.

The effect of wind velocity on soil desiccation cracking was also investigated and found to be significantly influenced the soil cracking process. Under a high wind speed, cracks initiate earlier in soil samples to form a complex crack pattern with a larger number of cracks. The crack density factor of the soil samples also increased with wind speed. However, at the end of the desiccation process, the crack density factors of all samples dried under different wind velocities are almost the same.

8.1.3. Development of numerical tools

Based on observations and measurements from the experimental tests and from experimental studies reported in the literature, DEM-based numerical frameworks were developed in this research to predict the processes of soil curling and soil desiccation cracking. In the first framework, the behaviour of clayey soil at the micro-level was considered to predict the mechanical behaviour of samples at lab-scale, while in the second framework, the behaviour of clayey soil at the meso-scale was considered to predict the coupled hydro-mechanical behaviour of soil during desiccation cracking at a large scale. Therefore, in the second framework, an approach was proposed to model unsaturated flow. Numerical algorithm was then developed to couple the hydraulic

behaviour and mechanical behaviour. In the following subsections, the different numerical frameworks are discussed.

8.1.3.1. A water particle concept for modelling soil curling

A new water particle concept was developed in this research for predicting soil curling that occurs during desiccation of clay slurries. Unlike existing DEM approaches that only consider the solid phase, the proposed method explicitly models both solid and liquid phases, i.e. soil and water, using spherical particles. The water loss can be explicitly simulated by shrinking the size of the water particles, while the solid phase particles remain unchanged. To model the soil-water interaction during drying, an existing liquid bridge force model commonly used in DEM to deal with unsaturated soils was modified to extend its working range to tackle problems involving soils with high water content. This new approach allows a close description of slurry soils mimicking actual experimental conditions and enabling the simulation of soil particles suspended in water including their transition to the semi-solid state as water evaporates during drying.

The proposed approach was then applied to simulate the soil curling behaviour of a Kaolin NY specimen during desiccation. The results show that the new approach can qualitatively capture key characteristics of soil curling occurring in the experimental sample as well as the effect of factors controlling the formation and development of soil curling. Therefore, the new approach is a promising computational tool to study soil curling as well as to provide insights into transition behaviour of soils from the slurry to semi-solid states involving both saturated and unsaturated soil conditions.

8.1.3.2. A DEM-based approach for modelling unsaturated flow

A new DEM-based approach was developed in this research for modelling unsaturated flow through soil media. In contrast with existing approaches where the discrete porous medium is often represented by a continuum medium or a background mesh is required, the proposed approach exploits the discrete contact network of solid particles to model unsaturated seepage flows. In the network, each particle has its own solid volume, carries unsaturated flow information (e.g. hydraulic conductivity and volumetric water content) and occupies an equivalent-continuum space, which can be approximated based on the volume of the solid particle and its surrounding porosity. Water flow that is governed by Darcy's law is assumed to occur through contact points between two particles and directly from the centre of the particle with a higher water content to that of the particle with lower water content. Thanks to this concept, the proposed approach is capable of describing the nature of flow in unsaturated porous media at the micro-scale level, in which water flows along the water films that adhere to particles. This unique feature also enables the proposed approach to naturally simulate water flows through the heterogeneous porous media without any ad-hoc treatments. The proposed approach was verified by predicting

infiltration and evaporation of water from an unsaturated soil column under different boundary conditions. Very good agreement was achieved between the predictions of the proposed approach when compared to predictions made by FDM, even for different particle packing and distributions. This demonstrates that the proposed approach is capable of accurately predicting unsaturated flow through soil media.

8.1.3.3. A hydro-mechanical framework for modelling soil cracking

A DEM-based hydro-mechanical framework was developed in this study for predicting soil desiccation cracking. In the proposed framework, a soil layer is represented by an assembly of DEM particles. Each DEM particle represents a clay aggregate that is a group of discrete clay particles linked together due to forces at a micro-level (e.g. van der Waal force, double layer force). During drying, these particles interact with each other via a system of normal and tangential springs. These springs can carry compressive, tensile and shear forces that represent the mechanical forces and forces caused by suction due to a reduction in water content within the soil layer. The behaviour of these springs is governed by a cohesive model, which takes into account the mixed-mode failure (a combination of tensile failure mode and shear failure mode). This feature ensures that the framework is able to capture cracking in the soil layer due to mixed-mode failure.

In addition, the approach proposed for modelling unsaturated flow through soil media was extended to accurately model water flow through deformed soil media by considering the presence of volumetric deformation of the soil skeleton in the governing equations of water flow. To couple hydraulic behaviour and mechanical behaviour, during every simulation time-step, the hydraulic behaviour of the soil layer was first analysed, which was then translated in changes in the parameters for the mechanical behaviour analysis (e.g. the soil strength, stiffness of springs and radii of particles). The proposed framework was validated by simulating the soil desiccation cracking process occurring in rectangular and circular experimental samples, which was then compared to physical experimental results. Very good agreement in both hydraulic behaviour (e.g. the evolution of water content) and mechanical behaviour (e.g. the occurrence and development of cracks) demonstrates that the proposed framework is a promising numerical tool for predicting hydro-mechanical behaviour of soil.

8.2. Recommendations for Future Work

A comprehensive understanding of soil curling and soil desiccation cracking has been established in this study through conducting both experimental and numerical tests. Numerical frameworks have been also successfully developed to predict the occurrence and development of these phenomena. However, to extend the understanding of these phenomena, the following studies should be conducted in the future:

1. To provide further understanding of the mechanism of these phenomena, experimental tests using advanced techniques, such as laser scanners and force, moisture and suction measurement sensors, should be conducted. With these techniques, the development of stresses as well as the heterogeneous distribution of water inside soil samples during soil curling and soil cracking can be quantified.
2. Numerical simulations using the proposed water particle approach should be conducted to investigate the soil curling process that occurs in Werribee clay samples, the effect of grain size on shrinkage and curling. More simulations should be conducted to find what would prevent this approach from simulating curling in sands, something which would not happen in reality. In addition, simulations using smaller particle sizes should be conducted. This could allow more insights into soil curling to be obtained.
3. As desiccation of soil involves thermodynamic processes, the proposed hydro-mechanical framework should be further developed to be able to describe the coupled thermal-hydro-mechanical behaviour of soil desiccation. The advanced framework could allow boundary conditions of tested samples to be properly described and the behaviour of the tested samples to be accurately predicted during the development of soil curling and soil desiccation cracking. More studies should also be conducted by using the proposed framework to investigate the effect of grain size and grain size distribution on soil cracking.

References

- Ai, J., Chen, J.-F., Rotter, J.M., and Ooi, J.Y. 2011. Assessment of rolling resistance models in discrete element simulations. *Powder Technology* **206**(3): 269-282. doi: 10.1016/j.powtec.2010.09.030.
- Albrecht, B.A., and Benson, C.H. 2001. Effect of Desiccation on Compacted Natural Clays. *Journal of Geotechnical and Geoenvironmental Engineering* **127**(1).
- Allen, J.R.L. 1986. On the curl of desiccation polygons. *Sedimentary Geology* **46**(1): 23-31. doi: 10.1016/0037-0738(86)90003-5.
- Amarasiri, A.L., Costa, S., and Kodikara, J.K. 2011a. Determination of cohesive properties for mode I fracture from compacted clay beams. *Canadian Geotechnical Journal* **48**(8): 1163-1173. doi: 10.1139/t11-031.
- Amarasiri, A.L., and Kodikara, J.K. 2013. Numerical Modeling of Desiccation Cracking Using the Cohesive Crack Method. *International Journal of Geomechanics* **13**(3).
- Amarasiri, A.L., Kodikara, J.K., and Costa, S. 2011b. Numerical modelling of desiccation cracking. *International Journal for Numerical and Analytical Methods in Geomechanics* **35**(1): 82-96.
- Amir, O., and Neuman, S.P. 2001. Gaussian Closure of One-Dimensional Unsaturated Flow in Randomly Heterogeneous Soils. *Transport in Porous Media* **44**(2): 355-383. doi: 10.1023/a:1010706223350.
- Asahina, D., Houseworth, J.E., Birkholzer, J.T., Rutqvist, J., and Bolander, J.E. 2014. Hydro-mechanical model for wetting/drying and fracture development in geomaterials. *Computers & Geosciences* **65**: 13-23.
- Bear, J.J., and Cheng, H.-D.A. 2010. Unsaturated Flow Models. *In Modeling Groundwater Flow and Contaminant Transport*. Springer Netherlands, Dordrecht. pp. 251-340.
- Bell, F.G. 2006. *Engineering Geology*. 2nd edition ed. Elsevier.
- Berg, P. 1999. Long-term simulation of water movement in soils using mass-conserving procedures. *Advances in Water Resources* **22**(5): 419-430. doi: 10.1016/S0309-1708(98)00032-3.
- Berney, E.S., Hodo, W.D., Peters, J.F., Myers, T.E., Olsen, R.S., and Sharp, M.K. 2008. Assessment of the effectiveness of clay soil covers as engineered barriers in waste disposal facilities with emphasis on modeling cracking behavior. US Army Corps of Engineers, Engineer Research and Development Center.
- Black, W.P.M. 1962. A method of estimating the california bearing ratio of cohesive soils from plasticity data. *Géotechnique* **12**(4): 271-282. doi: 10.1680/geot.1962.12.4.271.
- Blunt, M., King, M.J., and Scher, H. 1992. Simulation and theory of two-phase flow in porous media. *Physical Review A* **46**(12): 7680-7699. doi: 10.1103/PhysRevA.46.7680.
- Bradley, W.H. 1933. Factors that determine the curvature of mud-cracked layers. *American Journal of Science* **26**(151): 55-71. doi: 10.2475/ajs.s5-26.151.55.

- Bui, H.H., Kobayashi, T., Fukagawa, R., and Wells, J.C. 2009. Numerical and experimental studies of gravity effect on the mechanism of lunar excavations. *Journal of Terramechanics* **46**(3): 115-124. doi: 10.1016/j.jterra.2009.02.006.
- Bui, H.H., and Nguyen, G.D. 2017. A coupled fluid-solid SPH approach to modelling flow through deformable porous media. *International Journal of Solids and Structures* **125**: 244-264. doi: 10.1016/j.ijsolstr.2017.06.022.
- Bui, H.H., Nguyen, G.D., Kodikara, J., and Sanchez, M. 2015. Soil cracking modelling using the mesh-free SPH method. *In* 12th Australia New Zealand Conference on Geomechanics (ANZ12), Wellington, New Zealand.
- Cattafesta, L., Bahr, C., and Mathew, J. 2010. Fundamentals of Wind-Tunnel Design. *In* Encyclopedia of Aerospace Engineering.
- Celia, M.A., Bouloutas, E.T., and Zarba, R.L. 1990. A general mass-conservative numerical solution for the unsaturated flow equation. *Water Resources Research* **26**(7): 1483-1496. doi: doi:10.1029/WR026i007p01483.
- Cha, M., and Santamarina, J.C. 2014. Dissolution of randomly distributed soluble grains: post-dissolution k_0 -loading and shear. *Géotechnique* **64**(10): 828-836. doi: 10.1680/geot.14.P.115.
- Cha, M., and Santamarina, J.C. 2016. Effect of dissolution on the load–settlement behavior of shallow foundations. *Canadian Geotechnical Journal* **53**(8): 1353-1357. doi: 10.1139/cgj-2014-0370.
- Cho, W.J., Lee, J.O., and Chun, K.S. 1999. The temperature effects on hydraulic conductivity of compacted bentonite. *Applied Clay Science* **14**(1): 47-58.
- Cordero, J.A., Useche, G., Prat, P.C., Ledesma, A., and Santamarina, J.C. 2017. Soil desiccation cracks as a suction–contraction process. *Géotechnique Letters* **7**(4): 279-285. doi: 10.1680/jgele.17.00070.
- Corte, A.E., and Higashi, A. 1960. Experimental research on desiccation cracks in soil. **66**.
- Costa, S., Kodikara, J., and Shannon, B. 2013. Salient factors controlling desiccation cracking of clay in laboratory experiments. *Géotechnique* **63**(1): 18-29. doi: 10.1680/geot.9.P.105.
- Costa, W.D.S.M. 2009. Study of desiccation cracking and fracture properties of clay soils. Doctor of Philosophy Ph.D Thesis, Monash University.
- Cui, Y., Chan, D., and Nouri, A. 2017a. Coupling of solid deformation and pore pressure for undrained deformation—a discrete element method approach. *International Journal for Numerical and Analytical Methods in Geomechanics* **41**(18): 1943-1961. doi: 10.1002/nag.2708.
- Cui, Y., Chan, D., and Nouri, A. 2017b. Discontinuum Modeling of Solid Deformation Pore-Water Diffusion Coupling. *International Journal of Geomechanics* **17**(8): 04017033. doi: 10.1061/(ASCE)GM.1943-5622.0000903.

- Cundall, P.A., and Strack, O.D.L. 1979. A discrete numerical model for granular assemblies. *Géotechnique* **29**(1): 47-65. doi: 10.1680/geot.1979.29.1.47.
- Dagan, G. 1993. Higher-order correction of effective permeability of heterogeneous isotropic formations of lognormal conductivity distribution. *Transport in Porous Media* **12**(3): 279-290. doi: 10.1007/bf00624462.
- Dantec. 2017. Software manual Q-400 system. Dantec Dynamics, Denmark.
- Davarzani, H., Smits, K., Tolene, R.M., and Illangasekare, T. 2014. Study of the effect of wind speed on evaporation from soil through integrated modeling of the atmospheric boundary layer and shallow subsurface. *Water Resources Research* **50**(1): 661-680.
- Duan, K., Kwok, C.Y., Wu, W., and Jing, L. 2018. DEM modeling of hydraulic fracturing in permeable rock: influence of viscosity, injection rate and in situ states. *Acta Geotechnica* **13**(5): 1187-1202. doi: 10.1007/s11440-018-0627-8.
- Elbert Walter LeFevre, J. 1966. Soil plasticity dependency on surface area. Doctor of Philosophy Ph.D Thesis, Oklahoma State University.
- Eymard, R., Gutnic, M., and Hilhorst, D. 1999. The finite volume method for Richards equation. *Computational Geosciences* **3**(3): 259-294. doi: 10.1023/a:1011547513583.
- Fantech. 2008. Compact 2000 series. Fantech Pty. Ltd.
- Feddes, R.A., Kabat, P., Van Bakel, P.J.T., Bronswijk, J.J.B., and Halbertsma, J. 1988. Modelling soil water dynamics in the unsaturated zone — State of the art. *Journal of Hydrology* **100**(1): 69-111. doi: 10.1016/0022-1694(88)90182-5.
- Foster, M., Fell, R., and Spannagle, M. 2000. The statistics of embankment dam failures and accidents. *Canadian Geotechnical Journal* **37**(5): 1000-1024.
- Fredlund, D.G., and Rahardjo, H. 1993. Soil mechanics for unsaturated soils. John Wiley & Sons, Inc., New York.
- Fredlund, D.G., and Xing, A. 1994. Equations for the soil-water characteristic curve. *Canadian Geotechnical Journal* **31**(4): 521-532. doi: 10.1139/t94-061.
- Gan, Y., Maggi, F., Buscarnera, G., and Einav, I. 2013. A particle–water based model for water retention hysteresis. *Géotechnique Letters* **3**(4): 152-161. doi: 10.1680/geolett.13.00046.
- Ghazizade, M.J., and Safari, E. 2016. Analysis of Desiccation Crack Depth in Three Compacted Clay Liners Exposed to Annual Cycle of Atmospheric Conditions with and without a Geotextile Cover. *Journal of Geotechnical and Geoenvironmental Engineering*.
- Gili, J.A., and Alonso, E.E. 2002. Microstructural deformation mechanisms of unsaturated granular soils. *International Journal for Numerical and Analytical Methods in Geomechanics* **26**(5): 433-468. doi: doi:10.1002/nag.206.
- Gottardi, G., and Venutelli, M. 1993. Richards: Computer program for the numerical simulation of one-dimensional infiltration into unsaturated soil. *Computers & Geosciences* **19**(9): 1239-1266. doi: 10.1016/0098-3004(93)90028-4.

- Groisman, A., and Kaplan, E. 1994. An Experimental Study of Cracking Induced by Desiccation. *EPL (Europhysics Letters)* **25**(6): 415.
- Gui, Y. 2014. Desiccation cracking in unsaturated soils. Doctor of Philosophy Ph.D Thesis, The University of New South Wales.
- Gui, Y., and Zhao, G.F. 2015. Modelling of laboratory soil desiccation cracking using DLSSM with a two-phase bond model. *Computers and Geotechnics* **69**: 578-587.
- Gui, Y.L., Zhao, Z.Y., Kodikara, J., Bui, H.H., and Yang, S.Q. 2016. Numerical modelling of laboratory soil desiccation cracking using UDEC with a mix-mode cohesive fracture model. *Engineering Geology* **202**: 14-23. doi: 10.1016/j.enggeo.2015.12.028.
- Guo, Y., Han, C., and Yu, X. 2017. Laboratory characterization and discrete element modeling of shrinkage and cracking in clay layer. *Canadian Geotechnical Journal* **55**(5): 680-688. doi: 10.1139/cgj-2016-0674.
- Ha, N.S., Le, V.T., and Goo, N.S. 2017. Investigation of fracture properties of a piezoelectric stack actuator using the digital image correlation technique. *International Journal of Fatigue* **101**: 106-111.
- Ha, N.S., Le, V.T., and Goo, N.S. 2018. Investigation of punch resistance of the *Allomyrma dightoni* beetle forewing. *Journal of Bionic Engineering* **15**(1): 57-68. doi: 10.1007/s42235-017-0004-6.
- Ha, N.S., Vang, H.M., and Goo, N.S. 2015. Modal Analysis Using Digital Image Correlation Technique: An Application to Artificial Wing Mimicking Beetle's Hind Wing. *Experimental Mechanics* **55**(5): 989-998. doi: 10.1007/s11340-015-9987-2.
- Hasatani, M., Itaya, Y., and Hayakawa, K.-i. 1992. - VISCOELASTIC STRAIN-STRESS AND HEAT/MOISTURE TRANSFER. *Drying Technology* **10**(4): 1013-1036. doi: 10.1080/07373939208916493.
- Haverkamp, R., and Vauclin, M. 1979. A note on estimating finite difference interblock hydraulic conductivity values for transient unsaturated flow problems. *Water Resources Research* **15**(1): 181-187. doi: doi:10.1029/WR015i001p00181.
- Haverkamp, R., Vauclin, M., Touma, J., Wierenga, P.J., and Vachaud, G. 1977. A comparison of numerical simulation models for one-dimensional infiltration. *Soil Science Society of America Journal* **41**(2): 285-294. doi: 10.2136/sssaj1977.03615995004100020024x.
- Hernández, M.A.G., López, A.I.M., Jarzabek, A.A., Perales, J.M.P., Wu, Y., and Xiaoxiao, S. 2013. Design Methodology for a Quick and Low-Cost Wind Tunnel *In Wind Tunnel Designs and Their Diverse Engineering Applications*. Edited by N.A. Ahmed. InTechOpen. pp. 3-28.
- Hillel, D. 2003. *Introduction to Environmental Soil Physics*. Academic Press, Burlington.
- Hirobe, S., and Oguni, K. 2016. Coupling analysis of pattern formation in desiccation cracks. *Computer Methods in Applied Mechanics and Engineering* **307**: 470-488.
- Houlsby, G.T. 1997. The work input to an unsaturated granular material. *Géotechnique* **47**(1): 193-196. doi: 10.1680/geot.1997.47.1.193.

- Huat, B.B.K., Ali, F.H., and Choong, F.H. 2006. Effect of loading rate on the volume change behavior of unsaturated residual soil. *Geotechnical & Geological Engineering* **24**(6): 1527. doi: 10.1007/s10706-005-3366-1.
- Itasca. 2008. PFC 2D&3D user's manual, Itasca, Minneapolis.
- Iwashita, K., and Oda, M. 1998. Rolling Resistance at Contacts in Simulation of Shear Band Development by DEM. *Journal of Engineering Mechanics* **124**(3): 285-292. doi: 10.1061/(ASCE)0733-9399(1998)124:3(285).
- Jiang, M., Shen, Z., and Wang, J. 2015. A novel three-dimensional contact model for granulates incorporating rolling and twisting resistances. *Computers and Geotechnics* **65**: 147-163. doi: 10.1016/j.compgeo.2014.12.011.
- Jiang, M.J., Leroueil, S., and Konrad, J.M. 2004. Insight into shear strength functions of unsaturated granulates by DEM analyses. *Computers and Geotechnics* **31**(6): 473-489. doi: 10.1016/j.compgeo.2004.07.001.
- Kalkan, E. 2009. Influence of silica fume on the desiccation cracks of compacted clayey soils. *Applied Clay Science* **43**(3-4): 296-302.
- Kayyal, M.K. 1995. Effect of the moisture evaporative stages on the development of shrinkage cracks in soil. *In Proceedings of First International Conference on Unsaturated Soils*. pp. 373-379.
- Kharaghani, A., Metzger, T., and Tsotsas, E. 2012. An irregular pore network model for convective drying and resulting damage of particle aggregates. *Chemical Engineering Science* **75**: 267-278. doi: 10.1016/j.ces.2012.03.038.
- Kindle, E.M. 1917. Some factors affecting the development of mud-cracks. *The Journal of Geology* **25**(2): 135-144.
- Kindle, E.M. 1923. Notes on mud crack and ripple mark in recent calcareous sediments. *The Journal of Geology* **31**(2): 138-145. doi: 10.1086/622990.
- Kodikara, J., and Costa, S. 2013. Desiccation Cracking in Clayey Soils: Mechanisms and Modelling. *In Multiphysical Testing of Soils and Shales. Edited by L. Laloui and A. Ferrari*. Springer Berlin Heidelberg, Berlin, Heidelberg. pp. 21-32.
- Kodikara, J.K., and Choi, X. 2006. A Simplified Analytical Model for Desiccation Cracking of Clay Layers in Laboratory Tests. *In Unsaturated Soils 2006*. pp. 2558-2569.
- Kodikara, J.K., Nahlawi, H., and Bouazza, A. 2004. Modelling of curling in desiccating clay. *Canadian Geotechnical Journal* **41**(3): 560-566. doi: 10.1139/t04-015.
- Konrad, J.M., and Ayad, R. 1997. A idealized framework for the analysis of cohesive soils undergoing desiccation. *Canadian Geotechnical Journal* **34**(4): 477-488.
- Lakshmikantha, M.R., Prat, P.C., and Ledesma, A. 2012. Experimental evidence of size effect in soil cracking. *Canadian Geotechnical Journal* **49**(3): 264-284.
- Lambert, P., Chau, A., Delchambre, A., and Régnier, S. 2008. Comparison between Two Capillary Forces Models. *Langmuir* **24**(7): 3157-3163. doi: 10.1021/la7036444.

- Le, T.M.H., Gallipoli, D., Sanchez, M., and Wheeler, S.J. 2012. Stochastic analysis of unsaturated seepage through randomly heterogeneous earth embankments. *International Journal for Numerical and Analytical Methods in Geomechanics* **36**(8): 1056-1076. doi: 10.1002/nag.1047.
- Le, T.M.H., Sanchez, M., Gallipoli, D., and Wheeler, S. 2019. Probabilistic Study of Rainfall-Triggered Instabilities in Randomly Heterogeneous Unsaturated Finite Slopes. *Transport in Porous Media* **126**(1): 199-222. doi: 10.1007/s11242-018-1140-0.
- Lee, J.-S., Tran, M.K., and Lee, C. 2012. Evolution of layered physical properties in soluble mixture: Experimental and numerical approaches. *Engineering Geology* **143-144**: 37-42. doi: 10.1016/j.enggeo.2012.06.008.
- Levatti, H., Prat, P., Ledesma, A., Cuadrado, A., and Cordero, J. 2017. Experimental Analysis of 3D Cracking in Drying Soils Using Ground-Penetrating Radar. *Geotechnical Testing Journal* **40**(2): 221-243. doi: 10.1520/GTJ20160066.
- Levatti, H.U., Prat, P.C., and Ledesma, A. 2019. Numerical and experimental study of initiation and propagation of desiccation cracks in clayey soils. *Computers and Geotechnics* **105**: 155-167. doi: 10.1016/j.compgeo.2018.09.015.
- Liu, C., Tang, C.-S., Shi, B., and Suo, W.-B. 2013. Automatic quantification of crack patterns by image processing. *Computers & Geosciences* **57**: 77-80. doi: 10.1016/j.cageo.2013.04.008.
- Longwell, C.R. 1928. Three common types of desert mud cracks. *American Journal of Science* **15**(86): 136-145. doi: 10.2475/ajs.s5-15.86.136.
- Lytton, R.L., Boggess, R.L., and Spotts, J.W. 1976. Characteristics of expansive clay roughness of pavements. *In* 54th Annual Meeting of the Transportation Research Board. Transportation Research Board. pp. 9-23.
- Manzoli, O., Sánchez, M., Maedo, M., Hajjat, J., and Guimarães, L.J.N. 2018. An orthotropic interface damage model for simulating drying processes in soils. *Acta Geotechnica* **13**(5): 1171-1186. doi: 10.1007/s11440-017-0608-3.
- Minter, W.E.L. 1970. Origin of mud polygons that are concave downward: notes. *Journal of Sedimentary Research* **40**(2): 755-756.
- Mitchell, J.K., and Soga, K. 2005. *Fundamentals of Soil Behavior*. 3rd Edition ed. John Wiley & Sons, Inc.
- Moës, N., Dolbow, J., and Belytschko, T. 1999. A finite element method for crack growth without remeshing. *International Journal for Numerical Methods in Engineering* **46**(1): 131-150. doi: 10.1002/(sici)1097-0207(19990910)46:1<131::aid-nme726>3.0.co;2-j.
- Morris, P.H., Graham, J., and Williams, D.J. 1992. Cracking in drying soils. *Canadian Geotechnical Journal* **29**(2): 263-277.
- Muhunthan, B. 1991. Liquid limit and surface area of clays. *Géotechnique* **41**(1): 135-138. doi: 10.1680/geot.1991.41.1.135.
- Nahlawi, H. 2004. Behaviour of a reactive soil during desiccation. Master of Engineering Science, Monash University.

- Nahlawi, H., Chakrabarti, S., and Kodikara, J. 2004. A Direct Tensile Strength Testing Method for Unsaturated Geomaterials. *Geotechnical Testing Journal* **27**(4): 356-361.
- Nahlawi, H., and Kodikara, J.K. 2006. Laboratory experiments on desiccation cracking of thin soil layers. *Geotechnical & Geological Engineering* **24**(6): 1641-1664.
- Neriah, A.B., Assouline, S., Shavit, U., and Weisbrod, N. 2014. Impact of ambient conditions on evaporation from porous media. *Water Resources Research* **50**: 6696–6712.
- Nguyen, N.H.T., Bui, H.H., Nguyen, G.D., and Kodikara, J. 2017. A cohesive damage-plasticity model for DEM and its application for numerical investigation of soft rock fracture properties. *International Journal of Plasticity* **98**: 175-196. doi: 10.1016/j.ijplas.2017.07.008.
- Parlange, J.-Y. 1971. Theory of water-movement in soils: 2. One-dimensional infiltration. *Soil Science* **111**(3): 170-174.
- Peron, H., Delenne, J.Y., Laloui, L., and El Youssoufi, M.S. 2009a. Discrete element modelling of drying shrinkage and cracking of soils. *Computers and Geotechnics* **36**(1–2): 61-69. doi: 10.1016/j.compgeo.2008.04.002.
- Peron, H., Hueckel, T., Laloui, L., and Hu, L.B. 2009b. Fundamentals of desiccation cracking of fine-grained soils: experimental characterisation and mechanisms identification. *Canadian Geotechnical Journal* **46**(10): 1177-1201.
- Peron, H., Laloui, L., Hu, L.-B., and Hueckel, T. 2013. Formation of drying crack patterns in soils: a deterministic approach. *Acta Geotechnica* **8**(2): 215-221.
- Peters, W.H., and Ranson, W.F. 1982. *Digital Imaging Techniques In Experimental Stress Analysis*. SPIE.
- Philip, J.R. 1957. The theory of infiltration: 1. The infiltration equation and its solution. *Soil Science* **83**(5): 345-358.
- Plum, R.L., and Esrig, M.I. 1969. Some temperature effects on soil compressibility and pore water pressure.
- Prat, M. 2002. Recent advances in pore-scale models for drying of porous media. *Chemical Engineering Journal* **86**(1): 153-164. doi: 10.1016/S1385-8947(01)00283-2.
- Rodríguez, R., Sánchez, M., Ledesma, A., and Lloret, A. 2007. Experimental and numerical analysis of desiccation of a mining waste. *Canadian Geotechnical Journal* **44**(6): 644-658. doi: 10.1139/t07-016.
- Safari, E., Ghazizade, M.J., Abduli, M.A., and Gatmiri, B. 2014. Variation of crack intensity factor in three compacted clay liners exposed to annual cycle of atmospheric conditions with and without geotextile cover. *Waste Management* **34**(8): 1408-1415.
- Sanchez, M., Atique, A., Kim, S., Romero, E., and Zielinski, M. 2013. Exploring desiccation cracks in soils using a 2D profile laser device. *Acta Geotechnica* **8**(6): 583-596.

- Sánchez, M., Manzoli, O.L., and Guimarães, L.J.N. 2014. Modeling 3-D desiccation soil crack networks using a mesh fragmentation technique. *Computers and Geotechnics* **62**: 27-39.
- Scholtès, L., Chareyre, B., Nicot, F., and Darve, F. 2009a. Discrete modelling of capillary mechanisms in multi-phase granular media. *Computer Modeling in Engineering and Sciences* **3**: 297-318. doi: 10.3970/cmcs.2009.052.297.
- Scholtès, L., Hicher, P.-Y., Nicot, F., Chareyre, B., and Darve, F. 2009b. On the capillary stress tensor in wet granular materials. *International Journal for Numerical and Analytical Methods in Geomechanics* **33**(10): 1289-1313. doi: 10.1002/nag.767.
- Shannon, B.M. 2013. Fracture propagation of cohesive soils under tensile loading and desiccation. Doctor of Philosophy Ph.D Thesis, Monash University.
- Shimizu, H., Murata, S., and Ishida, T. 2011. The distinct element analysis for hydraulic fracturing in hard rock considering fluid viscosity and particle size distribution. *International Journal of Rock Mechanics and Mining Sciences* **48**(5): 712-727. doi: 10.1016/j.ijrmms.2011.04.013.
- Shin, H., and Santamarina, J.C. 2011. Desiccation cracks in saturated fine-grained soils: particle-level phenomena and effective-stress analysis. *Géotechnique* **61**(11): 961-972. doi: 10.1680/geot.8.P.012.
- Shogaki, T. 2007. EFFECT OF SPECIMEN SIZE ON UNCONFINED COMPRESSIVE STRENGTH PROPERTIES OF NATURAL DEPOSITS. *SOILS AND FOUNDATIONS* **47**(1): 119-129. doi: 10.3208/sandf.47.119.
- Sima, J., Jiang, M., and Zhou, C. 2014. Numerical simulation of desiccation cracking in a thin clay layer using 3D discrete element modeling. *Computers and Geotechnics* **56**: 168-180. doi: 10.1016/j.compgeo.2013.12.003.
- Song, W.-K., Cui, Y.-J., Tang, A.M., Ding, W.-Q., and Tran, T.D. 2013. Experimental study on water evaporation from sand using environmental chamber. *Canadian Geotechnical Journal* **51**(2): 115-128. doi: 10.1139/cgj-2013-0155.
- Stirling, R.A., Glendinning, S., and Davie, C.T. 2017. Modelling the deterioration of the near surface caused by drying induced cracking. *Applied Clay Science* **146**: 176-185.
- Style, R.W., Peppin, S.S.L., and Cocks, A.C.F. 2011. Mud peeling and horizontal crack formation in drying clays. *Journal of Geophysical Research: Earth Surface* **116**(F1): F01025. doi: 10.1029/2010JF001842.
- Sutton, M.A., Orteu, J.-J., and Schreier, H. 2009. Image correlation for shape, motion and deformation measurements. Springer US, New York, USA.
- Sutton, M.A., Wolters, W.J., Peters, W.H., Ranson, W.F., and McNeill, S.R. 1983. Determination of displacements using an improved digital correlation method. *Image and Vision Computing* **1**(3): 133-139. doi: 10.1016/0262-8856(83)90064-1.
- Take, A. 2003. The Influence of Seasonal Moisture Cycles on Clay Slopes. Cambridge University.

- Tang, C.-S., Cui, Y.-J., Shi, B., Tang, A.-M., and Liu, C. 2011a. Desiccation and cracking behaviour of clay layer from slurry state under wetting–drying cycles. *Geoderma* **166**(1): 111-118.
- Tang, C.-S., Cui, Y.-J., Tang, A.-M., and Shi, B. 2010. Experiment evidence on the temperature dependence of desiccation cracking behavior of clayey soils. *Engineering Geology* **114**(3–4): 261-266.
- Tang, C.-S., Shi, B., Cui, Y.-J., Liu, C., and Gu, K. 2012. Desiccation cracking behavior of polypropylene fiber–reinforced clayey soil. *Canadian Geotechnical Journal* **49**(9): 1088-1101.
- Tang, C.-S., Shi, B., Liu, C., Gao, L., and Inyang, H.I. 2011b. Experimental Investigation of the Desiccation Cracking Behavior of Soil Layers during Drying. *Journal of Materials in Civil Engineering* **23**(6). doi: 10.1061/(ASCE)MT.1943-5533.0000242.
- Tang, C.-S., Shi, B., Liu, C., Suo, W.-B., and Gao, L. 2011c. Experimental characterization of shrinkage and desiccation cracking in thin clay layer. *Applied Clay Science* **52**(1–2): 69-77. doi: 10.1016/j.clay.2011.01.032.
- Tang, C.-S., Wang, D.-Y., Cui, Y.-J., Shi, B., and Li, J. 2016. Tensile Strength of Fiber-Reinforced Soil. *Journal of Materials in Civil Engineering* **28**(7): 04016031. doi: doi:10.1061/(ASCE)MT.1943-5533.0001546.
- Tang, C., Shi, B., Liu, C., Zhao, L., and Wang, B. 2008. Influencing factors of geometrical structure of surface shrinkage cracks in clayey soils. *Engineering Geology* **101**(3–4): 204-217.
- Teodosio, B., Baduge, K.S.K., Mendis, P., and Heath, D. 2019. Prefabrication of substructures for single-detached dwellings on reactive soils: a review of existing systems and design challenges. *Australian Journal of Civil Engineering*.
- Timoshenko, S.P., and Gere, J.M. 1985. *Theory of elastic stability*. 2nd edition ed. Dover Publications, Inc., Mineola, New York.
- Tollenaar, R.N. 2017. *Experimental Investigation on the Desiccation and Fracturing of Clay*. Doctor of Philosophy Ph.D Thesis, Delft University of Technology.
- Trabelsi, H., Jamei, M., Zenzri, H., and Olivella, S. 2012. Crack patterns in clayey soils: Experiments and modeling. *International Journal for Numerical and Analytical Methods in Geomechanics* **36**(11): 1410-1433.
- Tran, H.T., Wang, Y., Nguyen, G.D., Jayanth, K., Sanchez, M., and Bui, H.H. 2019. Modelling 3D desiccation cracking in clayey soils using a size-dependent SPH computational approach. *Computers and Geotechnics*. doi: 10.1016/j.compgeo.2019.103209.
- Tran, M.K., Byun, Y.-H., Shin, H.-S., and Lee, J.-S. 2011a. Behaviors of Soluble Granular Media during Particle Dissolution. *International Journal of Geo-Engineering* **3**(2): 39-49.
- Tran, M.K., Cho, S.-H., Byun, Y.-H., Shin, H.-S., and Lee, J.-S. 2011b. Particle Dissolution Effects on Soluble Geo-Mixtures. *Journal of the Korean Geoenvironmental Society* **12**(12): 5-12.

- Tran, M.K., Park, J.-H., Byun, Y.-H., Shin, H., and Lee, J.-S. 2011c. Shear Strength Characteristics of Geo - Soluble - Materials. **27**. doi: 10.7843/KGS.2011.27.12.017.
- Tran, M.K., Shin, H., Byun, Y.-H., and Lee, J.-S. 2012. Mineral dissolution effects on mechanical strength. *Engineering Geology* **125**: 26-34. doi: 10.1016/j.enggeo.2011.10.014.
- Tran, T.-H. 2019. A coupled hydro-mechanical SPH framework to model desiccation cracking in clay soils.
- Truong, Q.H., Eom, Y.H., and Lee, J.S. 2010. Stiffness characteristics of soluble mixtures. *Géotechnique* **60**(4): 293-297.
- Uday, K.V., and Singh, D.N. 2013. Investigation on Cracking Characteristics of Fine-Grained Soils Under Varied Environmental Conditions. *Drying Technology* **31**(11): 1255-1266. doi: 10.1080/07373937.2013.785433.
- Van Genuchten, M.T. 1980a. A closed-form equation for predicting the hydraulic conductivity of unsaturated soils. *Soil Science Society of America Journal* **44**(5): 892-898. doi: 10.2136/sssaj1980.03615995004400050002x.
- van Genuchten, M.T. 1980b. A Closed-form Equation for Predicting the Hydraulic Conductivity of Unsaturated Soils1. *Soil Science Society of America Journal* **44**(5): 892-898. doi: 10.2136/sssaj1980.03615995004400050002x.
- Vo, T.D., Pouya, A., Hemmati, S., and Tang, A.M. 2017. Numerical modelling of desiccation cracking of clayey soil using a cohesive fracture method. *Computers and Geotechnics* **85**: 15-27.
- Vo, T.D., Pouya, A., Hemmati, S., and Tang, A.M. 2018. Modelling desiccation crack geometry evolution in clayey soils by analytical and numerical approaches. *Canadian Geotechnical Journal* **56**(5): 720-729. doi: 10.1139/cgj-2018-0105.
- Wang, H., and Anderson, M. 1995. *Introduction to Groundwater Modeling: Finite Difference and Finite Element Methods*. 1 ed. Academic Press.
- Wang, J.-P., Li, X., and Yu, H.-S. 2018a. A micro–macro investigation of the capillary strengthening effect in wet granular materials. *Acta Geotechnica* **13**(3): 513-533. doi: 10.1007/s11440-017-0619-0.
- Wang, L.-L., Tang, C.-S., Shi, B., Cui, Y.-J., Zhang, G.-Q., and Hilary, I. 2018b. Nucleation and propagation mechanisms of soil desiccation cracks. *Engineering Geology* **238**: 27-35. doi: 10.1016/j.enggeo.2018.03.004.
- Wang, Y.H., and Xu, D. 2007. Dual Porosity and Secondary Consolidation. *Journal of Geotechnical and Geoenvironmental Engineering* **133**(7): 793-801. doi: doi:10.1061/(ASCE)1090-0241(2007)133:7(793).
- Ward, F. 1923. Note on mud cracks. *American Journal of Science* **6**(34): 308-309.
- Wei, X., Hattab, M., Bompard, P., and Fleureau, J.-M. 2016. Highlighting some mechanisms of crack formation and propagation in clays on drying path. *Géotechnique* **66**(4): 287-300.

- Wilson, G.W., Fredlund, D.G., and Barbour, S.L. 1994. Coupled soil-atmosphere modelling for soil evaporation. *Canadian Geotechnical Journal* **31**(2): 151-161. doi: 10.1139/t94-021.
- Yao, M., and Anandarajah, A. 2003. Three-Dimensional Discrete Element Method of Analysis of Clays *Journal of Engineering Mechanics* **129**(6): 585-596. doi: 10.1061/(ASCE)0733-9399(2003)129:6(585).
- Yesiller, N., Miller, C.J., Inci, G., and Yaldo, K. 2000. Desiccation and cracking behavior of three compacted landfill liner soils. *Engineering Geology* **57**(1–2): 105-121.
- Yuan, C., and Chareyre, B. 2017. A pore-scale method for hydromechanical coupling in deformable granular media. *Computer Methods in Applied Mechanics and Engineering* **318**: 1066-1079. doi: 10.1016/j.cma.2017.02.024.
- Yuan, C., Chareyre, B., and Darve, F. 2018. Deformation and stresses upon drainage of an idealized granular material. *Acta Geotechnica* **13**(4): 961-972. doi: 10.1007/s11440-017-0601-x.
- Zaidel, J., and Russo, D. 1992. Estimation of finite difference interblock conductivities for simulation of infiltration into initially dry soils. *Water Resources Research* **28**(9): 2285-2295. doi: doi:10.1029/92WR00914.
- Zapata, C.E., Houston, W.N., Houston, S.L., and Walsh, K.D. 2000. Soil–water characteristic curve variability. *In Advances in Unsaturated Geotechnics*.
- Zaradny, H. 1978. Boundary conditions in modelling water flow in unsaturated soils. *Soil Science* **125**(2): 75-82.
- Zhang, D. 1998. Numerical solutions to statistical moment equations of groundwater flow in nonstationary, bounded, heterogeneous media. *Water Resources Research* **34**(3): 529-538. doi: 10.1029/97wr03607.
- Zhang, X.-D., Chen, Y.-G., Ye, W.-M., Cui, Y.-J., Deng, Y.-F., and Chen, B. 2017. Effect of salt concentration on desiccation cracking behavior of GMZ bentonite. *Environmental Earth Sciences* **76**(15): 531. doi: 10.1007/s12665-017-6872-6.
- Zhao, G.-F., Fang, J., and Zhao, J. 2011. A 3D distinct lattice spring model for elasticity and dynamic failure. *International Journal for Numerical and Analytical Methods in Geomechanics* **35**(8): 859-885. doi: 10.1002/nag.930.
- Zielinski, M., Sánchez, M., Romero, E., and Atique, A. 2014. Precise observation of soil surface curling. *Geoderma* **226–227**: 85-93. doi: 10.1016/j.geoderma.2014.02.005.
- Zienkiewicz, O.C., Huang, M., and Pastor, M. 1995. Localization problems in plasticity using finite elements with adaptive remeshing. *International Journal for Numerical and Analytical Methods in Geomechanics* **19**(2): 127-148. doi: doi:10.1002/nag.1610190205.